**This document is downloaded from DR-NTU (https://dr.ntu.edu.sg)
Nanyang Technological University, Singapore.**

Structural and functional insights into subunit a of Saccharomyces cerevisiae V-ATPase and the Escherichia coli Alkyl Hydroperoxide Reductase complex

Phat Vinh, Dip

2014

Phat Vinh, D. (2014). Structural and functional insights into subunit a of Saccharomyces cerevisiae V-ATPase and the Escherichia coli Alkyl Hydroperoxide Reductase complex. Doctoral thesis, Nanyang Technological University, Singapore.

https://hdl.handle.net/10356/55395

https://doi.org/10.32657/10356/55395

Downloaded on 20 Mar 2024 16:23:04 SGT

STRUCTURAL AND FUNCTIONAL INSIGHTS INTO SUBUNIT *a* OF *SACCHAROMYCES CEREVISIAE* V-ATPase AND THE *ESCHERICHIA COLI* ALKYL HYDROPEROXIDE REDUCTASE COMPLEX

PHAT VINH DIP

SCHOOL OF BIOLOGICAL SCIENCES

2014

STRUCTURAL AND FUNCTIONAL INSIGHTS INTO SUBUNIT *a* OF *SACCHAROMYCES CEREVISIAE* V-ATPASE AND THE *ESCHERICHIA COLI* ALKYL HYDROPEROXIDE REDUCTASE COMPLEX

PHAT VINH DIP

SCHOOL OF BIOLOGICAL SCIENCES

A thesis submitted to the Nanyang Technological University
in partial fulfilment of the requirement for the degree of
Doctor of Philosophy

2014

Acknowledgments

First of all I would like to give my sincere gratitude to my doctoral advisor (‘German Doktorvater’) Professor Dr. Dr. Gerhard Grüber, for his expertise and great encouragement. Without his guidance, support and patience, this thesis would not have been possible. He shared on countless moments his infinite knowledge and wealth of experience and this has provided a great learning experience for me. After all, he opened my eyes and taught me to see science from a different perspective.

Furthermore, I would like to give a special gratitude to Prof. Dr. Marshansky and Dr. Maria Merkulova for our extremely fruitful V-ATPase - ARNO collaboration during my PhD study. Moreover, I would like to give a cordial appreciation to Prof. Dr. Shee Mei Lok and especially her lab members Jonathan Ng Thiam Seng for imaging AhpC using cryo EM and Dr. Victor Kostyuchenko for his help in reconstructing the AhpC cryo EM structure. I would also like to give Prof. Dr. Manfred Roessle a special thank you for his effort in collecting $Sca_{104\text{-}363}$ and *Ec*AhpF SAXS data.

I am extremely thankful to Dr. Asha Balakrishna for her invaluable advice in crystallography, in particular for the crystallisation and the structural determination of *Ec*AhpF and *Ec*AhpC that actually made this thesis so wonderful. Furthermore, I am extraordinarily grateful to Dr. Ardina Grüber for her help and suggestions in crystallising the $a_{653\text{-}727}$ construct and for initial training in the field of protein crystallography that will surely help me a lot. I am exceptionally thankful to Dr. Malathy Sony Subramanian Manimekalai for her invaluable knowledge, helpful suggestions and fruitful discussions during the X-ray data collection of *Ec*AhpF and *Ec*AhpC in NSRRC (Taiwan) and during the *Ec*AhpF and *Ec*AhpC crystal structure determination as well as the solution structure determination of *Ec*AhpF and $Sca_{104\text{-}363}$ using SAXS. Moreover, I am enormously grateful and happy to work with Dr. Neelagandan Kamariah in our *Ec*AhpF and *Ec*AhpC project, who shared his exceptional ideas and scientific knowledge all the time with me. Further I would like to express my sincere thanks to Dr. Shovanlal Gayen to train me initially how to handle the NMR machine and for his guidance in structure determination of $a2_{1\text{-}17}$ and $a2_{368\text{-}395}$. Furthermore, I would like to thank Dr. Sankaranarayanan Rishikesan and Dr. Lim Jack Wee for their enthusiastic help and discussion in NMR, especially during the subunit *a*-Sec7 domain titration experiments. I am very thankful to Ms. Saw Wuan Geok for her enthusiasm and cooperative team work in our $Sca_{104\text{-}363}$ / $Sca_{106\text{-}324}$ project and for her comments and suggestions to this thesis. Many special thanks to Dr. Cornelia Hunke and Dr. Goran Biuković for their help and advice in molecular biology and

protein purification. In particular Dr. Cornelia Hunke, who made my stay in Singapore a wonderful experience with her bag of tricks and surprises. Beyond that I wish to thank Dr. Toh Yew Kwang for our scientific discussion and for reading this thesis. I owe a very special thanks to the alumni of our lab Dr. Youg Raj Thaker, who introduced and guided me initially in V-ATPase subunit *a* project, Dr. Anil Kumar, Dr. Vikram Singh Tadwal and Dr. Priya Ragunathan. Furthermore, I owe special thanks to my colleagues, Ms. Lavenya Sundararaman, Mr. Dhirendra Singh, Mr. Wilson Nartey and Ms. Claudia Karin Beushausen and to all my friends at NTU for all their help, support, interest and valuable hints as well.

After all, I would like to give a very special gratitude to my dear friend Sandip Basak, for his support, valuable suggestions and his helping hand through my entire PhD study.

I gratefully acknowledge the financial support rendered by A*STAR, SINGA (Singapore International Graduate Award) scholarship. I am also grateful to the academic and technical staff and facilities at the School of Biological Sciences, who have helped me in one way or another in my research work. I would also wish to acknowledge A*STAR BMRC (09/1/22/19/609) for the research support granted.

Last but not least, my heartily gratitude goes to my parents who are always proud of my academic achievements for their selfless support, encouragement, unconditional love and pure understanding during my study in Singapore. I also thank all my siblings heartily for inspiring, encouraging and supporting me to reach this stage.

dedicated to my mum and dad

Table of contents

ACKNOWLEDGMENTS I

TABLE OF CONTENTS IV

LIST OF FIGURES VII

ABBREVIATIONS X

ABSTRACT XII

1. INTRODUCTION 1

1.1 Eukaryotic V_1V_O ATPase (V-ATPase) 2
- 1.1.1. Function and regulation of V_1V_O ATPases 2
- 1.1.2 Structural feature of V_1V_O ATPases 4
- 1.1.3 Subunit *a* of V-ATPases 8
- 1.1.4 Cellular and physiological relevance of subunit *a* 10

1.2 Alkyl Hydroperoxide Reductase (AhpR), a response to oxidative stress 14
- 1.2.1 Alkyl hydroperoxide reductase system 18
- 1.2.2 Catalytic cycle of AhpF 21
- 1.2.3 Catalytic cycle of AhpC 23

1.3 Goals of this thesis 25

2. MATERIALS AND METHODS 26

2.1 Materials 28
- 2.1.1 Chemicals 28
- 2.1.1.1 Buffers and salts 28
- 2.1.2 Molecular biology materials 28
- 2.1.3 Chromatography materials 29
- 2.1.4 Gel filtration 29
- 2.1.5 Instruments and accessories 29
- 2.1.6 Protein concentration, estimation 29
- 2.1.7 Other instrumentation 29
- 2.1.8 Computer software 29

2.2 Cloning of subunit *a* (Vph1) constructs from *S. cerevisiae* V_1V_O ATPase 31
- 2.2.1 Electroporation transformation 33

2.3 Production and purification protein constructs 34
- 2.3.1 Induction test 34
- 2.3.2 Solubility test for recombinant proteins 34
- 2.3.3 Purification of $a_{104\text{-}363}$ construct of the *S. cerevisiae* V_1V_O-ATPase 35
- 2.3.4 Purification of $a_{104\text{-}363}$, $a_{653\text{-}727}$, $a_{582\text{-}649}$, $a_{673\text{-}731}$ *and* $a_{801\text{-}840}$ constructs 35
- 2.3.5 Purification of $a_{1\text{-}388}$ construct from *S. cerevisiae* 36
- 2.3.6 Purification of Sec7- domain of ARNO from human (*Homo sapiens)* 36
- 2.3.7 Purification of Alkyl Hydroperoxide Reductase subunit F (AhpF) from *E. coli* 37
- 2.3.8 Purification of Alkyl Hydroperoxide Reductase subunit C (AhpC) from *E. coli* 37

2.4 Western blotting 38

2.5 Quantification of proteins by bicinchoninic acid (BCA) method 39

2.6 Circular dichroism spectroscopy 39

2.7 Dynamic light scattering (DLS) 39

2.8 NADH dependent peroxidase activity 40

2.9 Solution X-ray scattering experiments and data analysis 40

2.10 *In silico* Sec7 and *a2*$_{1-17}$ docking experiments 42

2.11 Nuclear magnetic resonance (NMR) spectroscopy 42
2.11.1 ^{15}N single and ^{13}C ^{15}N double labelling of proteins 42
2.11.2 One dimensional (1D) ^{1}H and multi-dimensional (2D, 3D) ^{13}C-^{15}N NMR spectroscopy 43
2.11.3 NMR spectroscopy of *a2*$_{1-17}$ and *a2*$_{368-395}$ from *M. musculus* 43
2.11.4 Binding studies with NMR spectroscopy 44

2.12 Single Particle Reconstruction (SPR) using cryo-electron microscopy 44
2.12.1 Cryo-EM image collection and processing 44

2.13 Crystallisation of protein constructs 45
2.13.1 Crystallisation of subunit *a* constructs 45
2.13.2 Crystallisation of AhpF from *E. coli* 46
2.13.3 Crystallisation of *E. coli* AhpC 47

2.14 Crystal diffraction analysis of crystals 47

2.15 Data collection 47

2.16 Crystal structure determination 48
2.16.1 Crystal structure determination of *E. coli* AhpF 48
2.16.2 Crystal structure determination of *E. coli* AhpC 48

3. RESULTS 50

3.1 N-terminal segment of subunit *a* is involved in V-ATPase / ARNO association 52
3.1.1 Interaction studies between subunit *a2* of V-ATPase and Sec7 domain of ARNO from *M. musculus* 54
3.1.2 Secondary structure content of *a2*$_{1-17}$ 54
3.1.3 NMR solution structure of *a2*$_{1-17}$ from *Mus musculus* 55
3.1.4 NMR titration of *a2*$_{1-17}$ (*M. musculus*) with human Sec7 domain of ARNO 58
3.1.5 Secondary structural characteristics of subunit *a2*$_{368-395}$ from *Mus musculus* 60
3.1.6 Amino acid residue assignment for structure calculation of *a2*$_{368-395}$ 61
3.1.7 Structure calculation of *a2*$_{368-395}$ from *Mus musculus* 62
3.1.8 Nuclear magnetic resonance spectroscopy of Sec7 domain of ARNO from *H. sapiens* 64

3.2 Solution structure of V-ATPase subunit *a*$_{104-363}$ derived by SAXS revealing the importance of its C-terminus 70
3.2.1 Production, purification and secondary structure analysis of subunit *a*$_{104-363}$ of the *S. cerevisiae* V-ATPase 72
3.2.2 NMR titration experiments of *S. cerevisiae a*$_{104-363}$ and human Sec7 domain of ARNO 73
3.2.3 Solution structure of *S. cerevisiae* V-ATPase subunit *a*$_{104-363}$ derived using SAXS 75

3.3 Insights into the C-terminal transmembrane domain of the *S. cerevisiae* V-ATPase subunit *a* 78
3.3.1 Expression and purification of *a*$_{582-649}$, *a*$_{673-731}$ and *a*$_{653-727}$ 80
3.3.2 Secondary structure content of subunit *a*$_{582-649}$ and *a*$_{653-727}$ 82
3.3.3 Crystallisation of subunit *a*$_{653-727}$ from *S. cerevisiae* 82

3.4 The open conformation of Alkyl Hydroperoxide Reductase subunit F (AhpF) from *E. coli* at 2 Å resolution using X-ray crystallography 86
3.4.1 Alkyl Hydroperoxide Reductase system against oxidative stress 88
3.4.2 Production and purification of AhpF from *E. coli* 88
3.4.3 NADH dependent peroxidative activity assay of AhpF from *E. coli* 90
3.4.4 Low resolution structure of *E. coli* AhpF in solution 91
3.4.5 Crystallisation and data collection of AhpF crystals from *E. coli* 93
3.4.6 Data collection and structure determination of AhpF from *E. coli* 96
3.4.7 Crystal structure of AhpF from *E. coli* 100

3.5 Alkyl Hydroperoxide Reductase subunit C (AhpC) crystal structure from *E. coli* at 3.3 Å resolution in its oxidised form 108
3.5.1 Production and purification of AhpC from *E. coli* under oxidised condition 110
3.5.2 Crystallisation, data collection and structure determination of AhpC crystals 110
3.5.3 Crystal structure of AhpC from *E. coli* 113

3.6 Single Particle Reconstruction of *E. coli* AhpC in reduced form using Cryo-Electron Microscopy at 12 Å resolution 118

3.6.1 Production and purification of AhpC from *E. coli* under reducing condition 120
3.6.2 Dynamic Light Scattering (DLS) of reduced and oxidised form of AhpC 120
3.6.3 Single Particle Reconstruction (SPR) of AhpC from *E. coli* 121

4. DISCUSSION 126

4.1 Structural characterisation of subunit *a* binding to ARNO 128

4.2 Solution structure of the N-terminal segment of subunit *a*, $a_{104-363}$ from *S. cerevisiae* V-ATPase 131

4.3 Characterisation of the putative C-terminal topology of subunit *a* 134

4.4 Crystallisation of subunit *a* construct $a_{653-727}$ 137

4.5 Structural and functional characterisation of AhpR from *E. coli* 138

4.5.1 The overall structure of AhpF from *E. coli* reveals an elongated conformation 138
4.5.2 The elongated conformation of AhpF gives new insights into its catalytic cycle 139
4.5.3 The putative catalytic cycle of *Ec*AhpF 144
4.5.4 The redox active sites of AhpF from *E. coli* 148

4.6 Structural characterisation of AhpC from *E. coli* 150

4.6.1 The catalytic cycle of AhpC from *E. coli* 151
4.6.2 The decameric ring formation of AhpC from *E. coli* 154
4.6.3 The importance of the open conformation of AhpF and decameric ring formation of AhpC for the catalytic activity of AhpR from *E. coli* 159

5. CONCLUSIONS 166

6. REFERENCES 170

7. AUTHOR'S PUBLICATION RELATED TO THE PROJECTS 191

8. CONFERENCE ATTENDANCE 191

9. POSTERS AND ABSTRACTS 191

10. AWARDS 192

List of figures

Introduction

Figure 1.1: Model and localisation of V-ATPases. 2
Figure 1.2: Physiological roles of V-ATPases. 3
Figure 1.3: 3-D cryo-EM structure of V_1V_O ATPase from *S. cerevisiae* at 11 Å resolution. 6
Figure 1.4: Crystal structures of V-ATPase subunits. 7
Figure 1.5: Cartoon presentation of central stalk subunit F. 7
Figure 1.6: Fitting of V-ATPase crystal structures into EM structure of V-ATPase from *S. cerevisiae*. 8
Figure 1.7: Topological model of subunit *a*. 9
Figure 1.8: V-ATPase in endosomal trafficking and degradation pathways. 12
Figure 1.9: V-ATPases are linked to oxidative stress response in *S. cerevisiae*. 14
Figure 1.10: Exogenous and endogenous sources of hydrogen peroxide for *E. coli* cells. 16
Figure 1.11: OxyR operon for *ahpC* and *ahpF* genes. 17
Figure 1.12: Crystal structures of the C-terminal portion of AhpF from *E. coli.* 18
Figure 1.13: AhpF Crystal structure from *Salmonella typhimurium.* 19
Figure 1.14: Electron transfer of the Alkyl Hydroperoxide Reductase (AhpR) system. 21
Figure 1.15: Crystal structures of Thioredoxin Reductase (TrxR) from *E. coli.* 22
Figure 1.16: The catalytic cycle of AhpC. 23

Material and Methods

Figure 2.1: Modified pET-9d (+) vector 32

Results

Figure 3.1: CD spectrum of $a2_{1-17}$ between 190-260 nm. 55
Figure 3.2: Analysis of 2D NMR spectra of $a2_{1-17}$. 56
Figure 3.3: NMR structures of $a2_{1-17}$ from *Mus musculus*. 57
Figure 3.4: NMR titration spectra of $a2_{1-17}$ (*M. musculus*) and human Sec7 domain of ARNO. 59
Figure 3.5: Chemical shift and loss of intensity plot of $a2_{1-17}$ and Sec7 domain of ARNO. 59
Figure 3.6: The binding region of $a2_{1-17}$ (*M. musculus*) to human Sec7 domain. 60
Figure 3.7: Secondary structure analysis of subunit $a2_{368-395}$. 61
Figure 3.8: HN-NH region of $a2_{368-395}$ NOESY spectrum and its connectivity plot. 62
Figure 3.9: NMR structure of peptide $a2_{368-395}$ from *Mus musculus*. 63
Figure 3.10: 1D NMR spectrum of the human Sec7 domain of ARNO. 65
Figure 3.11: HSQC Spectrum of the human Sec7-domain of ARNO. 65
Figure 3.12: HSQC titration experiment of the human Sec7-domain of ARNO and mouse $a2_{1-17}$. 66
Figure 3.13: HSQC titration experiment of the human Sec7-domain of ARNO upon titration of yeast a_{1-388}. 68
Figure 3.14: Sequence comparison of the cytosolic N-terminal region of subunit *a*. 72
Figure 3.15: Size exclusion chromatography of $a_{104-363}$ from *S. cerevisiae* and its CD spectrum. 73
Figure 3.16: NMR HSQC spectra of Sec7 / $a_{104-363}$ titration. 74
Figure 3.17: Experimental scattering pattern (●) and its corresponding fitting curves. 75
Figure 3.18: The solution structure of *S. cerevisiae* $a_{104-363}$ is depicted in green spheres. 76
Figure 3.19: Induction test from subunit *a* constructs: $a_{801-840}$, $a_{582-649}$, $a_{653-727}$, $a_{468-552}$ and $a_{673-731}$. 80
Figure 3.20: Solubility test of subunit *a* construct $a_{653-727}$. 80
Figure 3.21: Size exclusion chromatography of subunit *a* constructs from *S. cerevisiae.* 81
Figure 3.22*:* Far UV-CD spectrum of subunit $a_{582-649}$ and $a_{653-727}$. 82
Figure 3.23: Selected pictures of initial $a_{653-727}$ needles. 82
Figure 3.24: Crystal pictures of $a_{653-727}$ after temperature optimisation to 25 °C. 83
Figure 3.25: Selected pictures of $a_{653-727}$ crystals using Hampton research additive screen. 83
Figure 3.26: Selected pictures of $a_{653-727}$ crystals. 84
Figure 3.27: Purification of *E. coli* AhpF. 89
Figure 3.28: Spectroscopic analysis of *E. coli* AhpF. 90
Figure 3.29: NADH dependent peroxidase activity of *E. coli* AhpF. 91

Figure 3.30: Small angle X-ray scattering pattern. **92**
Figure 3.31: Solution structure of *E. coli* AhpF generated by Dammin software. **93**
Figure 3.32: Optimisation of *E. coli* AhpF crystals. **94**
Figure 3.33: Optimisation of *E. coli* AhpF crystals. **95**
Figure 3.34: Crystal structure determination strategy. **96**
Figure 3.35: Crystallisation and data collection of *E. coli* AhpF crystals. **97**
Figure 3.36: Preliminary *E. coli* AhpF crystal structure. **98**
Figure 3.37: Cartoon view of the *E. coli* AhpF crystal structure coloured by domain. **101**
Figure 3.38: Close view to the three redox active centres. **102**
Figure 3.39: Close view to the NTD structure. **103**
Figure 3.40: *E. coli* AhpF dimer coloured by its four distinct regions, respectively. **104**
Figure 3.41: Six coordinated bonds of the cadmium ion. **105**
Figure 3.42: AhpC purification in oxidised condition. **110**
Figure 3.43: Crystal photograph of recombinant *E. coli* AhpC. **111**
Figure 3.44: Crystal structure of oxidised AhpC from *E. coli.* **114**
Figure 3.45: Dimer structure of oxidised AhpC from *E. coli*. **115**
Figure 3.46: Oligomer interface of AhpC. **116**
Figure 3.47: *E. coli* AhpC purification under reducing condition. **120**
Figure 3.48: Dynamic Lights Scattering experiments of *E. coli* AhpC. **121**
Figure 3.49: Cryo EM structure determination strategy. **121**
Figure 3.50: Cryo electron microscopy images of *E. coli* AhpC. **122**
Figure 3.51: 3D reconstruction of AhpC using cryo EM in surface rendered presentation. **123**
Figure 3.52: Close view of one segment. **124**
Figure 3.53: Fourier shell correlation (FSC) coefficient function of AhpC cryo EM data set. **124**
Figure 3.54: Cryo Electron Microscopy images of AhpC in pH 4.4. **125**

Discussion

Figure 4.1: Putative binding site of the Sec7 domain to the $a2_{1\text{-}17}$ peptide. **130**
Figure 4.2: Superimposition of $a_{104\text{-}363}$ with the crystal structure of the homologous subunit *a* (*Mra*). **132**
Figure 4.3: Interaction model between $Sca_{104\text{-}363}$ (green) and Sec7 domain of ARNO. **133**
Figure 4.4: Proposed interaction model between V-ATPase and Sec 7 domain of ANRO. **134**
Figure 4.5: Model of subunit *a* from *S. cerevisiae*. **136**
Figure 4.6: Superimpose of the *E. coli* AhpF solution structure and its crystal structure. **138**
Figure 4.7: Structural comparison between *Ec*AhpF and *St*AhpF. **140**
Figure 4.8: Overlay of *Ec*AhpF and *St*AhpF B-factors. **141**
Figure 4.9: Structural comparison between *Ec*AhpF and TrxR-Trx complex from *E. coli*. **142**
Figure 4.10: The putative catalytic cycle of AhpF from *E. coli* shown in a monomeric conformation. **146**
Figure 4.11: The putative catalytic cycle of AhpF from *E. coli* in dimer formation. **147**
Figure 4.12: NADH binding pocket of *Ec*AhpF and TrxR from *E. coli*. **148**
Figure 4.13: The proposed electron transfer among the redox active centres in *Ec*AhpF. **149**
Figure 4.14: The proposed electron transfer between the redox active centre of *Ec*AhpF and *Ec*AhpC. **151**
Figure 4.15: Superposition of AhpC dimer crystal structures. **152**
Figure 4.16: Structural comparison between AhpC oxidised and reduced dimer crystal structures. **153**
Figure 4.17: Structural comparison between the crystal structure and 3D reconstruction of *Ec*AhpC. **154**
Figure 4.18: Superposition of AhpC crystal dimer structures and its corresponding 3D reconstruction. **155**
Figure 4.19: The close view to the hydrophobic oligomer interface between two dimer structures. **156**
Figure 4.20: The side view to the hydrophobic oligomer interface between two dimer structures. **157**
Figure 4.21: *Ec*AhpF crystal structure in dimer conformation. **160**
Figure 4.22: Crystal structure of AhpC from *E. coli*. **160**
Figure 4.23: Putative orientation of the catalytic active state of AhpR from *E. coli*. **161**
Figure 4.24: Putative catalytical model of *Ec*AhpR. **163**

List of tables

Introduction

Table 1.1: Subunits of the catalytic V_1 and proton translocating V_O domains of *S. cerevisiae* V-ATPase. 5

Results

Table 3.1: Structural statistics for $a2_{1-17}$. 58
Table 3.2: Structural statistics for peptide $a2_{368-395}$. 64
Table 3.3: Summary of crystallographic data collection for *E. coli* AhpF. 99
Table 3.4: Statistics of crystallographic refinement for *E. coli* AhpF. 106
Table 3.5: Data collection statistics to *E. coli* AhpC. 112
Table 3.6: Statistics of crystallographic refinement for *E. coli* AhpC. 116

Abbreviations

1D	One-dimensional
2D	Two-dimensional
3D	Three-dimensional
Å	Angström
AhpF	Alkyl Hydroperoxide Reductase subunit F
AhpC	Alkyl Hydroperoxide Reductase subunit C
ADP	Adenosine diphosphate
ATP	Adenosine triphosphate
BSA	Bovine Serum Albumin
CD	Circular Dichroism
CSI	Chemical shift index
DLS	Dynamic light scattering
DSS	2, 2-dimethyl-2-silapentane-5-sulphonate
DTT	Dithiothreitol
E. coli	*Escherichia coli*
EM	Electron microscopy
EDTA	Ethylenediaminetetraacetic acid
$FADH_2$	Flavin adenine dinucleotide
FPLC	Fast protein liquid chromatography
HSQC	Heteronuclear single quantum correlation
Hz	Hertz
IPTG	Isopropyl-β-D-thiogalactoside
kDa	kilo-Dalton
LLG	Log likelihood gain
NADH	Nicotinamide adenine dinucleotide
nm	Nanometre
NMR	Nuclear magnetic resonance
NOE	Nuclear Overhauser effect
NOESY	Nuclear Overhauser effect spectroscopy
NTA	Nitrilotriacetic acid
NTD	N-terminal domain
PAGE	Polyacrylamide Gel Electrophoresis

PCR	Polymerase Chain Reaction
PDB	Protein Data Bank
PPM	Parts per million
r.m.s.d.	Root mean square deviation
SDS	Sodium dodecyl sulphate
TFE	2,2,2-Trifluoroethanol
TOCSY	Total correlation spectroscopy
Tris	Tris-(hydroxymethyl) aminomethane

Abstract

Abstract

V_1V_O ATPases are complex multimeric proteins that provide, via proton pumping activity, an appropriate environment for diverse processes of membrane trafficking and maintaining a constant state of cellular pH homeostasis. Subunit *a* of eukaryotic V-ATPases is proposed to be directly involved in the proton conduction, assembly and organelle-specific targeting of V-ATPase. Moreover, subunit *a* has been described as pH sensor element of V_1V_O ATPase, where it was found to interact with ARNO (ADP-ribosylation factor Nucleotide site Opener) [1], an activator of small GTPase, Arf6 (ADP-ribosylation factor 6) in a pH dependent manner. Here, two important binding sites $a2_{1-17}$ and $a2_{368-395}$ (1-17 a.a. and 368-395 a.a.) of mouse subunit *a2*, which are involved in the ARNO binding, have been characterised by NMR spectroscopy and CD spectroscopy, indicating a proper folding of α-helical formation of both peptides. The binding amino acids of *a2* ($a2_{1-17}$) responsible for binding to the Sec7 (Secretory7) domain of ARNO, have been identified and show a defined binding of the residues F6, E8, M10 and Q14 [2]. Further cloning, expression and NMR titration studies of subunit *a* construct $a_{104-363}$ from *Saccharomyces cerevisiae* that lacks the two ARNO binding sites, $a2_{1-17}$ and $a2_{368-395}$ revealed weak interaction to ARNO. Small Angle X-ray Scattering (SAXS) of $a_{104-363}$, revealed an elongated S-shaped conformation. Docking of $a_{104-363}$ to the Sec7 domain on the basis of $a2_{1-17}$ / Sec7 binding indicates N-terminal domain of subunit *a* is located near the hinge region that links soluble N-terminal- with the membrane-integrated C-terminal domain, which is involved in proton-translocation [3]. In conclusion, the interaction between Sec7 of ARNO and the N-terminal domain of subunit *a* may cause structural changes at the hinge region of subunit *a*, which might affect the structure of the C-terminal domain and therefore also the proton-pumping activity [3].

Besides the pH dependent acid-base reaction and structure formation of proteins, regulated via V-ATPases, redox reactions are also highly significant for the survival of the cell to protect itself from superoxide and hydrogen peroxide, which are potential sources of damage to all macromolecules [4-7]. Alkyl Hydroperoxide Reductase (AhpR) is the primary hydroperoxide scavenger that reduces hydroperoxide to water and its corresponding alcohol and preventing therefore damages like protein oxidation, lipid peroxidation and DNA damages [4-7]. In this thesis, the crystal structure of both subunits of AhpR, the 56 kDa alkyl hydroperoxide reductase subunit F (AhpF) and 21 kDa subunit C (AhpC) from *Escherichia coli* have been solved to 2 Å and 3.3 Å resolution, respectively. AhpF crystal structure as well as solution structure derived from SAXS analysis revealed an elongated open conformation structure. The AhpC crystal structure has been solved in its oxidised state that revealed five molecules in an asymmetric unit. The ring shape decamer conformation was generated using its symmetry related molecule. Furthermore, the AhpC structure in its reduced state has been reconstructed to 12 Å resolution using single particle cryo electron microscopy (cryoEM). In addition, dynamic light scattering (DLS) data and size exclusion chromatography reveal AhpF with a molecular mass of 126 kDa, which is corresponding to dimer conformation. Furthermore DLS data and EM micrographs indicate AhpC in be in a steady state between dimer and decamer conformation in solution. Taken the elongated open conformation of AhpF and the ring shape AhpC crystal structures together, the molecular mechanism of AhpR has been deduced using the so far known crystal structure of AhpF and AhpC from *Salmonella typhimurium* and the mechanism from the homologous Thioredoxin Reductase (TrxR) and Thioredoxin. The overall mechanism of AhpR is described for the first time and gives new insights into the molecular mechanism of AhpR that AhpF dimer prefers to form complex with AhpC decamer to accelerate the catalytic activity and thus, increase the chance in rescuing the cell from reactive oxygen species (ROS), like hydroperoxides.

Beside hydrogen peroxide, bacterial cells are exposed to low pH in phagosomes of macrophages. In this study, DLS data and EM micrographs reveal that AhpC forms high molecular weight complexes indicating the second function of AhpC as molecular chaperon. The ring structures are stacked from 2 to 7 rings on top of another giving the possibility to prevent aggregation of proteins in low pH within its tube shape conformation.

1. Hurtado-Lorenzo, A., Skinner, M., Annan, J.E., Futai, M., Sun-Wada, G.-H., Bourgoin, S., Casanova, J., Wildeman, A., Bechoua, S., Ausiello, D.A., Brown, D., and Marshansky, V. (2006). *V-ATPase interacts with ARNO and Arf6 in early endosomes and regulates the protein degradative pathway.* Nat. Cell Biol. **8**: 124-136.

2. Hosokawa, H., Dip, P.V., Merkulova, M., Bakulina, A., Zhuang, Z., Khatri, A., Jian, X., Keating, S.M., Bueler, S.A., Rubinstein, J.L., Randazzo, P.A., Ausiello, D.A., Grüber, G., and Marshansky, V. (2013). *The N termini of a-subunit isoforms are involved in signaling between vacuolar* H^+*-ATPase (V-ATPase) and cytohesin-2.* J. Biol. Chem. **288**: 5896-5913.

3. Dip, P.V., Saw, W.G., Roessle, M., Marshansky, V., and Grüber, G. (2012). *Solution structure of subunit a,* $a_{104-363}$*, of the Saccharomyces cerevisiae V-ATPase and the importance of its C-terminus in structure formation.* J. Bioenerg. Biomembr. **44**: 341-350.

4. Ames, B.N. (1983). *Dietary carcinogens and anticarcinogens. Oxygen radicals and degenerative diseases.* Science **221**: 1256-1264.

5. Fridovich, I. (1978). *The biology of oxygen radicals.* Science **201**: 875-880.

6. Gutteridge, J.M. and Halliwell, B. (1989). *Iron toxicity and oxygen radicals.* Baillieres Clin. Haematol. **2**: 195-256.

7. Sies, H. (1993). *Strategies of antioxidant defense.* Eur. J. Biochem. **215**: 213-219.

1. Introduction

1.1 Eukaryotic V_1V_O ATPase (V-ATPase)

1.1.1. Function and regulation of V_1V_O ATPases

Eukaryotic cells are compartmentalised with membrane-bound organelles, defined with specific functions. These compartments probably evolved to provide distinctive environments with a specific pH for optimal process of its respective metabolic pathways as well as to keep energy in the form of electrochemical gradients across the membrane [8]. Theoretically, all proteins are dependent on their environmental pH to maintain their structure as well as their catalytic activity and function. Protonation and deprotonation are essential for acid-base reaction and hence, crucial part of numerous metabolic reactions [9]. Furthermore, the proton motive force (ψH^+) is the key for generation and conversion of cellular energy in the form of ATP, which has highly potential phosphoanhydride bonds. Because of the importance of intracellular pH in eukaryotic cells, it is stringently regulated.

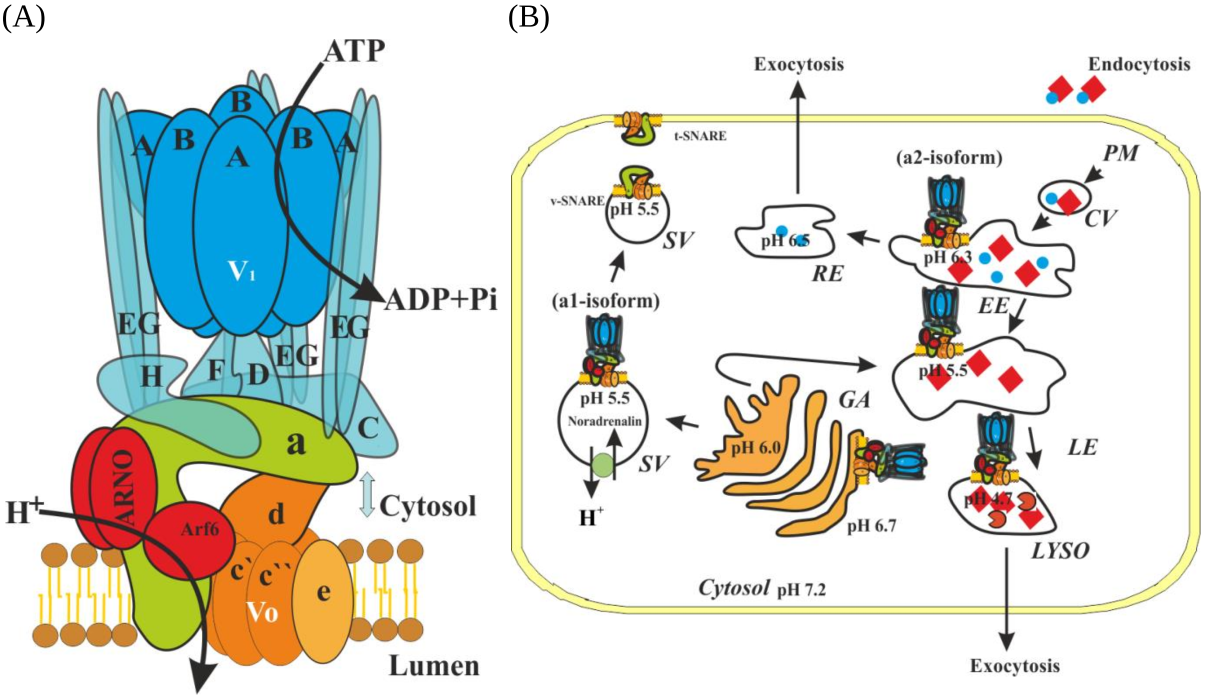
(A)
(B)
ATP
B
A
B
A
B
A
V1
ADP+Pi
EG
EG
EG
H
F
D
a
C
ARNO
Arf6
d
Cytosol
H+
c`
c``
Vo
e
Lumen
Exocytosis
Endocytosis
t-SNARE
v-SNARE
pH 5.5
SV
(a2-isoform)
PM
CV
pH 6.5
RE
pH 6.3
(a1-isoform)
EE
pH 5.5
pH 5.5
Noradrenalin
GA
LE
pH 6.0
SV
H+
pH 6.7
pH 4.7
LYSO
Cytosol pH 7.2
Exocytosis

Figure 1.1: Model and localisation of V-ATPases. (A) Energy released during ATP hydrolysis on the V1 catalytic domain of V-ATPases is used to drive the proton transport across the intracellular or plasma membrane (VO domain), (B) to acidify the respective cellular compartments and to generate the proton gradient across the membrane that is utilised for the endo- and exocytic protein trafficking as well as coupled transport via anti- and symporters such as electrophoretic uptake of malate in the plant cell vacuoles, electrophoretic transport of Cl– across endosomal membranes via Cl^-/H^+ antiporter (ClC-5) and uptake of neurotransmitter via VMAT. EE = early endosomes; LE = late endosomes; LYSO = lysosome; PM = plasma membrane; CV = clathrin-coated vesicles; GA = trans-Golgi apparatus; RE = recycling endosome; SV = secretory vesicle. The V-ATPase model is modified according to Grüber and Marshansky, 2008 [10].

The pH varies among different cell organelles. The enzyme, which regulates pH of the organelles, is the vacuolar-type of H^+-ATPases (V-ATPases). V-ATPases are ATP dependent proton pumps and expressed on both surface of the cell and membrane of distinct compartment and modulate the pH inside and outside the cell (Figure 1.1A) [11]. V-ATPase is present on the endomembrane systems such as vacuoles, Golgi, lysosomes, secretory vesicles, storage vesicles, synaptic vesicles and endosomes (Figure 1.1B), and with increasing examples of V-ATPase being associated with the plasma membrane such as kidney intercalated cells, osteoclasts, male reproductive tract and tumour cells to regulate the pH of the distinct environment of the cell (Figure 1.2) [10, 12-16]. Moreover, V-ATPases are involved in various physiological processes such as intracellular protein trafficking, targeting and degradation, enzyme maturation in lysosomes, accumulation and secretion of neurotransmitters, receptor mediated endocytosis besides the functions linked to their plasma membrane presence such as membrane energisation, bone resorption, acid secretion by macrophages, acid secretion and protein reabsorption of kidney cells, maintenance of pH for sperm maturation and keeping sperms in immotile state during its passage through *vas deferens* and epididymis are few of the functions that can be ascribed to V_1V_O ATPases [10, 12, 14, 16, 17].

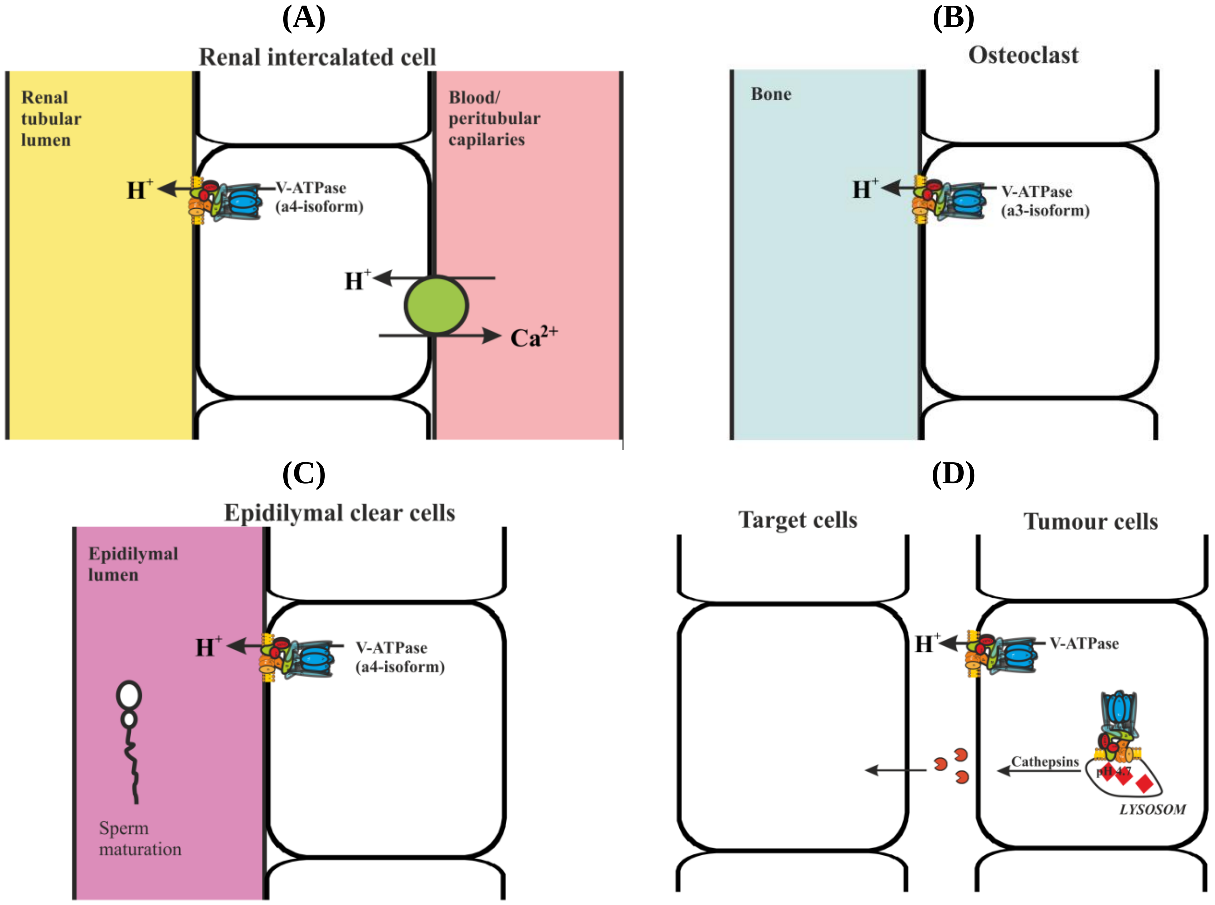
(A)
Renal intercalated cell
Renal tubular lumen
Blood/ peritubular capilaries
H+
V-ATPase (a4-isoform)
H+
Ca2+
(B)
Osteoclast
Bone
H+
V-ATPase (a3-isoform)
(C)
Epidilymal clear cells
Epidilymal lumen
H+
V-ATPase (a4-isoform)
Sperm maturation
(D)
Target cells
Tumour cells
H+
V-ATPase
Cathepsins
pH 4.7
LYSOSOM

Figure 1.2: Physiological roles of V-ATPases. V-ATPases located at the plasma membrane of (*A*) kidney intercalated cells, (*B*) osteoclasts, (*C*) male reproductive tract and (*D*) tumour cells to maintain the pH of the distinct environment in the cell. (Modified from Forgac, 2007) [11].

Furthermore, V-ATPases are components in the midgut alkalisation of lepidopteran insects such as tobacco hornworm (*Manduca sexta*) larva and mosquito *(Aedes aegypti)* larva, where pH can go beyond 11 [18-20]. In the midgut goblet cells plasma membrane, a high amount of V-ATPases generate an electrochemical gradient of protons (H^+). The generated proton gradient is then coupled to a $2H^+/K^+$ antiporter to transfer K^+ to the midgut, producing a high alkalinisation [18]. High midgut pH in the insects is thought to help in the breakdown of dietary tannins, to aid in the absorption process [20]. Vacuolar ATPases play an essential role in the accumulation of neurotransmitter at nerve endings during synaptic activity. Moreover, studies have also been shown that membrane fusion formed by the merger of two opposing V_O domains of V-ATPase [21], in *D. melanogaster* and *C. elegans* and it has been found as a separate function of V-ATPase, independent of its proton pumping activity [11].

Insights into the roles of V-ATPases in the physiological processes besides the proton pumping are constantly growing. V-ATPase was found to directly associate with Arf6 (ADP-ribosylation factor 6), a low molecular GTPase and ARNO (ADP-ribosylation Factor Nucleotide site Opener), a GEF (GTP/GDP Exchange Factor) of Arf6, via subunit *c* and subunit *a2* in mouse V-ATPase [1]. Arf interacts with ARNO on the scaffold provided by V-ATPase in a pH dependent manner and disruption of this interaction resulted in the reversible inhibition of endocytosis and blockage of protein trafficking between early and late endosomes [1, 22]. Arf and ARNO proteins are also involved in diverse signalling pathways such as cytoskeleton organization, maintenance of Golgi structure and function, synaptic transmission, epithelial cell migration and many more [23-25].

1.1.2 Structural feature of V_1V_O ATPases

V-ATPases are multisubunit complexes, composed of two main structural and functional components. Most V-ATPases are composed of 14 defined subunits and some accessory subunits [10, 26]. The V_1 sector comprises eight subunits in the stoichiometry of $A_3:B_3:C:D:E_3:F:G_3:H$ (Table 1.1) [10, 27-30]. The headpiece, $A_3:B_3$ forms the core of the catalytic centre that hydrolyses ATP. V_O is mostly membrane-embedded and comprised of six different subunits, $a_1:d_1:c_{4\text{-}5}:c'_1:c''_1:e$ in yeast V-ATPase (Table 1.1) [10, 11]. In higher eukaryotes, *c'* subunit is missing, whereas accessory subunits Ac45 [31, 32] and M8-9 [33, 34] are found to be attached to the V_O domain. A glycosylated V_O associated subunit M9.7 has been identified in midgut and Malpighian tubules of *M. sexta* [35].

Various subunits of V-ATPases are expressed in different isoforms, especially in higher eukaryotes and multicellular complex organism, to achieve the target specific functions in the endomembrane system [36, 37]. These include subunit *d* [38], subunit G [39], subunit C [40, 41], subunit E [42] and subunit *a* [37, 43]. In *Paramecium tetraurelia*, 17 isoforms of subunit *a* have been identified, representing the highest number of isoform found in single organism for any of V-ATPase subunits [44]. In yeast, all subunits are encoded in single isoform by their respective single genes (Table 1.1), with the exception of subunit *a*, which is expressed in two different isoforms, Vph1 (vacuole specific) [45] and Stv1 (Golgi specific) [46].

Domain	Subunits	Yeast Gene	MW (kDa)	Function
V_1	A	*VMA1*	70	Catalytic site, Nucleotide-binding
	B	*VMA2*	60	Nucleotide-binding, regulatory, actin and aldolase binding
	C	*VMA5*	40	Activity, assembly, reversible dissociation, actin binding
	D	*VMA8*	34	Assembly, rotary
	E	*VMA4*	33	Activity, assembly, peripheral stalk, RAVE, aldolase binding
	F	*VMA7*	14	Activity, assembly, coupling
	G	*VMA10*	13	Activity, assembly, peripheral stalk
	H	*VMA13*	50	Regulator subunit, assembly
V_O	*a*	*VPH1,STV1*	100	Proton pumping, targeting, assembly, peripheral stalk, pH sensor
	d	*VMA6*	40	Coupling, activity
	c	*VMA3*	17	Proton transport, bafilomycin binding
	c'	*VMA11*	17	Proton transport
	c''	*VMA16*	21	Proton transport
	e	*VMA9*	9	unknown

Table 1.1: Subunits of the catalytic V_1 and proton translocating V_O domains of *S. cerevisiae* V-ATPase. V-ATPase subunit genes are shown along with the respective molecular weight of the protein subunits. Subunit function is also shown adapted from [10, 12, 15].

Recently, the EM structure of the entire V-ATPase complex from *S. cerevisiae* has been solved at 11 Å resolution by single particle reconstruction using cryo electron microscopy [27]. The cryo-EM structure reveals the A_3:B_3 headpiece joined to the three peripheral stalks connecting V_1 and V_O segments (Figure 1.3) [27]. The peripheral stalk is made up of EG-heterodimers and linked to the subunit B of the headpiece. The non-homologous region (NHR) of subunit A is clearly visible. Further subunit arrangement indicating subunit H, C and the N-terminal domain of subunit *a* to be involved in EG-heterodimers association (Figure 1.3).

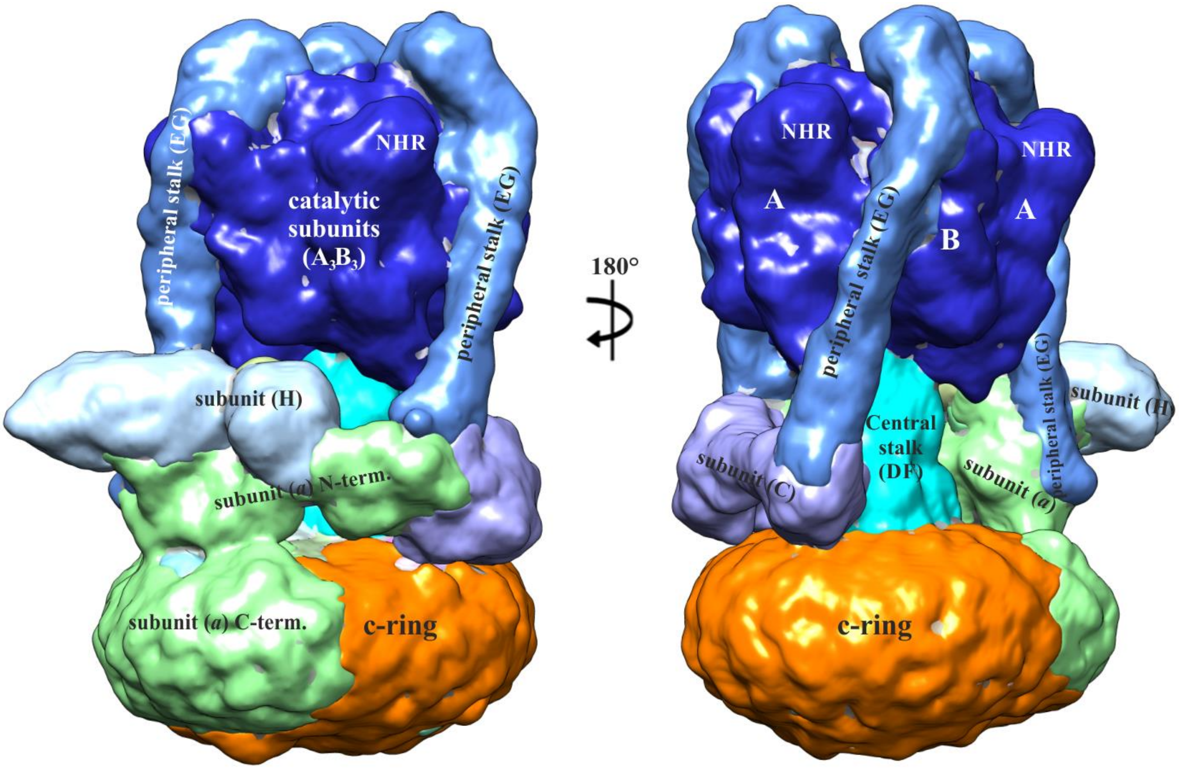
peripheral stalk (EG)
NHR
catalytic subunits (A_3B_3)
peripheral stalk (EG)
subunit (H)
subunit (*a*) N-term.
subunit (*a*) C-term.
c-ring
180°
NHR
A
NHR
A
B
peripheral stalk (EG)
subunit (C)
Central stalk (DF)
subunit (*a*)
peripheral stalk (EG)
subunit (H)
c-ring

Figure 1.3: 3-D cryo-EM structure of V_1V_O ATPase from *S. cerevisiae* at 11 Å resolution. The EM structure is revealing the subunit arrangement within an intact complex (EM Data Base ID: EMD-5476) [27]. NHR: Non-homologous region.

V-ATPases are regulated by reversible disassembly causing dissociation of V_1V_O ATPase into V_1 and V_O in response to various physiological stress such as glucose deprivation [47] or a drop in the ATP to ADP ratio [48, 49]. Such regulatory mechanism is absent in the related A- and F-ATP synthase. Subunit C has been shown to be important in the regulation of this process [12, 48, 50]. This is the only subunit of V_1V_O ATPase that is proposed to be lost during this physiological regulatory process, when V_1 is released from V_O, via its binding to the actin cytoskeleton [12, 51]. Mutational analysis of subunit C has demonstrated that it plays a critical role in balancing activities such as V_1V_O assembly and ATPase activity [52]. Subunit C has no counterpart in A- as well as in F-ATP synthases. Its crystallographic structure reveals an elongated boot-shaped formation (Figure 1.4A) [53]. Other high resolution structures of the eukaryotic V_1 ATPase that had been solved so far are the N-terminal segment E_{1-69} [54] and the C-terminal segment $E_{133-222}$ [55] of subunit E from yeast and the N-terminal segment G_{1-59} [30] and the C-terminal segment G_{61-101} [56] of subunit G from *S. cerevisiae*. The subunits E and G are required for ATPase activity. They form the peripheral stalk and are therefore important for the assembly of V_1V_O. Their structure is mainly α- helices, whereas the C-terminal part $E_{133-222}$ of subunit E reflects β- sheet formation [30, 54-56]. The N-terminal domain of subunit E (residues 19-39) has been mapped to bind with subunit G [57]. Moreover the EG heterodimer including the head region from residues 158 to 277 of subunit C has been crystallised recently (Figure 1.4B) [58].

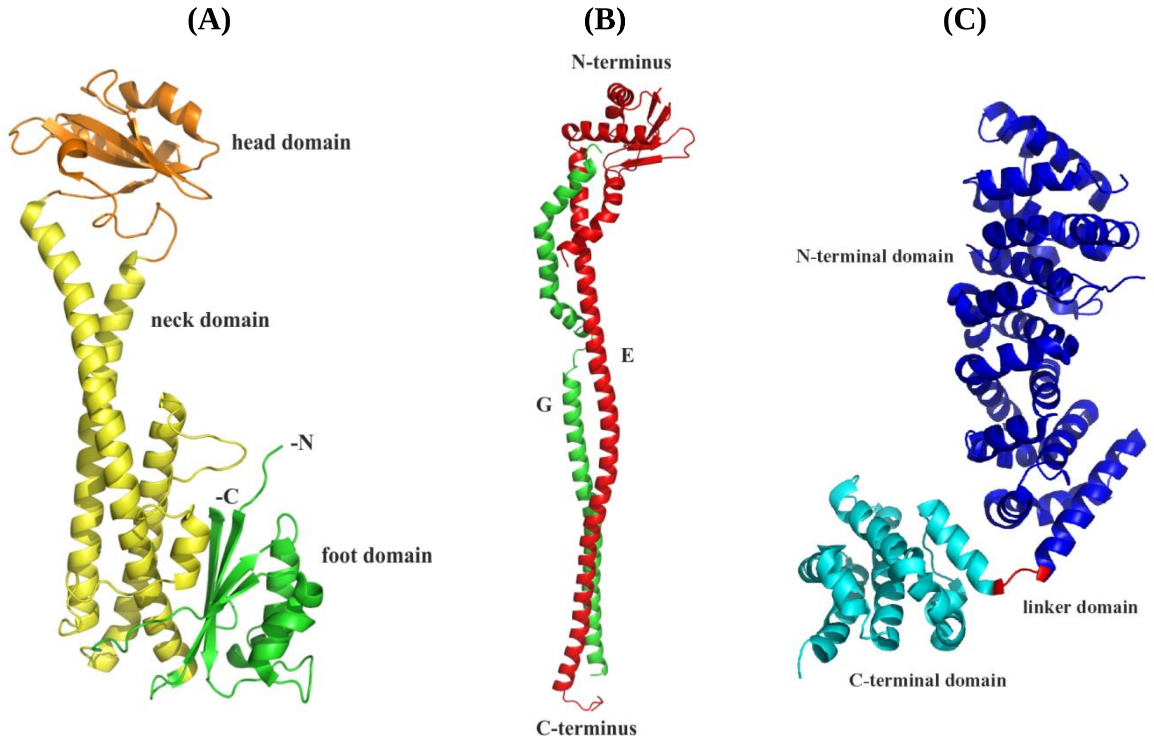

Figure 1.4: Crystal structures of V-ATPase subunits. High resolution structures of (*A*) subunit C (PDB: 1U7L), (*B*) EG heterodimer (PDB: 4DL0) (*C*) subunit H (PDB: 1HO8) in cartoon presentation.

The crystal structure of EG heterodimer highlights a noncanonical coiled coil formation, that is stabilized by its N-terminal end by binding to the head region of subunit C (Figure 1.4B) [58]. Moreover, the crystal structure of subunit H is comprised of mainly α-helices and divided into a large N-terminal domain, forming a shallow groove, and a small C-terminal domain, connected by a four-residue loop (Figure 1.4C) [59].

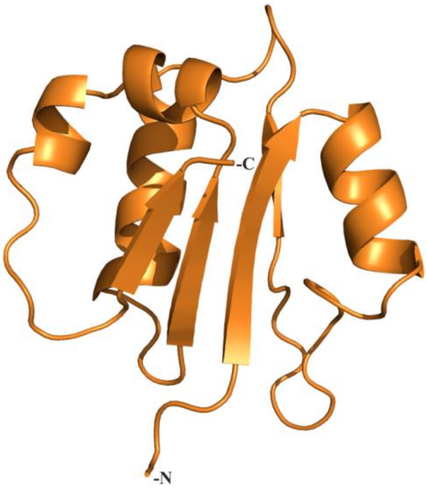

Figure 1.5: Cartoon presentation of central stalk subunit F (PDB: 4IX9) [60].

Lastly, the full length structure of central stalk subunit F has been solved in a combined manner using small angle X-ray scattering (SAXS), NMR and crystallography. The crystal structure of $F_{1\text{-}94}$ shows a globular formation in Rossman fold with alternative α-helices and β-sheets and a protruding flexible elongated C-terminal region $F_{90\text{-}116}$, with the latter being solved using NMR (Figure 1.5) [60].

Other subunits, whose low resolution structures are known so far by using SAXS analysis, are the boxing glove-shape structure of subunit *d* [61] and the egg like shape structure of subunit F [62]. The crystal structures of the V-ATPase subunits C, E, F, G and H from *S. cerevisiae* accommodate well into their corresponding EM map of the entire yeast V-ATPase EM structure (Figure 1.6) [27].

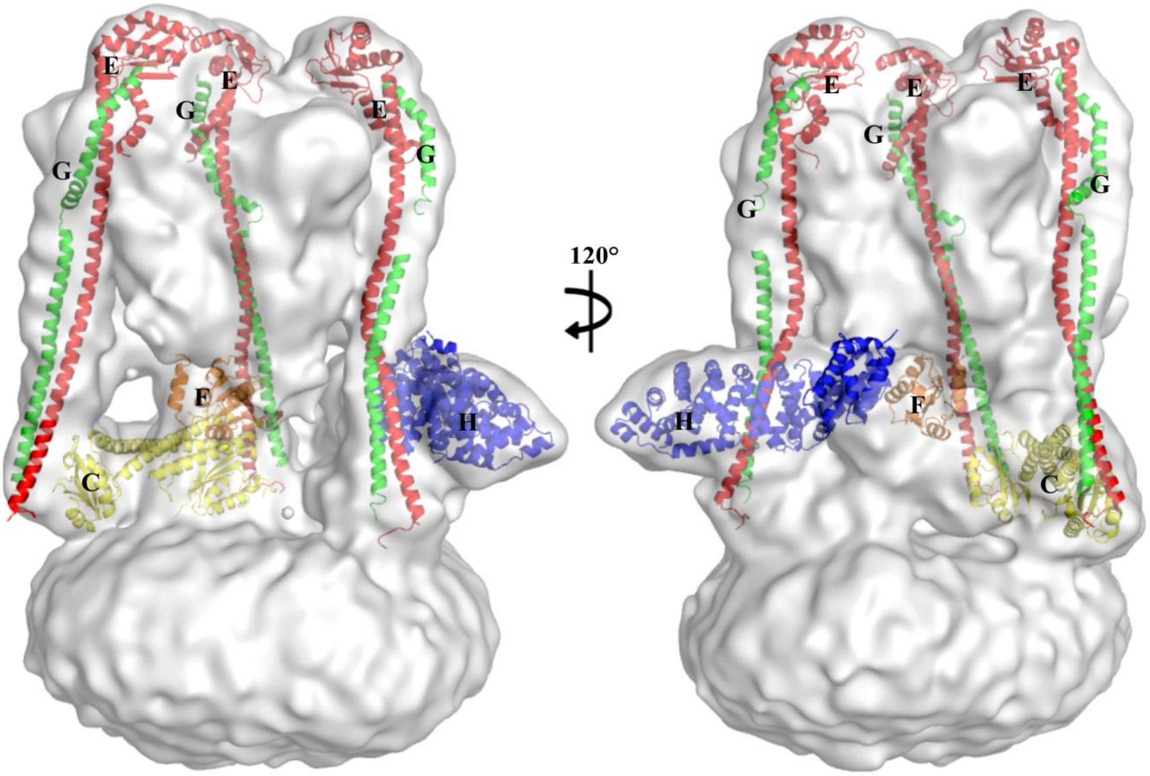

Figure 1.6: Fitting of V-ATPase crystal structures into EM structure of V-ATPase from *S. cerevisiae*. The crystal structure of subunits C (yellow), E (red), F (orange), G (green) and H (blue) were fitted into their map segment (semi-transparent grey), respectively (EM Data Base ID: EMD-5476) [27].

Moreover, the electron microscopy data suggests that the V_O membrane sector consist of a single subunit *a* associated with a hexameric complex of the four helical bundle subunit *c* (Vma3) [27, 63, 64]. The N-terminal cytosolic part of subunit *a* lies horizontally, partially associated to the C-terminal domain of subunit H along its length and faces to subunit C end to end (Figure 1.3) [27].

1.1.3 Subunit *a* of V-ATPases

Subunit *a* is essentially involved in the process of proton conduction across the membrane [65]. All *a* subunits of V-ATPases consist of ~850 residues with a size of ~100 kDa [10]. In mice and humans, four different *a* isoforms (*a*1, *a*2, *a*3 and *a*4) have been described. Different isoforms are responsible for the localisation of V-ATPases to plasma membranes or specific intracellular compartments defined by specific function of the cell type respectively [66-70]. In *Mus musculus* all four isoforms are found in kidney proximal tubule cells. The *a*1-isoform, *a*3-isoform, and *a*4-isoform are located at the plasma membrane, while the *a*2-isoform is targeted to early endosomes *in situ* [71]. In yeast, two *a* subunit isoforms are identified and coded by VPH1 and STV1 [15]. These two isoforms are responsible for the localisation of V_O section to vacuolar or Golgi compartments [72]. Besides the role in the localisation of V-ATPase, chimeric experiments demonstrated the difference in *S. cerevisiae* Vph1p (vacuole specific) and Stv1p (Golgi specific) isoforms. A chimeric protein containing the N-terminus of the Golgi isoform Stv1p and C-terminus of the vacuole isoform, Vph1p, was targeted to the Golgi and the complex did not show reversible disassembly during glucose depletion [72], demonstrating that information for correct targeting is located on the N-terminus of subunit *a* and different isoforms have varied response to physiological conditions [66]. Whereas the C-terminus has been shown to be involved in proton conducting and assembly of V-ATPases [73]. Thus, different isoforms containing V-ATPases exhibit function in the context of their location, making V-ATPases a functionally and regulatory diverse complex in cellular milieu.

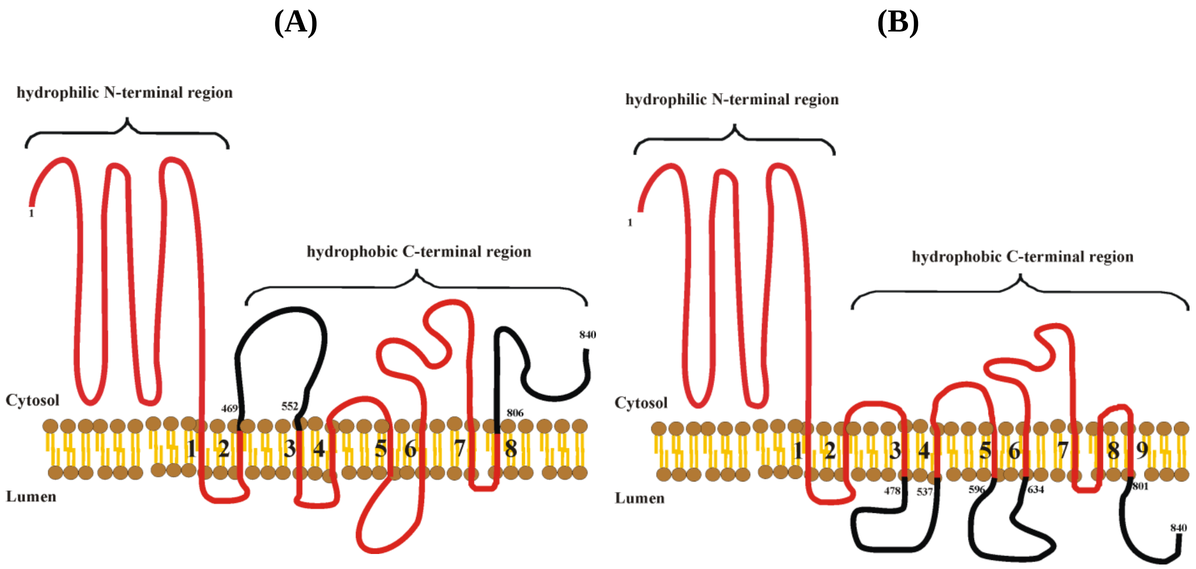
(A)
(B)
hydrophilic N-terminal region
1
hydrophobic C-terminal region
Cytosol
Lumen
469
552
806
840
1
2
3
4
5
6
7
8
hydrophilic N-terminal region
1
hydrophobic C-terminal region
Cytosol
Lumen
1
2
3
4
5
6
7
8
9
478
537
596
634
801
840

Figure 1.7: Topological model of subunit *a*. All *a* subunits consist of ~850 amino acids with a size of ~100 kDa. The N-terminal region is facing to the cytosol, whereas the C-terminal region is membrane embedded. Currently two subunit *a* models are available with eight or nine transmembrane regions in discussion. These subunit *a* models are modified according to the predictions of *(A)* Marshansky, 2007 and Ochotny *et al*., 2006 by using *in silico* analysis and of *(B)* Nishi *et al*., 2003 by using crosslink and cysteine mutagenesis experiments. Differences of transmembrane segments facing to lumen or cytosol are highlighted in black. The obvious difference is in the very C-terminal segment $a_{801\text{-}840}$/$a_{806\text{-}840}$, in one model, it faces the cytosol *(A)* and in the other model into the lumen *(B)*.

On the other hand, N-terminal domain has been proposed to interact with subunit *d* and they may form the peripheral stator connecting V_1 with V_O together [74], to prevent energy loss through futile rotation of V_1 with respect to V_O, and reportedly suggested to interact with subunit A and subunit H [61, 75, 76]. It has been also suggested that the cavity of the boxing glove-shape structure of subunit *d* enables the binding of *a*-*d* domain to the non-homologous region (NHR) of subunit A in the process of reversible disassembly [30, 61]. The NHR is a stretch of 90 unique amino acids of subunit A, found only in the V-ATPase and the A-ATP synthase [30, 77]. Subunit *a* was initially identified in the clathrin-coated vesicles and the chromaffin granules, which was partially exposed to the cytosolic face of the membrane due to free labelling with lactoperoxidase-catalysed radioiodination [78]. Unlike other peripheral stalk subunits, subunit *a* could be labelled by hydrophobic probes indicating that a second domain of subunit *a* is membrane embedded [78]. Subsequent analysis of various membrane preparations from diverse plant and animal origin confirmed that subunit *a* consists of a cytoplasmic N-terminal hydrophilic domain, and a C-terminal membrane hydrophobic domain (Figure 1.7; [79]). Trypsin cleavage experiments indicated that Vph1p is exposed in V-ATPases and more interestingly, its susceptibility to cleavage in the presence of ATP and divalent cations varied [80]. Differences in cleavage sensitivity disappeared when V_1 was released from the membranes [80]. These results showed that subunit *a* adopts a single conformation in the absence of the V_1 domain and structural changes are accompanied during catalysis in the A_3:B_3 sector and possibly transmitted to the V_O via subunit *a*, thus physically linking the catalytic sector, V_1 with the proton channel, $V_{O.}$ To understand the topology and transmembrane helices orientation of Vph1p, single cysteine residue containing forms of subunit *a* were prepared by mutagenesis and their orientation was studied by the use of either membrane impermeable sulfhydryl reagent, AMS (4-acetamido-4’- maleimidylstilbene-2,2’-disulfonic acid) or membrane permeable, MBP (3’-N-maleimidylpropionyl) biocytin [81]. Later, using cysteine mediated cross-linking, it was shown that R_{735} in TM7 helix is essential for proton conduction and is in contact with E_{145} in the TM4 of c and c’ and TM2 of c’’ of yeast V-ATPase [65, 82, 83]. According to these data and additional NMR structure and dynamic studies of a TM7 region peptide, involved in the proton conduction, showed that this 25 amino acid region forms two helices separated by a ball-and-joint type two amino acid linker that controls the opening and closing of a proposed swivelling interaction model between the helices of subunit *c* and *a*, in the proton hemi-channel of subunit *a* during proton conduction [83, 84].

1.1.4 Cellular and physiological relevance of subunit *a*

Since V-ATPases and especially subunit *a* are involved in versatile physiological processes in different cell types, mutations in different subunit *a* isoforms cause various diseases. The *a4* isoform is mainly expressed in the kidney cells [68]. Mutations in the gene encoding subunit *a4* have been associated with distal (or type 1) renal tubular acidosis (dRTA) [83, 85] while mutation in the *a3* isoform leads to a severe form of infantile malignant osteopetrosis, characterised by defective osteoclast bone resorption [86, 87]. This disease is associated with the loss of hearing and visual impairment [86]. Furthermore, reported finding with genetic models showed that mutations in subunit *a* leading to disease conditions such as impaired glycosylation and *cutis laxa,* indicating the important role of this protein in processing and transport at the Golgi apparatus [88]. Mutations in *v100*, an *a1* isoform in *Drosophila melanogaster,* showed impaired release of neurotransmitters and cause endosomal and phagosomal accumulation of degenerated photoreceptors, which lead to visual impairments [89]. Besides the classical role of V-ATPases to acidify the cellular compartments, additional phenomenon such as membrane fusion has been attributed to subunit *a*. These novel findings indicate the involvement of subunit *a* in the process of microglia cells mediated phagocytosis of dead neurons in the brain [90]. Moreover, physiological importance of V-ATPase in the kidney proximal tubule (PT) cells has been demonstrated, with the use of specific inhibitors of V-ATPase (for example, bafilomycin and concanamycin) and acidification uncouplers (for example, NH_4Cl) (Figure 1.8B) [91]. Pathophysiological conditions such as Dent’s disease and related Fanconi’s syndrome are associated with deficient protein reabsorption and proteinuria in the kidney PT cells [1].

The phenomenon of endosomal V-ATPase mediated trafficking has now been understood in more detail, with the findings, that endosomal pH directly regulates vesicular signalling proteins, ARNO and Arf6, to control endosomal degradative pathways (Figure 1.8A) [1]. Subunit *a2* has been demonstrated to be essentially involved, collectively with Arf6 and its cognate exchanger ARNO, in the endosomal pH sensory complex to regulate the protein sorting and degradation in the early endosomes in a pH dependent manner (Figure 1.8A) [1, 2, 67]. Subunit *a2* of mouse V-ATPase was found to associate with ARNO and subunit *c* with Arf6 directly. Inhibition of this interaction resulted in the reversible abrogation of endocytosis [1, 22]. The absence of endosomal acidification leads to disruption of membrane trafficking of carrier vesicles between early and late endosomes, causing the accumulation of cargo protein in early endosomes and therefore, inhibit of endocytosis (Figure 1.8B) [1, 91]. ARNO belongs to GEF (**g**uanine nucleotide **e**xchange **f**actor), also known as cytohesin-2 and responsible for GTP/GDP exchange on small GTPase protein, Arf 6 (ADP-ribosylation factor 6) to activate and regulate its activities [24]. ARNO/Arf6 is involved in the regulation of endosomal vesicular trafficking [10], cytoskeleton organisation [92], lipid modification and rearrangement [25, 93], cell motility [94], membrane recycling [95], exocytosis in the neuroendocrine cells [23], and more interestingly carrier vesicle coat formation that is required to bud off vesicles from the early endosomes [1, 22]. ARNO is also known to undergo protein kinase C (PKC) mediated phosphorylation *in vivo* at residue S392, however, the function of this modification remained largely unknown, as phosphorylation did not cause the activation of ARNO [96, 97].

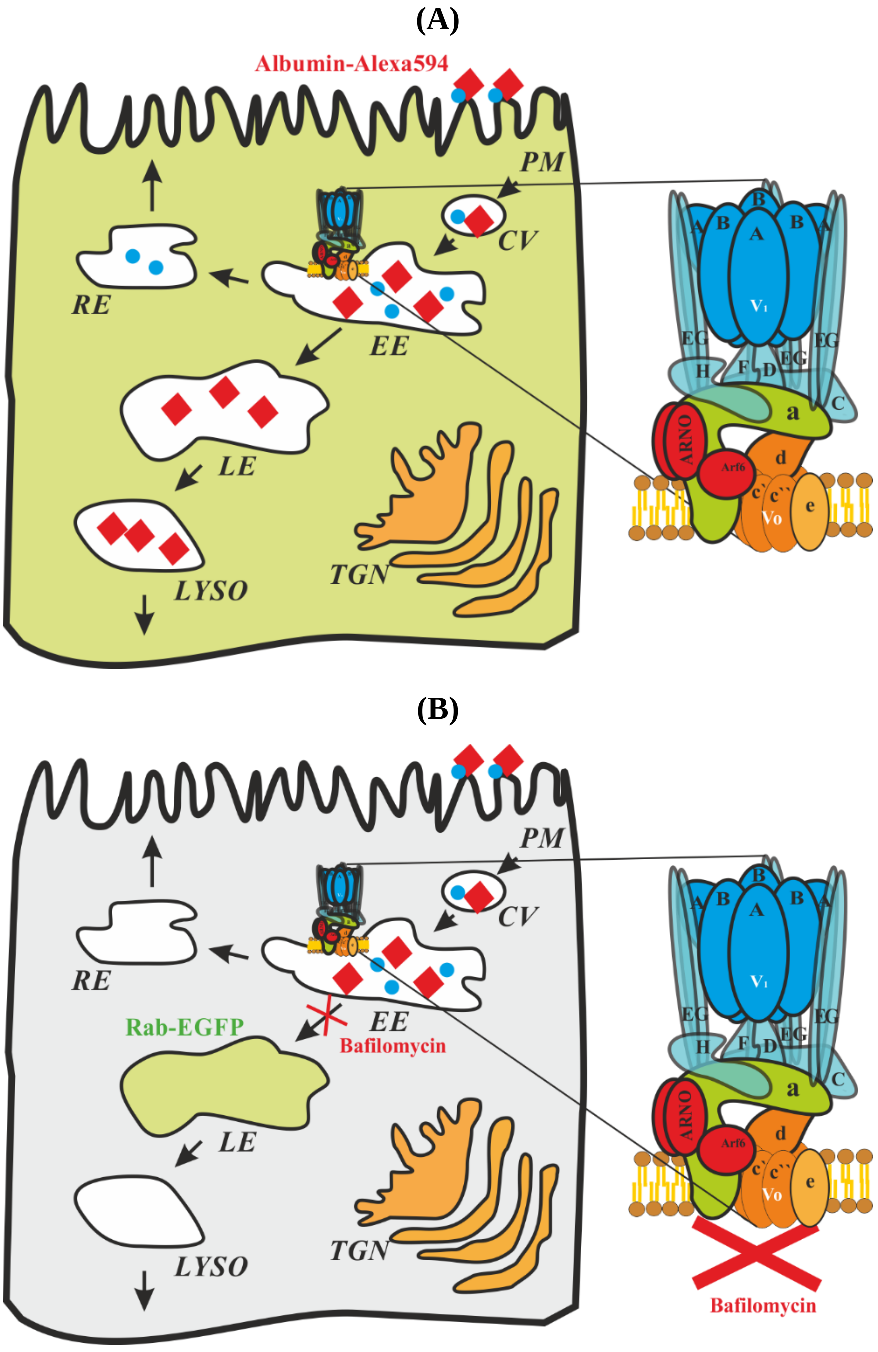
(A)
Albumin-Alexa594
PM
CV
RE
EE
LE
LYSO
TGN
B
A
B
A
A
V₁
EG
EG
H
F
D
EG
C
a
ARNO
Arf6
d
c'
c''
Vo
e
(B)
PM
CV
RE
EE
Rab-EGFP
Bafilomycin
LE
LYSO
TGN
B
A
B
A
A
V₁
EG
EG
H
F
D
EG
C
a
ARNO
Arf6
d
c'
c''
Vo
e
Bafilomycin

Figure 1.8: V-ATPase in endosomal trafficking and degradation pathways of kidney proximal tubule (PT) cells. *(A)* Megalin and cubilin are multi-ligand receptors on the PT cells involve in the reabsorption of low molecular weight proteins (for example, albumin) [91]. Uptake of Alexa594 flurophore labelled albumin (red squares) is shown and its passage through early endosomes (EE) and late endosomes (LE) occurs in a pH dependent manner, generated by V-ATPase [91]. PM = Plasma membrane; CV = clathrin-coated vesicles; TGN = trans-Golgi network; RE = recycling endosome *(B)* Experimental approach that was used in the study of membrane trafficking between early and late endosomes. LE was labelled with green florescence, Rab7-EGFP. Bafilomycin blocked the cargo, albumin alexa594, passage between early and late endosomes. Mechanism of this membrane transport has been known to involve V-ATPase and small GTPase ARNO to modulate the endosomal trafficking and degradation pathways in a pH dependent manner, making V-ATPase a novel component of pH sensing machinery [1]. This model is modified according to Marshansky, 2007 [91].

In spite of considerable studies during the past few years, subunit *a* has emerged in performing vital roles and diverse functions of V-ATPase, the structural and biochemical data of this subunit is scant so far. Even the structural topology and positioning inside V-ATPase complex in particular the C-terminal membrane embedded part are not well understood and the interacting partners have not been studied thoroughly. Emerging roles of this enzyme with respect to the signalling proteins such as ARNO are also at very premature stages.

1.2 Alkyl Hydroperoxide Reductase (AhpR), a response to oxidative stress

Besides the pH dependent acid-base reaction and structure formation of proteins that are regulated via V-ATPases, also redox reactions are highly significant for the survival of the cell. Exposure to hyperoxia, thus growth in 100% oxygen is a danger to the cells and leads to superoxide related damages. In *S. cerevisiae* V-ATPase genes were identified to be involved against high O_2 damages and oxidative stress [104, 105]. Furthermore, besides multiple iron uptake genes, microarray study of *vma2Δ* mutant demonstrated the up regulation of one antioxidant gene, called the peroxiredoxin *TSA2* [99]. Further studies revealed that V-ATPase inhibition with concanamycin A and *vma2Δ*, *vma4Δ*, *vma10Δ*, *vph1Δ* and *stv1Δ* mutations induce the up-regulation of the TSA2- promoter (Figure 1.9) [98].

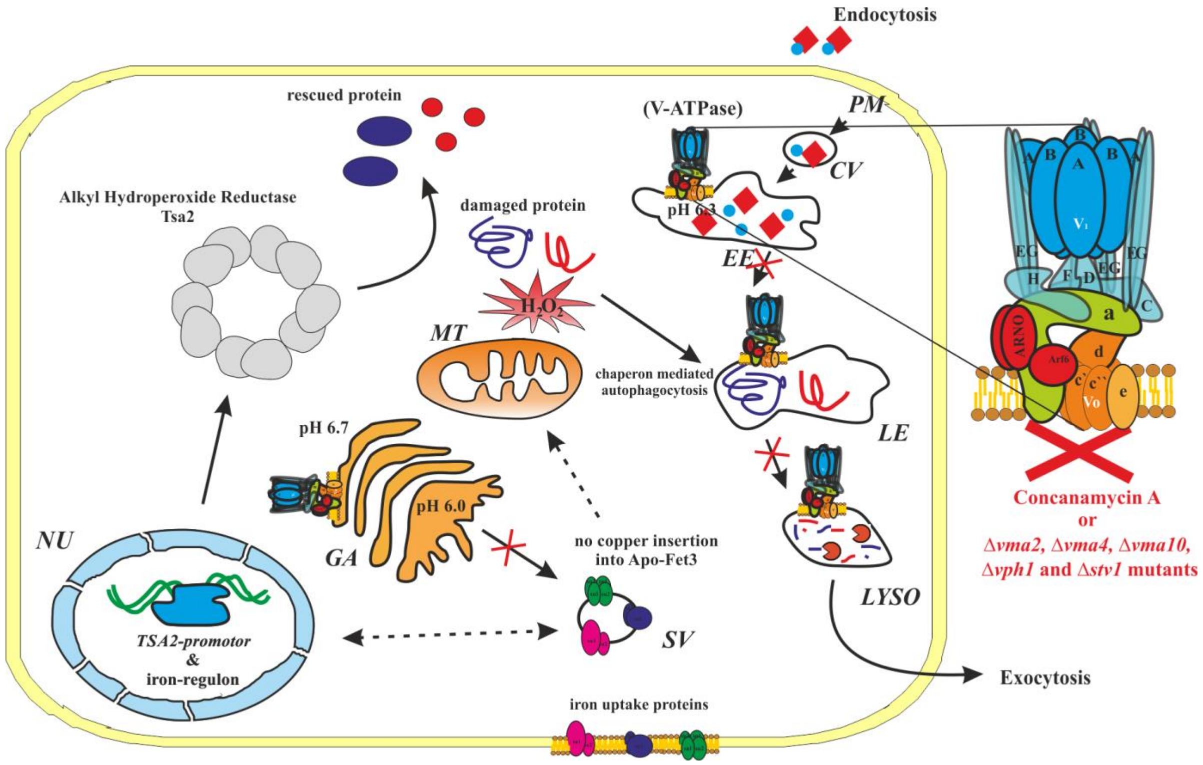
Endocytosis
rescued protein
(V-ATPase)
PM
CV
pH 6.3
EE
Alkyl Hydroperoxide Reductase
Tsa2
damaged protein
H₂O₂
MT
chaperon mediated
autophagocytosis
LE
pH 6.7
pH 6.0
GA
NU
no copper insertion
into Apo-Fet3
LYSO
TSA2-promotor
&
iron-regulon
SV
Exocytosis
iron uptake proteins
B
A
B
A
B
A
V₁
EG
EG
EG
H
F
D
C
a
ARNO
Arf6
d
c'
c''
Vo
e
Concanamycin A
or
Δvma2, Δvma4, Δvma10,
Δvph1 and Δstv1 mutants

Figure 1.9: V-ATPases are linked to oxidative stress response in *S. cerevisiae*. V-ATPases lack in activity indicates a connection between cellular pH, iron, and redox homeostasis. Several *vma* mutants, in particular *Δvma2* mutant as well as V-ATPases inhibited with concanamycin A induced up-regulation of an antioxidant gene, namely TSA2 and the iron regulon [98]. V-ATPases are involved in vacuolar protein sorting and vacuolar acidification, required for resistance to oxidative stress and removing damaged protein in lysosomal degradative pathway. During oxidative stress or in *vma* mutants (*vma2Δ*, *vma4Δ*, *vma10Δ*, *vph1Δ* and *stv1Δ*), TSA2 is up-regulated to support the folding of damaged protein as molecular chaperon [98-101]. Moreover, *vma* mutants revealed to be iron-deprived, possibly caused by the inability to mature Fet3p (ferrous transport 3), the multicopper oxidase required for high affinity iron transport [102]. The maturation requires the insertion of copper into Apo-Fet3 located in an acidic post-Golgi compartment. The *vma* mutants fail therefore to provide an acidic environment in Golgi [102]. Thus the inability to mature Fet3 causes a defective iron transport and low iron level in *vma* mutants [102]. The up-regulation of iron up-taking proteins is regulated by iron-sensing transcription factor, Aft1 that binds to the iron regulon [103]. The up-regulation of iron up-taking proteins might be involved in repairing the respiratory chain. EE = early endosomes, LE = late endosomes; LYSO = lysosome, PM = plasma membrane; GA = Golgi apparatus; NU = nucleus; SV = secretory vesicle; MT = mitochondrium.

The loss of pH homeostasis in Golgi and lysosome may lead to disruption of the pH dependent copper cluster insertion into Apo-Fet3p in the Golgi compartment and the pH dependent lysosomal protein degradation of oxidative damaged protein [99, 105]. The up-regulation of TSA2- promoter and iron regulon is hence a defence to oxidative stress in *vma* mutants (*vma2Δ*, *vma4Δ*, *vma10Δ*, *vph1Δ* and *stv1Δ*). TSA2, an Alkyl Hydroperoxide homologous protein might be involved in rescuing oxidative damage of the protein by preventing their aggregation as molecular chaperon (Figure 1.9). Furthermore bacterial TSA2, called AhpC (Alkyl Hydroperoxide Reductase, subunit C) reveals hemin binding activity and might protect heme for oxidative degradation [106]. Moreover, *vma* mutants revealed a lack of iron [107], possibly due to an uncompleted maturation of Fet3p (ferrous transport 3), the multicopper oxidase, which is part of the high affinity iron transport [102]. The copper loading of Apo-Fet3 occurs in the post-Golgi compartment. The inability to mature Fet3 causes therefore the insertion of Apo-Fet3 into the cell surface and hence a defective iron transport and a low iron level in *vma* mutants [102]. The iron-sensing transcription factor, Aft1 binds to the iron regulon and is responsible for the up-regulation of iron up-taking proteins [103]. High iron intake might be also involved in repairing respiratory chain complexes (Figure 1.9).

Superoxide and hydrogen peroxide are potential sources in damaging all types of macromolecules that lead to protein oxidation, lipid peroxidation and DNA damages, including deamination of bases [4-7]. Eukaryotic cells as well as amoebae release therefore reactive oxygen species (ROS) including H_2O_2 (hydroperoxide) as a response against bacterial invasion [108-110]. A concentration of exogenous H_2O_2 (~30 µM) is sufficient to inhibit the growth of *E. coli* [111]. The protection from toxic and damaging effect of oxygen are regulated and coordinated in the bacterial system at least through redox sensitive proteins [112]. Active oxygens like superoxide and hydroperoxides occur endogenously from incomplete reduction of oxygen in the respiratory chain or through external agents like light, UV radiation and redox-cycling drugs (Figure 1.4) [6, 7]. The main source of endogenous H_2O_2 is probably flavoenzymes, since they are abundant and prone to form univalent electron transfer reaction that produces superoxide and H_2O_2 as side products [113, 114]. In *E. coli*, the formation of endogenous hydrogen peroxides (H_2O_2) in aerobic condition is 10-15 µM/s [115], but despite the rapid H_2O_2 production, the steady-state level is restrained to 20 nM (Figure 1.4) [111]. Furthermore, exogenous O_2^- cannot penetrate the bacterial membrane due to its negatively charged, while exogenous H_2O_2 can cross the lipid bilayer with similar permeability coefficient like water at physiological condition [111, 116]. When exogenous H_2O_2 concentration is higher than 0.2 µM the influx of H_2O_2 into *E. coli* exceed the endogenous H_2O_2 production that increases the overall H_2O_2 within the cell [111].

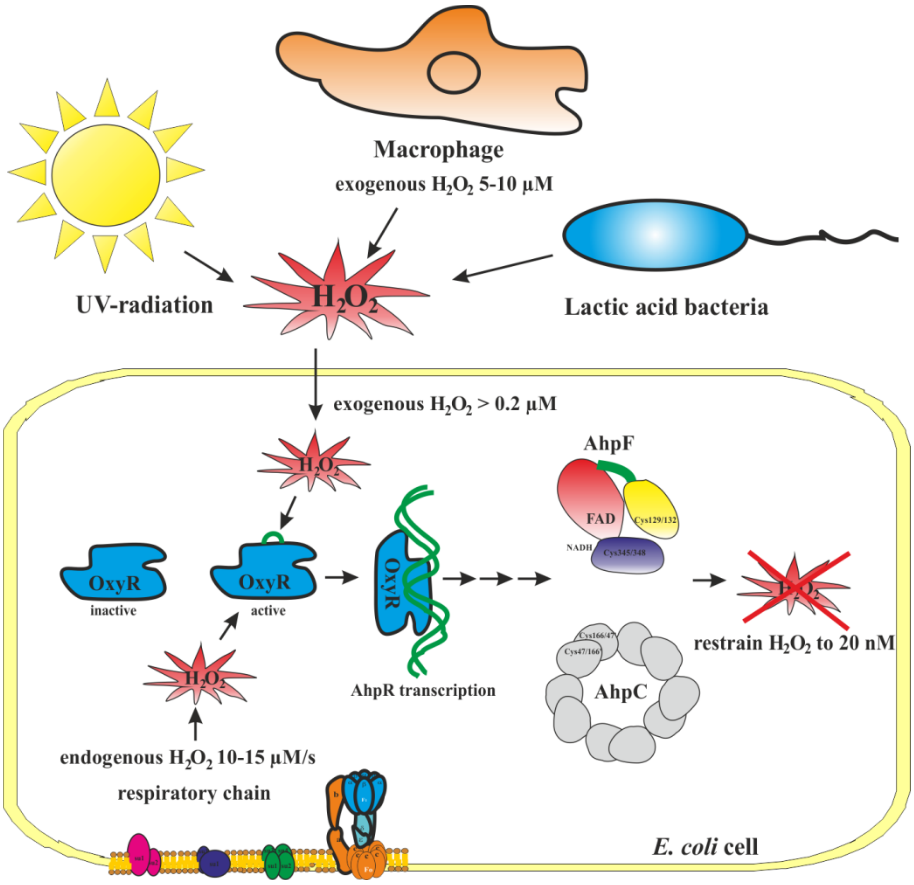
Macrophage
exogenous H_2O_2 5-10 µM
UV-radiation
H_2O_2
Lactic acid bacteria
exogenous H_2O_2 > 0.2 µM
H_2O_2
AhpF
FAD
NADH
OxyR
inactive
OxyR
active
OxyR
AhpR transcription
H_2O_2
restrain H_2O_2 to 20 nM
AhpC
H_2O_2
endogenous H_2O_2 10-15 µM/s
respiratory chain
E. coli cell

Figure 1.10: Exogenous and endogenous sources of hydrogen peroxide for *E. coli* cells. Exogenous sources of hydrogen peroxide include H_2O_2-excreting microbes such as lactic acid bacteria, the NADPH oxidase responses of plants and macrophages and photochemically driven redox reactions. Endogenous source of hydrogen peroxide is the incomplete reduction of oxygen in the respiratory chain. OxyR protein in *E. coli* is the transcription factor for *ahpC* and *ahpF* genes in response to hydrogen peroxide and is sensitive to H_2O_2 level of 0.1 µM. This figure has been adopted with modification from Mishra and Imlay, 2012 [117].

High exogenous H_2O_2 level for bacteria cells occurs in the presence of lactic acid bacteria that excrete H_2O_2 competitively [110]. More prominently, bacteria trapped in phagosomes of macrophages encounter ROS, like H_2O_2 concentration of 5-10 µM, a concentration high enough to boost the intracellular H_2O_2 concentration [118]. As an adaptive defence against such high level of H_2O_2 the OxyR protein is well characterised in *E. coli* as a transcription factor. H_2O_2 activates OxyR protein via oxidising a crucial cysteine residue that leads to disulfide bond formation between C199 and C208 and hence to an active conformation [119, 120]. OxyR is sensitive to H_2O_2 level of 0.1 µM, to ensure a quick response when H_2O_2 concentration rises higher than the basal 20 nM [111, 121]. Deletion of the oxyR gene shows 10- to 55-fold higher frequencies of spontaneous mutagenesis and oxidative damages to DNA [122]. It has been shown that over-expression of alkyl hydroperoxide reductase (AhpR) reduces the frequency of spontaneous mutagenesis in *oxyR* deletion mutant [122]. Subsequent studies identified two proteins, AhpF (Alkyl Hydroperoxide Reductase subunit F) and AhpC (Alkyl hydroperoxide Reductase subunit C), to be part of the peroxidase system and member of the OxyR H_2O_2 regulon. The coding DNA sequence of *ahpC* and *ahpF* are in the same operon (Figure 1.11). The *ahpF* gene lies adjacent to the upstream gene *ahpC* and can be co-transcribed. The only known regulation of the transcription of *ahpC* and *ahpF* is through the global oxidative stress activator OxyR as a response to oxidative stress (Figure 1.11) [123].

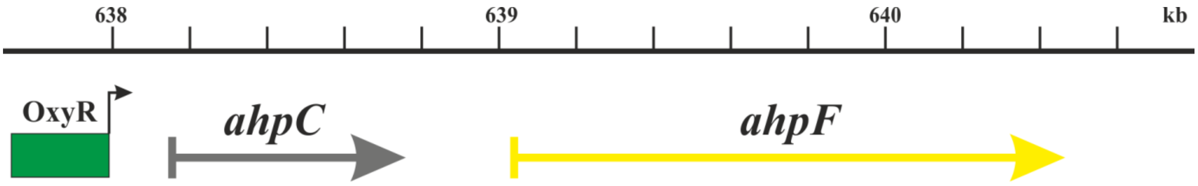

Figure 1.11: OxyR operon for *ahpC* and *ahpF* genes. The OxyR DNA binding site (green) is located ~53 bp before the transcription start. Two genes, *ahpC* (grey) and *ahpF* (yellow) have the Gene ID: 12930899 and 12931712, respectively [124, 125].

The corresponding proteins to the *ahpF* and *ahpC* genes are the 56 kDa flavoprotein (AhpF) and 21 kDa protein (AhpC), which lacks a chromophoric cofactor [126]. Both proteins are soluble and important for the NADH and NADPH dependent reduction of H_2O_2 substrates to their corresponding alcohols and water. Amino acid sequence alignments identify AhpF as a member of the thioredoxin reductase (TrxR) like proteins, the branch of flavoprotein pyridine nucleotide and the family of disulfide oxidoreductase enzyme. The known active site cysteinyl residues of TrxR correspond to two conserved cysteine (C345/C348) in AhpF [127]. Although AhpF has 27 % identity to the *E. coli* TrxR, almost 200 amino acids at the N-terminal region within AhpF has no counterpart in TrxR [127, 128]. Sequence comparison of the C-terminal portion of AhpF to the corresponding TrxR sequence reveals 32 % identity. AhpC, however, does not show similarities to thioredoxin (Trx) in amino acid sequence, but AhpC homologues appear to be conserved throughout all kingdoms and belong to the family of peroxiredoxins [127]. Members of this family are primarily found in the cytosol, but also abundant within the mitochondria, chloroplast and peroxisomes, associated with nuclei and membranes [129]. AhpC and its peroxiredoxin family members are highly expressed in the cell, especially in *E. coli* it is among the ten most abundant proteins [130]. It has been suggested that the redox active cysteine disulfide of AhpF and AhpC are involved in the catalysis of hydroperoxide reduction [131].

1.2.1 Alkyl hydroperoxide reductase system

The Alkyl hydroperoxide reductase system consists of AhpF and AhpC. AhpF is a 57 kDa protein, proposed to form a homo-dimer, and belongs to FAD-dependent NADH protein-disulfide reductase, which catalyses the reduction of redox-active disulfides in AhpC [128, 132]. AhpC is a homodecamer of 21 kDa subunits and a member of the peroxiredoxin family [127, 133, 134]. In overall AhpF has three domains: N-terminal domain (NTD) containing a redox-active disulfide centre, FAD binding domain (FAD) harbouring the redox active flavin, and NADH binding and redox-active disulfide-containing domain (NADH/SS) [128, 132, 135]. Limited proteolysis of AhpF from *Salmonella typhimurium* (*St*AhpF) revealed two soluble fragments. Both *St*AhpF fragments are important for the NADH-dependent reduction of the redox active disulfide of AhpC [132, 136]. The larger fragment (37 kDa), comprised of the C- terminal amino acids from 203 to 521, includes the FAD and NADH/SS domains. The NADH-dependent transhydrogenase and oxidase activities of the larger fragment remain active, but this fragment alone is only poorly capable to reduce AhpC [132]. The alignment of the larger fragment alone to the homologous *E. coli* thioredoxin reductase (TrxR) reveals a sequence identity of 33 %, including the conserved redox-active disulfide C345/C348 in the NADH/SS domain [127, 128, 132]. The redox active C345/C348 in AhpF is corresponding to C138 in TrxR (Figure 1.12).

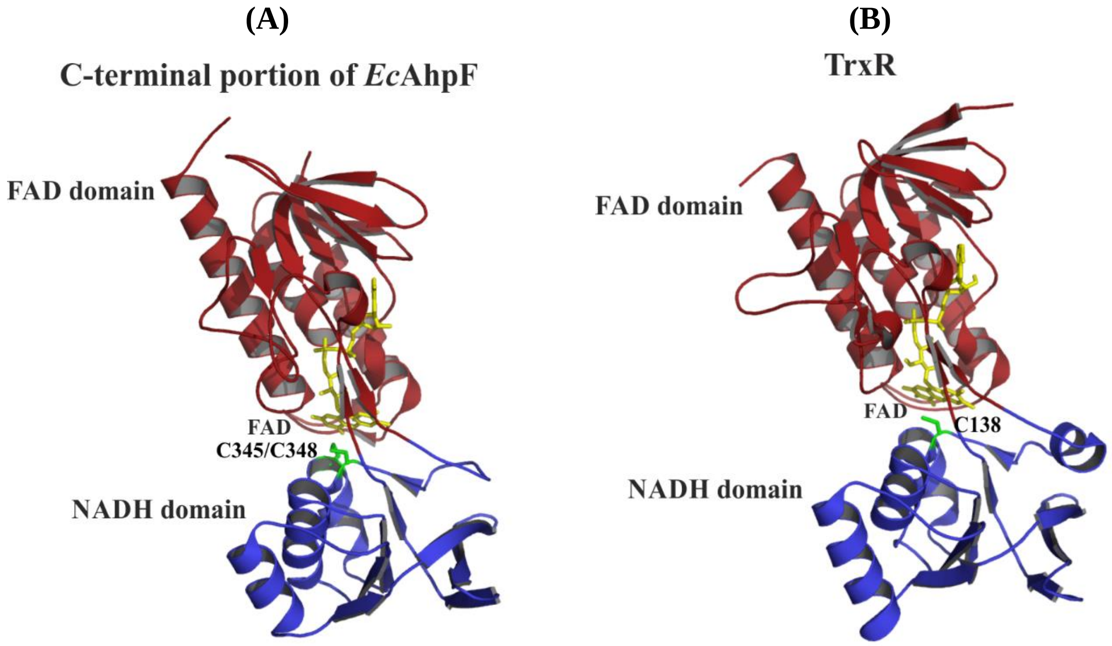

Figure 1.12: Crystal structures of the C-terminal portion of AhpF from *E. coli* (*Ec*AhpF212-521, PDB: 1FL2) *(A)* and Thioredoxin Reductase (TrxR) from *E. coli* (PDB: 1TDF) [137, 138]. Both structures are depicted as monomer and both consist of two domains, the FAD domain (red) and the NADH domain (blue) *(B)*. The redox active C345/C348 in *Ec*AhpF$_{212-521}$ and the corresponding redox active C138 in TrxR are labelled in green sticks and FAD in yellow sticks, respectively.

Furthermore, the crystal structure of the C-terminal portion of AhpF from *E. coli* (*Ec*AhpF$_{212\text{-}521}$) comprised of 311 residues (A212-A521) (Figure 1.12A), which correspond closely to the large proteolytic fragment from *St*AhpF (residues 203-521), confirmed the structural homology to TrxR (Figure 1.12B) [137]. The C-terminal portion forms like TrxR a homodimer with a head-to-tail configuration. *Ec*AhpF$_{212\text{-}521}$ consists of a FAD domain and a NADH domain, whereas the N-terminal domain (NTD) and the linker region are absent. Its redox active cysteines C345/C348 are located closely to isoalloxazine ring of the FAD molecule (Figure 1.12A) [137]. Moreover, two further cysteine residues (C476/C489) were found in the large C-terminal fragment, exist as free thiols in oxidised AhpF and might not be involved in catalysis [137]. The smaller proteolytic fragment comprised of the residues 1-202 including NTD and the redox-active disulfide centre C129/C132 [127, 132, 136]. Both redox-active disulfide centres in AhpF (C345/348 and C129/C132) have the CXXC structural motif, which is also present in thioredoxin (Trx) and TrxR form. Mutations in AhpF from *S. typhimurium*, involving the two disulfide centres C129S/C132S or C345S/C348S, highlight that both redox active disulfide are essential for the catalytic activity of AhpF, and support the role of C129/C132 in the NTD to mediate the electron transfer between C345/C348 to AhpC active disulfide C47/C166 (Figure 1.14) [139]. The NTD of AhpF is directly responsible to reduce the redox-active disulfides in AhpC [132, 136]. Moreover, it has been shown that a chimeric protein composed of the first 207 N-terminal residues of AhpF from *S. typhimurium* followed by the full length TrxR from *E. coli*, has preserved catalytic activity in AhpF/AhpC reductase assays [140]. Two mutants C132S and C345S of the chimeric protein highlighted the importance of both redox active centres in AhpC reductase activity, while TrxR activity requires only the C-terminal redox active centre [140]. This indicates that the C-terminal portion of AhpF and TrxR have redundant mechanism, whereas NTD of AhpF is critical and directly involved in AhpC reduction [140]. Furthermore, the NTD is assumed to be homologous to

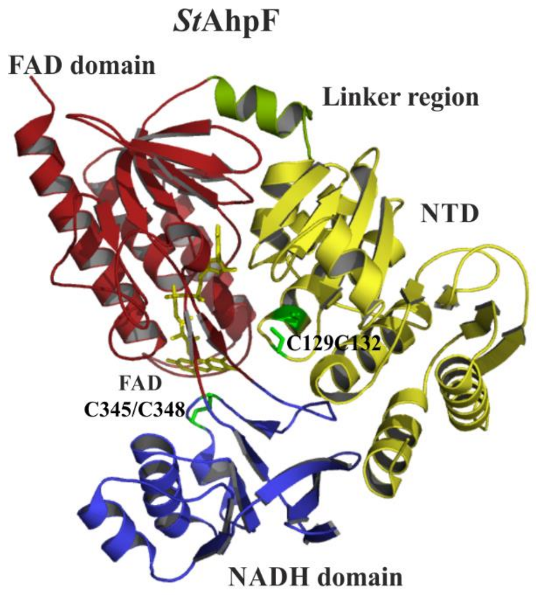

Figure 1.13: AhpF Crystal structure from *Salmonella typhimurium* (*St*AhpF, PDB: 1HYU) [135]. N-terminal domain (NTD), linker region, FAD domain and NADH domain are coloured in yellow, green, red and blue, respectively. The redox active C129/132 and C345/C348 are coloured in green sticks and FAD in yellow sticks.

thioredoxin and **p**rotein **d**isulfide **o**xidoreductase (PDO), a thioredoxin-like (Trx-like) protein from *Pyrococcus furiosis* (*Pf*PDO) (23% identical sequence), as shown earlier in the AhpF crystal structures from *S. typhimurium* (PDB ID: 1HYU) (Figure 1.13) [135, 136, 141]. The crystal structures of *S. typhimurium* as well as *Pf*PDO revealed the existence of two fused thioredoxin like folds in the NTD [135, 141]. In *Pf*PDO, each thioredoxin fold consists of one active disulfide centre, whereas the NTD of *S. typhimurium* comprises only one redox active disulfide centre, namely in the second thioredoxin fold with a distinct CXXC active site motif [135, 141]. The *St*AhpF crystal structure reveals all 521 amino acids are visible, highlighting all four regions (Figure 1.13). Electron transfer within AhpF starts from NADH and goes via FAD to the redox active disulfide C345/C348 at the C-terminal portion and from this disulfide to the N-terminal C129/C132 disulfide centre (Figure 1.14) [139]. The electron movement from AhpF to AhpC is predicted to occur via the redox centres C129/C132 of AhpF to the disulfide centre C47/C166 of AhpC (Figure 1.14) [140]. The crystal structure of AhpF from *S. typhimurium* is a homodimer, and positioned in a similar manner than the Trx/TrxR system (Figure 1.13, Figure 1.15) [135, 142]. The distance of both redox active centres in one monomeric AhpF molecule is 33 Å apart, whereas the distances between N- and C-terminal redox active centres among the AhpF homodimer are 35 Å. This conformation thus favours an inter- as well as an intramolecular reduction between the C- to N-terminal redox active disulfide of AhpF [135]. In fact, the electron transfer between the two disulfide centres occurs in an intramolecular manner, demonstrated via two heterodimeric AhpFs, in which either one of the two possible pathways was abolished, while the other pathway was kept intact in each heterodimeric AhpF constructs [143]. One heterodimer comprises of one C-terminal portion N208-A521 and one AhpF C345, C348S mutant without intramolecular activity. Hence this heterodimer has only the intersubunit electron transfer pathway active for the AhpC reductase. Likewise, the other heterodimer comprised of one C-terminal portion of N208-A521 with C345, C348S mutation and one intact wild type AhpF, which allows the electron transfer only through the intrasubunit pathway [143]. Indeed, the second heterodimer exhibited 42% AhpC reductase activity compared with wild type AhpF homodimer, whereas the first engineered heterodimer presented no activity [143].

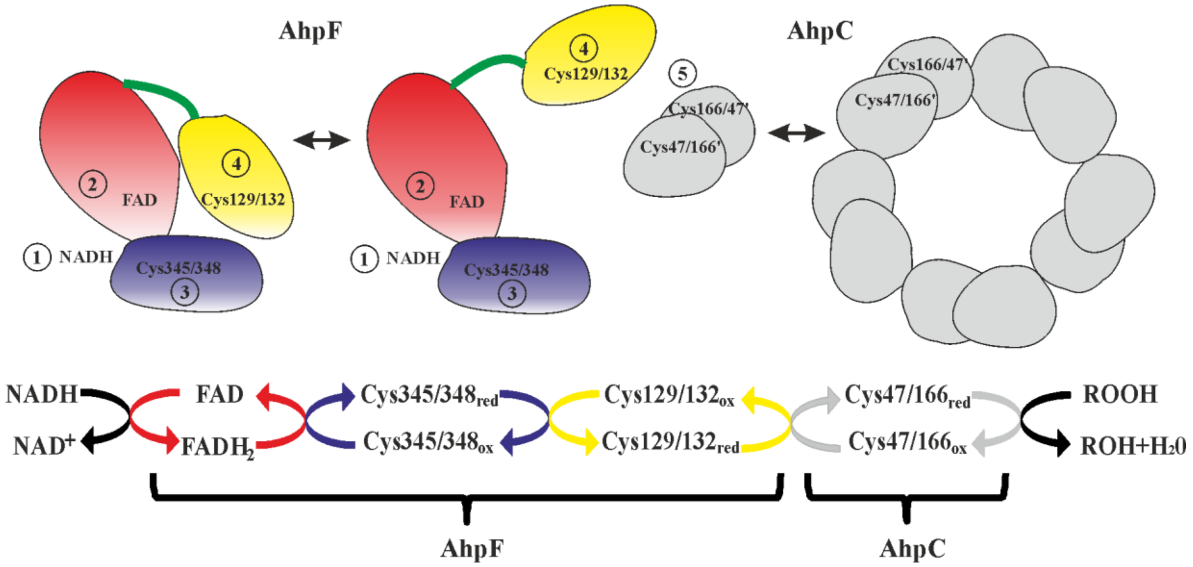
AhpF
AhpC
④ Cys129/132
② FAD
① NADH
Cys345/348 ③
⑤
Cys166/47'
Cys47/166'
NADH
NAD+
FAD
FADH2
Cys345/348red
Cys345/348ox
Cys129/132ox
Cys129/132red
Cys47/166red
Cys47/166ox
ROOH
ROH+H20
AhpF
AhpC

Figure 1.14: Electron transfer of the Alkyl Hydroperoxide Reductase (AhpR) system. This figure has been adopted with modification from Wood *et al.* 2001 [135]

The second subunit of AhpR is AhpC. In AhpC, both cysteines C47 as well as C166 are conserved. C47 is located at the N-terminal region within a valosin-containing protein (VCP) motif, which is also conserved in AhpC. Mutational studies using C47S mutants reveal no peroxidase activity, whereas in C166S mutants a 60% activity remains, highlighting the importance of C47 in the catalytic peroxidatic activity [144]. In NBD-Cl assays, the sulphur of C47 residue oxidises to cysteines sulfenic acid (RSOH) by peroxide substrates [145]. This sulfenic acid leads to a local unfolding of α2-helix residues into the loop region at the active site, that cause C47 to be exposed in close contact to C166 of the other AhpC subunit in a head to tail conformation and allowing the intermolecular disulfide bond formation [132, 134].

1.2.2 Catalytic cycle of AhpF

AhpF catalyses the hydride transfer from NADH via flavin and two different redox active disulfide bridges to the dithiol centre of AhpC [140]. AhpC facilitates significantly the peroxidative turnover rate and is the natural substrate of AhpF. AhpF alone recognises peroxides as substrate very poorly and AhpC by itself does not catalyse the NADH-dependent peroxide reduction [144]. Since the NTD of AhpF is homologous to Trx and the C-terminal portion, containing NADH/SS and FAD is homologous to TrxR, the catalytic mechanism of AhpF has been deduced analogously to the Trx/TrxR system [135, 138, 142].

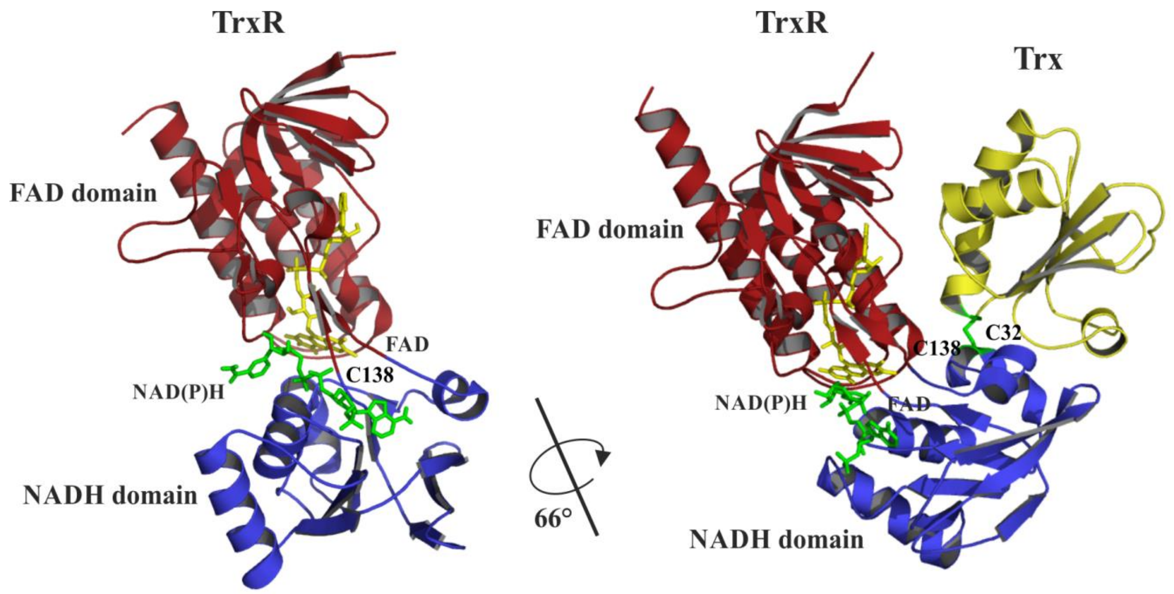

Figure 1.15: Crystal structures of Thioredoxin Reductase (TrxR) from *E. coli* (left, PDB: 1TDF) and the heterodimeric crystal structure of the Thioredoxin Reductase and Thioredoxin complex (right, TrxR-Trx) from *E. coli* (PDB: 1F6M). Trx is coloured in yellow, FAD domain in red and NADH domain in blue. The redox active C138 correspond to C345/C348 in *Ec*AhpF212-521 are labelled in green sticks. FAD and NAD(P)H are depicted in yellow and green stick, respectively.

Furthermore, comparison of the *Ec*AhpF C-terminal portion and TrxR with the twisted conformation of TrxR in complex with Trx suggests a domain movement favouring the intramolecular hydride transfer from the C- to the N-terminal disulfide centres [135, 137, 138, 142, 146]. It was therefore proposed that during catalytic activity, the NADH/SS domain turns 66° closely to FAD, this movement brings a bound NADH to the *re* face of the isoalloxazine ring of flavin for its oxidation (Figure 1.15) [142]. The rotation of the NADH/SS domain brings also the reduced dithiol (C345/348) to the surface, where it might be in position to reduce the NTD disulfide C129/C132 [135]. After the reduction of the NTD, the NADH/SS turns 66° back, bringing C345/C348 back to the *re* face of the flavin group, and the NAD^+ to the surface for exchange with new NADH. The catalytic cycle of AhpF is complete after the hydride from NADH reached the redox active cysteines in NTD [135]. The NTD has two important roles. Firstly, it acts as a substrate for the C-terminal redox active disulfide bond, and then in turn reduced NTD acts as a protein disulfide reductase for redox active disulfide in AhpC [132, 135, 140, 142]. However, despite the vast studies so far, the mechanisms for the dithiol-disulfide exchange from AhpF to AhpC are still poorly understood. Furthermore, the conformation of AhpF and its catalytic relevant intermediate while reducing AhpC is not known so far.

1.2.3 Catalytic cycle of AhpC

AhpC from *E. coli* is a member of the peroxiredoxin family [127, 133, 134]. Peroxiredoxins have three different classes, the typical 2-C, atypical 2-C and 1-C enzymes on the basis of the number and sequence positions of cysteinyl residues [147]. AhpC from *E. coli* belongs to the typical 2-C peroxiredoxins. X-ray crystal structures of various 2-C peroxiredoxin (Prx) reveal the decameric ring formation [134, 148-152].

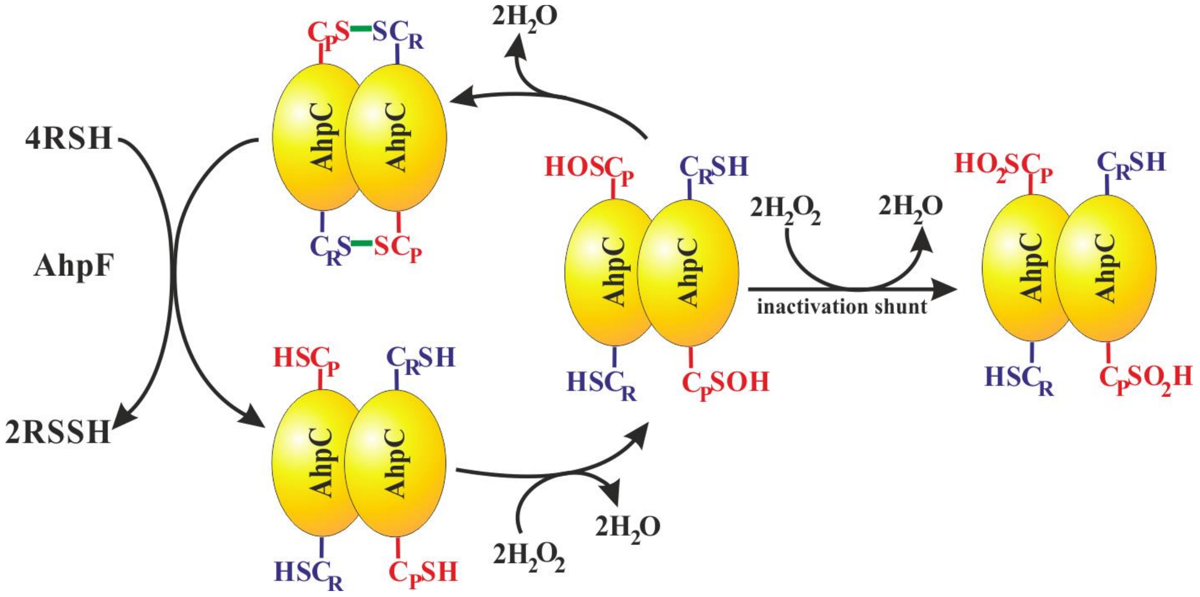

Figure 1.16: The catalytic cycle of AhpC. The peroxidatic cysteine is shown as (C_PH), sulfenic acid (C_POH), sulfinic acid (C_PO_2H) and the disulfide with resolving cysteine (C_RH). The flavoprotein AhpF reduces AhpC. The figure is adopted with modification from Wood *et al*., 2003.

For its catalytic activity, AhpC consists of two redox active cysteines (C47/C166). The cysteine residue 47 is the peroxidatic cysteine (C_P) that attacks the hydroperoxide or alkyl hydroperoxide (ROOH) [153]. All AhpC enzymes catalyse its reaction with C_P, a threonine (or serine) and an arginine. The C_P and the T (S) belongs to a conserved motif consists of P-X-X-X-T/S-X-X-C_P, whereas the R is located apart in the AhpC primary structure [147, 154-156]. It is proposed that both S and R stabilize the C_P sidechain in its transition state between thiolate form (C_P-S^-) and peroxide during the nucleophilic attack [157-159]. During this attack, the thiol group (C_P-SH) of the peroxidatic cysteine (C47) oxidised to sulfenic acid (C_P-SOH) with the release of H_2O. The oxidation of C_P unwinds the α-helix allowing the help of the other redox active cysteine 166, so called resolving cysteine (C_R) located at the C-terminal end of the neighbouring monomer, to condensate sulfenic acid to an intermolecular disulfide bond (C_PS-SC_R) [134]. The disulfide bond is guided with a partial unfolding of the α-helix that contains C_P [153]. Therefore, during its catalytic cycle, AhpC alternates between locally unfolded when oxidised and fully folded when reduced [153]. The regeneration of oxidised AhpC is carried out by the disulfide C129/C132 in the NTD of AhpF. It acts as an electron donor and reduces the disulfide bond between C_P and C_R to two catalytic active thiol groups [144]. Besides oxidative stress, eukaryotic AhpC is also involved in signal transduction at high H_2O_2 concentration. AhpC undergoes an irreversible over oxidation from the sulfenic acid (C_P-SOH) to sulfinic acid (C_P-SO_2H) [160-162]. This overoxidation is also coupled with structural and a functional change. During such overoxidation, AhpC loses its peroxidative activity to induce its second function as molecular chaperon. This functional change is guided with an assembly to higher order oligomers to high molecular weight (HMW) [100, 163-165]. Investigating the factors of AhpC to form HMW complexes might be therefore of great interest. For the hydroperoxidase activity, AhpCs are mandatory dimer that can reversible assemble to a decameric (α2)5 formation [134]. Despite the studies that has been done so far, the importance for AhpC decamerisation as well as the molecular mechanism for AhpC regeneration by AhpF is still not understood. Characterisation of AhpF and AhpC will give new insights into oxidative stress, since it is heavily involved in quite a number of diseases, such as rheumatoid arthritis, inflammatory bowel disorders, and atherosclerosis, and it is emerging as one of the most important causative agents of mutagenesis, tumor genesis, and aging [4, 166-169].

1.3 Goals of this thesis

Since the interaction between subunit *a* and ARNO (ADP-ribosylation factor nucleotide site opener), a guanine nucleotide exchange factor (GEF) of the small G protein ADP ribosylation factor (Arf) is of great interest, investigation of the binding site will be done by using NMR spectroscopy experiments.

In order to characterise the binding motifs of subunit *a* to ARNO, the structure of two peptides (1-17 aa and 368-395 aa) of subunit *a2* (mouse V-ATPase) involved in the ARNO association, will be investigated using NMR spectroscopy. Moreover, the first binding site of *a2* ($a2_{1-17}$) with the Sec7 domain of ARNO, will be assessed using NMR titration experiments. These data will provide the first step to determine the interaction mechanism between subunit *a* and ARNO in high resolution. Further NMR titration experiments with subunit *a* construct, $a_{104-363}$ with ARNO will prove and provide more structural features into the binding mechanism. Structural investigation of $a_{104-363}$ using small angle X-ray scattering (SAXS) and crystallisation will be performed.

Besides the cytosolic N-terminal hydrophilic charged domain, subunit *a* consists also of the C-terminal membrane hydrophobic domain that is responsible for the proton translocation and putatively for pH sensing [72]. To get an insight into the topology of subunit *a*, the constructs: $a_{468-552}$, $a_{582-649}$, $a_{673-731}$, $a_{478-537}$, $a_{596-634}$, $a_{653-727}$ and $a_{801-840}$ from *S. cerevisiae* that contain putative soluble regions, facing either to the lumen or the cytosolic side were designed. Soluble constructs will be purified and undergo structural investigation using NMR and crystallisation.

In addition to the pH dependent vesicle formation that is regulated via V-ATPases and ARNO association, redox reactions are also highly significant for the survival of the cell and are used as a defence against reactive oxygen species (ROS) during oxidative stress. Therefore, Alkyl Hydroperoxide Reductase (AhpR) subunits F and C will undergo structural characterisation using SAXS, crystallisation and cryo electron microscopy.

The crystal structures of AhpF and AhpC from *E. coli* will give new insights into the mechanisms for the dithiol-disulfide exchange from AhpF to AhpC. New structural conformation of AhpF will be derived by SAXS analysis that helps to understand catalytic relevant intermediates of AhpF in reducing AhpC, a so far undescribed catalytic event. CryoEM studies of AhpC will provide information regarding its dynamics in oligomerisation and the importance for AhpC decamerisation for its dual activity as anti-oxidant enzyme and molecular chaperon in rescuing the cell from harmful hydroperoxides and low pH.

2. Materials and methods

2.1 Materials

2.1.1 Chemicals

All the chemicals used for the study were of at least analytical grade. Chemicals were purchased from the following companies:

2.1.1.1 Buffers and salts

	Sigma (St. Louis, MO, USA)
	USB (Sampscott, MA)
	Calbiochem (Darmstadt, Germany)
	Fluka (Sigma, Buchs Germany)
	Roth (Karlsruhe, Germany)
	Serva (Heidelberg, Germany)
DTT	Hoefer (San Francisco, CA, USA)
Ni^{2+}-NTA	QIAGEN (Hilden, Germany)
Pefabloc^{SC}	BIOMOL (Hamburg, Germany)
PMSF	Sigma (St. Louis, MO, USA)
$^{15}NH_4Cl$	Cambridge Isotopes Lab (USA)
LB Media	BD (Sparks, MD, USA)

2.1.1.2 Electrophoresis Chemicals

(Agarose, SDS, Glycine, APS etc.)	Bio-Rad (Hercules, CA, USA)
Antibiotics	Calbiochem, Sigma and Gibco (Invitrogen)
IPTG	Fermentas (Vilnius, Lithuania)
BSA	GERBU (Heidelberg, Germany)

2.1.2 Molecular biology materials

Genomic DNA	*Saccharomyces cerevisiae* (AH104 strain)
Primers	1st Base and Research Biolabs (Singapore)
Peptides	NTU proteomics core facility, School of Biological Sciences, Nanyang Technological University, Singapore
Pfu DNA Polymerase	Fermentas (Glen Burnie, MD, USA)

NcoI, SacI	Fermentas and New England Biolabs
T4 DNA Ligase	Fermentas and NEB
Precision Proteases	(GE Healthcare, Uppsala, Sweden)
Miniprep Plasmid Kit	Qiagen (Hilden, Germany)
Nucleobond AX mediprep Kit	MN & Co (Düren, Germany)
Escherichia coli expression strains	DH5α, BL21 (DE3)
pET-9d1	Grüber *et al.*, 2002 [170]

2.1.3 Chromatography materials

2.1.4 Gel filtration

Superdex 75 HR (10/30)	GE Healthcare (Uppsala, Sweden)
Superdex 200 HR (10/30)	GE Healthcare (Uppsala, Sweden)

2.1.5 Instruments and accessories

Akta FPLC	GE Healthcare (Uppsala, Sweden)
Millex Filters (0.45 μM)	Millipore (Bradford, USA)
Syringe, needles and accessories	BD Biosciences

2.1.6 Protein concentration, estimation

Centriprep YM10	Millipore (Co-cork, Ireland)
Amicon ulta (3-30kDa)	Millipore (Co-cork, Ireland)
BCA Assay Kit	Pierce (Rockford, IL, USA)

2.1.7 Other instrumentation

PCR Thermocycler:	
Biometra T personal	Biometra
Biometra T gradient	Biometra
Sonoplus Sonicator	Bendelin
Micropulser Electroporator	Bio-Rad (Hercules, CA, USA)
Ultraspec 2100 Pro-Spectrophotometer	Amersham Biosciences
BioSpec-Nano	Shimadzu, Tokyo, Japan

2.1.8 Computer software

Vector NTI 10.3.0	Invitrogen

SPARKY	Goddard and Kneller, 1997 [171]
Topspin 1.3	Bruker Biospin
CYANA 2.1	Günthert *et al.*, 1997 [172]
TALOS	Cornilescu *et al.*, 1999 [173]
MOLMOL	Koradi *et al.*, 1996 [174]
PyMOL v0.99	DeLano Scientific LLC, USA [175]
HKL2000 package	Zbyszek and Wladek, 1997 [176]
Refmac5 (CCP4 package)	Murshudov *et al.*, 1997 [177]
MOLREP	Vagin and Taplyakov, 1997 [178]
PHASER	McCOY *et al.*,2007 [179]
CNS	Brunger *et al.*, 1998 [180]
Coot	Emsley and Cowtan, 2004 [181]
Ramachandran plot	Ramachandran *et al.*, 1963 [182]
PROCHECK	LASKOWSKI *et al.*, 1993 [183]
Quantity One	Bio-Rad (Hercules, CA, USA)
CCP4	1994
PRIMUS	Svergun, 1993 [184]
Gasbor	Svergun *et al.*, 2001 [185]
SUBCOMB	Svergun *et al.*, 2001 [185]
EMAN2	Tang *et al.*, 2007 [186]
UCSF Chimera	Pettersen *et al.*, 2004 [187]

2.2 Cloning of subunit *a* (Vph1) constructs from *S. cerevisiae* V_1V_O ATPase

To amplify the *Vph1* coding region, oligonucleotide primers incorporating *NcoI* or *SacI* restriction site (underlined), were designed.

Construct		**Oligonucleotide sequence 5'-3'**
$\boldsymbol{a}_{104\text{-}363}$	forward	CGTTCCACCCATGGGTTCAGTGATAGATGATTATGTCCGG
	reverse	TTGGATAATGAGCTCTTAATCAATACCCAATCTTGCGATCATTTC
$\boldsymbol{a}_{468\text{-}552}$	forward	GTCCATGGGTGTCTTTTCCATGTACACAGG
	reverse	ATGAGCTCTTAAGAATAGGTCATGTGGATGAACC
$\boldsymbol{a}_{582\text{-}649}$	forward	GTCCATGGGTATCTTTGGTTATCTTTCCG
	reverse	ATGAGCTCTTATAGCAACCAAGGAATACAAACCAAG
$\boldsymbol{a}_{673\text{-}731}$	forward	GTCCATGGGTGCAGATGCTAGTTCTGAAGATTTG
	reverse	ATGAGCTCTTATGCAGTGTGCGAAACACAATTCAAAC
$\boldsymbol{a}_{478\text{-}537}$	forward	GTCCATGGGTATCTTCTCTAAAACTATGACTATTTTCAAG
	reverse	ATGAGCTCTTACATTTTGTAAGAATTAGAAAATAACAAAG
$\boldsymbol{a}_{596\text{-}634}$	forward	GTCCATGGGTGTTAAGGACGGAAAGCCTG
	reverse	ATGAGCTCTTATTGGACCTTTGCTTGATGAGGGTATAATTC
$\boldsymbol{a}_{653\text{-}727}$	forward	GTCCATGGGTTTACATTTCAAATTCACTCATAAAAAG
	reverse	ATGAGCTCTTAAACACAATTCAAACAGAATTCAATTGTATGAATAAC
$\boldsymbol{a}_{801\text{-}840}$	forward	GTCCATGGGTCACTGGGTTGAATCTATGTCC
	reverse	ATGAGCTCTTAGCTTGAAGCGGAAGAGCTTGCACTAG

S. cerevisiae genomic DNA was used as template for polymerase chain reaction (PCR). PCR was set up in a total volume of 50 µl on ice as mentioned below with the appropriate concentration of constituents as:

Reagents	**Amount**
Pfu buffer (10x)	5 µl
DNTP's (2 mM)	1.5 µl
Primers (100 µM)	2 x 0.5 µl
Template (genomic DNA)	1 µl
MilliQ water	40.5 µl
Pfu DNA polymerase	1 µl

All reagents were pipetted into a PCR tube kept on ice all the time, mixing of the reagents was done by short centrifugation. PCR thermocycler (Biometra T personal) was preheated to 95 ºC before reaction tubes were placed inside the machine. The following PCR thermocycler program was used for amplification:

Cycle steps	Temperature	Time	
Lid	99 ºC		
Initial denaturation	96 ºC	3 min	
Cycle denaturation	96 ºC	30 sec	30 cycles
Annealing	58 ºC	45 sec	
Extension	72 ºC	60 sec	
Final extension	72 ºC	5 min	
End	4 ºC		

Cycle denaturation, annealing and extension steps were repeated for another 29 cycles. Total time taken for the PCR program was 1 h 43 min 49 sec.

After amplification, the PCR product was stored at -20°C, 5 µl of which was then applied onto an analytical agarose gel (1.5%) to check its quality. The gel was kept in ethidium bromide solution for 20 min and observed under UV light. The size of the PCR product was confirmed with the appropriate DNA marker. Remaining reaction mixture was applied onto a 1.5% preparative agarose gel. The portions corresponding to the correct PCR product were cut out immediately and purified by gel extraction kit (QIAGEN) as per the manufacturer's protocol. The product was finally eluted in 30 – 50 µl volume of water or Tris-HCl buffer of pH 8.0. 1 µl of gel extracted PCR product was applied onto 1.5% analytical agarose gel for estimating the purity of the sample. Purified DNA was double digested overnight at 37 ºC by taking appropriate amount of *Nco*I and *Sac*I enzymes. After overnight digestion, the reaction mixture was purified by enzyme reaction purification kit from QIAGEN again. Subsequently, ligation reactions between vector (Figure 2.1) and amplified PCR product were setup at room temperature. The reagents used were as follows:

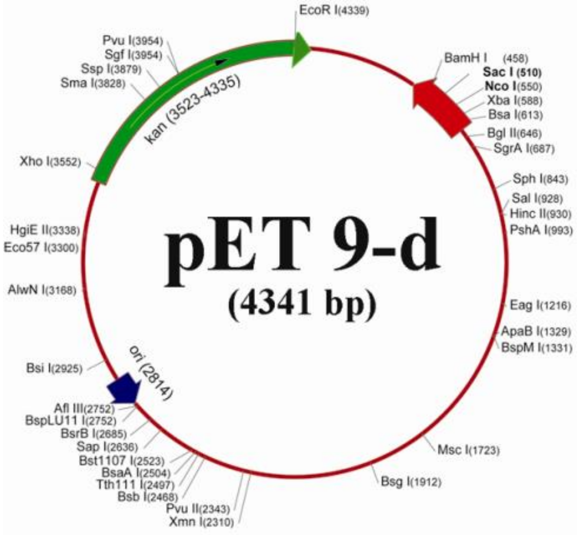
EcoR I(4339)
Pvu I(3954)
Sgf I(3954)
Ssp I(3879)
Sma I(3828)
kan (3523-4335)
Xho I(3552)
HgiE II(3338)
Eco57 I(3300)
AlwN I(3168)
Bsi I(2925)
ori (2814)
Afl III(2752)
BspLU11 I(2752)
BsrB I(2685)
Sap I(2636)
Bst1107 I(2523)
BsaA I(2504)
Tth111 I(2497)
Bsb I(2468)
Pvu II(2343)
Xmn I(2310)
BamH I (458)
Sac I (510)
Nco I(550)
Xba I(588)
Bsa I(613)
Bgl II(646)
SgrA I(687)
Sph I(843)
Sal I(928)
Hinc II(930)
PshA I(993)
Eag I(1216)
ApaB I(1329)
BspM I(1331)
Msc I(1723)
Bsg I(1912)
pET 9-d
(4341 bp)

Figure 2.1: Modified pET-9d (+) vector showing full map and unique multiple cloning sites (MCS) that has been used to clone various genes [170].

Ligase buffer (10x)	1.5 µl
Vector (V)	50-100 ng
Insert (I)	Variable (1-5 times of vector)
T4 Ligase	1 µl
MilliQ water	variable
Total	15 µl

The ligation mixture was kept at room temperature for 2 hrs. The reaction was terminated by precipitation of DNA from rest of the reaction mixture by adding 85 µl of Milli Q water to make a final volume of 100 µl. 1 ml of butanol was added into the mixture and mixed thoroughly. Then the mixture was centrifuged at 13,000 x *g* (using Eppendorf Mini-centrifuge) for 10 min., and the supernatant was discarded gently. The pellet was resuspended in 150 µl of 70% ethanol and centrifuged again for 5 min. Supernatant was again removed and the pellet was re-dissolved in 10 µl of elution buffer (10 mM Tris-HCl, pH 8.5; EB buffer, QIAGEN) or Milli Q water. 5 – 10 µl of ligation mixture was used for the transformation into *Escherichia coli* DH5α cells. Single colonies were picked from the transformation plate on the next day and were incubated at 37 °C. The plasmid DNA was isolated using standard protocol (QIAGEN mini-prep kit) and subsequently double digested and applied onto 1.5% agarose gel, in order to confirm the presence of ligated insert. Size of insert and vector were compared with appropriate controls and markers. Verified plasmid was finally transformed into *E. coli* BL21 (DE3) or Rosetta-gami^{TM}2 (DE3) cells for protein production. *E. coli* BL21 (DE3) and Rosetta-gami^{TM}2 (DE3) cells were both grown on 30 µg/ml kanamycin-containing Luria-Bertoni (LB) agar plates, while the LB agar plates for Rosetta-gami^{TM}2 (DE3) cells have additional 12.5 µg/ml tetracycline and 100 µg/ml chloramphenicol. *E. coli* BL21 or Rosetta-gami^{TM}2 (DE3) expression strains were purchased from Novagene (Darmstadt, Germany).

2.2.1 Electroporation transformation

Reagents
SOB media: 20 g/l Tryptone
5 g/l Yeast Extract
0.58 g/l NaCl
0.18 g/l KCl
10 ml Mg-solution (1 M $MgCl_2 6H_2O$, 1 M $MgSO_4$)
SOC media: *SOB* 100 mM Glucose

Electroporation was done for the transformation of plasmid into electro-competent cells. Electro-competent cells were prepared as per the protocol from Current Protocols in Molecular

Biology (Wiley InterScience) manual. 1 – 50 ng of plasmid was added to 80 – 100 µl of competent cells and incubated on ice for 5 – 10 min. Electroporation was done at constant voltage of 2 500 V (Micropulser Electroporator, Bio-Rad). The cuvette was then immediately placed back on ice for 1 min., following addition of LB or SOC (SOB + 100 mM Glucose) media to total volume of 1 ml. The mixture was incubated at 37 °C for 1 h. Appropriate dilutions were prepared before plating the cells on antibiotic selection plates.

2.3 Production and purification protein constructs

2.3.1 Induction test

Reagents for 4 x lysis buffer:	250 mM Tris/HCl, pH 6.8
	9.2% SDS
	40% Glycerol
	0.2% Bromophenol Blue
	1 mM DTT

At least 3-4 single colonies were randomly picked up. They were grown to OD_{600} of 0.6 - 0.7 at 37 °C with shaking of 170 – 200 rpm (Infors HT Minitron shaker). Final concentration of 0.5-1 mM IPTG was then added to start induction. Mixture was kept at 30 – 37 °C for 2 – 3 h. The concentration of IPTG depends on the characteristics of protein being produced and the conditions that have been optimised for respective protein. Respective controls were left uninduced under identical conditions. Cells were pelleted down and resuspended with 60 µl of 1x lysis buffer in presence of 1 mM DTT. Resuspended cell mass was heated at 95 ºC for 5 min and 15 – 20 µl of each sample was loaded onto a 17% SDS polyacrylamide gel. The expression was more in the induced cultures ((+) supplemented with IPTG) than uninduced cultures ((-) not supplemented with IPTG). A representative induction gel is shown in Figure 3.19.

2.3.2 Solubility test for recombinant proteins

Following the successful induction of proteins with appropriate concentration of IPTG at the optimised temperature and shaking conditions, solubility of the produced proteins was tested in various buffers as shown in Figure 3.20. 50 ml of culture was grown and induced with IPTG. Cells were pelleted down into five equal fractions by centrifuging at 10 000 x g for 10 min. Freshly prepared protease inhibitors Pefabloc^{SC} in water and/or 100 mM PMSF (dissolved in isopropanol) were added to a final concentration of 2 – 8 mM (Pefabloc^{SC}) or 1 – 2 mM (PMSF). Reducing agent such as DTT (1 mM) was used in the preparation. Resuspension was sonicated at 15% power with KE 76 tip of sonicator (Bandelin Sonoplus) three times for one min each, with a cooling interval of two min between each cycle. Supernatant was then separated from the pellet by centrifugation at 10,000 x g and transferred to a fresh tube. Pellets were resuspended in the respective buffers as shown in the Figure 3.20. All the steps were carried on ice. 10 – 15 µl of pellet and supernatant were loaded onto a 17% SDS gel.

2.3.3 Purification of $a_{104-363}$ construct of the *S. cerevisiae* V_1V_O-ATPase

To express His$_6$-$a_{104-363}$, liquid cultures were shaken in LB medium containing kanamycin (30 µg/ml) for about 6 h at 30 °C until an optical density OD_{600} of 0.6 - 0.7 was reached. To induce expression of His$_6$-$a_{104-363}$, the cultures were supplemented with isopropyl (thio)-β-D-galactoside (IPTG) to a final concentration of 1 mM. Following incubation for another 16 h at 20 °C, the cells were harvested at 8 500 x *g* for 12 min, 4 °C. Subsequently, they were lysed on ice by sonication for 3 x 1 min in buffer A (50 mM Tris/HCl, pH 8.5, 200 mM NaCl, 1 mM DTT, 2 mM PMSF and 2 mM Pefabloc^{SC} (BIOMOL)). Precipitated material was separated by centrifugation at 10 000 x *g* for 35 min. The supernatant was filtered (0.45 µm; Millipore) and passed over a 2 ml Ni^{2+}-NTA resin column to isolate subunit $a_{104-363}$, according to Grüber *et al.* (2002) [170]. The His-tagged protein was allowed to bind to the matrix for 1.5 h at 4 °C and eluted with an imidazole-gradient (25 - 250 mM) in buffer A. Fractions containing His$_6$-subunit $a_{104-363}$ were identified by SDS-PAGE [188], pooled and concentrated as required using Centricon YM-3 (3 kDa molecular mass cut off) spin concentrators (Millipore). Imidazole was removed by gel filtration chromatography using a Superdex 75 HR 10/30 column (GE Healthcare) and a buffer of 50 mM Tris/HCl, pH 8.5, 200 mM NaCl and 10 mM EDTA. The purity and homogeneity of all protein samples were analysed by SDS-PAGE [188]. SDS-gels were stained with Coomassie Brilliant Blue G250. Protein concentrations were determined by bicinchoninic acid assay (BCA; Pierce, Rockford, IL., USA).

2.3.4 Purification of $a_{104-363}$, $a_{653-727}$, $a_{582-649}$, $a_{673-731}$ *and* $a_{801-840}$ constructs

After successful solubility tests, proteins were then purified in large scale. To produce His$_3$-$a_{653-727}$, liquid cultures were incubated in kanamycin-positive (30mg/ml) LB medium at 37 °C with shaking of 180 rpm, until an optical density OD_{600} of 0.6 - 0.7 was achieved. Expression of His$_6$-$a_{653-727}$ was obtained by adding of isopropyl (thio)-β-D-galactopyranoside (IPTG) to a final concentration of 1 mM. Following incubation for another 4 h at 37 °C, the cells were harvested at 8 500 x *g* for 12 min, 6 °C. Subsequently, they were lysed on ice by sonication for 3 x 1 min in buffer A (50 mM Tris/HCl, pH 8.5, 500 mM NaCl, 2 mM PMSF and 2 mM Pefabloc^{SC} (BIOMOL). Precipitated material was separated by centrifugation at 10 000 x *g* for 35 min. Supernatant was filtered (0.45 µm; Millipore) and passed over a 2 ml Ni^{2+}-NTA resin column to isolate subunit *a*, according to Grüber *et al.*, (2002) [170]. His-tagged protein was allowed to bind to the matrix for 1.5 h at 4 °C and eluted with an imidazole-gradient (25 - 600 mM) in buffer A. Fractions containing His-tagged $a_{653-727}$ were identified by SDS-PAGE [188], pooled and concentrated as required using Centricon YM-3 (3 kDa molecular mass cut off) spin concentrators (Millipore). Imidazole was removed by gel filtration chromatography using a Superdex 75 HR 10/30 column (GE Healthcare) and a buffer of 50 mM Tris/HCl (pH 8.5), 500 mM NaCl and 5 mM EDTA.

The other subunit *a* constructs: $a_{582-649}$, $a_{673-731}$ and $a_{801-840}$ have been purified in the same way as described above. To produce His$_6$-$a_{104-363}$, liquid cultures were incubated in kanamycin-positive (30 mg/ml) LB medium at 30 °C with shaking of 180 rpm, until an optical density OD_{600} of 0.6 - 0.7. After adding of IPTG to a final concentration of 1 mM, the liquid culture were incubated for another 16 h at 20 °C, the cells were harvested at 8 500 x *g* for 12 min, 6 °C. The lysis buffer buffer A (50 mM Tris/HCl, pH 8.5, 200 mM NaCl, 2 mM PMSF and 2 mM Pefabloc^{SC} (BIOMOL)) differs for sonication and the following purification steps accordingly. The imidazole gradient was 25 mM to 300 mM. The purity and homogeneity of all protein samples were analysed as described in section 2.3.3.

2.3.5 Purification of a_{1-388} construct from *S. cerevisiae*

Subunit His$_6$-a_{1-388} containing N-terminal His-tag was cloned and kindly provided by Dr. Raj Thaker [189]. The over expression was produced in Rosetta-gami^{TM} 2 cells and purified using the two-step protocol. The first step involved enrichment of His-tagged subunit a_{1-388} protein by specific binding to Ni^{2+}-NTA matrix and the second step employed ion-exchange chromatography using Resouce^{TM} Q column (GE Healthcare), to remove remaining impurities. Buffer A of a_{1-388} purification contains: 50 mM Tris/HCl, pH 7.5, 500 mM NaCl, 2 mM PMSF and 2 mM Pefabloc^{SC} (BIOMOL).

2.3.6 Purification of Sec7- domain of ARNO from human (*Homo sapiens)*

Recombinant Sec7-domain coding plasmid containing N-terminal GST-tag and C-terminal His-tag in pGex6-P1 was kindly provided by Prof. Dr. Vladimir Marshansky (MGH, Harvard University, Boston, USA). The over-expression was performed in BL21 cells and purified using the three-step protocol as described in section 2.3.3 above. The first step involved enrichment of His-tagged Sec7 recombinant protein by specific binding to Ni^{2+}-NTA matrix. In order to cleave the N-terminal GST-tag from the Sec7-domain, eluted protein in the imidazole concentration of 75-200 mM were digested overnight with Precision Proteases (GE Healthcare). The second step employed affinity chromatography using GSTrap^{TM} column (GE Healthcare). GST binds to the GSTrap^{TM} column (GE Healthcare), whereas Sec7-domain of ARNO remains in the flow through. The final step was performed by using a Superdex 75 HR 10/30 column (GE Healthcare). All purification steps were done in buffer A (50 mM Hepes, 300 mM NaCl, pH 7.5).

2.3.7 Purification of Alkyl Hydroperoxide Reductase subunit F (AhpF) from *E. coli*

The expression of AhpF was produced in Rosetta-gami^{TM} 2 cells and purified using the two-step protocol as described above in section 2.3.3. The first step involved enrichment of AhpF by specific binding to Ni^{2+}-NTA matrix. Eluted protein in the imidazole concentration of 20-100 mM were pooled and used for the second step employed ion-exchange chromatography using Resouce^{TM} Q column (GE Healthcare), to remove remaining impurities. Buffer A of AhpF purification contains: 50 mM Tris/HCl, pH 7.5, 200 mM NaCl, 2 mM PMSF and 2 mM Pefabloc^{SC} (BIOMOL). The final step was carried out in size exclusion chromatography using Superdex75 (GE Healthcare). AhpF eluted as single peak at 9 ml column volume. The purity and homogeneity of AhpF samples were analysed as described in section 2.3.3 on page 35. Protein concentrations were determined by bicinchoninic acid assay (BCA; Pierce, Rockford, IL., USA) as well as absorbance at 280 nm in spectrophotometer (BioSpec-Nano, Shimadzu) using extinction coefficients 34 755 M^{-1} cm^{-1}.

2.3.8 Purification of Alkyl Hydroperoxide Reductase subunit C (AhpC) from *E. coli*

For the production of AhpC, *E. coli* strain BL21 (DE3) was used. The first purification step of recombinant His_6-AhpC involved NiNTA resin column as described above in section 2.3.3. To purify the oxidised form of recombinant proteins AhpC, no DTT was used in all following buffers. To avoid remaining DTT from the lysis buffer A, the Ni^{2+}-NTA was initially washed with 10 column volumes of respective buffers without DTT and subsequently eluted with an imidazole gradient (0–300 mM) (Figure 3.42A). Buffer A of AhpC purification under oxidising condition contains: 50 mM Tris/HCl, pH 7.5, 200 mM NaCl, 2 mM PMSF and 2 mM Pefabloc^{SC} (BIOMOL). Afterwards the second step employed ion-exchange chromatography carried out in Resource^{TM} Q column (GE Healthcare) was used, to clear impurities that bind to the column, whereas the AhpC remains in flow through. The flow through protein were pooled and concentrated using Centricon YM-10 (10 kDa molecular mass cut off) spin concentrators

(Millipore). To obtain the purest AhpC and to remove the final impurities size exclusion chromatography was applied using a Superdex 75 HR 10/30 column (GE Healthcare) and a buffer of 50 mM Tris/HCl, pH 7.5, 200 mM NaCl.

To obtain AhpC in its reduced form, all three columns Ni-NTA, Resource$^{\mathrm{TM}}$ Q column (GE Healthcare) and Superdex 75 HR 10/30 column (GE Healthcare) were used in the same order like in oxidising condition, except buffer A of the purification contains additional 0.8 mM DTT during Ni-NTA column and 1 mM DTT in Resource$^{\mathrm{TM}}$ Q column (GE Healthcare) and Superdex 75 HR 10/30 column (GE Healthcare). The purity and homogeneity of AhpC samples in oxidised and reduced form were verified as described in section 2.3.3. Protein concentrations were determined by bicinchoninic acid assay (BCA; Pierce, Rockford, IL., USA) as well as absorbance at 280 nm in spectrophotometer (BioSpec-Nano, Shimadzu) using extinction coefficients 24 075 M^{-1}cm^{-1} for AhpC in oxidised form and 23 950 M^{-1}cm^{-1} in its reduced form.

2.4 Western blotting

Reagents
Blot transfer buffer: 25 mM Tris/HCl pH 8.3
192 mM Glycine
20% Methanol
PBS: 10 mM sodium phosphate, pH 7.4
150 mM NaCl

Proteins were separated on 17% resolving SDS-polyacrylamide gel at 15 mA constant for 45 min and transferred onto transfer buffer equilibrated nitrocellulose or 100% methanol activated PVDF membrane (Amersham) by wet transfer method (Bio-Rad). The membrane was blocked with 3% gelatine PBS-T (PBS; 0.1% Tween-20) for 1 h at room temperature, washed with PBS-T three times for 10 min each followed by incubated with primary antibody (diluted in 1% gelatine prepared in PBS-T) for additional 1 h at room temperature. After primary antibody binding, the membrane was washed as described above and incubated with HRP-conjugated secondary antibody for 1 h at room temperature. The membrane was washed again with PBS-T three times for 10 min each at room temperature and partially dried with Whatman paper to prepare for the development. Western blot was developed using chemiluminescent method with ECL Plus$^{\mathrm{TM}}$ or Lumigen LMA 6 reagents (GE Healthcare, UK) as per the manufacturer's specifications on Kodak X-ray film development station in the dark room.

2.5 Quantification of proteins by bicinchoninic acid (BCA) method

BSA is used as a standard for protein quantification by BCA method. BCA reagent is available in kit form from Pierce (Rockford, IL, USA.) and instruction for measuring protein concentration was followed. In general, two dilutions of protein samples were taken and each of them was measured in triplicate to avoid any error in the measurement. Optical density was measured at 562 nm against blank. Standard curve with 50 µg/ml, 125 µg/ml, 200 µg/ml and 250 µg/ml of BSA was then drawn from the OD_{562} and fitting equation was derived. That equation was used to calculate protein concentration.

2.6 Circular dichroism spectroscopy

Circular dichroism spectroscopy measures the difference between the absorption of right- and left handed circularly polarized light, arising due to the symmetry of particular molecule under consideration. Circular dichroism can be used to determine the secondary structure contents of protein in far UV range, where the peptide bond acts as active chromophore. Steady state CD spectra were measured in 0.1 mm quartz Hellma cell (60 µl volume) at 18 ºC on CHIRASCAN spectropolarimeter (Applied Photophysics) instrument at a step resolution of 1 nm from 180 – 260 nm far UV range, of spectrum under continuous purging of N_2 gas. Protein samples were buffer exchanged, reduced or oxidised by appropriate protocols before measurements. Each protein sample was measured in triplicates at a concentration of 2 mg/ml, with the buffer reading taken before and after protein sample. Averaged buffer base line was subtracted from average protein values using in built Chirascan software. Initial degree cm^2 $dmol^{-1}$ units were converted into mean molar residue ellipticity (Θ) with the help of Chirascan software by giving appropriate cell path length, molecular weight, number of amino acid residues and protein concentration values. Final plotting was done in MS Excel (2003). In order to analyse the CD spectrum, the following algorithms were used: Varselec [190], Selcon [191], Contin [192], K2D [193]all methods as incorporated into the program Dicroprot [194] and Neural Net [195].

2.7 Dynamic light scattering (DLS)

Dynamic light scattering (DLS) of AhpF and reduced and oxidised AhpC were carried out using Malvern Zetasizer Nano ZS spectrophotometer. DLS were measured in low-volume quartz batch cuvette (ZEN2112, Malvern Instruments) using 12 µl of 1-10 mg/ml of respective protein solution. After 60 s equilibration time, the backscattering at 173° was detected for all proteins, accordingly. Scattering intensities were analysed by using the inbuilt software, Zetasizer to calculate the hydrodynamic diameter (D_H), size, and volume distribution.

2.8 NADH dependent peroxidase activity

The NADH dependent peroxidase assay was monitored at 340 nm following the decrease in NADH absorbance. The assay were carried out at 25° C in a total volume of 100 µl containing 300 µM of NADH, 1 mM of hydrogen peroxide, 1 µM of both AhpC and AhpF and 50 mM of phosphate buffer at pH 7.0, containing 100 mM of ammonium sulfate and 0.5 mM EDTA. All the reaction mixtures were added in the reaction buffer except the NADH, which is added at the end to start the reaction. The background reaction measured for all mixture without the AhpF is taken as a control. The maximum NADH oxidation activity shown in the presence of AhpC and the reaction is saturated at 6 min. The NADH oxidation was measured with multi wavelength scanning ranging from 280-540 nm at two different time scale. The first measurement was carried out immediately after all the reaction mixture was added and the second measurement was done after 6 min, when the NADH oxidation is saturated for AhpC.

2.9 Solution X-ray scattering experiments and data analysis

Small angle X-ray scattering (SAXS) data for $a_{104\text{-}363}$ from *S .cerevisiae* and *E coli* AhpF were kindly collected by Prof. Dr. Manfred Roessle using standard procedures on the X33 SAXS camera [196, 197] of the EMBL Hamburg located on a bending magnet (sector D) on the storage ring DORIS III of the Deutsches Elektronen Synchrotron (DESY). A photon counting Pilatus 1M pixel detector (67 x 420 mm^2) was used at a sample - detector distance of 2.4 m covering the range of momentum transfer $0.1 < s < 4.5$ nm^{-1} ($s = 4p \sin(q)/l$, where q is the scattering angle and $l = 0.15$ nm is the X-ray wavelength). The s-axis was calibrated by the scattering pattern of Silver-behenate salt (d-spacing 5.84 nm). The scattering from the buffer alone was measured before and after each sample measurement and the average of the scattering before and after each sample is used for background subtraction. A range of protein concentrations (1.5 to 6.4 mg/ml) and (2.5 to 6.1 mg/ml) were measured for *S. cerevisiae* $a_{104\text{-}363}$ and *E coli* AhpF, accordingly, to assess and remove any concentration-dependant inter-particle effects. Construct $a_{104\text{-}363}$ was measured in 50 mM Tris/HCl (pH 8.5) and 200 mM NaCl, 10 mM EDTA and 1 mM DTT and *E coli* AhpF in 50 mM Tris/HCl (pH 7.5) and 200 mM NaCl, 10 mM EDTA and 1 mM DTT, respectively. The protein as well as the buffer samples have been injected automatically using the sample-changing robot for solution scattering experiments at the SAXS station X33 [198]. All the data processing steps were performed automatically using the program package PRIMUS [184]. The forward scattering $I(0)$ and the radius of gyration R_g were evaluated using the Guinier approximation [199] assuming that for spherical particles at very small angles ($s < 1.3/R_g$) the intensity is represented by $I(s) = I(0) \exp(-(sR_g)^2/3)$. These parameters were also computed from the entire scattering patterns using the indirect transform package GNOM [185], which also provide the distance distribution function $\rho(r)$ of the particle as defined:

$$\rho(r) = 2\pi \int I(s) sr \sin(sr)\, ds$$

The molecular mass of both proteins were calculated by comparison with the forward scattering from the reference solution of bovine serum albumin (BSA). From this procedure a relative calibration factor for the molecular mass (MM) can be calculated using the known molecular mass of BSA (66.4 kDa) and the concentration of the reference solution by applying

$$MM_p = I(0)_p / c_p \times \frac{MM_{st}}{I(0)_{st} / c_{st}}$$

where $I(0)_p$, $I(0)_{st}$ are the scattering intensities at zero angle of the studied and the BSA standard protein, respectively, MM_p, MM_{st} are the corresponding molecular masses and c_p, c_{st} are the concentrations. Errors have been calculated from the upper and the lower I(0) error limit estimated by the Guinier approximation.

Low-resolution models of *S. cerevisiae* $a_{104\text{-}363}$ and *E. coli* AhpF were built by the program GASBOR and kindly guided by Dr. Malathy Sony S. Manimekalai [185]. GASBOR structure represents the protein as an assembly of dummy atoms forming a chain-compatible model inside a search volume defined by a sphere of the diameter D_{max}. The spatial positions of these dummy atoms are approximately corresponding Cα atoms in the protein structure. The number of residues is equal to that in the protein. Starting from a random model, GASBOR employs simulated annealing to build a scattering equivalent model fitting the experimental data $I_{exp}(s)$ to minimize discrepancy:

$$\chi^2 = \frac{1}{N-1} \sum_j \left[\frac{I_{exp}(s_j) - cI_{calc}(s_j)}{\sigma(s_j)} \right]^2$$

where N is the number of experimental points, c is a scaling factor and $I_{calc}(s_j)$ and $\sigma(s_j)$ are the calculated intensity and the experimental error at the momentum transfer s_j, respectively. In order to compare the solution structure of $a_{104\text{-}363}$ with the atomic structure of the stalk subunit *a* of the A_1A_O ATP synthase from *M. ruber* (PDB entry 3RRK, [200]), or the *E. coli* AhpF solution structure with the *E. coli* AhpF crystal structure determined in this thesis, the high resolution models have been aligned, respectively, using SUBCOMB [185]. This program aligns all possible pairs of models and arranges the smallest average discrepancy among the models.

2.10 *In silico* Sec7 and *a2$_{1-17}$* docking experiments

The AutoDock v.4 and AutoDock 4 Tools programs (The Scripps Research Institute) were used for docking of *a2$_{1-17}$* peptide to Sec7 domain [201, 202]. Spatial structure of Sec7 domain was taken from the crystal structure of the complex of Sec7/Arf1 with brefeldin A as a stabilization agent (PDB: #1S9D) [203] and all water molecules were removed from Sec7 structure. The NMR structure of *a2$_{1-17}$* in solution was also used for these docking experiments (Figure 3.3B). The Sec7 structure was rigid during docking. All backbone torsions in the helical part of *a2$_{1-17}$* were also treated as non-rotatable, while most of other torsions were rotatable. The Sec7 domain was covered by 8 grids with 126 x 126 x 126 grid points and grid spacing has default value 0.375 Å. For each grid, the 1000 runs of the Lamarckian genetic algorithm with default settings were performed. Thus, in total 8 000 blind and random *in silico* docking experiments have been done. All docking results were sorted by final docked energy. The contact areas for peptide residues were estimated with PyMOL v.1.4 software (Schrödinger) [175] as a difference between solvent accessible areas without Sec7 and with Sec7.

2.11 Nuclear magnetic resonance (NMR) spectroscopy

NMR spectroscopy is a powerful technique used to study the structural and functional aspects of macromolecules such as proteins. With NMR technique, we can determine the solution structure of protein. We can also study biochemical and biophysical properties such as protein-ligand interaction to demonstrate new binding partners as well as to map the binding regions down to single amino acid level. Since hydrogen is one of the most receptive and abundant NMR active nuclei besides other isotopes such as ^{15}N, ^{13}C, ^{31}P etc., it can be observed in magnetic resonance. Any nuclei having mass number, which exhibits net intrinsic magnetic momentum and angular momentum, can be defined as NMR active. All the NMR experiments were collected on Bruker Avance 600 MHz machines at SBS NMR-core facility.

2.11.1 ^{15}N single and ^{13}C ^{15}N double labelling of proteins

Reagents for Minimal Media (M9):	42 mM Na_2NPO_4
	22 mM KH_2PO_4
	8.5 mM NaCl
	1 g/L $^{15}NH_4Cl$
	0.1 mM $CaCl_2$
	2 mM $MgSO_4$
	10 g D-Glucose

30 µM $FeCl_3$
5 ng/l Thiamin
Antibiotic
LB Media

For NMR experiments, either single (^{15}N) or double (^{13}C ^{15}N) labelled recombinant proteins were produced in *E. coli* BL21 (DE3) cells and purified as explained above using established protocols. The clones were grown in M9 minimal media to get labelled protein. 30 ml of overnight culture was pelleted down at low centrifugal force at room temperature and washed with minimal media and then transferred to large volume of minimal media with OD_{600} of 0.1. Grow (37 ºC, 180 rpm) till OD_{600} of 0.6 - 0.7 was achieved. The culture was then induced with 1 mM IPTG for 3 – 5 h or alternatively induced overnight at 20 ºC. Cells were harvested and frozen in liquid nitrogen and stored at –80 ºC till purification.

2.11.2 One dimensional (1D) ^{1}H and multi-dimensional (2D, 3D) ^{13}C-^{15}N NMR spectroscopy

1D NMR spectra of various proteins were collected at temperatures ranging from 283 K to 308 K on core facility Avance 600 MHz instruments (Bruker, Billerica, MA). Unlabelled or labelled protein sample in phosphate buffer, pH 6.8 was used in presence of 10% D_2O (v/v) to record the spectrum. For 2D experiments like HSQC (Hetero nuclear Single Quantum Coherence), ^{15}N labelled proteins in 90% H_2O and 10% D_2O in 25 mM phosphate buffer (pH 6.8) was used to collect data. Other 2D experiments used in the study were 2D NOESY and 2D TOCSY for peptide data collection. Different parameters including temperature, buffer and protein concentration were optimised before making final measurements and pulse was also calibrated accordingly. ^{15}N-^{13}C labelled samples were utilized to collect 3D spectra such as CBCA(CO)NH, HNCACB in 10% (v/v) D_2O lock signal. Baseline corrections were applied wherever necessary. The proton chemical shift was referenced to the methyl signal of DSS (2, 2-dimethyl-2-silapentane-5-sulphonate) [Cambridge Isotope Laboratories] as an external reference to 0 ppm.

2.11.3 NMR spectroscopy of $a2_{1\text{-}17}$ and $a2_{368\text{-}395}$ from *M. musculus*

For structure determination, appropriate amount of peptide $a2_{1\text{-}17}$ was dissolved in 25 mM phosphate buffer 300 mM NaCl, pH 6.5 and 50% TFE. TOCSY and NOESY spectra of the peptide were recorded with mixing times of 80 and 300 ms, respectively, at a temperature of 25 ºC. TopSpin (Bruker Biospin) and Sparky suite [171] of programs were used for spectra processing, visualization and peak picking. Standard procedures based on spin-system identification and sequential assignment were adopted to identify the resonances [204]. Inter proton distances were obtained from the NOESY spectra. NOESY peaks were categorized as strong, medium and weak based on the signal intensity and were translated into distance constraints as 3.0, 4.0 and 5.0 Å, respectively. Dihedral angle restraints as derived from TALOS [173] were employed to generate the three dimensional structure of the peptide in the CYANA 2.1 package [172]. In total 100 structures were calculated and an ensemble of 10 structures with lowest total energy was chosen for structural analysis.

2.11.4 Binding studies with NMR spectroscopy

Interaction studies were performed between $a2_{1\text{-}17}$ and the Sec7 domain of ARNO using highly precise and reproducible technique of NMR. Binding studies with NMR have the advantage of monitoring interactions at single amino acid level. ^{1}H-^{15}N heteronuclear single quantum coherence (HSQC) spectrum of labelled protein was used as starting point, which was recorded at optimised condition. Ligand protein was added at increasing amounts under optimised temperature and buffer conditions. Respective ^{1}H-^{15}N HSQC spectra were then recorded. A constant amount (2 µM) of $a2_{1\text{-}17}$ was used, followed by adding unlabelled Sec7 as binding partner at increasing amounts to a molar ratio of 1:1 – 1:2. Changes in chemical shift were then monitored in HSQC spectrum. Experiments were performed on Bruker Avance 600 machine using Topspin for acquisition and processing of spectra. Respective spectra were overlapped to monitor chemical shift changes, further analyses were done in SPARKY [171].

2.12 Single Particle Reconstruction (SPR) using cryo-electron microscopy

Single particle electron microscopy is becoming a commonly used method to examine macromolecular structures. Using in comparison to X-ray crystallisation and NMR, small amount of purified protein that are applied onto a grid before quickly vitrified into liquid ethane and kept under liquid nitrogen temperatures. Under this conditions the structure of proteins are excellent preserved, close to physiological condition at high resolution within the vitrified buffer. Isolated molecules collected data can be average into a 3D reconstruction.

2.12.1 Cryo-EM image collection and processing

The data was kindly collected by Jonathan Ng Thiam Seng in NUS Centre for BioImaging Sciences at the National University of Singapore (NUS). For cryo-EM image collection, 2.5 µl purified AhpC of 1 mg/ml concentration was applied onto C-Flat Holey Carbon Grids and subsequently blotted with filter paper for 1 s to reduce excess buffer before flash-frozen in liquid ethane at 170 K using the FEI Vitrobot Mark IV plunger. Image acquisitions were performed on FEI Titan Krios electron microscope operating at 300 kV at liquid nitrogen temperature with a nominal magnification of 75 000 and an electron dose of 20-25 e/Å^2. The images were recorded on a 4,096- by 4,096 FEI Falcon direct electron detector. After calibration, the image pixel size was determined to be 1.14 Å. In total, 54 images were collected. Individual AhpC particle were selected semi-automatically, aided by the e2boxer tool, in Swarm mode, from EMAN2 [186] software package. A total of 1 183 particles were selected for image reconstruction. The defocus for each micrograph was estimated with EMAN2 and was in range between 2-6 µm underfocus. Initial model was built using EMAN2 software and refinements were performed using multipath simulated annealing (MPSA) software assuming D5 symmetry [205]. Dr. Victor Kostyuchenko was kindly guiding me through the EMAN2 software and kindly performed the MPSA refinement. The final geometry of the AhpC cryo EM structure was checked, compared to the *E. coli* AhpC crystal structure and figures were created using Chimera software [187].

2.13 Crystallisation of protein constructs

X-ray crystallography has an enormously high impact in providing accurate structural details at atomic resolution for bio-macromolecules and gives a deeper insight into the way how proteins may interact with each other and therefore capable to indicate molecular mechanism and biological functions of biomolecules. In this thesis, the crystal optimisation, data collection and data reduction were kindly guided by Dr. Asha M. Balakrishna, Dr. Malathy Sony S. Manimekalai and Dr. Ardina Grüber. In particular during $a_{653-727}$ crystallisation, Dr. Ardina Grüber gave me helpful advises and Dr. Asha M. Balakrishna guided me fruitfully through the AhpF and AhpC crystallisation. Furthermore Dr. Asha M. Balakrishna and Dr. Malathy Sony S. Manimekalai guided me thoroughly through the AhpF and AhpC structure determination.

2.13.1 Crystallisation of subunit *a* constructs

Crystallisation of $a_{653-727}$ was attempted using vapour diffusion method. Sparse matrix screens from Hampton research, Molecular dimensions and Emerald biosystems were used for the initial screening. Hanging drops were set up by mixing 1 µl of the purified $a_{653-727}$ protein (3-16 mg/ml) in buffer B (50 mM Tris/HCl, pH 8.5, 500 mM NaCl) with 1 µl of the precipitant solution and incubated at 25 °C [206]. Initial needles were seen in Hampton research crystal screen 1 and Emerald biosystems Wizard screen 2. All these conditions were optimised for precipitant concentration, protein concentration, salt concentration, pH and temperature. Crystals of $a_{653-727}$ were produced in 10-15% (v/v) polyethylene glycol 3350 (PEG 3350), 0.2 M $MgCl_2$, $6H_2O$, 0.1 M Na- cacodylate (pH 6.5). Once protein crystals were confirmed, the crystallisation condition was further optimised via Hampton research additive screen or seeding, to decrease the nucleation and promote further crystal growth. Cryoprotectant solution was also optimised by testing different percentages of glycerol. The final cryoprotectant solution comprised of 15% (v/v) polyethylene glycol 3350 (PEG 3350), 0.1 M $MgCl_2$, $6H_2O$, 0.1 M Na- cacodylate (pH 6.5), 25% (v/v) glycerol. The crystals were quickly dipped in cryoprotectant solution and were flash-frozen in liquid nitrogen at 100 K. Optimised $a_{653-727}$ crystals were tested in the in-house machine.

Attempt was also taken to crystallize subunit a_{1-388} by setting up drops in different crystallisation screen. Hampton research, Molecular dimensions and Emerald biosystems were used for the initial screening. The crystal screens were set up in hanging drops method by mixing 1 µl of the purified a_{1-388} protein (3-16 mg/ml) in buffer B (50 mM Tris/HCl, pH 7.5, 150 mM NaCl) with 1 µl of the precipitant solution and incubated at 18 °C.

2.13.2 Crystallisation of AhpF from *E. coli*

Crystallisation of *E. coli* AhpF was attempted in similar manner like subunit *a* constructs. The crystal screens from Hampton research, Molecular dimensions and Emerald biosystems were used for the initial screening. Hanging drops were set up in a 1:1 µl ratio of AhpF (3-16 mg/ml) in buffer B (50 mM Tris/HCl, pH 7.5, 150 mM NaCl) and precipitant solution and incubated at 18 °C [206]. Initial needle bundles were seen in Hampton research crystal screen 1, condition 39, which contains 100 mM Na- HEPES, pH 7.5, 2% (v/v) PEG 400 and 2M Ammonium sulfate. All these conditions were optimised for precipitant concentration, protein concentration, salt concentration, pH and temperature. AhpF produces crystal sheet bundles in 0.1 M Na HEPES (pH 7.0), 2.5% (v/v) PEG 400 and 2 M Ammonium sulfate at 25 °C. Further improvement of larger crystal formation was obtained by using Hampton Research Additive Screen^{TM}. The adding of 10 mM cadmium chloride leads to crystal formation into the third dimension. Larger AhpF crystals suitable for X-ray diffraction measurements were finally obtained by the sitting-drop vapour diffusion method at 25 °C from a solution containing 10 mM cadmium chloride, 100 mM Na- HEPES, pH 7.5, 2.5 % (v/v) PEG 400 and 2 M Ammonium sulfate. According to the improved condition, 1 µl protein solution of 2 mg/ml protein concentration was mixed with an equal volume of reservoir solution and equilibrated against 150 µl reservoir solution. The low protein concentration of 2 mg/ml reduced the nucleation, hence only few and therefore larger sized crystals were obtained in 7 days.

2.13.3 Crystallisation of *E. coli* AhpC

Recombinant *E. coli* AhpC of 10 mg/ml concentration was used to set up crystals drops in Hampton Research crystal screen HR-110 and HR-112 and Emerald biosystems Wizard screen 1 and Wizard screen 2, in hanging drop plates with 2 µl droplet size per well in 1:1 µl ratio of AhpC in buffer B (50 mM Tris/HCl, pH 7.5, 200 mM NaCl) and precipitant solution at 18 °C. Initial needle bundles were observed in Hampton research crystal screen 2 #25 (HR2#25) after two days and in Hampton research crystal screen 2 #23 (HR2#23), small crystal formation after 14 days. Both conditions were similar in their composition: HR2#25 contains 1.8 M Ammonium sulfate, 100 mM MES (2- (*N*-**m**orpholino) **e**thane**s**ulfonic acid), pH 6.5, and 10 mM cobalt chloride, whereas HR2#23 includes 1.6 M Ammonium sulfate, 100 mM MES, pH 6.5, and 10 % dioxane. Both conditions were optimised simultaneously. Ammonium sulfate concentration, protein concentration, dioxane concentration, pH and temperature were optimised to improve the growth and diffraction capability of AhpC crystals. The first larger size crystals that showed reflections in the diffraction image using the in-house machine (Rigaku) were observed under the condition 1.6 M Ammonium sulfate, 100 mM MES, pH 6.5, and 5 % dioxane using 8 mg/ml protein concentration.

2.14 Crystal diffraction analysis of crystals

The diffraction of $a_{653\text{-}727}$ from *S. cerevisiae* V-ATPase and *E. coli* AhpF and AhpC crystals were tested in-house at 100 K on a Rigaku RAXIS IV image plate detector with a Rigaku RA-Micro 7 HFM rotating copper anode generator (Rigaku/MSC). All the diffraction data were indexed, integrated and scaled using the HKL2000 suite program and were kindly guided by Dr. Asha M. Balakrishna and Dr. Malathy Sony S. Manimekalai [176].

2.15 Data collection

Together with Dr. Malathy Sony S. Manimekalai, single-wavelength datasets for *E. coli* AhpF and AhpC crystals were collected at 140 K on beamline 13B1 at the National Synchrotron Radiation Research Center (NSRRC, Hsinchu, Taiwan) using the ADSC Quantum 315 CCD detector. Staff at beamline 13B1 (NSRRC) kindly provided technical assistance. All the diffraction data were indexed, integrated and scaled using the HKL2000 suite program [176]. All the crystals belong to tetragonal space group C2 and have similar unit cell parameters.

Single wavelength datasets of AhpC from *E. coli* were also collected at the protein crystallography beamline S06 PX at the Swiss Light Source (SLS) with a PILATUS 6M detector by Dr. Neelagandan Kamariah. Data sets were collected as a series of 0.2° oscillation images with 0.2 s exposure time with a detector distance of 500 mm. All diffraction data reduction, including indexing, integration and scaling was carried out in iMosflm program [207].

2.16 Crystal structure determination

2.16.1 Crystal structure determination of *E. coli* AhpF

The structure of AhpF from *Salmonella typhimurium* (PDB 1HYU; [135]) was used as model for structure determination by molecular replacement method using the programs PHASER [179] and MOLREP [178]. Since the AhpF structure from *S. typhimurium* reveals a close confirmation structure, which leads to high R-factor, different domains from the residues 1-182 and 203-521 have been used for molecular replacement separately. Rigid body refinement was carried out followed by difference Fourier syntheses calculations. Inspection of the F_O–F_C and $2F_O$–F_C maps for the protein-ligand complexes, the AhpF clearly showed electron density corresponding to a bound flavin adenine dinucleotide (FAD) molecule as well as a cadmium ion. The ligand-bound form of *E. coli* AhpF was confirmed by omit map calculations using the CNS program [180]. Iterative cycles of model building and refinement were carried out using the programs COOT [181] and REFMAC5 [177] of the CCP4 suite (1994). The densities for all 521 amino acids, even for the linker region 192-202 are detectable. The latter is highly flexible as evident by the high B-factors (residues 192-202) > 70 Å^2 for C_α atoms. High solvent content may have caused flexibility and since this region forms predominantly loops. The geometry of the final models was checked with PROCHECK [183] and the figures are drawn using the program PyMOL [175]. Structural comparison analysis are carried out using the SUPERPOSE program [208] as included in the CCP4 suite.

2.16.2 Crystal structure determination of *E. coli* AhpC

Initial phases for AhpC structure determination from *E. coli* were obtained by molecular replacement method using the related AhpC structure from *S. typhimurium* (PDB 3EMP, *St*AhpC) [209] using the programs PHASER [179]. Chainsaw software was used for model editing (Stein, 2008). Rigid body refinement was carried out followed by difference Fourier syntheses calculations. Inspection of the F_O–F_C and $2F_O$–F_C maps reveals no clashes between the monomeric chains. The preliminary AhpC structure from *E. coli* (*Ec*AhpC) clearly showed electron density corresponding to additional amino acids. Since the crystal structure of all five *St*AhpC monomer chains in an asymmetric unit consist of 162 amino acids, amino acids were manually added to N- and C-terminal of the *Ec*AhpC structure during iterative refinement and model building using the software COOT [181] and Refmac5 [177]. The final densities of 167 amino acids from the 187 amino acids full length were observed in *Ec*AhpC. The missing 20 amino acids were located at the C-terminal segment reflecting a highly flexible part as evident by the high B-factors >70 Å^2 for C_α atoms from C-terminal residue 163-167. The final geometry of the *E. coli* AhpC structure was checked with PROCHECK [183] and figures were created using program PyMOL [175]. Structural comparison analysis were carried out using the SUPERPOSE program [208] as included in the CCP4 suite.

3. Results

3.1 N-terminal segment of subunit *a* is involved in V-ATPase / ARNO association

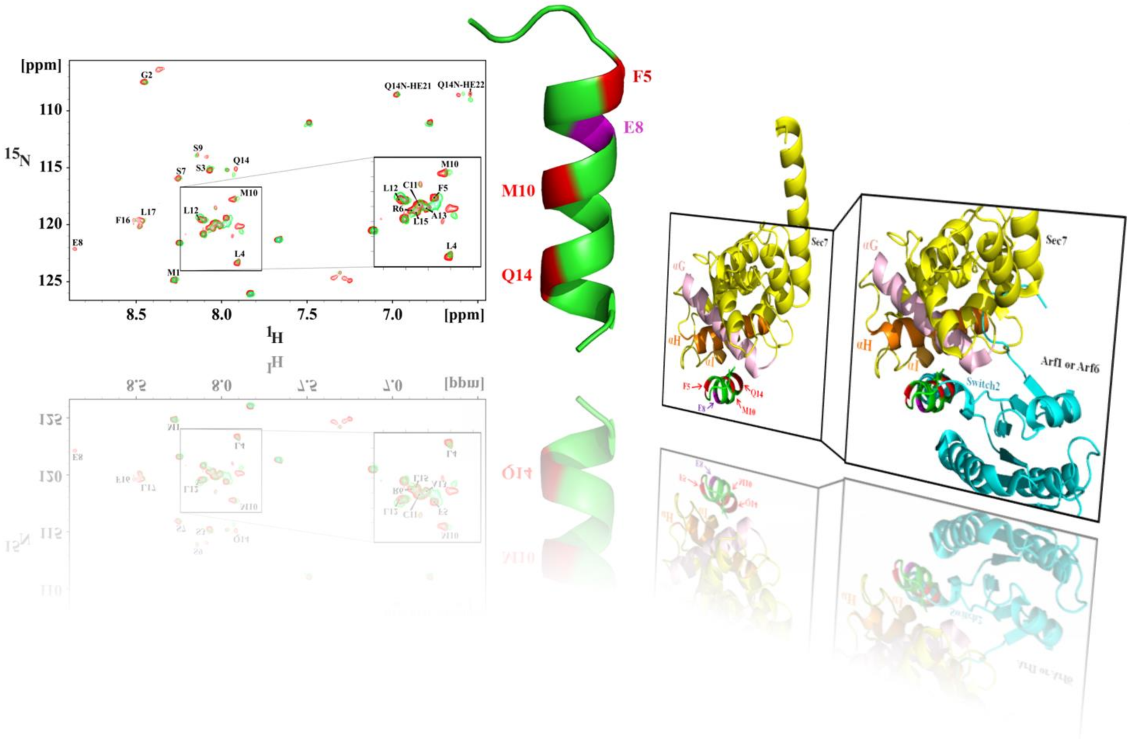
[ppm]
110
115
120
125
^{15}N
G2
Q14N-HE21
Q14N-HE22
S9
S3
Q14
S7
L17
F16
E8
L12
M10
L4
M1
C11
F5
R6
A13
L15
8.5
8.0
7.5
7.0
[ppm]
^{1}H
F5
E8
M10
Q14
Sec7
αG
αH
αI
Switch2
Arf1 or Arf6

3.1.1 Interaction studies between subunit *a2* of V-ATPase and Sec7 domain of ARNO from *M. musculus*

The new function as an endosomal pH sensing receptor for V-ATPases involves the interaction with ARNO in multiple sites in a pH-dependent manner [1, 96]. Precipitation assays of recombinant subunit *a2* from mouse with GST-tagged ARNO and its Sec7- domain of ARNO revealed that they are associated to each other [1]. However, the amino acids of the N-terminal part from subunit *a*, responsible for subunit *a*-ARNO interaction, have remained undefined so far. To identify these amino acid residues of subunit *a*, two important regions (1-17 aa, called $a2_{1-17}$ and 368-395aa, called $a2_{368-395}$) of subunit *a2* (mouse V-ATPase), which are involved in ARNO binding, kindly provided by Prof. Dr. Vladimir Marshansky (MGH, Harvard University, Boston, USA), have been structurally characterised in this thesis.

3.1.2 Secondary structure content of $a2_{1-17}$

Among all subunit *a* peptides, the $a2_{1-17}$ peptide has the strongest binding affinity to Sec7 domain of ARNO with dissociation constant K_d = 0.344 µM, which is comparable to the interaction between the entire cytosolic N-terminal *a2*N to full length ARNO protein with dissociation constant K_d = 0.313 µM [96]. While subunit *a* shows the strongest binding to the catalytic Sec7 domain and much weaker binding to the PH- and PB- domain, it is therefore of great importance to focus on the structural features of $a2_{1-17}$ first. To analyse the secondary structure of $a2_{1-17}$, circular dichroism (CD) spectrum was collected at the range between 190-260 nm (Figure 3.1). For the CD-measurement the peptide $a2_{1-17}$ was dissolved in dissolved in water and 50% TFE (2,2,2-Trifluoroethanol). The spectrum showed a characteristic pattern for α-helical formation in the $a2_{1-17}$ peptide, which has a maximum (193 nm) and two minima (208 and 222 nm). In overall there is 70% α-helix and 30% random coil present in this peptide, comparable to the secondary structure predictions based on the primary sequence of $a2_{1-17}$ peptide. The ratio between the molar ellipticity values at 208 nm and at 222 nm is 0.93.

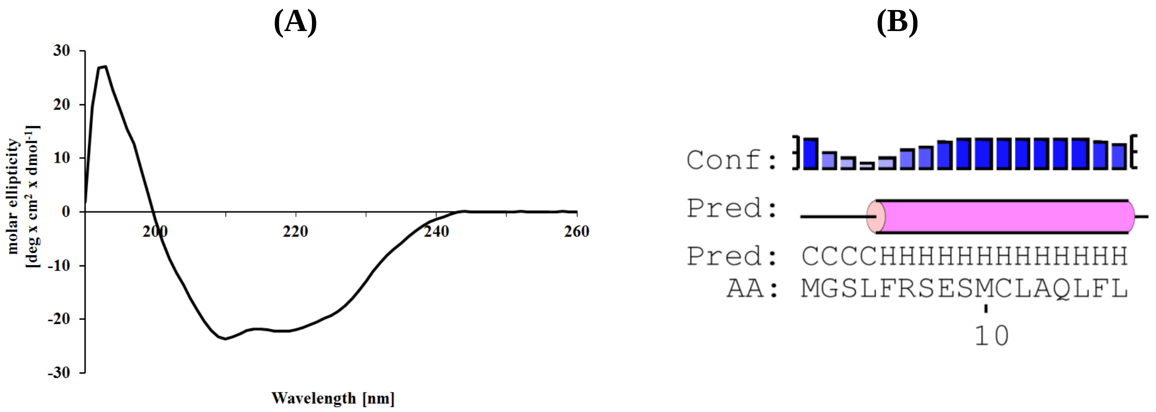

Figure 3.1: CD spectrum of $a2_{1-17}$ between 190-260 nm. *(A)* Far UV-CD spectrum of $a2_{1-17}$. *(B)* Secondary structure prediction of $a2_{1-17}$ by psipred, where α-helix = ⬭ , coil = ▬ and confidence of prediction = ▮ [2, 210].

3.1.3 NMR solution structure of $a2_{1-17}$ from *Mus musculus*

In order to understand the interaction mechanism between *a2N* and ARNO, the solution structure of $a2_{1-17}$ with the sequence $_1$MGSLFRSESMCLAQLFL$_{17}$, has been solved using NMR. All residues of $a2_{1-17}$ peptide were assigned using 2D homonuclear total correlation spectroscopy (TOCSY) and 2D nuclear Overhauser effect spectroscopy (NOESY) experiments (Figure 3.2) [204]. In TOCSY and NOESY experiments, $a2_{1-17}$ was dissolved in 25 mM phosphate buffer, pH 6.5, 300 mM NaCl and 50 % TFE to a final concentration of 2 mM. 2D TOCSY and 2D NOESY were performed with 80 ms and 300 ms mixing times, respectively, at 25 ºC. The spectra of the $a2_{1-17}$ were processed using TopSpin programs (Bruker Biospin), and Sparky suite [171], which were used to visualise the spectrum and peak assignment.

For the assignment of $a2_{1-17}$ peptide, standard procedures based on spin-system identification and sequential assignment using homonuclear TOCSY and NOESY experiments were used (Figure 3.2A). The resonances of all 17 amino acids were identified [204]. HN-HN region of the NOESY spectrum shows cross peaks for α-helical formation (Figure 3.2A). Distances between protons were obtained from the NOESY spectrum. Signal intensities of NOESY peaks were classified into strong, medium and weak, and converted into distance constraints of 3.0 Å, 4.0 Å and 5.0 Å, respectively. Dihedral angle restraints were obtained using TALOS software [173]. Using both distance constraints as well as dihedral angle restraints, the three dimensional solution structure of the $a2_{1-17}$ peptide was calculated in CYANA 2.1 package [172].

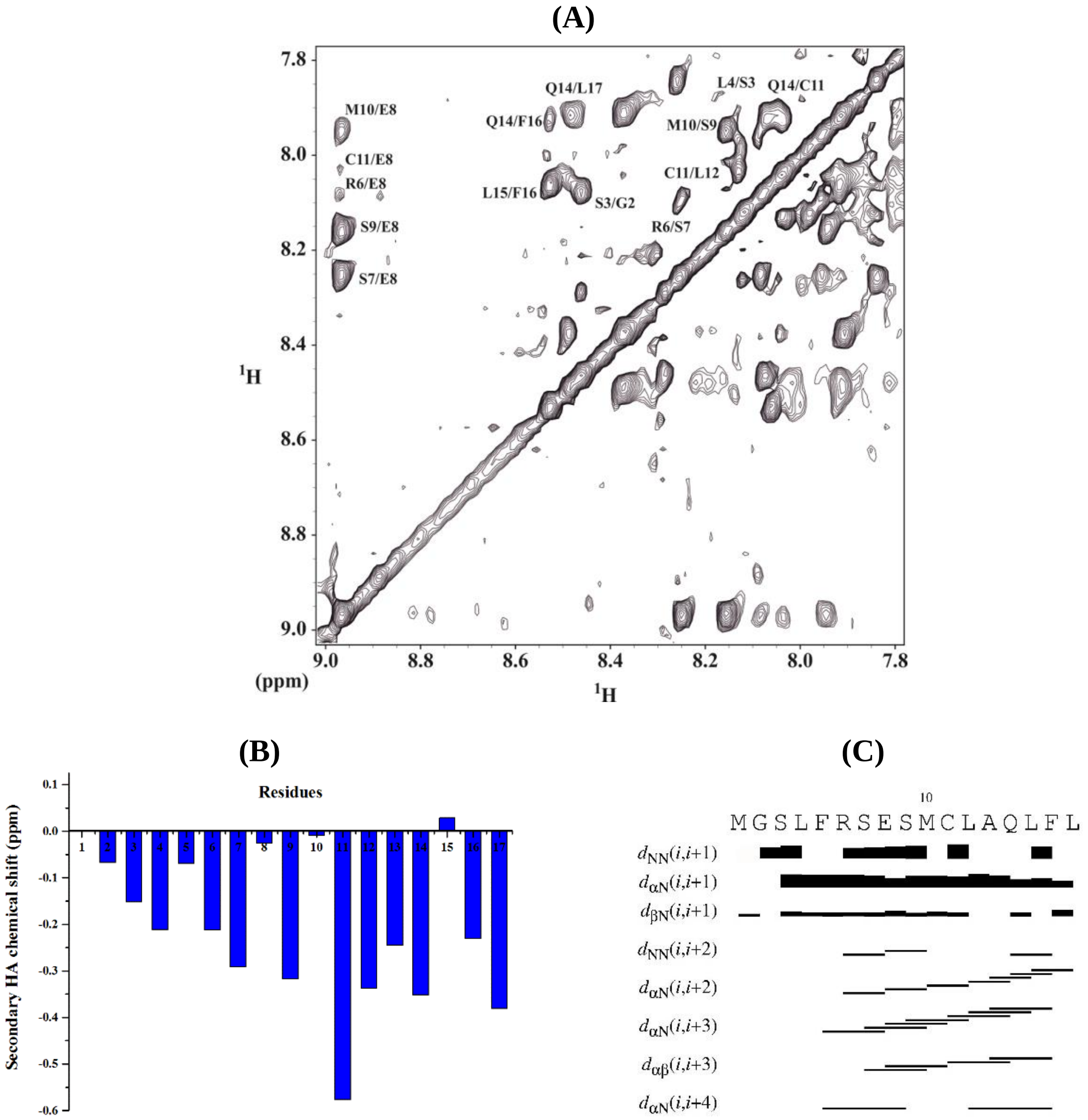

Figure 3.2: Analysis of 2D NMR spectra of *a2₁₋₁₇*. *(A)* Cross-peaks assignment of the HN-HN region of the NOESY spectrum of *a2₁₋₁₇*. Peak assignment was carried out in Sparky 3.1 software using TOCSY and NOESY spectrum [2, 171]. *(B)* Secondary structure prediction of *a2₁₋₁₇* using Hα chemical shifts in comparison to their corresponding random coil values (BMRB) [2]. *(C)* The NOESY connectivity plot of peptide *a2₁₋₁₇* [2].

Secondary structure was predicted using Hα chemical shifts, which reflects α-helical formation between the residues F_5 – L_{17} (Figure 3.2B). The NOESY connectivity plot of the peptides highlights HN–HN, Hα–HN(i, i+3), Hα–HN(i, i+4), and Hα–Hβ (i, i+3) connectivity (Figure 3.2C), supporting α-helical formation in the C-terminal region of *a2₁₋₁₇*. The 10 lowest energy structures were selected out of 100 generated structures for further characterisation. All 10 calculated structures reveal an overall mean root square deviation (r.m.s.d.) of 0.31 Å in backbone alignment and 1.36 Å for the heavy atoms (Figure 3.3A). All 10 structures reveal energies lesser than -100 kcal/mol (Swiss-PdbViewer 4.1.0), no NOE violations larger than 0.3 Å and no dihedral violations wider than 5°. The respective statistic for 10 structures are summarised in Table 3.1. The representative single structure depicts a maximum length of

25.78 Å, revealing α-helical formation from the residues 5 to 17 (21.1 Å) and an N-terminal region that is flexible and formed by amino acids 1-4, respectively (Figure 3.3B). Molecular surface electrostatic potential of the $a2_{1\text{-}17}$ peptide is highlighted in Figure 3.3C-E. The charged distribution of the helix reveals an amphiphilic surface. At one side of the peptide, the residues L4, M10, C11, L15, and L17 form a line of hydrophobic surfaces (Figure 3.3C). The opposite side reflects an amphiphilic surface potential, formed by positive charged R6 and the hydrophobic residues L12, A13, F16 and L17. In a 90° view to the amphiphilic surface, the peptide is mainly negative charged, formed by E8 (Figure 3.3C-E).

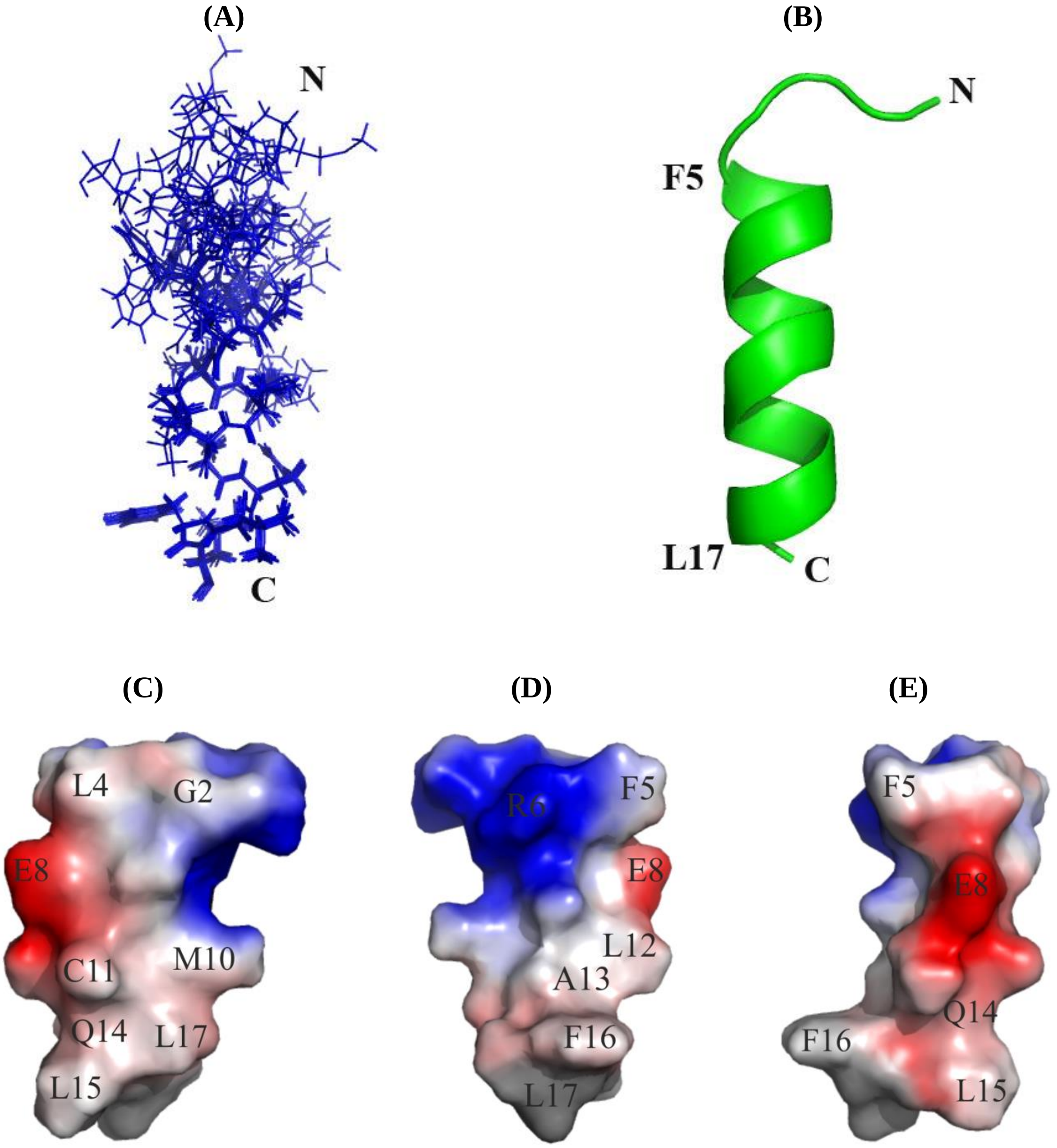

Figure 3.3: NMR structures of $a2_{1\text{-}17}$ from *Mus musculus*. *(A)* Overlay of ten lowest $a2_{1\text{-}17}$ energy structure. *(B)* Single NMR structure represented in cartoon [2]. *(C-E)* The molecular surface electrostatic potential of peptide $a2_{1\text{-}17}$ calculated using Pymol [2, 175]. Positive and negative potentials are highlighted in blue and red accordingly [2].

Distance restraints	
Total	233
Intraresidue (i – j = 0)	77
Sequential (|i-j| = 1)	81
Medium-range (2 ≤ |i–j| ≤ 4)	75
Long-range (|*i*–*j*| = 5)	0
Average number of violations	
Distance violations > 0.5 Å	0
Ramachandran plot^2 **(%)**	
Residues in most favoured regions	78.2
Residues in additionally allowed regions	21.8
Residues in generously allowed regions	0
Residues in disallowed regions	0
Average r.m.s.d. to Mean (Å)	
Residues 11-19, Backbone (C^α, C', and N)	0.311
r.m.s.d. heavy atoms	1.355

Table 3.1: Structural statistics for $a2_{1-17}$ [2].

3.1.4 NMR titration of $a2_{1-17}$ (*M. musculus*) with human Sec7 domain of ARNO

To analyse the interaction interface of subunit *a* involved in binding with Sec7 domain of ARNO, ^1H - ^{15}N heteronuclear single quantum coherence (HSQC) spectra of $a2_{1-17}$ in 1 mM concentration were collected at 298 K as a starting point. All 17 amino acids in the HSQC spectrum are referable to the $a2_{1-17}$ structure. For the titration assay, $a2_{1-17}$ and Sec7 protein of ARNO were dissolved in or buffer exchanged to 25 mM sodium phosphate (pH 6.5) buffer, 300 mM NaCl and 50% TFE prior to the binding experiments.

After optimising the HSQC spectra of $a2_{1-17}$, series of $a2_{1-17}$ HSQC experiments in the presence and absence of Sec7-domain of ARNO (22.1 kDa) [173] have been performed (Figure 3.4) to identify the $a2_{1-17}$ residues involved in subunit *a* and Sec7-domain of ARNO assembly. The proteins were incubated 30 min prior for binding. The changes of chemical shifts reflect the binding residues of $a2_{1-17}$ and were observed in the HSQC spectra. The HSQC spectrum of 1 mM $a2_{1-17}$ after titration with 1 mM of Sec7 domain of ARNO shows changes in chemical shifts, peak shapes and intensities.

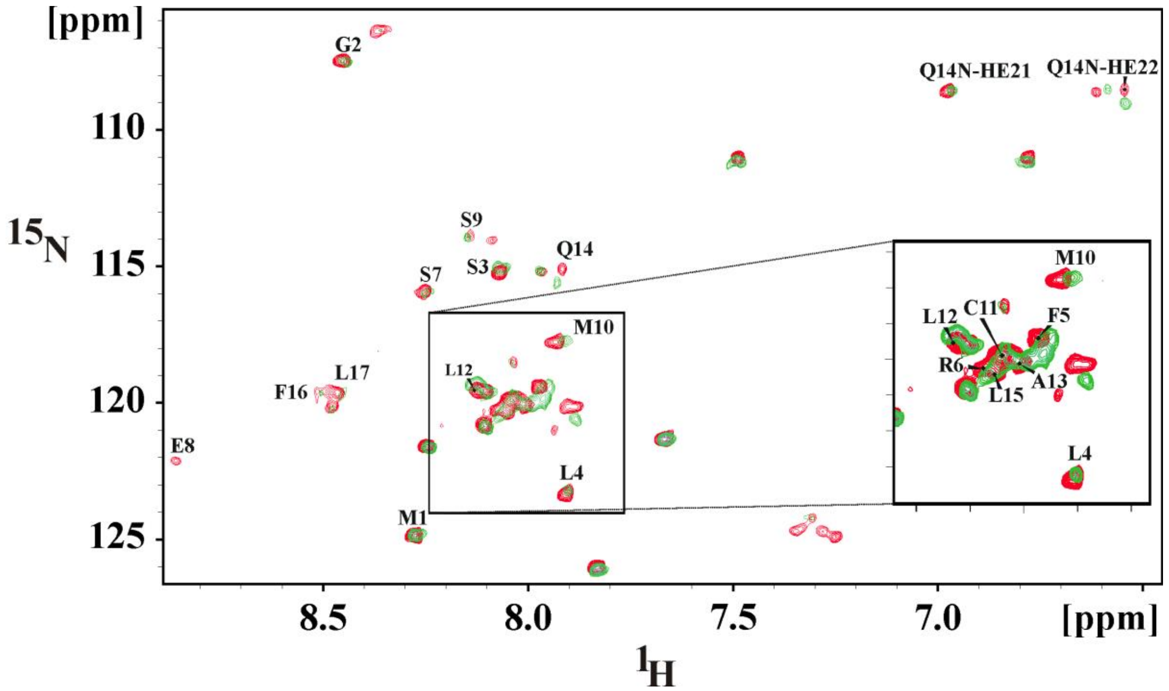

Figure 3.4: NMR titration spectra of $a2_{1-17}$ (*M. musculus*) and human Sec7 domain of ARNO. Overlay of 2D ^{1}H-^{15}NHSQC spectrum of $a2_{1-17}$ alone (red) and $a2_{1-17}$ with Sec7 domain of ARNO (green), in 25 mM sodium phosphate buffer (pH 6.5) 300 mM NaCl at 298 K [2].

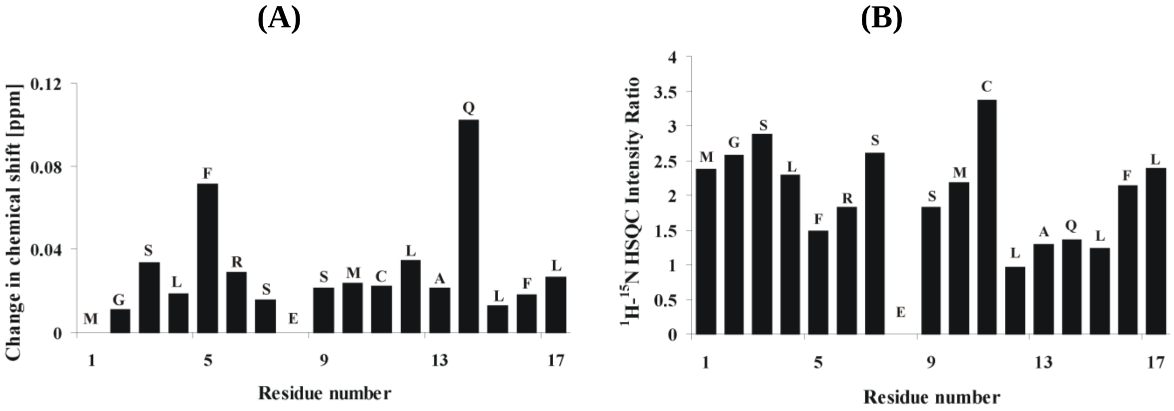

Figure 3.5: Chemical shift and loss of intensity plot of $a2_{1-17}$ and Sec7 domain of ARNO. *(A)* Change in chemical shift and *(B)* Loss of peak intensity after adding of unlabelled Sec7 domain of ARNO to unlabelled $a2_{1-17}$ at a molar ratio of 0.5. The stronger the decrease of the peak intensity upon titration the higher the plotted intensity ratio [2].

Binding of Sec7 induces a structural change in $a2_{1-17}$, which is indicated by changes in chemical shift, intensity and/or broadening in the resonance with respect to the NMR spectrum (Figure 3.4). After adding of equimolar amount of Sec7 domain to $a2_{1-17}$, significant changes in the chemical shift were observed for residues F5, M10 and Q14 in the ^{1}H–^{15}N HSQC spectrum (Figure 3.5A) [2]. The residue E8 reveals a loss of signal intensity in the HSQC spectrum (Figure 3.5B). The loss of intensity of E8 may not be affected by direct amino acid interaction of E8 with the residue of the Sec7 domain of ARNO, but rather be caused of structural alteration at the actual binding site at F5, M10 and Q14. These four residues of $a2_{1-17}$ are conserved with other mouse isoforms and the yeast homologue (Figure 3.6A). The interface forming amino acid M10 is also conserved from yeast to mouse with only one substitution to V10, which is found in mouse *a3*-subunit V-ATPase (Figure 3.6A). It is also noteworthy that E8 residue is also conserved with one substitution to Ala in yeast Vph1p (Figure 3.6A). The binding region of *a2*$_{1\text{-}17}$ is highlighted in the structure in red, whereas E8 in magenta (Figure 3.6B-C).

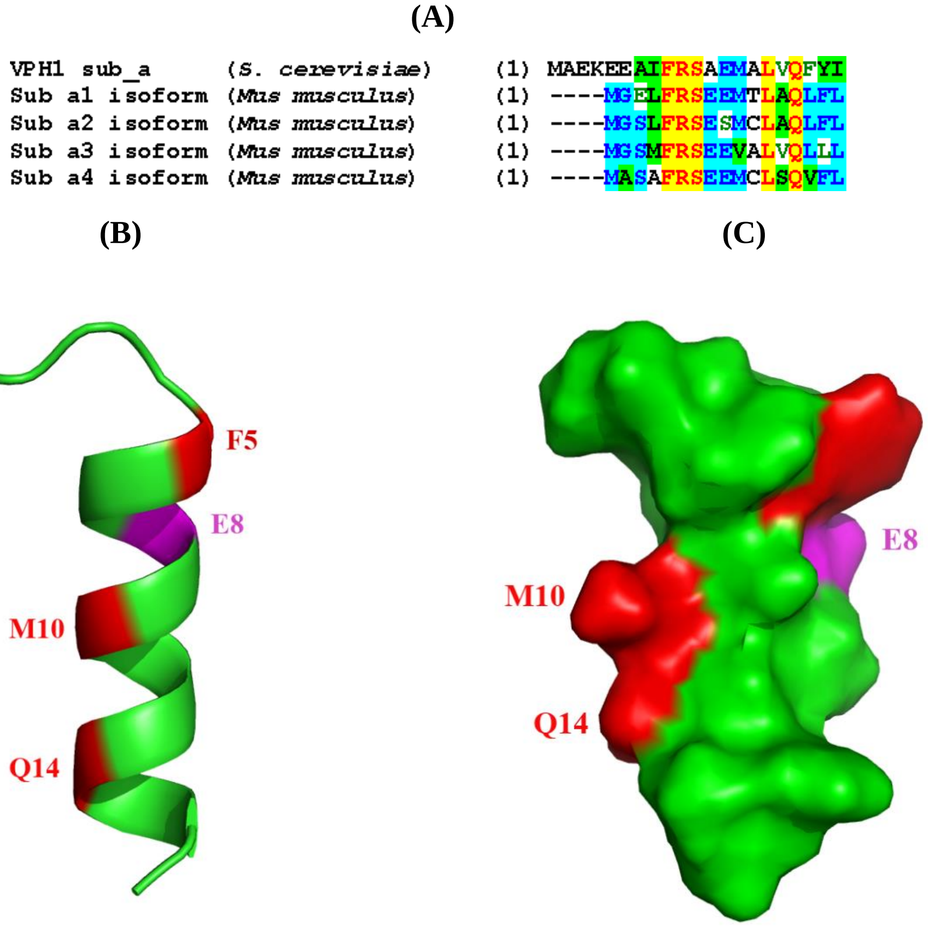

```
VPH1 sub_a       (S. cerevisiae)      (1) MAEKEEAIFRSAEMALVQFYI
Sub a1 isoform (Mus musculus)         (1) ----MGELFRSEEMTLAQLFL
Sub a2 isoform (Mus musculus)         (1) ----MGSLFRSESMCLAQLFL
Sub a3 isoform (Mus musculus)         (1) ----MGSMFRSEEVALVQLLL
Sub a4 isoform (Mus musculus)         (1) ----MASAFRSEEMCLSQVFL
```

Figure 3.6: The binding region of *a2*$_{1\text{-}17}$ (*M. musculus*) to human Sec7 domain. *(A)* Protein sequence alignment of subunit *a* isoforms and yeast homologue. Alignment was created using AlignX software part of Vector NTI v9 InforMax package. Identical amino acids are highlighted in yellow. *(B)* F5, M10 and Q14 are directly involved in Sec7 domain of ARNO association and highlighted in red and E8, which shows a conformational change caused by the actual binding site, is highlighted in purple. *(C)* Surface electrostatic potential of peptide highlighted in red or purple accordingly [2].

3.1.5 Secondary structural characteristics of subunit *a2*$_{368\text{-}395}$ from *Mus musculus*

The peptide *a2*$_{368\text{-}395}$ is an elongated peptide comprised of the amino acids from 386 to 402 of the subunit *a2* isoform from *Mus musculus*. This peptide binds to ARNO as well, which is however not at the catalytic Sec7 domain, putatively at the regulative PH-domain [96]. To analyse how subunit *a* is involved in regulating ARNO and the control of endosomal carrier vesicle formation, attention has been paid to *a2*$_{368\text{-}395}$. Firstly, the secondary structure content of *a2*$_{368\text{-}395}$ peptide (2 mg/ml) dissolved in water and 50% TFE was determined using CD spectroscopy (Figure 3.7A). Further, the secondary structure of subunit *a* was predicted using PSIPRED algorithm [210], showing the peptide is an α-helical structure in nature with an α-helical content of 42%, 53% random coil and 5% β-sheet, which is in line with CD measurement (Figure 3.7B).

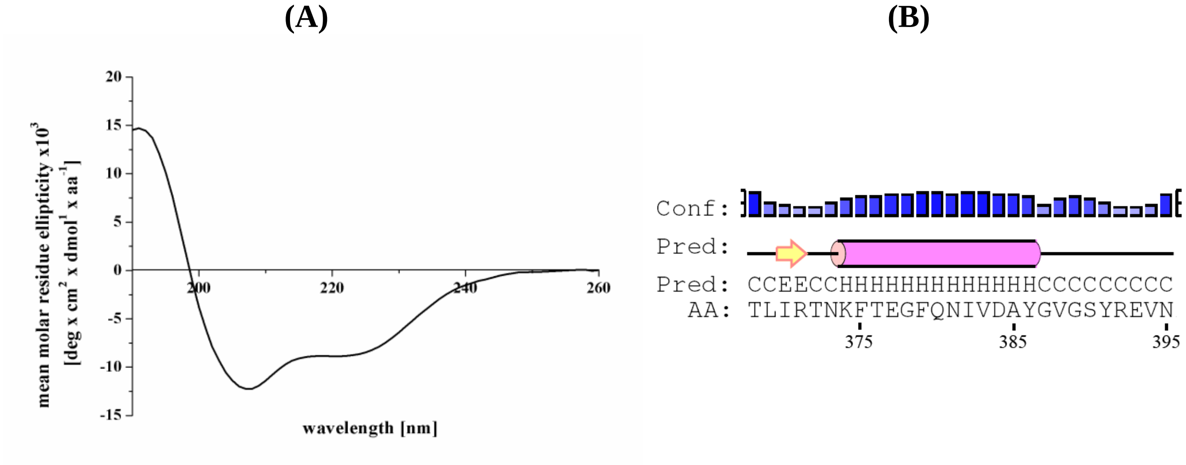

Figure 3.7: Secondary structure analysis of subunit *$a2_{368\text{-}395}$*. *(A)* CD spectrum of subunit *$a2_{368\text{-}395}$* measured at 18 ˚C. *(B)* Secondary structure analysis by online algorithm PSIPRED [210].

3.1.6 Amino acid residue assignment for structure calculation of *$a2_{368\text{-}395}$*

The region 368 – 395 of mouse V-ATPase subunit *a2* isoform has been shown to be involved in ARNO protein association [96], regulating vital physiological processes of protein trafficking and degradation at the cellular level in a tightly co-ordinated and regulated manner [1, 91]. To solve the NMR structure, 2D experiments of NOESY and TOCSY were recorded at a mixing time of 100 ms and 80 ms, respectively. 2D NOESY experiments recorded at 200 ms and 350 ms did not show any variation. All raw data were processed using Topspin software (Bruker). The amino acids in the primary structure of both ARNO peptides were assigned using standard procedures described in method section 2.11.3. All amino acids were assigned using both NOESY and TOCSY data. Figure 3.8A shows the assigned NH region of the 2D NOESY spectrum. Using the sequential walking, the primary protein sequence and their corresponding cross peaks were assigned in the overlaid 2D TOCSY and 2D NOESY spectrum. Identified cross peaks in HN-HN region are displayed in the Figure 3.8A, indicating α-helical features in the peptide. HN–HN, Hα–HN(i, i+3), Hα–HN(i, i+4), and Hα–Hβ (i, i+3) connectivity from the assigned NOESY spectrum were plotted in Figure 3.8B. Hα–HN(i, i+3) indicates α-helical formation between the residues G_{378} to Y_{387}, whereby Hα–HN(i, i+2) between T_{372} and F_{375} indicates a potential α-helical turn.

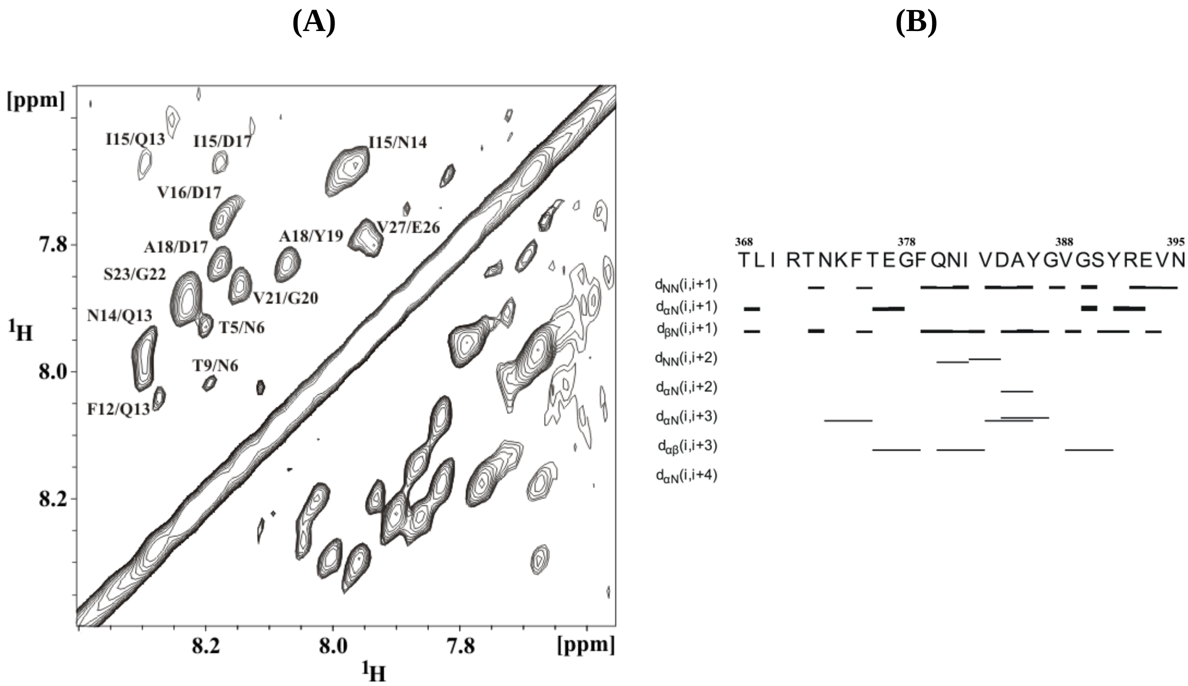

Figure 3.8: HN-NH region of *a2$_{368\text{-}395}$* NOESY spectrum and its connectivity plot. *(A)* Assigned cross-peaks in NH-NH region of the NOESY spectrum. Peaks were selected in sparky 3.1 software and identified based on TOCSY-NOESY spectra. *(B)* NOESY connectivity plot of *a2$_{368\text{-}395}$* peptide shows the cross talk of residues in space, indicating the presence of helical formation.

3.1.7 Structure calculation of *a2$_{368\text{-}395}$* from *Mus musculus*

Peak height and coordinates from assigned 2D NOESY spectra, the dihedral torsion angle from Hα, which were derived from TALOS software [173] and the primary amino acid sequence were used for automated structure calculation of *a2$_{368\text{-}395}$* by Cyana 2.1 package [172]. A compilation of 20 calculated *a2$_{368\text{-}395}$* structures reveal an r.m.s.d. of 0.297 Å for the residues 378-387 (Figure 3.9A). All 20 structures have energies lower than -100 kcal mol^{-1} (Swiss-PdbViewer 4.1.0), no NOE violations larger than 0.3 Å and no dihedral violations wider than 5º. The statistics for 20 structures is summarised in table 3. The representative single structure of *a2$_{368\text{-}395}$* shows a total length of 43.05 Å and forms a flexible N-terminal region from 368-371 with helix extending from 372-375, followed by a short loop from 376-378 and a second helix at 379-387, while the remaining C-terminal region is flexible (Figure 3.9A-B).

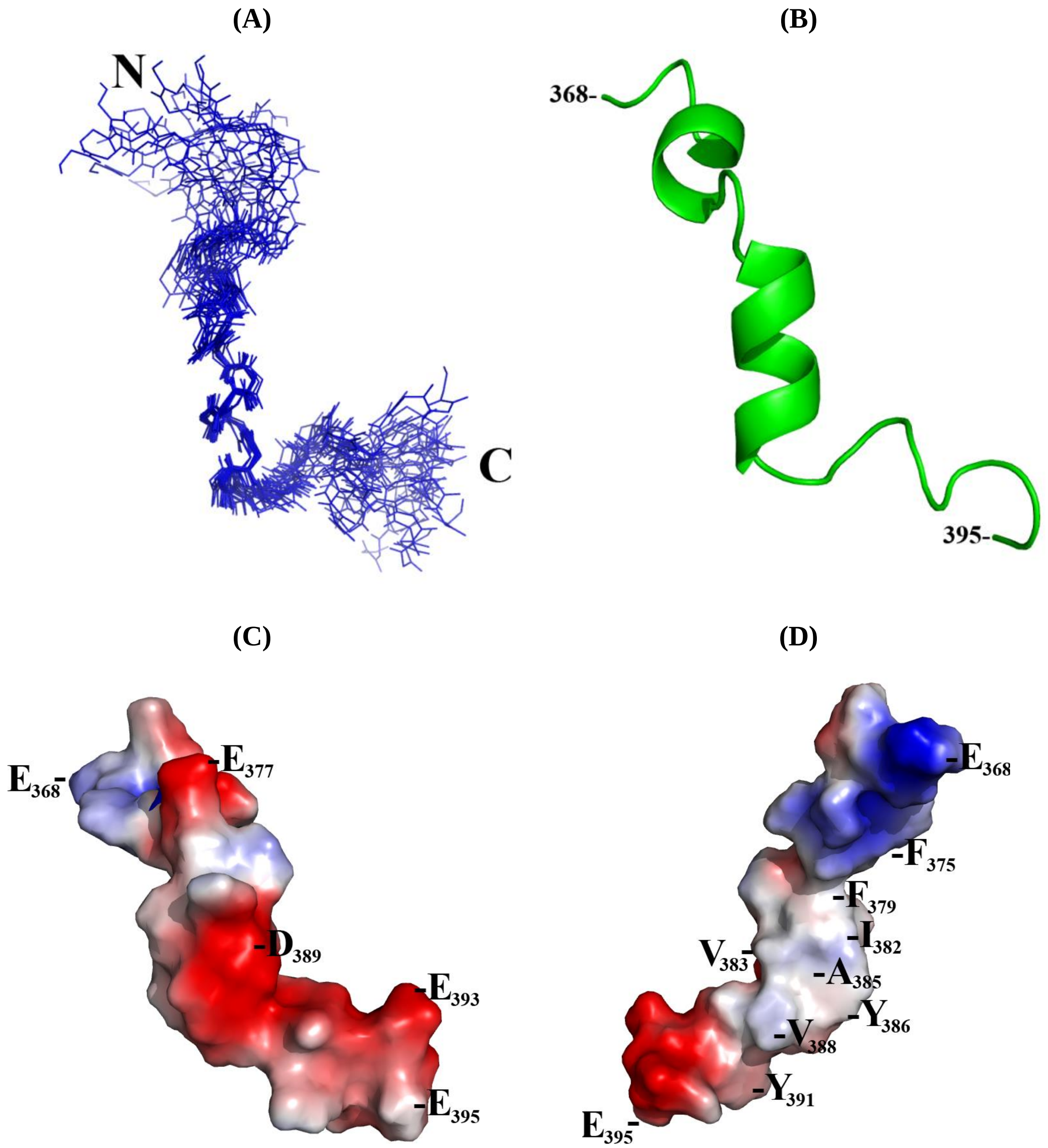

Figure 3.9: NMR structure of peptide *$a2_{368\text{-}395}$* from *Mus musculus*. *(A)* NMR structure of the peptide *$a2_{368\text{-}395}$* showing superimposition of 20 structures calculated by Cyana 3.1 package revealing a partially α-helical. *(B)* Cartoon representation of a single NMR structure. *(C) $a2_{368\text{-}395}$* and *(D)* its 180 view, respectively, created by Pymol [175]. The positive and negative potentials are depicted in blue and red, whereas hydrophobic in light grey.

The α-helical regions of *$a2_{368\text{-}395}$* are indicated in the NOE plot (Figure 3.8B). Analysis of the calculated structures showed therefore that two helices are present (Figure 3.9B), which might be crucial for the interaction with ARNO. Molecular surface electrostatic potential of the *$a2_{368\text{-}395}$* peptide reveals an amphiphilic surface (Figure 3.9C-D). At one side of the peptide, residues E377, D384 and E393 form a negative charged surface (Figure 3.9C). The opposite side reflects an amphiphilic surface potential, formed by the N-terminal positive charge and hydrophobic residues F375, F379, I382, V383, A385, Y386 V388 and Y391 (Figure 3.9C-D). The peptide at the helix region between G_{378}-Y_{386} are either negatively charged or hydrophobic, which may allow ARNO to interact with this peptide.

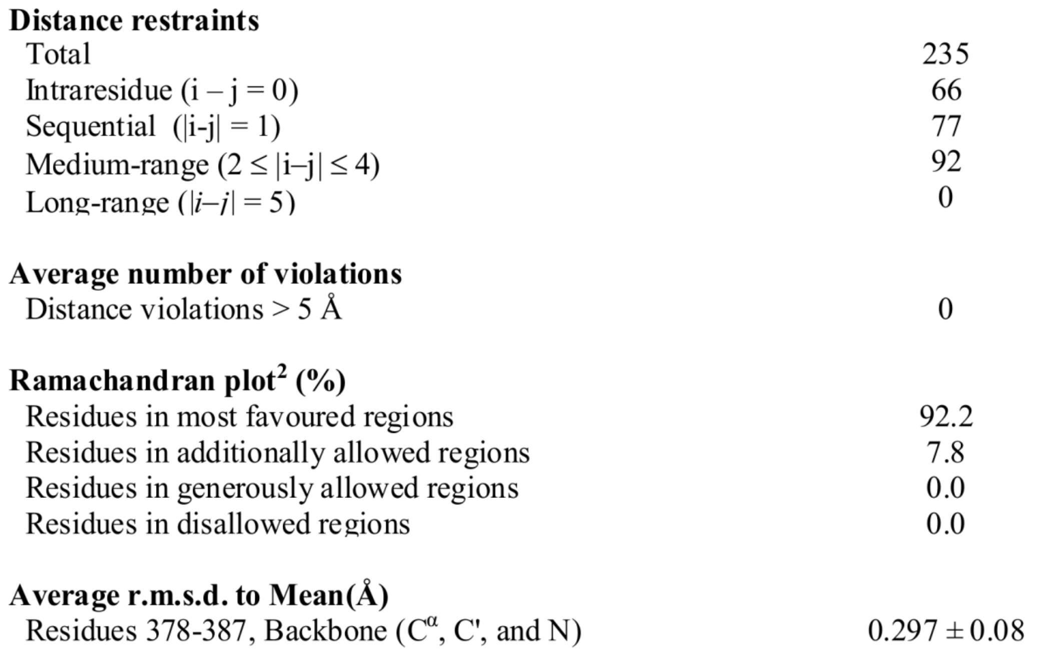

Distance restraints	
Total	235
Intraresidue (i – j = 0)	66
Sequential (|i-j| = 1)	77
Medium-range (2 ≤ |i–j| ≤ 4)	92
Long-range (|*i*–*j*| = 5)	0
Average number of violations	
Distance violations > 5 Å	0
Ramachandran plot^2 (%)	
Residues in most favoured regions	92.2
Residues in additionally allowed regions	7.8
Residues in generously allowed regions	0.0
Residues in disallowed regions	0.0
Average r.m.s.d. to Mean(Å)	
Residues 378-387, Backbone (C^{α}, C', and N)	0.297 ± 0.08

Table 3.2: Structural statistics for peptide *a2*$_{368\text{-}395}$.

3.1.8 Nuclear magnetic resonance spectroscopy of Sec7 domain of ARNO from *H. sapiens*

In order to investigate the interaction interface of Sec7 domain (R_{61} to R_{252}) of ARNO with subunit *a* and to verify a proper folding of this protein, one-dimensional NMR spectrum of Sec7 domain of ARNO was performed. The one dimensional NMR spectrum recorded in 25 mM phosphate buffer, 300 mM NaCl (pH 6.5) revealed that the protein was folded. This was concluded from the characteristic pattern of peaks and well dispersed resonance lines of amide protons (6 to 10 ppm), α-protons (3.5 to 5 ppm), and especially from the uphill shifted methyl protons (-0.5 to 1.0 ppm; Figure 3.10) [211].

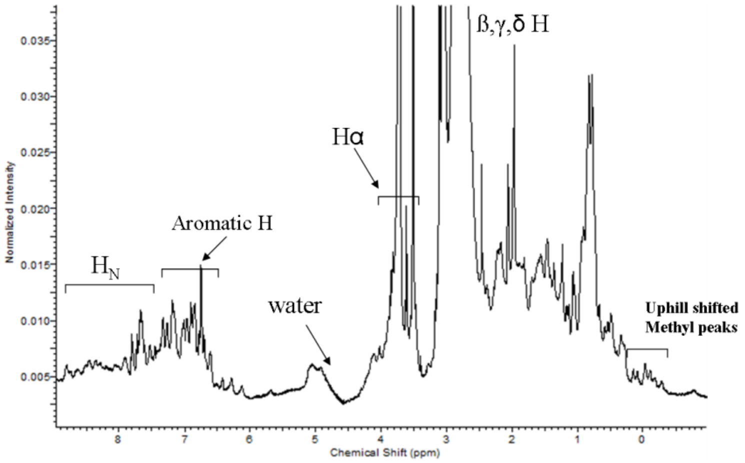

Figure 3.10: 1D NMR spectrum of the human Sec7 domain of ARNO. *(A)* One dimensional NMR spectrum of Sec7 domain was recorded at 298 K in 25 mM PO_4 buffer, 300 mM NaCl (pH 6.5) on Bruker Avance 600 MHz machine. Well dispersion of resonance peaks in HN region, α-protons and uphill shifted methyl peaks are the characteristics of natively folded protein. Strong peaks at 4.7 ppm represents water signal.

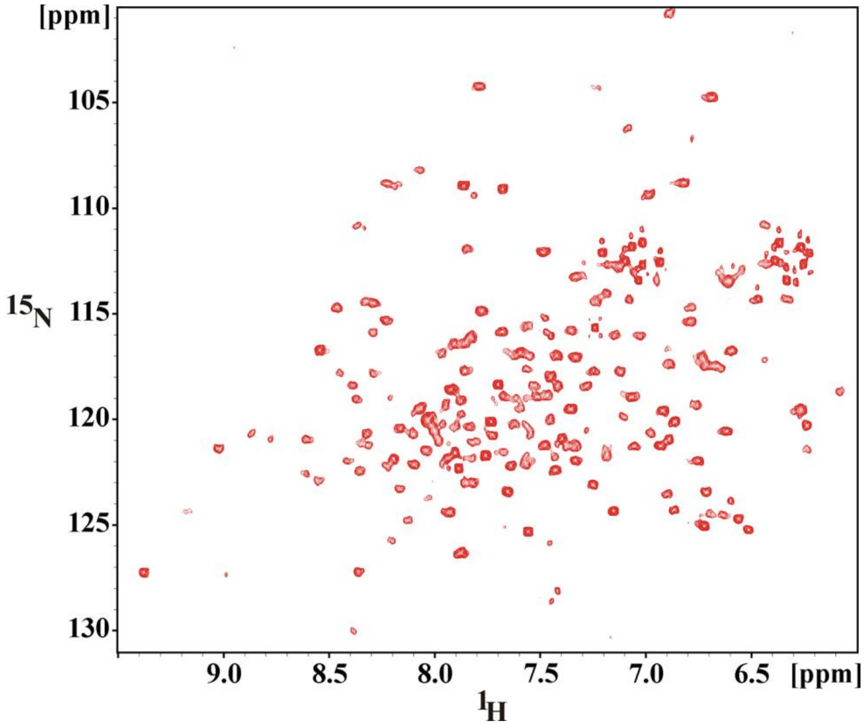

Figure 3.11: HSQC Spectrum of the human Sec7-domain of ARNO. 2D^1H-^{15}N HSQC NMR spectrum of Sec7 domain of ARNO was recorded at 298 K in 25 mM phosphate buffer, 300mM NaCl (pH 6.5) on a Bruker Avance 600 MHz machine.

HSQC experiments have been optimised in 25 mM phosphate buffer, 300 mM NaCl, pH 6.5 by changing different parameters, *e.g.* temperature and concentration of protein. The well dispersed peaks and their line shape in the HSQC spectra (Figure 3.11) indicate that Sec7 domain is folded. In total, 170 amino acids can be observed from the 22 kDa protein. In order to have an insight into the binding interface of Sec7 domain of ARNO to *a2*$_{1\text{-}17}$, ^1H-^{15}N HSQC spectra of this protein were recorded at 298 K with a fixed concentration of 0.4 mM. The peptide *a2*$_{1\text{-}17}$ was titrated with 0.6 mM (1:1.5) to the Sec7 domain of ARNO.

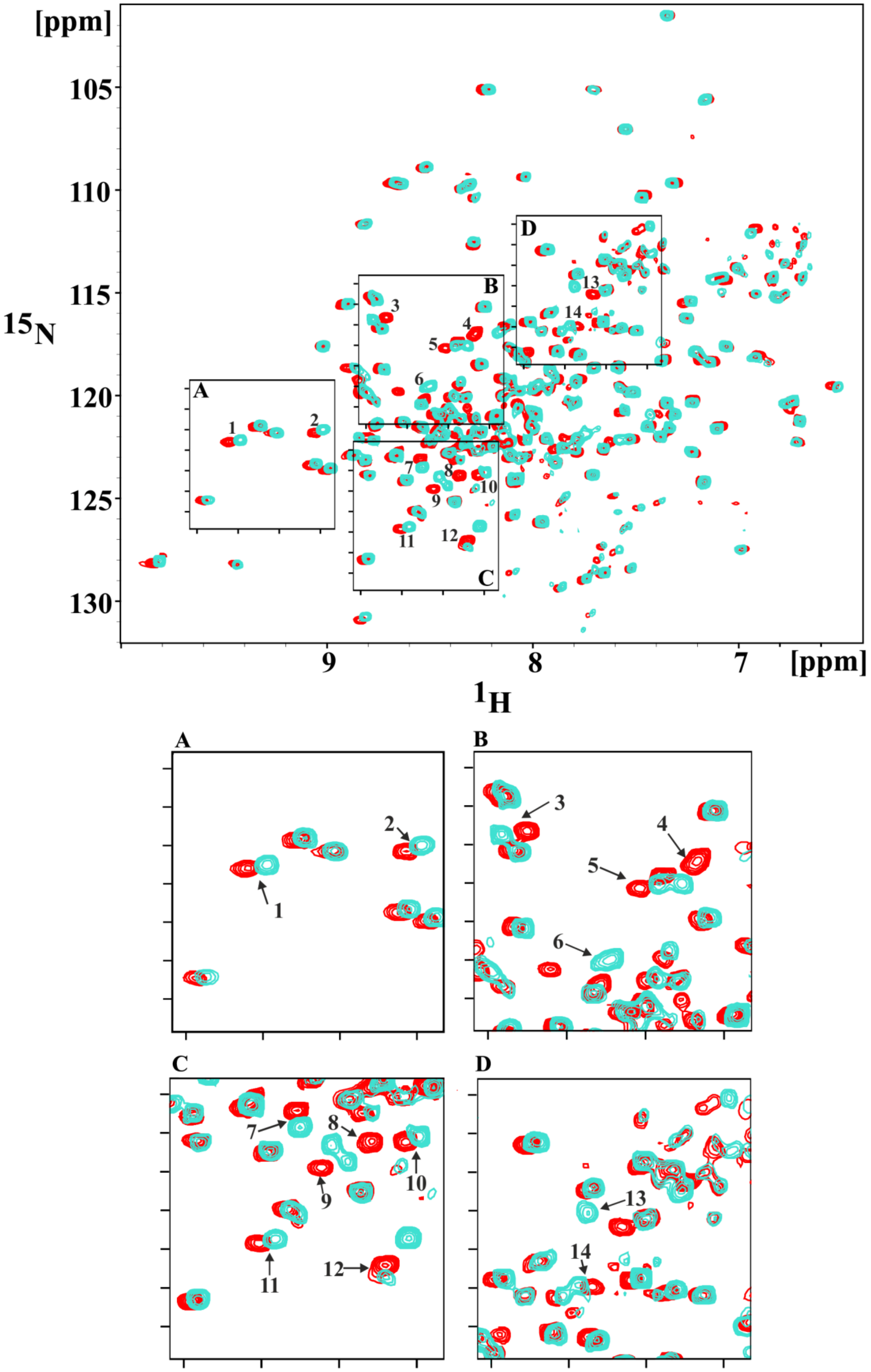

Figure 3.12: HSQC titration experiment of the human Sec7-domain of ARNO and mouse *a2*$_{1\text{-}17}$. Overlay of 2D ^{1}H-^{15}N HSQC NMR spectrum of Sec7 domain of ARNO alone (red) and Sec7 domain of ARNO after titration of 0.6 mM *a2*$_{1\text{-}17}$ (blue) [2].

After adding of 0.6 mM of $a2_{1\text{-}17}$ peptide to Sec7 domain of ARNO, significant changes in the chemical shift were observed, indicating binding of $a2_{1\text{-}17}$ to the Sec7 domain of ARNO (Figure 3.12). The changes are zoomed in the section and highlighted with an arrow (Figure 3.12A-D). In total, 14 peaks with significant changes were identified. Nine of these peaks showed changes along the proton axis with decrease of ppm values, whereas three peaks showed changes with increase of ppm. Along the nitrogen axis, two shifts were observed (Figure 3.12D). One peak, labelled as 7 at [123.1/8.55ppm $^{15}N/^{1}H$] has increased ppm at the nitrogen axis [123.5/8.55ppm $^{15}N/^{1}H$], and the peak 12 reflects a combined change with decreased ppm of nitrogen and proton from [127.1/8.32 ppm $^{15}N/^{1}H$] to [126.3/8.26 ppm $^{15}N/^{1}H$] (Figure 3.12D). Changes in shape or intensity of the peaks are not intensive, since all 170 peaks are present and referable after the addition of $a2_{1\text{-}17}$ peptide. Broadening or losses of NMR signals in the resonances are therefore not affected by the binding. The significant changes in chemical shifts suggest that the binding between Sec7 and $a2_{1\text{-}17}$ is strong.

In order to test whether binding and signalling between of V-ATPase and ARNO is evolutionary conserved in all eukaryotes, the interaction of the entire soluble region of recombinant yeast $a_{1\text{-}388}$ proteins with human ARNO Sec7 domain was also studied by NMR spectroscopy in 25 mM phosphate buffer, 300 mM NaCl, pH 6.5. In these experiments, 14 amino acids have also shown chemical shifts and losses in peak intensity, which are labelled with an arrow (Figure 3.13). Crucial shifts and intensity changes are highlighted in the section of Figure 3.13. Importantly, 12 out of the 14 peaks are showing chemical shifts and loss of intensity, which are comparable with those in $a2_{1\text{-}17}$-Sec7 titration experiment (Figure 3.12). This indicates that yeast $a2_{1\text{-}388}$ has the same Sec7 binding site as mammalian $a2_{1\text{-}17}$. The two additional changes in chemical shifts (peak 13 and 14) might be caused by the residues of $a_{1\text{-}388}$ that are not present in $a2_{1\text{-}17}$.

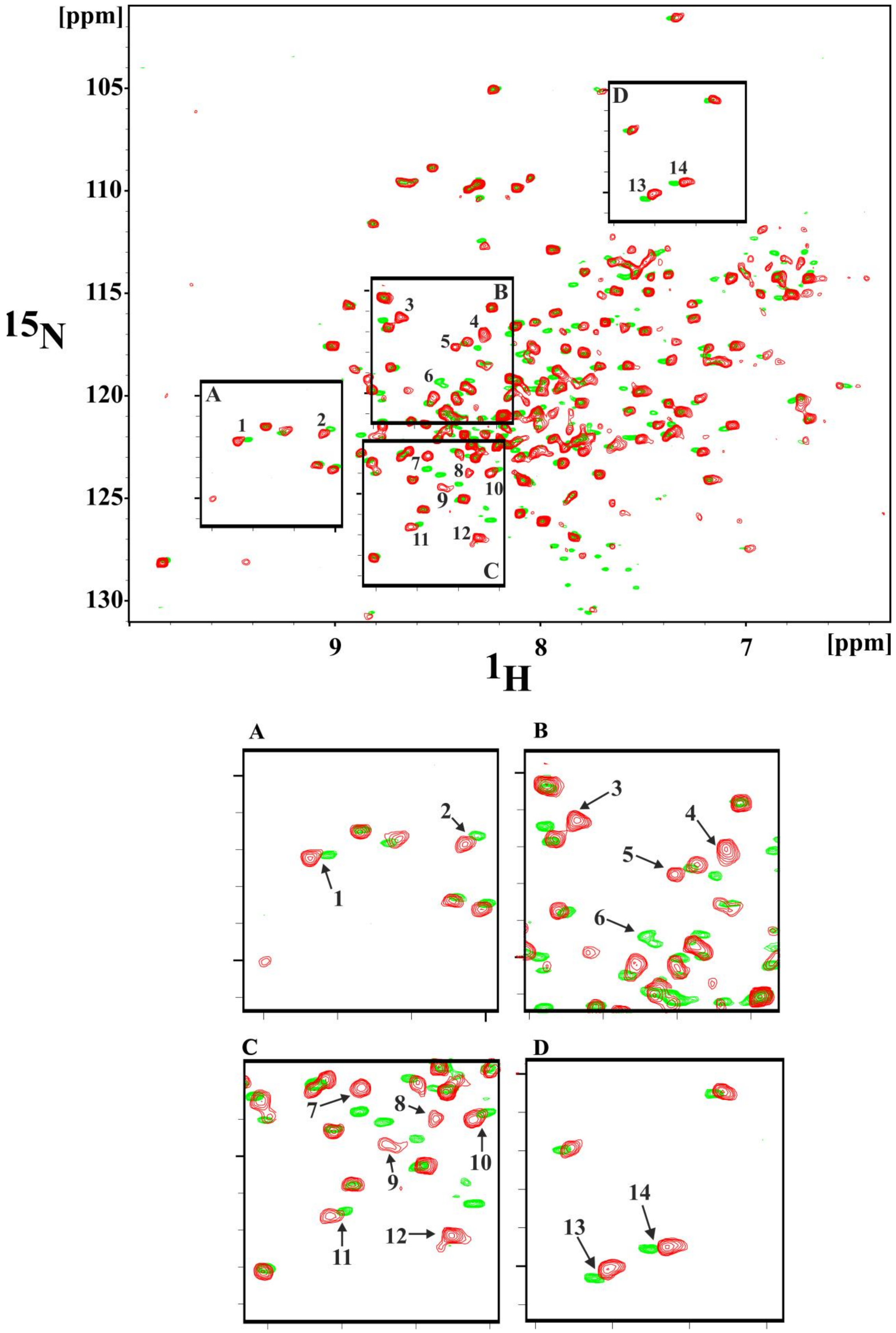

Figure 3.13: HSQC titration experiment of the human Sec7-domain of ARNO upon titration of yeast $a_{1\text{-}388}$. Overlay of 2D^{1}H-^{15}N HSQC NMR spectra of Sec7 domain of ARNO alone (red) and Sec7 domain of ARNO after adding of 0.3 mM $a2_{1\text{-}388}$ (green). 12 Peaks are changed either in chemical shift or in intensity and these changes are similar as the $a2_{1\text{-}17}$ titration in Figure 3.12.

The changes after adding $a2_{1-388}$ to Sec7 are smaller in comparison with $a2_{1-17}$ titration. This can be due to the use of the yeast isoform (a_{1-388}, *S. cerevisiae*) that has 70% sequence similarity and 41% sequence identity to the $a2_{1-17}$ (*M. musculus*) (Figure 3.6A). In comparison, $a2_{1-17}$ has F5, E8 M10 and Q14 as a binding site to Sec7 of ARNO, while construct a_{1-388} has the conserved amino acids F9, M14 and Q18 (Figure 3.6A). Only one amino acid of a_{1-388} is different to the binding site of $a2_{1-17}$, namely A12 instead of E8. This change in amino acid sequence can affect the binding affinity of a_{1-388} to the Sec7 domain. Furthermore, compared to the $a2_{1-17}$ peptide, a_{1-388} is larger and has a three-dimensional folded structure, which might block the putative binding region at F9, A12, M14 and Q18, and thus makes it less accessible to the Sec7 domain of ARNO.

3.2 Solution structure of V-ATPase subunit $a_{104\text{-}363}$ derived by SAXS revealing the importance of its C-terminus

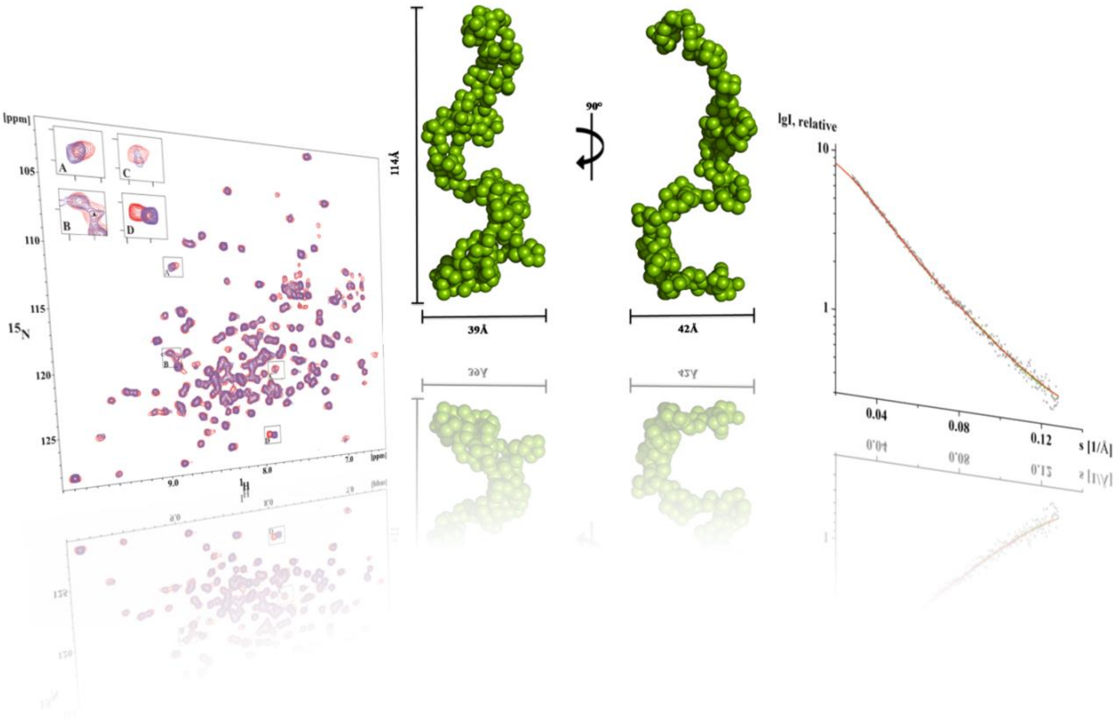

Solution structure of V-ATPase subunit $a_{104\text{-}363}$ derived by SAXS revealing the importance of its C-terminus

3.2.1 Production, purification and secondary structure analysis of subunit $a_{104\text{-}363}$ of the *S. cerevisiae* V-ATPase

In order to confirm the interaction at the very N-terminal $a2_{1\text{-}17}$ region, further NMR titration experiments of Sec7 protein with an N-terminal truncation of subunit *a*, $Sca_{104\text{-}363}$ have been performed. Specific binding region, $a2_{1\text{-}17}$ of subunit *a* at the very N-terminal segment has been investigated prior of this study, which might be potentially involved in modulation of GDP/GTP exchange (GEF) activity of ARNO to its substrate Arf6 and Arf1, the GTP-binding proteins. Together with V-ATPase, ARNO and Arf6 regulate the switch in the endocytic pathway [2]. Since the interaction of Sec7 domain of ARNO with $a2_{1\text{-}17}$ and $a_{1\text{-}388}$ of *S. cerevisiae* has been described, further analysis on different interaction sites of subunit *a* must be performed to understand the control and regulation of the vesicular trafficking within the endocytotic and exocytotic pathway [96]. Earlier, six peptides of the mouse *a2* isoform ($a2_{1\text{-}17}$, $a2_{35\text{-}49}$, $a2_{198\text{-}214}$, $a2_{215\text{-}230}$, $a2_{313\text{-}331}$ and $a2_{386\text{-}402}$) showed interaction with ARNO, from which two peptides $a2_{1\text{-}17}$ and $a2_{35\text{-}49}$ have the strongest binding to the catalytic Sec7 domain of ARNO (Figure 3.14, [96]). Hence, to verify the Sec7 domain interaction, construct $a_{104\text{-}363}$, which does not contain the terminal binding domains $a2_{1\text{-}17}$, $a2_{35\text{-}49}$ and $a2_{386\text{-}402}$ of subunit *a*, has been constructed, purified and analysed before undergoing ARNO interaction studies.

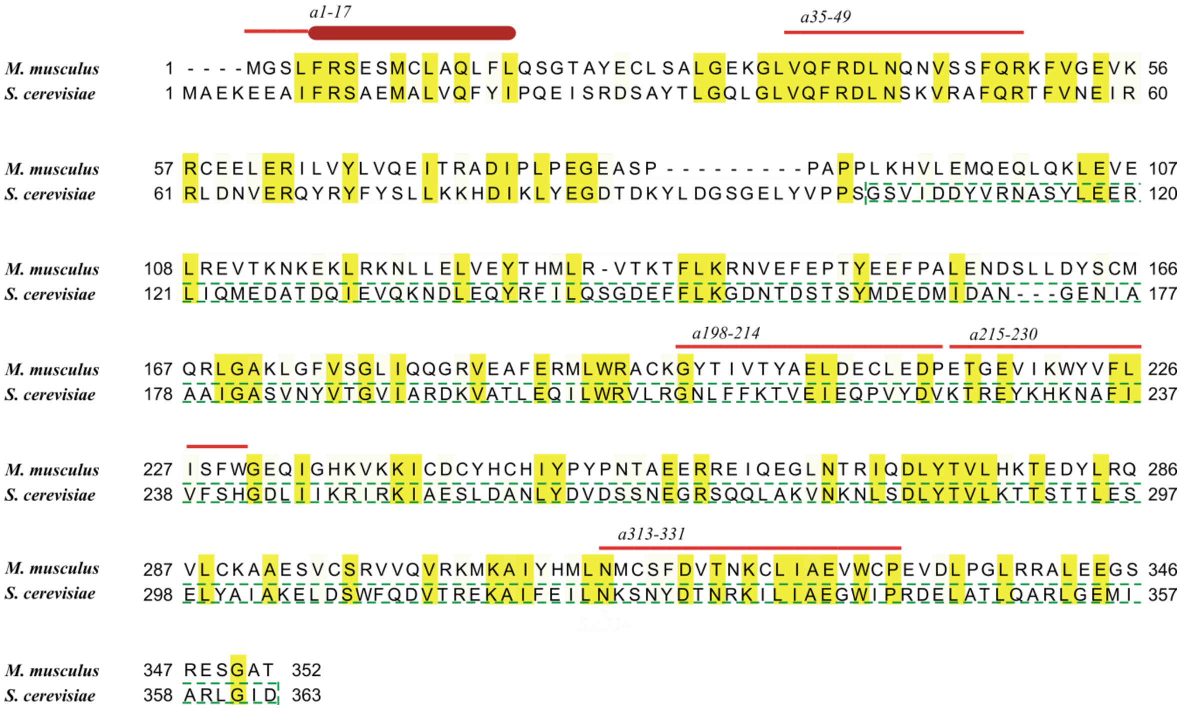

M. musculus 1 ----MGSLFRSESMCLAQLFLQSGTAYECLSALGEKGLVQFRDLNQNVSSFQRKFVGEVK 56
S. cerevisiae 1 MAEKEEAIFRSAEMALVQFYIPQEISRDSAYTLGQLGLVQFRDLNSKVRAFQRTFVNEIR 60

M. musculus 57 RCEELERILVYLVQEITRADIPLPEGEASP---------PAPPLKHVLEMQEQLQKLEVE 107
S. cerevisiae 61 RLDNVERQYRYFYSLLKKHDIKLYEGDTDKYLDGSGELYVPPSGSVIDDYVRNASYLEER 120

M. musculus 108 LREVTKNKEKLRKNLLELVEYTHMLR-VTKTFLKRNVEFEPTYEEFPALENDSLLDYSCM 166
S. cerevisiae 121 LIQMEDATDQIEVQKNDLEQYRFILQSGDEFFLKGDNTDSTSYMDEDMIDAN---GENIA 177

M. musculus 167 QRLGAKLGFVSGLIQQGRVEAFERMLWRACKGYTIVTYAELDECLEDPETGEVIKWYVFL 226
S. cerevisiae 178 AAIGASVNYVTGVIARDKVATLEQILWRVLRGNLFFKTVEIEQPVYDVKTREYKHKNAFI 237

M. musculus 227 ISFWGEQIGHKVKKICDCYHCHIYPYPNTAEERREIQEGLNTRIQDLYTVLHKTEDYLRQ 286
S. cerevisiae 238 VFSHGDLIIKRIRKIAESLDANLYDVDSSNEGRSQQLAKVNKNLSDLYTVLKTTSTTLES 297

M. musculus 287 VLCKAAESVCSRVVQVRKMKAIYHMLNMCSFDVTNKCLIAEVWCPEVDLPGLRRALEEGS 346
S. cerevisiae 298 ELYAIAKELDSWFQDVTREKAIFEILNKSNYDTNRKILIAEGWIPRDELATLQARLGEMI 357

M. musculus 347 RESGAT 352
S. cerevisiae 358 ARLGID 363

Figure 3.14: Sequence comparison of the cytosolic N-terminal region of subunit *a* from *M. musculus* and *S. cerevisiae* using Jalview 2.7 [212]. The secondary structure $a2_{1\text{-}17}$ solved by NMR and the major binding sites to the Sec7 domain are depicted above the sequence [2]. The other binding sites of subunit *a* to Sec7 domain of ARNO are drawn in red lines [96]. The construct $a_{104\text{-}363}$ is highlighted in green dashes [3].

Soluble His$_6$-recombinant protein $a_{104-363}$ was purified using Ni^{2+}-NTA affinity chromatography. A gradient of increasing imidazole concentration from 25 to 250 mM in 50 mM Tris/HCl (pH 8.5), 200 mM NaCl, 10 mM EDTA and 2 mM PMSF has been used for protein elution. $a_{104-363}$ eluted at 75 to 125 mM imidazole fractions which were subsequently applied to a Superdex 75 column (Figure 3.15A) to obtain the purest and monodispersed protein. Isolated $a_{104-363}$ protein was applied onto an SDS-PAGE to verify the high purity of the protein (Figure 3.15A, *lane 2*).

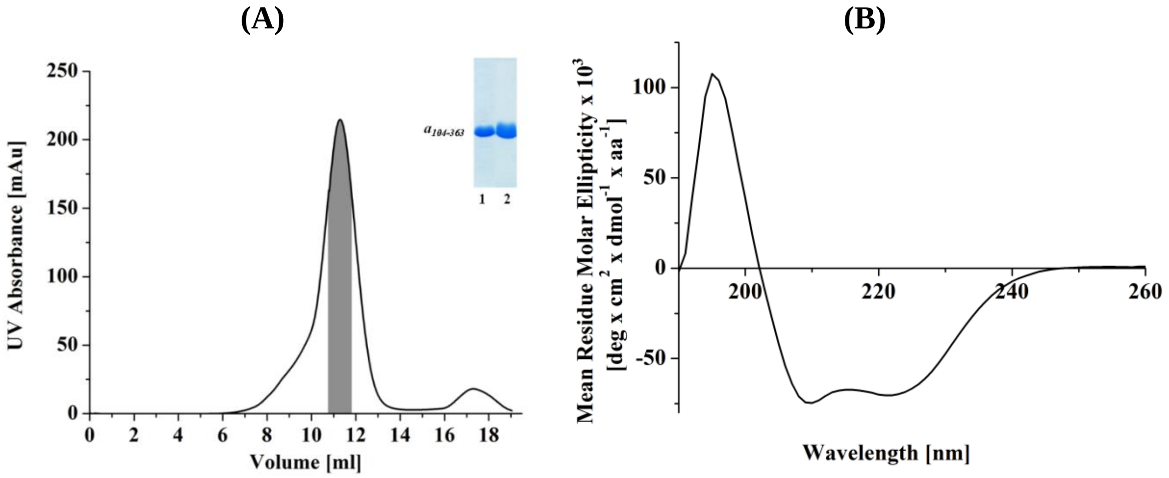

Figure 3.15: Size exclusion chromatography of $a_{104-363}$ from *S. cerevisiae* and its CD spectrum. (*A*) Purification of $a_{104-363}$ protein using Ni^{2+}-NTA resin. Eluted proteins were pooled and applied onto a Superdex 75 column using buffer (50 mM Tris/HCl, pH 8.5, 200 mM NaCl, 10 mM EDTA). Inserted SDS gels show purified $a_{104-363}$ after Ni^{2+} -NTA resin (*lane 1*), and after Superdex 75 (*lane 2*) from the indicated fraction of the elution profile, respectively. *(B)* Far UV-CD spectrum of $a_{104-363}$ (—) indicates the formation of α-helical content.

To analyse the secondary structure of recombinant $a_{104-363}$, circular dichroism spectroscopy was applied (Figure 3.15B). Overall, 87.6% α-helix, 0.5% β-sheet and 11.9% random coil were calculated from the CD-spectrum, which is in line to the corresponding secondary structure predictions of $a_{104-363}$ amino-acid sequence. The ratio of the molar ellipticity of both minima at 208 nm and at 222 nm is 0.96 [3].

3.2.2 NMR titration experiments of *S. cerevisiae* $a_{104-363}$ and human Sec7 domain of ARNO

In order to investigate the binding of *S. cerevisiae* $a_{104-363}$ to the human Sec7 domain of ARNO, NMR titration were performed as described in section 2.11.4 [171]. The recombinant protein $a_{104-363}$ as well as Sec7 domain of ARNO was buffer exchanged to 25 mM phosphate buffer, pH 6.5 and 300 mM NaCl. ^{1}H-^{15}N HSQC spectrum of Sec7 domain (residues R_{61} to R_{252}) of ARNO was used as a starting point as described in earlier NMR titration experiments with *a2*$_{1\text{-}17}$ and *a*$_{1\text{-}388}$ (Figure 3.16, red peaks). The data acquisitions of ^{1}H-^{15}N HSQC spectra were performed with fixed concentration of 0.2 mM of Sec7 domain at 298 K. Subsequently *a*$_{104\text{-}363}$ was titrated with 0.4 mM (1:2) to Sec7. The overlay of spectra from the titration experiments showed changes in chemical shift, especially in four peaks of the Sec7 domain, which are highlighted in the boxes (Figure 3.16), indicating the binding of *a*$_{104\text{-}363}$ to Sec7 domain [3]. In comparison to the Sec7 and *a*$_{1\text{-}388}$ NMR titration (Figure 3.13), which include 14 changes in chemical shifts, the NMR titration experiments of *a*$_{104\text{-}363}$ to Sec7 domain showed only four chemical shift changes, suggesting weaker binding (Figure 3.13). Furthermore NMR titration between Sec7 and *Sca*$_{1\text{-}388}$ showed more and wider chemical shifts, indicating stronger binding of *a*$_{1\text{-}388}$ mainly via its very N-terminal site [2]. This result indicates that *a*$_{104\text{-}363}$ is properly folded and also involved in association with ARNO, which may occur via the remaining homologues binding segments *a2*$_{198\text{-}214}$, *a2*$_{215\text{-}230}$ and/or *a2*$_{313\text{-}331}$ (Figure 3.14).

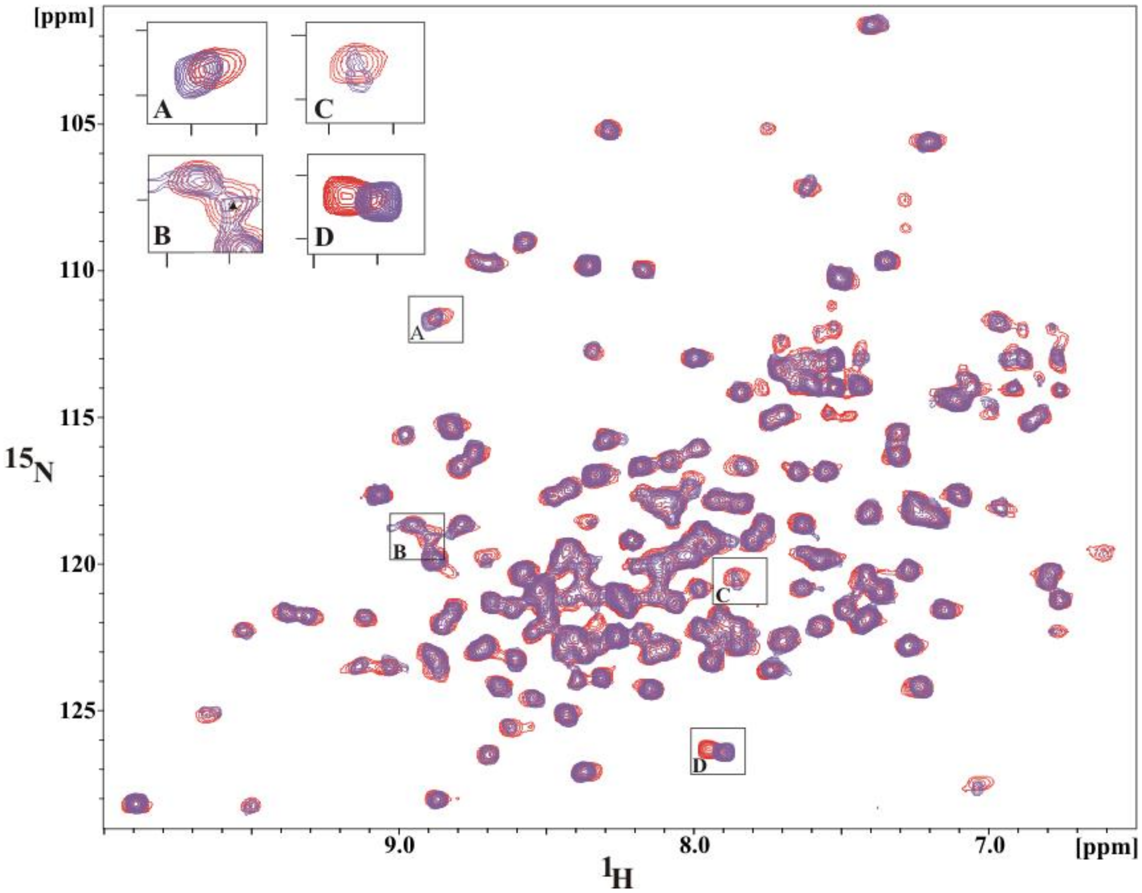

Figure 3.16: NMR HSQC spectra of Sec7 / *a*$_{104\text{-}363}$ titration. Overlay of 2D ^{1}H-^{15}N HSQC spectrum of Sec7 domain of ARNO alone (red) and upon titration of *Sca*$_{104\text{-}363}$ (1:2, purple) in 25 mM sodium phosphate buffer (pH 6.5) 300 mM NaCl at 298 K. The titration experiments reveal chemical shifts of four peaks, highlighted in the section A-D [3].

3.2.3 Solution structure of *S. cerevisiae* V-ATPase subunit $a_{104-363}$ derived using SAXS

The high purity of recombinant $a_{104-363}$ protein allows the data collection from small-angle X-ray scattering (SAXS) to analyse its folding in solution and to obtain the first low resolution structure of the eukaryotic V-ATPase N-terminal cytosolic segment of subunit *a*. SAXS patterns from $a_{104-363}$ were obtained as described in Material and Methods section 2.9. SAXS data for $a_{104-363}$ was collected by Prof. Dr. Manfred Roessle [196, 197] and the calculation was guided by Dr. Malathy Sony S. Manimekalai. The final scattering curve reflects a monodispersed protein in solution (Figure 3.17A). Low angles of the Guinier plots reveal good data quality without protein aggregation. The distance distribution curve of protein $a_{104-363}$ describes all paired distances within a structure, showing a radius of gyration R_g of 38.8 Å and a maximum dimension D_{max} of 120 Å (Figure 3.17B). The comparison between the forward scattering values of the bovine serum albumin (BSA; 66.4 ± 2 kDa) as reference solution and $a_{104-363}$ revealed a molecular mass of 30 ± 2 kDa for $a_{104-363}$, which is in line to the size exclusion chromatography results (Figure 3.15). $a_{104-363}$ is therefore in a monomeric state at the concentrations of 2 mg/ml used in this SAXS experiment. The distance distribution function *ρ(r)* reflects a single peak with an elongated tail. Its maximum *p(r)* is at 36 Å (Figure 3.17B), whereas the tailed shoulder from 84 Å to 120 Å represents the characteristics of an elongated $a_{104-363}$ protein.

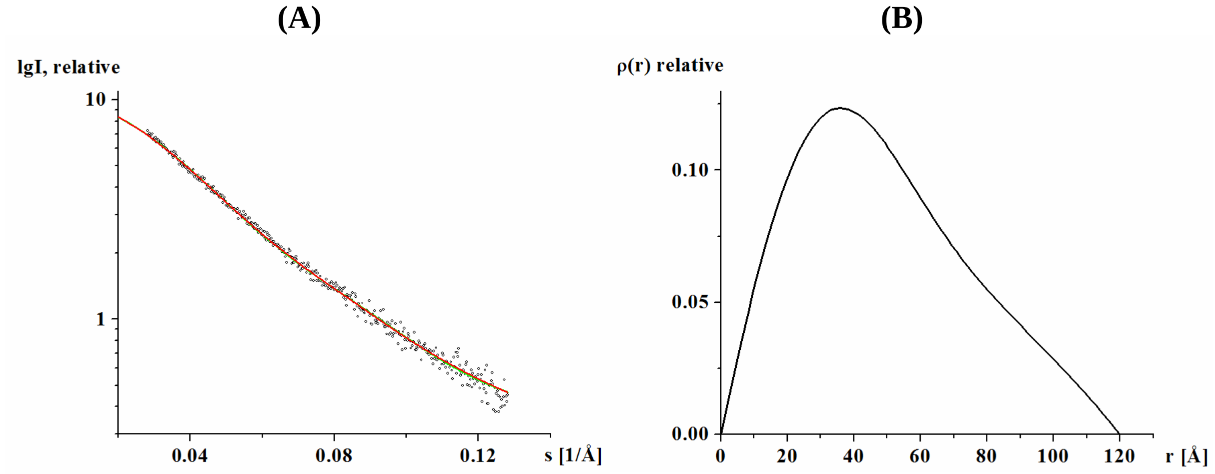

Figure 3.17: Experimental scattering pattern (•) and its corresponding fitting curves (*green line*: experimental, *red line:* calculated) *(A)*. (*B*) Distance distribution functions of $a_{104-363}$, respectively. The curves of $a_{104-363}$ are displayed in logarithmic unit for clarity [3].

From the scattering patterns, the solution structure of $a_{104-363}$ was calculated *ab initio* using GASBOR, as shown in Figure 3.18 [185]. The generated $a_{104-363}$ protein shape and its corresponding fitting curve reflect a good fitting within the experimental data with a deviation to the experimental curve of χ^2 = 1.08 for the entire scattering range (Figure 3.17A). The calculated SAXS structure of $a_{104-363}$ reveals an elongated formation with an S-like shape (Figure 3.18, column1). The shape has a length of about 114 Å and a width of 39 Å.

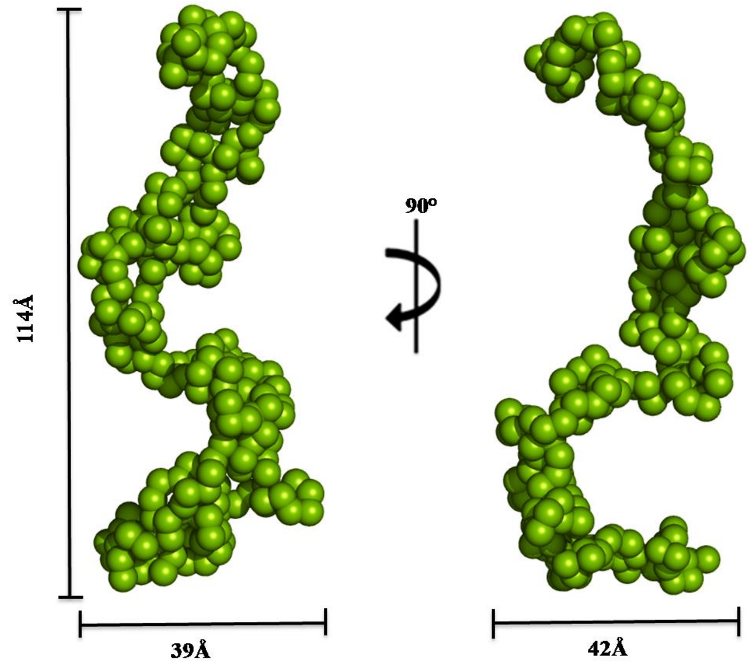

Figure 3.18: The solution structure of *S. cerevisiae* $a_{104-363}$ is depicted in green spheres. The overall structure of $a_{104-363}$ reveals a monomeric molecule in an elongated shape. The length of this model is 114 Å, whereas the width is 42 Å [3].

3.3 Insights into the C-terminal transmembrane domain of the *S. cerevisiae* V-ATPase subunit *a*

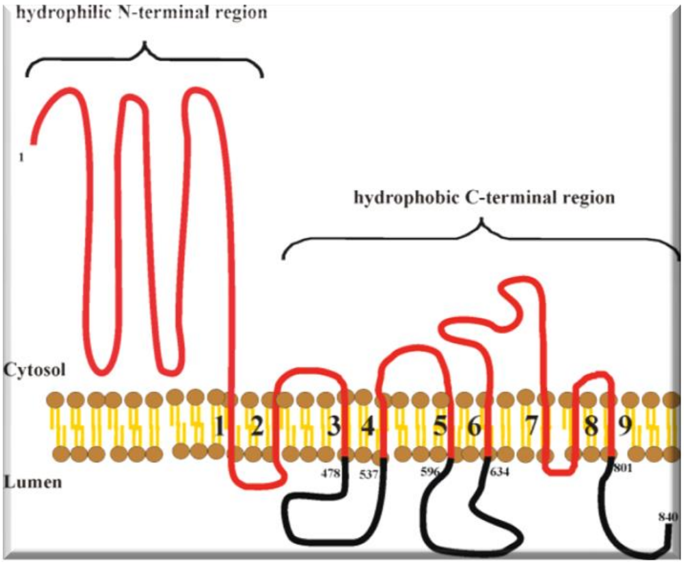
hydrophilic N-terminal region
1
hydrophobic C-terminal region
Cytosol
1
2
3
4
5
6
7
8
9
Lumen
478
537
596
634
801
840

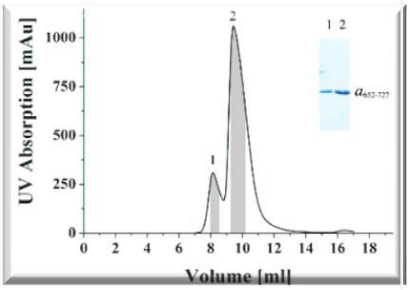

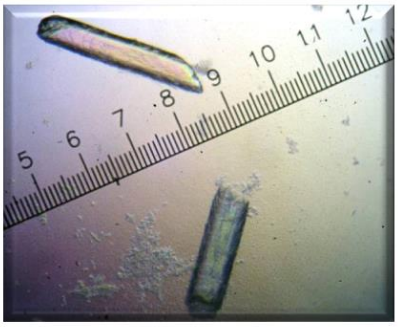

3.3.1 Expression and purification of $a_{582-649}$, $a_{673-731}$ and $a_{653-727}$

In order to investigate the recruiting and scaffolding of small GTPases as well as the pH-sensoring of subunit *a* [1], C-terminal constructs were designed according to predicted membrane topologies using ‘kyte Doolittle’ algorithm [91] or experimental studies with cysteine mutants [15]. In several studies, mammalian transmembrane proteins have been identified as having pH sensing capability whereby histidine residues have been identified in all of these proteins as an important component of the pH sensing mechanism [91].

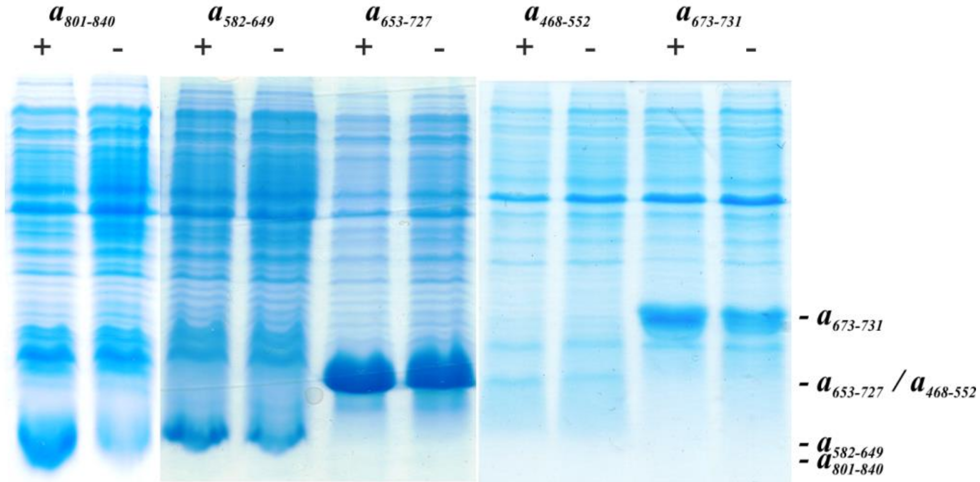

Figure 3.19: Induction test from subunit *a* constructs: $a_{801-840}$, $a_{582-649}$, $a_{653-727}$, $a_{468-552}$ and $a_{673-731}$. The depicted SDS gel demonstrates induced (+) and uninduced (-) samples used in the current study. Induction was done with 1 mM IPTG at 37 °C. Whole cell lysate was prepared by heating cells in 1x lysis buffer at 95 °C for 5 min and followed by electrophoresis on a 17% SDS gel.

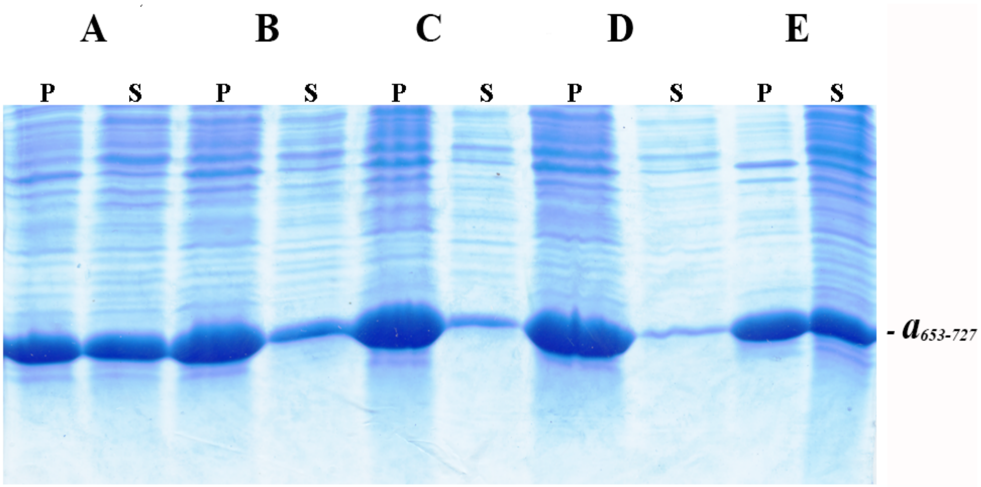

Figure 3.20: Solubility test of subunit *a* construct $a_{653-727}$. *(A)* 17% SDS gel showing solubility test results from a representative protein, $a_{653-727}$. Pellet (P) and supernatant (S) in various buffers (A-E) is shown on the gel representing preponderance of protein in the supernatant of various buffers. Buffer A: 50 mM Tris/HCl, 200 mM NaCl, pH 8.5; Buffer B: 50 mM Tris/HCl, 200 mM NaCl, pH 7.5; Buffer C: 25 mM Hepes, 200 mM NaCl, pH 7.5; Buffer D: 25 mM MES, 200 mM NaCl, pH 7.0; Buffer E: 50 mM phosphate, 200 mM NaCl, pH 6.5.

These constructs $a_{468-552}$, $a_{582-649}$, $a_{673-731}$, $a_{478-537}$, $a_{596-634}$, $a_{653-727}$ and $a_{801-840}$ contain a soluble C-terminal region facing either to cytosol or to the lumen, respectively, which might be involved in association with other subunits E, F, G, H or C of the V_1 complex. To study protein-protein interaction of these constructs of subunit *a* and to get the diffractable quality crystals, these subunit *a* constructs were cloned using PCR method by direct amplification from genomic DNA of *S. cerevisiae* as described in methodology section 2.2. The successfully cloned construct proteins were induced to overproduce protein in *E. coli* BL21 (DE3) (Figure 3.19). Subunit $a_{582-649}$, $a_{673-731}$ and $a_{653-727}$ were soluble and have been purified as described in 2.3.4 (Figure 3.21). Since $a_{653-727}$ shows overlapping sequences with $a_{673-731}$ and is compared to $a_{673-731}$ highly expressed and can be purified in high amount, all experiments were focused on $a_{653-727}$, instead of $a_{673-731}$.

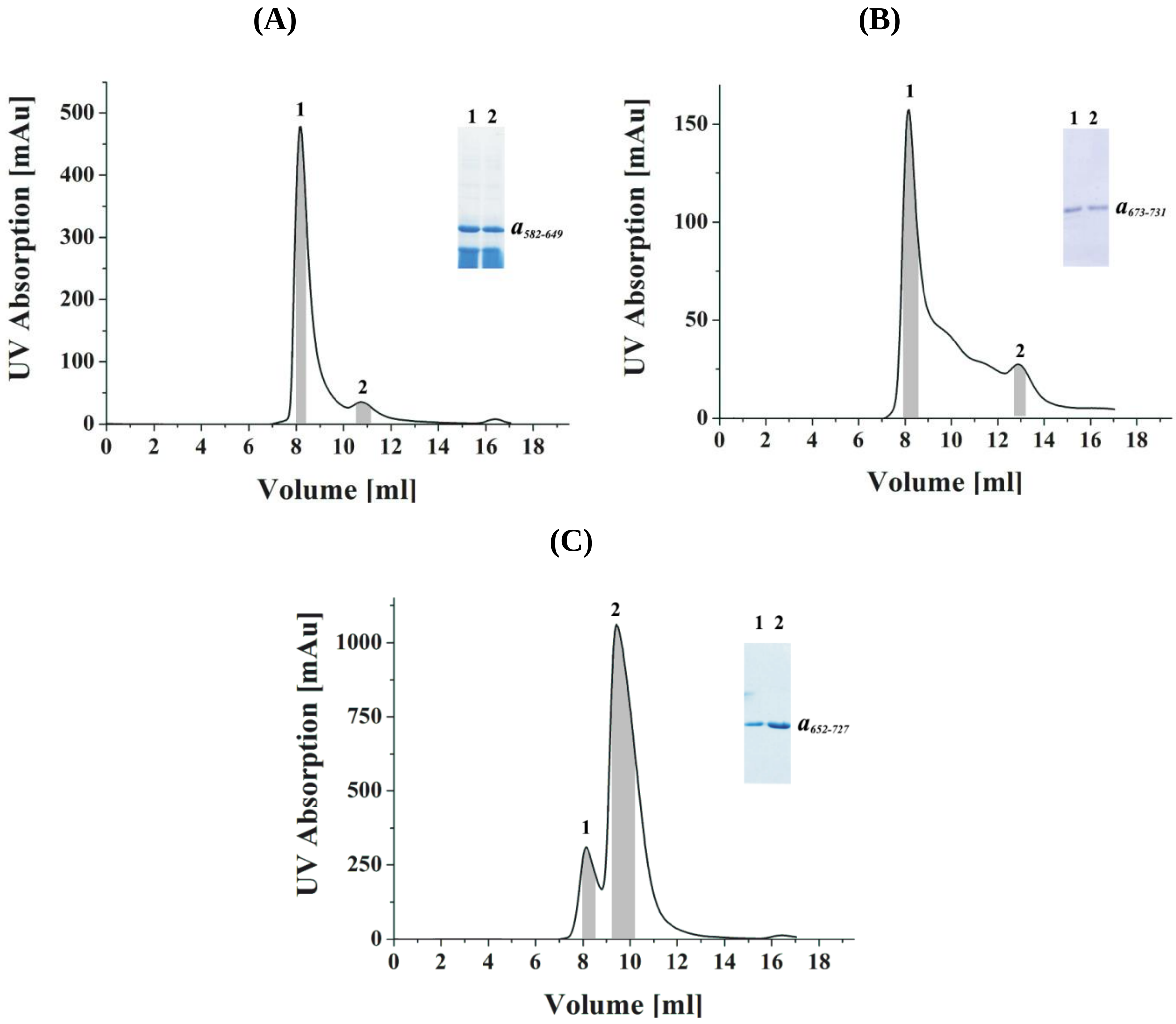

Figure 3.21: Size exclusion chromatography of subunit *a* constructs from *S. cerevisiae*. *(A)* $a_{582-649}$, *(B)* $a_{673-731}$ and *(C)* $a_{653-727}$, all three purifications were started on Ni^{2+}-NTA resin and subsequently followed on Superdex 75 column using buffer (50 mM Tris/HCl, pH 8.5, 500 mM NaCl, 5 mM EDTA). Inserted section in figure is the respective SDS gel from elution peaks 1 and 2 after Superdex 75 (lane 2) of the corresponding construct.

3.3.2 Secondary structure content of subunit $a_{582\text{-}649}$ and $a_{653\text{-}727}$

Secondary structure of $a_{582\text{-}649}$ and $a_{653\text{-}727}$ were assessed by CD spectroscopy from 190 to 260 nm (Figure 3.22). According to the maximum at 192 nm and minima at 208 and 222 nm, both constructs reveal α-helical features. The resulting average secondary structure composition of $a_{582\text{-}649}$ was 45% α-helix, 14% β-sheet and 41% random coil. In case of $a_{653\text{-}727}$, 37% α-helix and 63% random coil were identified.

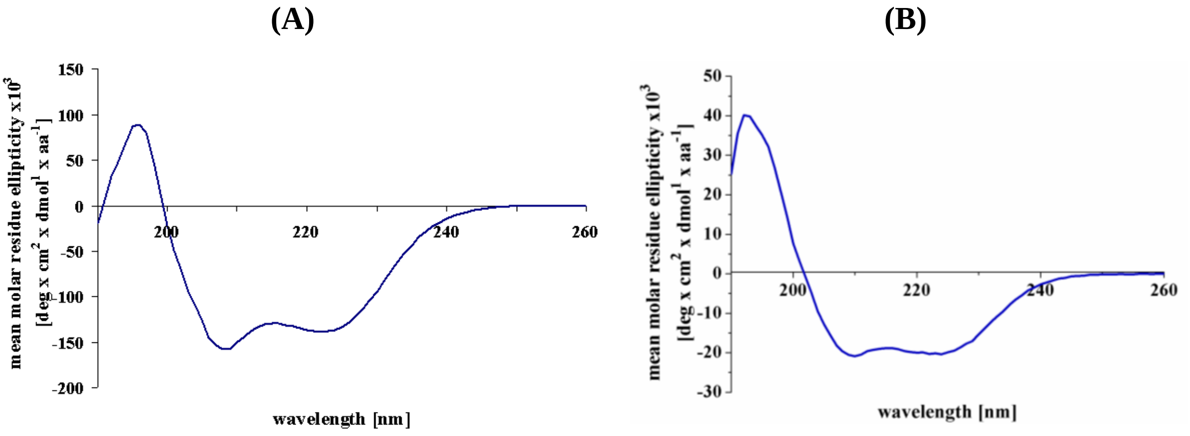

Figure 3.22*: Far UV-CD spectrum of subunit $a_{582\text{-}649}$ (A) and $a_{653\text{-}727}$ (B).*

3.3.3 Crystallisation of subunit $a_{653\text{-}727}$ from *S. cerevisiae*

Crystallisation of construct $a_{653\text{-}727}$ was performed to obtain the three-dimensional structure. Pure subunit $a_{653\text{-}727}$ was used to set up crystallisation trials. The Hampton Research crystal screen HR-110 and HR-112 and Emerald biosystems Wizard screen 1 and Wizard screen 2 were used for initial screening, with a protein concentration of 4 – 16 mg/ml and 2 µl droplets per well in hanging drop plates. Initially, several kinds of needles were seen in Hampton research crystal screen 1 and Emerald biosystems Wizard screen 2 (Figure 3.23).

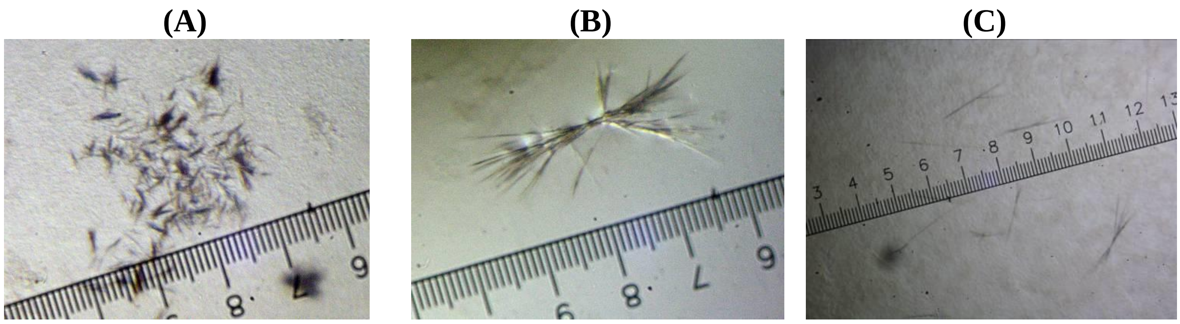

Figure 3.23: Selected pictures of initial $a_{653\text{-}727}$ needles *(A)* Formation of $a_{653\text{-}727}$ needles in the condition of 0.2 M $MgCl_2$, 0.1 M Hepes, pH 7.5, 30% iso-propanol at 18 ºC. *(B)* Formation of $a_{653\text{-}727}$ needles in the condition of 0.2 M $MgCl_2$, 0.1 M Hepes, pH 7.5, 30% iso-propanol at 25 ºC. *(C)* Formation of $a_{653\text{-}727}$ needles in the condition of 0.2 M $MgCl_2$, 0.1 M cacodylate, pH 6.5, 10% PEG3000.

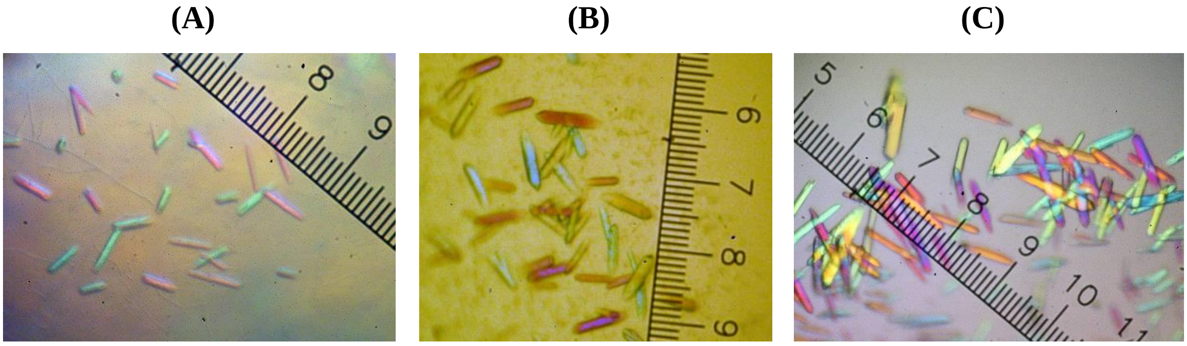

Figure 3.24: Crystal pictures of $a_{653\text{-}727}$ after temperature optimisation to 25 ºC. Formation of $a_{653\text{-}727}$ crystals in the condition of 0.2 M $MgCl_2$, 0.1 M cacodylate, pH 6.5, 15% PEG3350 by *(A)* with 5 mg/ml *(B)* with 6 mg/ml *(C)* by paraffin oil.

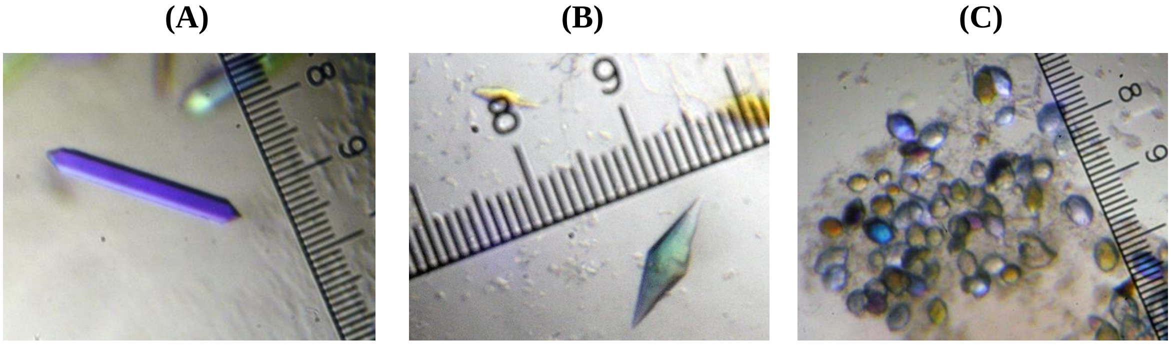

Figure 3.25: Selected pictures of $a_{653\text{-}727}$ crystals using Hampton research additive screen. Crystallisation drops were done in the condition 0.2 M $MgCl_2$, 0.1 M cacodylate, pH 6.5, 15% PEG3350 at 25 °C. *(A)* by adding of butandiol (4%). *(B)* by adding of sucrose (3%). *(C)* Condition of crystallisation drop is 0.01 M $MgCl_2$, 0.1 M Hepes pH 7.0, 15% PEG3350 and 5 mM $NiCl_2$.

Optimisation of these conditions was done by varying the precipitant and salt concentration, changing buffer or pH in grid screens, and changing temperatures. This resulted in the formation of small crystals in a condition containing 0.2 M $MgCl_2$, 0.1 M cacodylate, pH 6.5, 15% PEG3350 (Figure 3.24). Numerous tiny crystals were observed after quick nucleation. These crystals were small in size (0.17 mm x 0.07 mm x 0.01 mm) and not diffracting in the in-house X-ray machine (Rigaku). Additional optimisation was performed with vary protein concentration, replacement of salt and adding of paraffin oil. These resulted in little improvements in the size of the crystals (Figure 3.24C). Attempts were also made by using additional Grid screens and Additive Screen™, besides micro- and macro-seeding at various steps (Figure 3.25). Nonetheless, crystal growth at 25 ºC and various protein concentrations resulted in bigger crystals (Figure 3.26). First, crystals diffracted to 4-5 Å (Figure 3.26) in the in-house machine (Rigaku). The diffraction pattern is not uniform and indicates an anisotropic pattern. After indexing the diffraction data of ten diffraction images of different angles by HKL2000 suite program [176], $a_{653\text{-}727}$ showed high unit cell parameters (a = 545 Å, b = 177 Å, c = 295 Å), indicating that they are not single crystal and twinned. Diffraction spots are not in line and interfering or overlapping with other spots in the same image. Therefore, a series of optimisations were made by varying different parameters and still under progress. However, additional conditions in different temperature and pH have to be optimised in future experiments. Moreover, crystallisation conditions in sitting drop method have to be set up as well.

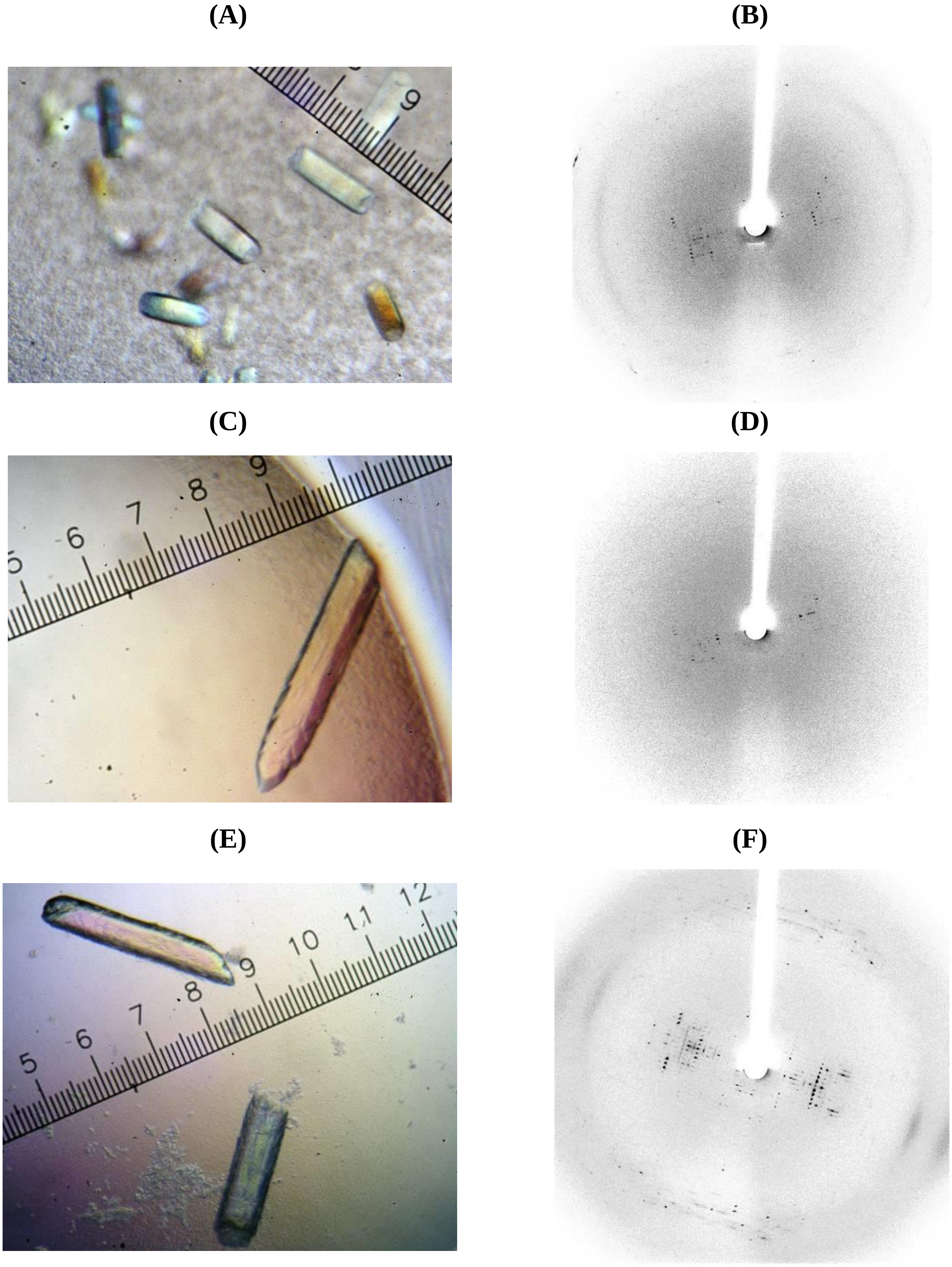

Figure 3.26: Selected pictures of $a_{653\text{-}727}$ crystals with different protein concentration and its corresponding diffraction pattern. Crystal drops were set up in the condition 0.2 M $MgCl_2$, 0.1 M cacodylate pH 6.5, 10% PEG3350 at 25 °C. *(A)* Crystallisation drop with 10 mg/ml *(C)* with 16 mg/ml. *(E)* with 7 mg/ml are showing diffraction pattern respectively to *(B)* 10 mg/ml *(D)* 16 mg/ml and *(F)* with 7 mg/ml.

3.4 The open conformation of Alkyl Hydroperoxide Reductase subunit F (AhpF) from *E. coli* at 2 Å resolution using X-ray crystallography

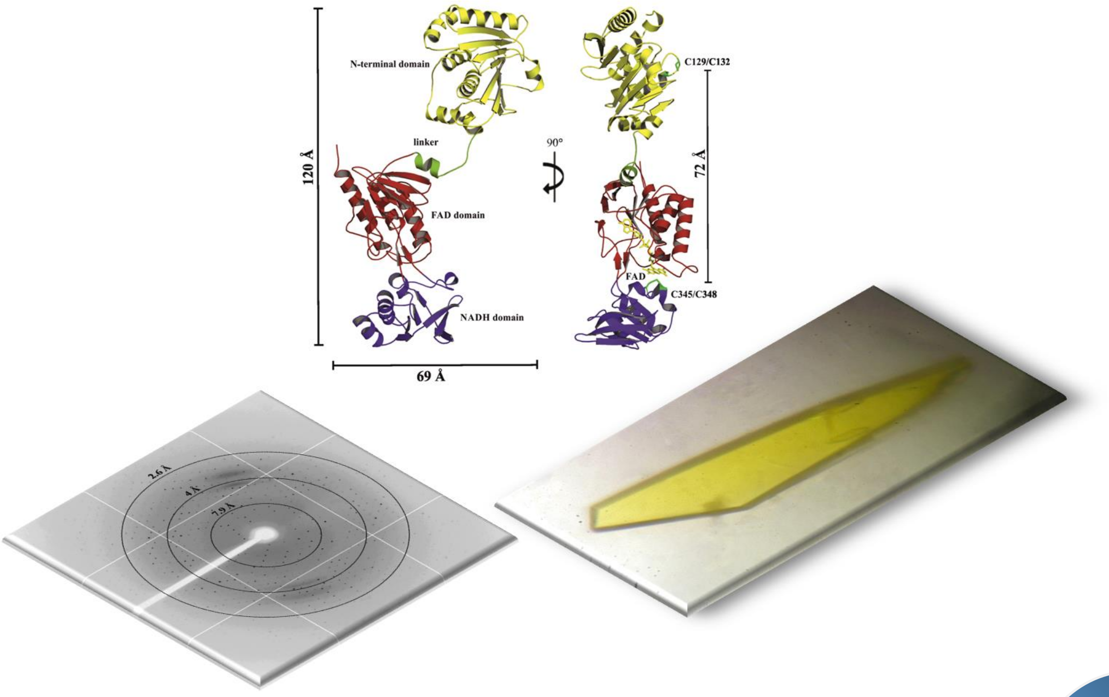
N-terminal domain
linker
FAD domain
NADH domain
120 Å
69 Å
90°
C129/C132
72 Å
FAD
C345/C348
2.6 Å
4 Å
7.9 Å

3.4.1 Alkyl Hydroperoxide Reductase system against oxidative stress

The mechanism for cell survival under oxidative stress has not yet been fully understood. An adaptive defence against reactive oxygen species (ROS) is characterised in *E. coli*, the OxyR protein, which is a transcription factor that induces the expression of AhpR under level of 0.1 µM H_2O_2 [4-7], to ensure a quick response when H_2O_2 concentration rises higher than the basal level, 20 nM [111, 121]. *E. coli* cells trapped in phagosomes of eukaryotic cells encounter ROS, a H_2O_2 concentration that is high enough to boost the intracellular H_2O_2 concentration of the *E. coli* cell [108-110, 118]. As a response to oxidative stress, the global oxidative stress activator OxyR induces the transcription of the AhpR genes, *ahpC* and *ahpF* [123]. The corresponding proteins to the *ahpF* and *ahpC* genes are the 57 kDa flavoprotein (AhpF) and 21 kDa protein (AhpC), which lacks a chromophoric cofactor [126]. It has been shown that the overexpression of both AhpR proteins reduces the frequency of spontaneous mutants in *oxyR* deletion mutant under oxidative stress [122]. Hence, there is a great interest to investigate the structure and functional mechanism of both AhpF and AhpC, since superoxide and hydrogenperoxids are potential sources to damage all macromolecules leading to protein oxidation, lipid peroxidation and DNA damages, including deamination of bases[4-7]. New insights into the mechanism of the AhpR system may not only provide further information for anti-microbial targets, but also a step closer against ROS.

3.4.2 Production and purification of AhpF from *E. coli*

In order to accumulate pure *E. coli* AhpF, the affinity chromatography method, Ni^{2+}-NTA was used as the first purification step (Figure 3.27). Afterwards the ion-exchange chromatography column Resource™ Q (GE Healthcare) was used to clear the remaining impurities, of which details are described in section 2.3.7. Pure *E. coli* AhpF is shown in SDS-PAGE of Figure 3.27. In order to improve the purity and monodispersity of AhpF for crystallisation, an additional gel filtration step using Superdex 75 column was applied. AhpF eluted as a single peak at 9 ml column volume that corresponds to dimer conformation of AhpF (Figure 3.27C). Isolated *E. coli* AhpF was applied onto an SDS-PAGE and it showed high purity of the protein (Figure 3.27C). To confirm the monodispersity of AhpF, dynamic light scattering (DLS) was carried out using Malvern Zetasizer Nano ZS spectrophotometer as described in section 2.7 (Figure 3.28A). After 60 s equilibration time, the backscattering at 173° was detected for AhpF revealing a diameter of 9.4 nm and a molecular weight of 126.5 kDa ± 14.8 kDa, which is in line with size exclusion chromatography, suggesting a dimer conformation of AhpF (Figure 3.28A). Moreover, the DLS profile of *E. coli* AhpF revealed monodispersity of 11.7 %, which is suitable for crystallisation studies. To confirm the presence of AhpF, western blot of purified AhpF has been performed for N-terminal sequencing analysis using Edman degradation method (ABI Procise® 494 Protein Sequencer). The protein sequencing result of MLDTNMKTQLKA confirmed the presence of *E. coli* AhpF in solution.

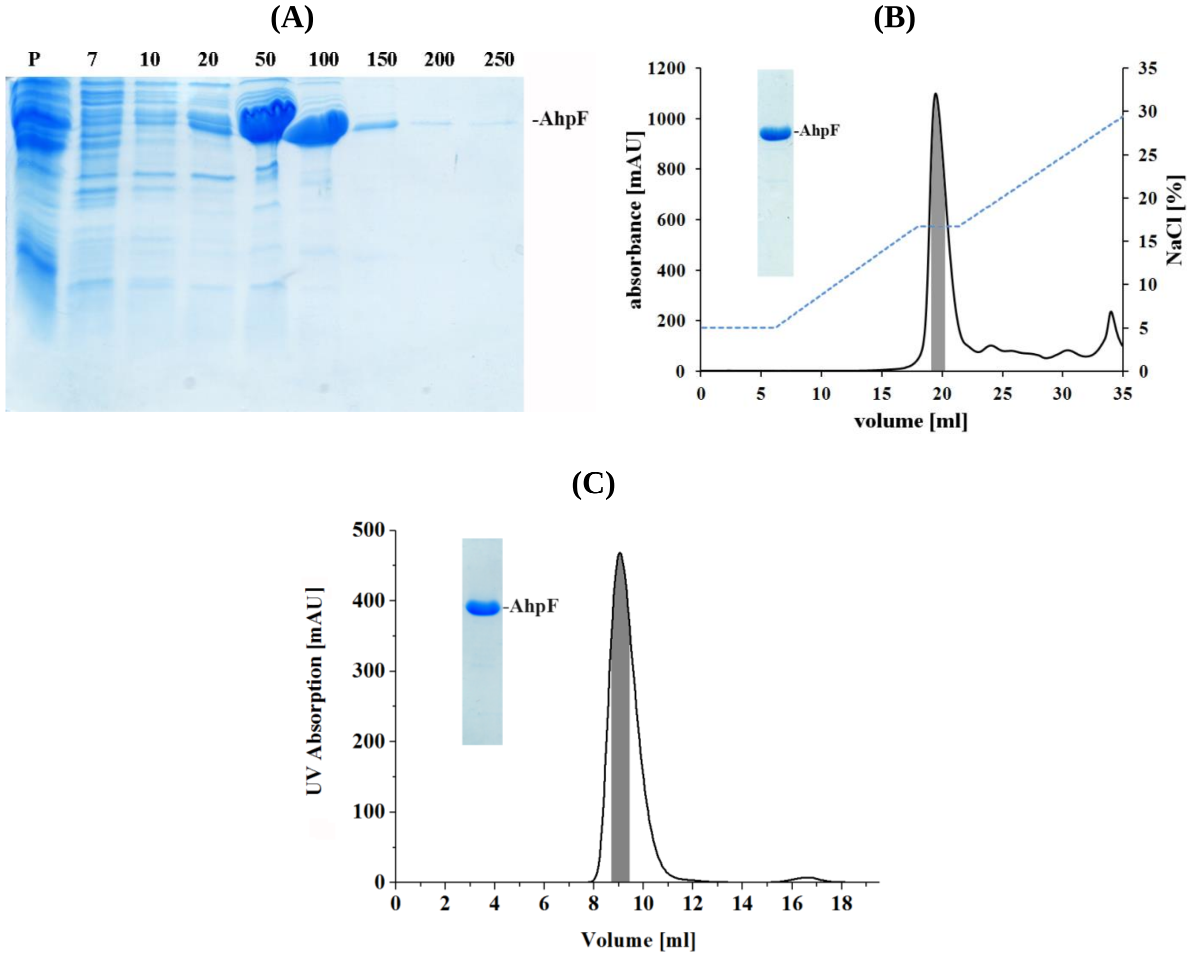

Figure 3.27: Purification of *E. coli* AhpF *(A)* The purification was performed in buffer 50 mM Tris/HCl, pH 7.5, 200 mM NaCl using an imidazole step gradient (0 – 250 mM) for elution of Ni^{2+}-NTA bound protein. Fractions from 20 – 100 mM imidazole were pooled together for further purification steps. *(B)* Ion-exchange purification of *E. coli* AhpF. Protein containing fractions of Ni^{2+}-NTA from AhpF were diluted with 50 mM Tris, pH 7.5 to reduce the salt concentration to 50 mM and applied onto the anion exchange column (Resource Q, 6 ml) for additional purification step. Protein bound to column media was eluted using a linear gradient (---) of buffer A (50 mM Tris/HCl, 50 mM NaCl, pH 7.5) and B (50 mM Tris/HCl, 1 M NaCl, pH 7.5) resulting in the protein separation as a sharp peak, containing pure protein (shaded peak area volume was pooled). SDS-PAGE section shows 1 µl of pure eluted protein applied on a 17% SDS gel. *(C)* AhpF eluted as single peak at 9 ml in Superdex 75 column that indicates AhpF in a dimer formation.

Secondary structure of AhpF was determined by CD spectroscopy, from 190 to 260 nm (Figure 3.28B). The resulting average secondary structure composition was 19 % α-helix, 31 % β-sheet and 50 % random coil.

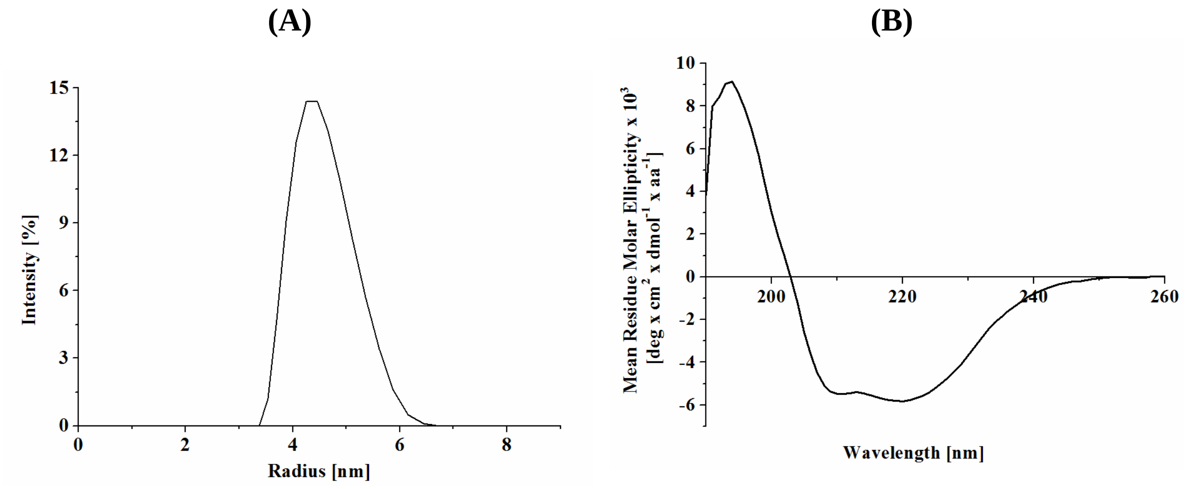

Figure 3.28: Spectroscopic analysis of *E. coli* AhpF. *(A)* Dynamic Light Scattering (DLS) of *E. coli* AhpF reveals a hydrodynamic radius of 4.7 nm, a molecular weight of 126.5 ± 14.8 kDa and a monodispersity of 11.7 %. *(B)* Far UV-CD spectrum of *E. coli* AhpF (—) indicates the formation of α-helical content.

3.4.3 NADH dependent peroxidative activity assay of AhpF from *E. coli*

In order to analyse the catalytic activity of AhpF from *E. coli*, the NADH dependent peroxidase assay was monitored at 340 nm following the decrease in NADH absorbance. Oxidised (NAD^+) and reduced (NADH) forms of this coenzyme revealed a difference in ultraviolet absorption spectra at 340 nm that makes it simple to measure the conversion from NADH to NAD^+ and *vice versa* in peroxidase assay using a spectrophotometer. The decrease in NADH absorbance reflects the electron transfer within AhpF from NADH via FAD to the redox active disulfide C345/C348 at the C-terminal portion and to the N-terminal C129/C132 disulfide centre [139, 143]. During peroxidative activity and reduction of AhpC, electron transfer may occur from AhpF to AhpC via the redox centres C129/C132 of AhpF to the disulfide centre C47/C166 of AhpC [140]. To illustrate the NADH oxidation, the peroxidase assay was measured with multi wavelength scanning ranging from 280-540 nm at two different time scale. The assay was carried out as described in section 2.8. All the reaction mixtures were added in the reaction buffer except for NADH, which was added lastly to start the reaction. The peroxidase assay was performed with AhpF alone (red lines), AhpC alone (green lines) and AhpF/AhpC together (black lines) (Figure 3.29). The absorbance of 300 µM NADH at reaction start (0 min) was 1.7 for both AhpF alone and AhpC alone, whereby AhpF/AhpC together revealed a starting absorbance of 1.6 that indicates high catalytic activity (Figure 3.29). The maximum NADH oxidation activity was shown indeed in the presence of AhpF/AhpC together (Figure 3.29, black line) and the reaction was saturated at 6 min with an absorbance of 0.29 (Figure 3.29, black dashed line). The NADH oxidation activity of *E. coli* AhpF alone, in the absence of *E. coli* AhpC, revealed an absorbance of 0.82 which indicates much lesser NADH oxidation compared to AhpF/AhpC together (Figure 3.29, red dashed lines).

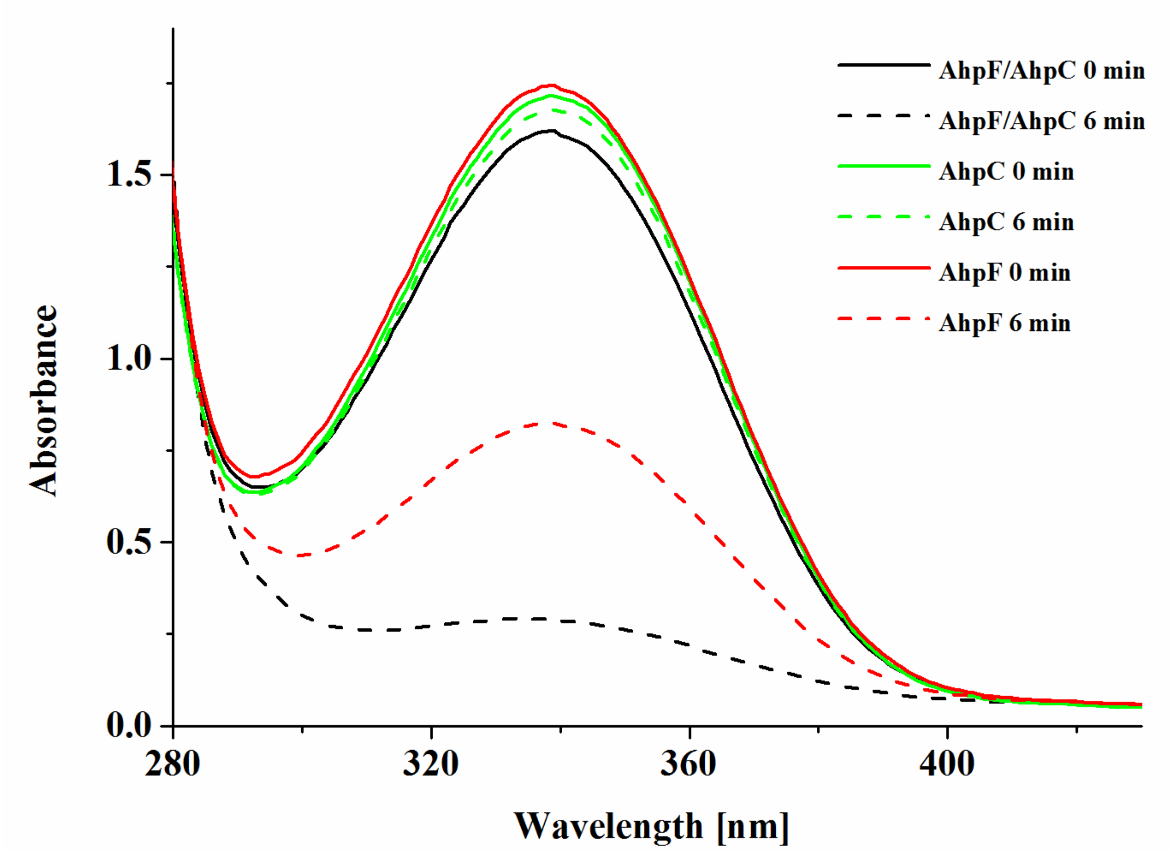

Figure 3.29: NADH dependent peroxidase activity of *E. coli* AhpF. The absorption of NADH (300 µM) at 340 nm was observed in a range from 280-540 nm in presence of 1 µM *E coli* AhpF and/or AhpC, 1 mM hydrogen peroxide, 100 mM ammonium sulphate and 0.5 mM EDTA in 50 mM phosphate buffer, pH 7.0. NADH oxidation activity of AhpF in presence of AhpC is depicted in black line and the reaction was saturated at 6 min (black dashed line). The NADH oxidation activity of *E. coli* AhpF alone was also observed revealing an absorbance of 0.82 after 6 min (red dashed line). To analyse the background reaction, a mixture of AhpC alone was taken as a control, indicated as green line at reaction start and green dashed line after 6 min.

To analyse the background reaction, a mixture of AhpC alone, in the absence of AhpF, was taken as a control (Figure 3.29, green lines), showing no NADH oxidation after 6 min (Figure 3.29, green dashed lines). Hence, NADH oxidation occurs only in the presence of AhpF, while AhpC facilitate this reaction.

3.4.4 Low resolution structure of *E. coli* AhpF in solution

In order to get structural insights of AhpF in solution, the first low-resolution structure has been solved using SAXS. SAXS patterns of AhpF were measured by Prof. Dr. Manfred Roessle as described earlier in Material and Methods section 2.9. With the help of Dr. Malathy Sony S. Manimekalai the model was built using GASBOR software [185]. The final scattering curve reflects a monodispersed protein in solution (Figure 3.30A). The low angles of the Guinier plot highlight a good data quality and no protein aggregation. The *E .coli* protein AhpF in solution reveals a radius of gyration R_g of 38.6 ± 1.3 Å and a maximum dimension D_{max} of 135 ± 3 Å (Figure 3.30B). The molecular mass of *E. coli* AhpF was calculated as 75 ± 2 kDa based on the value of forward scattering obtained from bovine serum albumin (BSA; 66.4 ± 2 kDa). Deviation in molecular mass estimation can occur for elongated proteins, since the reference protein BSA is a globular protein. The distance distribution function *ρ(r)* showed a single peak with a maximum in *p(r)* at 38 Å (Figure 3.30B) and an elongated tail from 84 Å to 126.6 Å, which is the typical pattern for an extended protein.

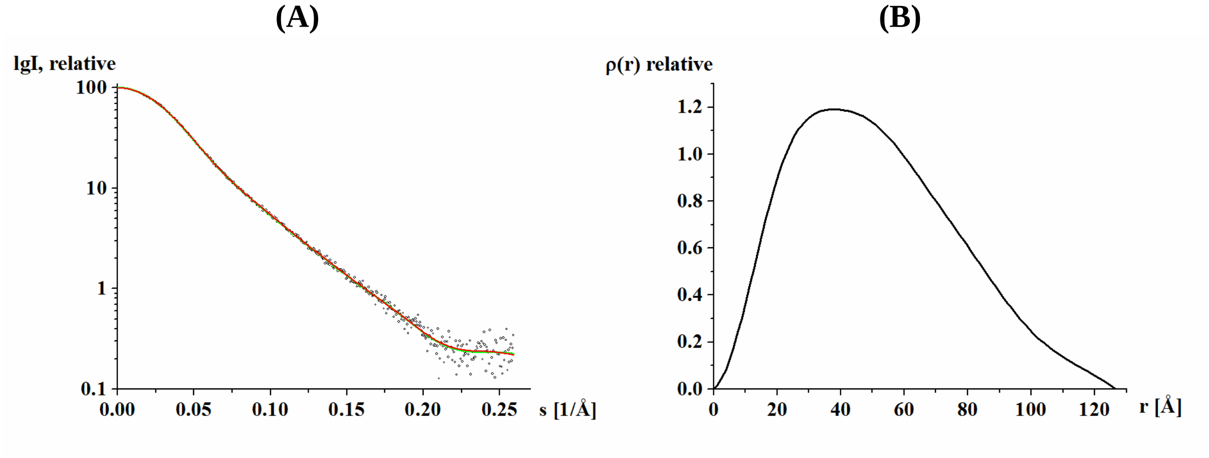

Figure 3.30: Small angle X-ray scattering pattern (●) and its corresponding fitting curves (—; *green*: experimental, *red*: calculated) *(A)*. The curves of *E .coli* AhpF are displayed in logarithmic unit for clarity. (*B*) Distance distribution functions of AhpF.

The solution structure of *E .coli* AhpF was generated *ab initio* using GASBOR software [185] from the scattering patterns (Figure 3.30A). The calculated fit, coloured in red of the AhpF shape accommodates well into the experimental data of the entire scattering curve (Figure 3.30A). The deviation of the calculated fit to the experimental fit, which is coloured in green, has a χ^2 value of 1.13 (Figure 3.30A). The protein shape with the lowest χ^2 is depicted in Figure 3.31, which appears to be an oval shape conformation at one side and on its 90° view, a flat and elongated molecule (Figure 3.31). The measured maximum length of the shape is about 125.7 Å, whereas the width is around 80.2 Å. The solution structure indicates the flexible- and dynamic-state of a protein, whereas the rigid crystal structure reveals a structure in solid-state. Hence the overall shape of AhpF solution structure appears to be broader with three prominent bulges (Figure 3.31). The *E. coli* AhpF shape reveals three distinct domain features, lower domain with dimensions of 31.1 x 36.2 Å, the middle domain with 52.5 x 31.2 Å and upper domain with 44.6 x 61.8 Å. The three bulges in the shape correlate with the different AhpF domain, namely the N-terminal domain, the linker segment, FAD domain as well as NADH domain (Figure 3.31). The 90° view reveals a flat and stretched molecule, indicating the linker segment sit at the narrow region in the middle of the shape and connects the N-terminal domain to the FAD domain (Figure 3.31).

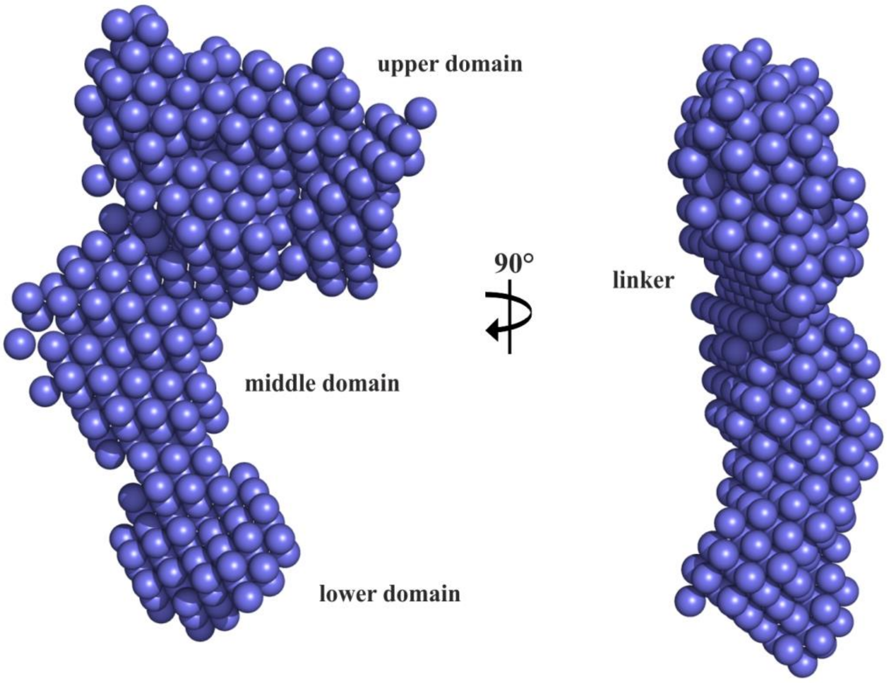

Figure 3.31: Solution structure of *E. coli* AhpF generated by Dammin software [213]. The shape of *E .coli* AhpF reveals an oval conformation with three prominent bulges, indicating the three domains, NADH domain, FAD domain and N-terminal domain. The 90° view highlights rather a flat and stretched molecule, suggesting the linker segment at the narrow region in the middle of the shape.

3.4.5 Crystallisation and data collection of AhpF crystals from *E. coli*

Initial crystallisation trials of *E .coli* AhpF have been set up by using different crystallisation screens from Hampton Research, Molecular Dimensions and Emerald Biosystems. Small crystals were observed under the condition 0.1 M Hepes, pH 7.5 and 20% (w/v) PEG 10 000 and needle bundles in 2 M ammonium sulfate, 100 mM Na-HEPES, pH 7.5 and 2% (v/v) PEG 400 in hanging drops method. The crystal screens were set up by mixing 1 µl of the purified AhpF (3-10 mg/ml) in buffer B (50 mM Tris/HCl, pH 7.5, 150 mM NaCl) with 1 µl of the precipitant solution and incubated at 18 °C. Both conditions have been optimised simultaneously. The small crystals that were observed under the first condition 0.1 M Hepes, pH 7.5 and 20% (w/v) PEG 10 000 appeared unfrequently and rarely in 12 weeks that may due to a low nucleation rate. Hence reproducing these crystals were difficult under this condition. Since the crystallisation condition did not comprise of any salt, optimisation by adding different salt, using StockOptions^{TM} Salt from Hampton research has been performed, which resulted in no significant improvement in crystal growth. Furthermore, crystallisation trials with varying protein concentrations and additional grid screens of precipitant concentration and Additive Screen^{TM}, micro- and macro-seeding at various steps have been carried out with no significant improvement of crystal growth as well.

Since nucleation was a crucial step, Naomi's Nucleants^{TM} from Molecular dimensions has been used to facilitate the crystal formation. The addition of a single nucleant grain into the crystallisation drop 24 hours after drop setup has shorten the crystallisation time from 12 weeks to 1 week (Figure 3.32). Also the numbers of crystals were increased from 2-3 crystals to more than a dozen of crystals in each drop, showing these nucleant grains facilitate crystal formation. However, the size of crystal under this crystallisation condition still has to be further optimised.

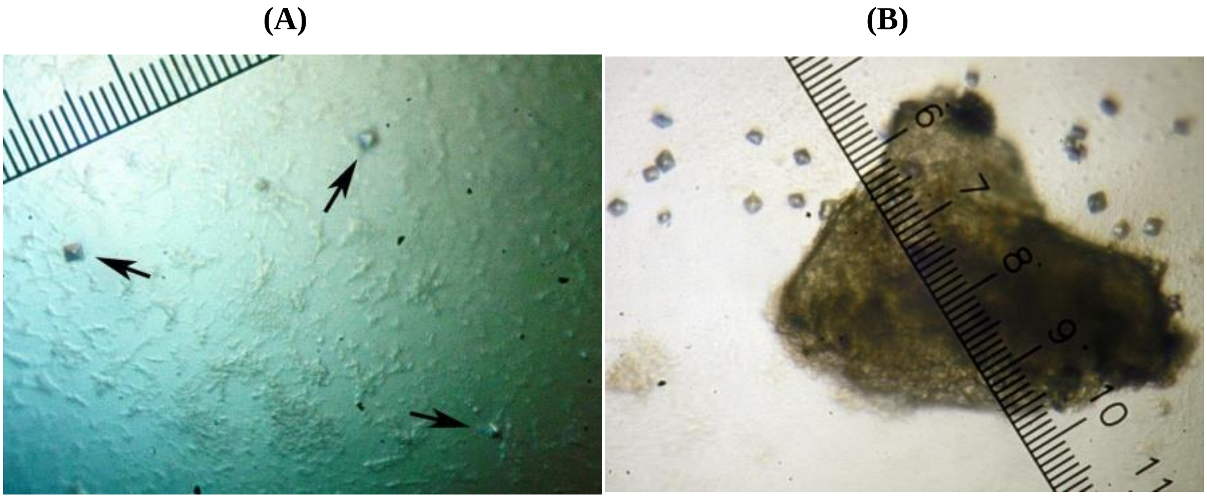

Figure 3.32: Optimisation of *E. coli* AhpF crystals. (*A)* Initial edge truncated octahedron shaped crystals, highlighted with black arrow, were observed after 12 weeks with 10 mg/ml protein concentration in Hampton research crystal screen 2, condition 38, containing 100 mM Na-HEPES, pH 7.5 and 20% (v/v) PEG 10000. *(B)* The addition of Naomi's Nucleant^{TM} has facilitated the crystallisation to 1 week with high number of crystals.

Nonetheless, the simultaneous optimisation of the condition 2 M ammonium sulfate, 100 mM Na-HEPES, pH 7.5 and 2% (v/v) PEG 400 revealed larger crystal, whereupon more attention had been focused to this condition. Initial cluster bundles were seen in crystallisation drops with 10 mg/ml protein concentration in Hampton research crystal screen 1, condition 39 (Figure 3.33A). Hence conditions were optimised by changing precipitant concentration, protein concentration, salt concentration and pH. AhpF formed needle bundles in 2 M ammonium sulfate, 0.1 M Na-HEPES (pH 7.0), 2.5% (v/v) PEG 400 at 18 °C (Figure 3.33B). The formation of two dimensional, flake-like crystal bundles were obtained by increasing the incubation temperature to 25 °C. The plate shape crystals were observed after quick nucleation in comparison to the other crystallisation condition, Hampton research crystal screen 2, condition 38 (Figure 3.32, Figure 3.33C).

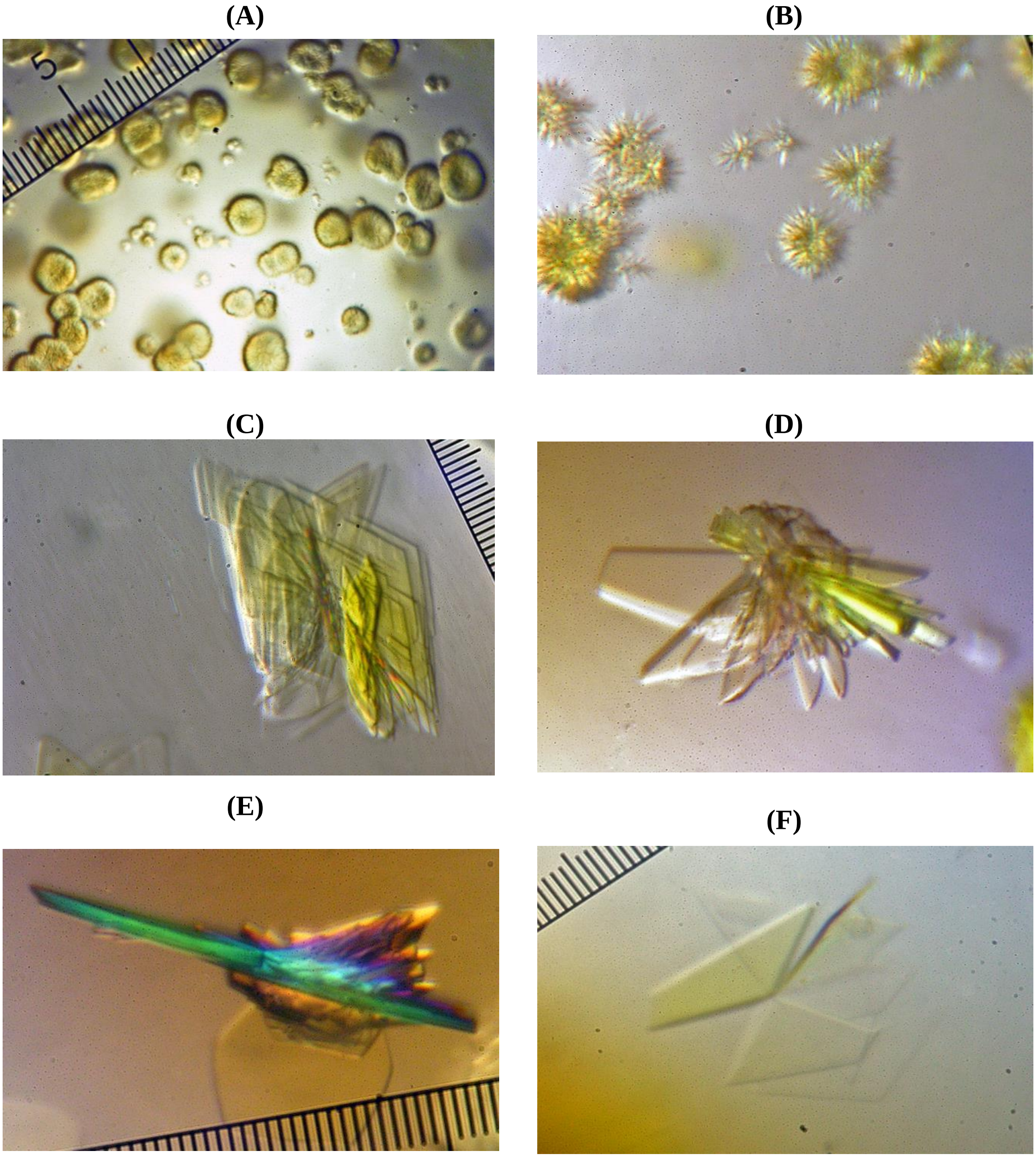

Figure 3.33: Optimisation of *E. coli* AhpF crystals. *(A)* Initial cluster bundles were seen in crystallisation drop with 10 mg/ml protein concentration in Hampton research crystal screen 1, condition 39, which contains 2 M ammonium sulfate, 100 mM Na-HEPES, pH 7.5 and 2% (v/v) PEG 400. *(B)* Conditions were optimised for precipitant concentration, protein concentration, salt concentration and pH. AhpF produces needle bundles in 2 M ammonium sulfate, 0.1 M Na-HEPES (pH 7.0). 2.5% (v/v) PEG 400 at 18 °C. *(C)* Two dimensional, flake like crystal bundles are formed at 25 °C. *(D)* Topview of crystal formation after using Hampton Research Additive Screen^{TM}. The adding to final concentration of 10 mM cadmium chloride initiates the formation of crystal bundles into the third dimension. *(E)* Side view of crystal formation after adding of 10 mM cadmium chloride in polarized light. *(F)* Micro seeding of crystal formation using pre equilibrated drops of 2 mg/ml induced the formation of single crystals, which remain thin in the third dimension.

The adding of final concentration of 10 mM cadmium chloride from Hampton Research Additive Screen^{TM} initiates the formation of crystal bundles into three dimension and the polarisation of light (Figure 3.33D-E). Crystal formation using 2 mg/ml protein concentration and micro seeding using overnight pre equilibrated drops in 2 mg/ml lead to nucleation of 2-3 crystals per drop. The low concentration of protein induces fewer nucleation and slow growth of crystal. Hence the formation of few or single crystals results in further grow into three dimension (Figure 3.33F, Figure 3.35A).

3.4.6 Data collection and structure determination of AhpF from *E. coli*

Suitable crystals with the dimensions of (0.3 x 0.12 x 0.05 mm) were used for data collection. Firstly, AhpF crystals were mounted into crystal loops and subsequently dipped into cryoprotectant solution containing additional 20% (w/v) glycerol to the crystallisation solution and then immediately flash cooled in -170 °C by plunging the crystal into liquid nitrogen (Figure 3.35A). These single frozen AhpF crystals were used for single-wavelength native datasets collection. The measurements were performed together with Dr. Malathy Sony S. Manimekalai on beamline 13B1 at the National Synchrotron Radiation Research Center (NSRRC, Hsinchu, Taiwan), at 140 K (Figure 3.35B). In total, 360° of data were collected with

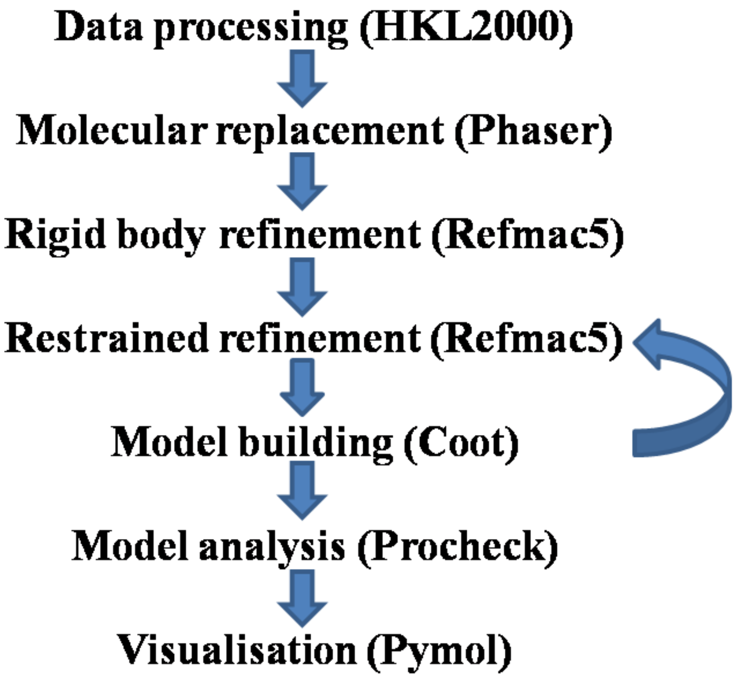
Data processing (HKL2000)
Molecular replacement (Phaser)
Rigid body refinement (Refmac5)
Restrained refinement (Refmac5)
Model building (Coot)
Model analysis (Procheck)
Visualisation (Pymol)

Figure 3.34: Crystal structure determination strategy. Indexing, integration and scaling of collected diffraction data set were carried out in HKL2000 suite program [176]. Molecular replacement were performed for structure determination using PHASER program [179]. For initial rigid body refinement REFMAC5 software was used [177] followed by difference Fourier syntheses calculations. AhpF structure was iterative refined by model building and restrained refinement in a combined manner using the software COOT [181] and REFMAC5 [177]. The 3D structure of the final model was analysed with PROCHECK [183] and for visualisation of AhpF model, PyMOL software were used [175].

10 s per 1° frame using ADSC Quantum 315 CCD detector. The staff at beamline 13B1 (NSRRC) kindly provided technical assistance.

All collected diffraction data sets were indexed, integrated and scaled with HKL2000 suite program and were guided by Dr. Asha M. Balakrishna and Dr. Malathy Sony S. Manimekalai (Figure 3.34) [176]. The crystals belong to monoclinic crystal system with C2 space defined by α, $\gamma = 90^{\circ}$ and $\beta \neq 90^{\circ}$. The cell unit parameter and the molecular weight of *E. coli* AhpF (56 177 Da) were used to analyse the Matthews coefficient and solvent content [214]. The software Matthews_Coef of the CCP4 suite (1994) revealed a solvent content of 59.11 % and Matthews coefficient *Vm* of 3.01, indicating 0.99 AhpF molecule in the asymmetric unit.

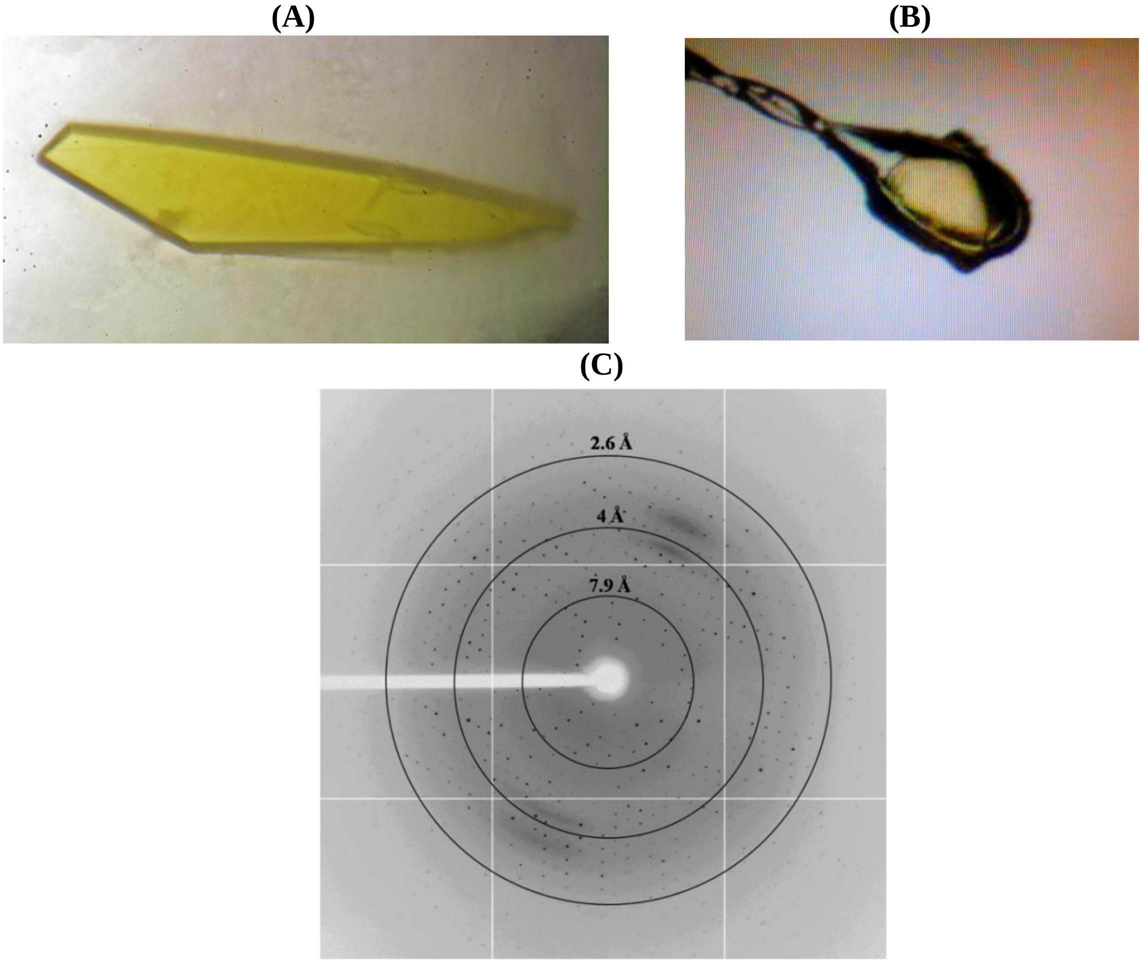

Figure 3.35: Crystallisation and data collection of *E. coli* AhpF crystals. *(A) E. coli* AhpF crystals used for X-ray diffraction were finally obtained by sitting-drop vapour diffusion method under the condition, 2 M ammonium sulfate, 100 mM Na-HEPES, pH 7.5, 2.5 % (v/v) PEG 400 and 10 mM cadmium chloride. The low protein concentration of 2 mg/ml reduced the nucleation time, hence only few and therefore larger sized crystals have been obtained. *(B)* Single frozen crystal of *E. coli* AhpF mounted in crystal loop for diffraction data collection in NSRRC. *(C)* Representative diffraction image of *E. coli* AhpF crystal until 2 Å resolution.

The AhpF crystal structure of *Salmonella typhimurium* (*St*AhpF, PDB 1HYU; [135]) was exploited for initial phasing by molecular replacement using PHASER program (Figure 3.34)

[179] and MOLREP [178]. To validate the quality of the obtained model, two scores were considered, the log-likelihood-gain (LLG) and the Z-score. The LLG indicates the quality of the predicted model in comparison to a random-atom model to the same data. The Z-score judges the signal-to-noise by comparing the LLG values of the predicted model with LLG values for a set of random rotations or translations. Z-score above 5 indicates a possible solution. Initial trial with *St*AhpF resulted in LLG of 102 and Z-score for the fast rotational function (RFZ) of 7.1 and fast translational function (TFZ) of 10.4 in Phaser, which is an acceptable solution [179]. To obtain a good solution for molecular replacement, the LLG has to be above 120. To further improve LLG value as well as the Z-score, *St*AhpF were separated into the N-terminal segment 1-182 aa and C-terminal segment 202-521 aa for model prediction using Phaser [179]. The putative flexible linker segment has been omitted in the model for the molecular replacement.

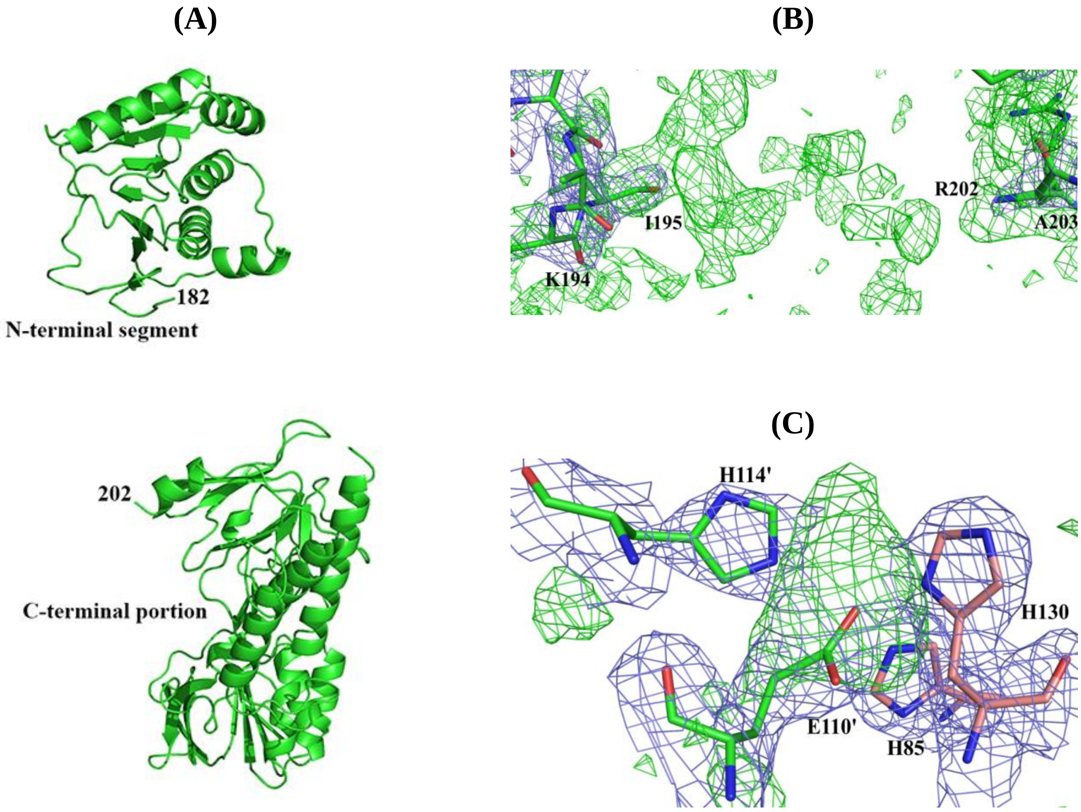

Figure 3.36: Preliminary *E. coli* AhpF crystal structure. *(A)* The preliminary *E. coli* AhpF structure reflects one elongated molecule in asymmetric unit. The linker region is not present in this structure. *(B)* The overlay of F_O–F_C and $2F_O$–F_C maps of AhpF linker region of the preliminary AhpF structure after few rounds of manual refinements. Amino acids were attached to the N-terminal segment according to the green electron density. *(C)* The overlay of F_O–F_C and $2F_O$–F_C maps of AhpF clearly showed the green electron density corresponding to the heavy metal cadmium (Cd^{2+}) used in crystallisation set up.

After separating the N- and C-terminal portion for molecular replacement, the LLG for the N-terminal segment arose to 210 and Z-scores, RFZ and TFZ were 17.7 and 15.6, respectively and the C-terminal part reached a LLG of 452 with Z-scores of RTZ 9.7 and TFZ

29.5, reflecting a very good solution for both segments. The obtained predicted structure was subsequently used for rigid body refinement using the program Refmac5 (Figure 3.34) [177]. Initial rigid body refinements carried out in REFMAC5 software achieved an overall R-factor of 27.15 % and free R-factor of 28.53 %. (Figure 3.34) [177]. The initial structure reflects an elongated molecule.

Data collection statistics

Wavelength (Å)	1.0
Space group	C2
Unit cell parameters (Å)	
a	106.49
b	58.70
c	123.99
$\alpha = \gamma$ (°)	90
β (°)	114.58
Resolution range (Å)	30.0 – 2.0
Solvent content (%)	59.11
Number of unique reflections	47609
I/σ^a	20.41 (2.04)
Completeness (%)	99.7 (98.6)
R merge^b (%)	6.7 (49.6)
Multiplicity	7.3 (6.3)

Table 3.3: Summary of crystallographic data collection for *E. coli* AhpF.
^{a} Values in parentheses refer to the corresponding values of the highest resolution shell (2.07 - 2.00 Å). ^{b} Rmerge = ΣΣi|Ih - Ihi|/ΣΣi Ih, where Ih is the mean intensity for reflection h.

The omitted linker region, residues 181-201 was not present in the structure (Figure 3.36). The overlay of F_O–F_C and $2F_O$–F_C maps of *E. coli* AhpF clearly showed the green electron density corresponding to amino acids of the linker region and the heavy metal cadmium (Cd^{2+}) used for crystallisation set up (Figure 3.36BC). Iterative cycles of model building and refinement were performed in a combined manner using the programs COOT [181] and REFMAC5 [177] of the CCP4 suite (1994) (Figure 3.34). Each cycle of model building allowed the attachment of an additional amino acid to its correspond green density of the linker region (Figure 3.36B). After manual refinement and model building of AhpF main chain as well as side chain, 484 water molecules, 8 sulfates, 8 PEG molecules, 13 glycerol and 2 Tris molecules were added into the corresponding green electron density of the $F_O–F_C$ map. The overall R-factor as well as free R-factor reached 14.14 % and 18.45 %, respectively (Table 3.4). The final model was validated with PROCHECK [183], and the software PyMOL was used for visualisation of AhpF model [175]. For structural comparison analysis, the program SUPERPOSE [208] was applied.

3.4.7 Crystal structure of AhpF from *E. coli*

The crystal structure of AhpF from *E. coli* (*Ec*AhpF) reveals one molecule in an asymmetric unit and appears to be in an open conformation with the dimension of 120.5 Å x 58.9 Å x 44.2 Å (Figure 3.37). All 521 residues of *Ec*AhpF were modelled clearly into the 2Fo-Fc electron density map, except for few residues in the loop region (residues 198-201), which have high temperature factors (>70 $Å^2$ for C_α atoms). The overall *Ec*AhpF structure consists of four distinct regions: the N-terminal domain (NTD, residues 1-196), the linker segment (residues 197-209), the FAD domain (residues 210-327 and 450-521), and the NADH/SS domain (residues 328-449). Overall, three redox centres are present in the structure, the FAD in the FAD domain, C345/C348 in the NADH/SS domain as well as C129/C132 in the NTD. The redox-active disulfide (C345/C348) is in close distance to flavin, but it is 72 Å apart from the C129/C132 in the NTD (Figure 3.37).

The C-terminal portion of *Ec*AhpF (residues 210-521) includes the FAD- and NADH/SS domain that is homologous to the Thioredoxin Reductase (TrxR). Similarly, both NADH/SS and FAD domains consist of a central five-stranded β-sheet conformation, sandwiched on one side by a smaller three-stranded β-sheet, and on the other side by three α-helices in the FAD domain and two α-helices in the NADH/SS domain (Figure 3.37).

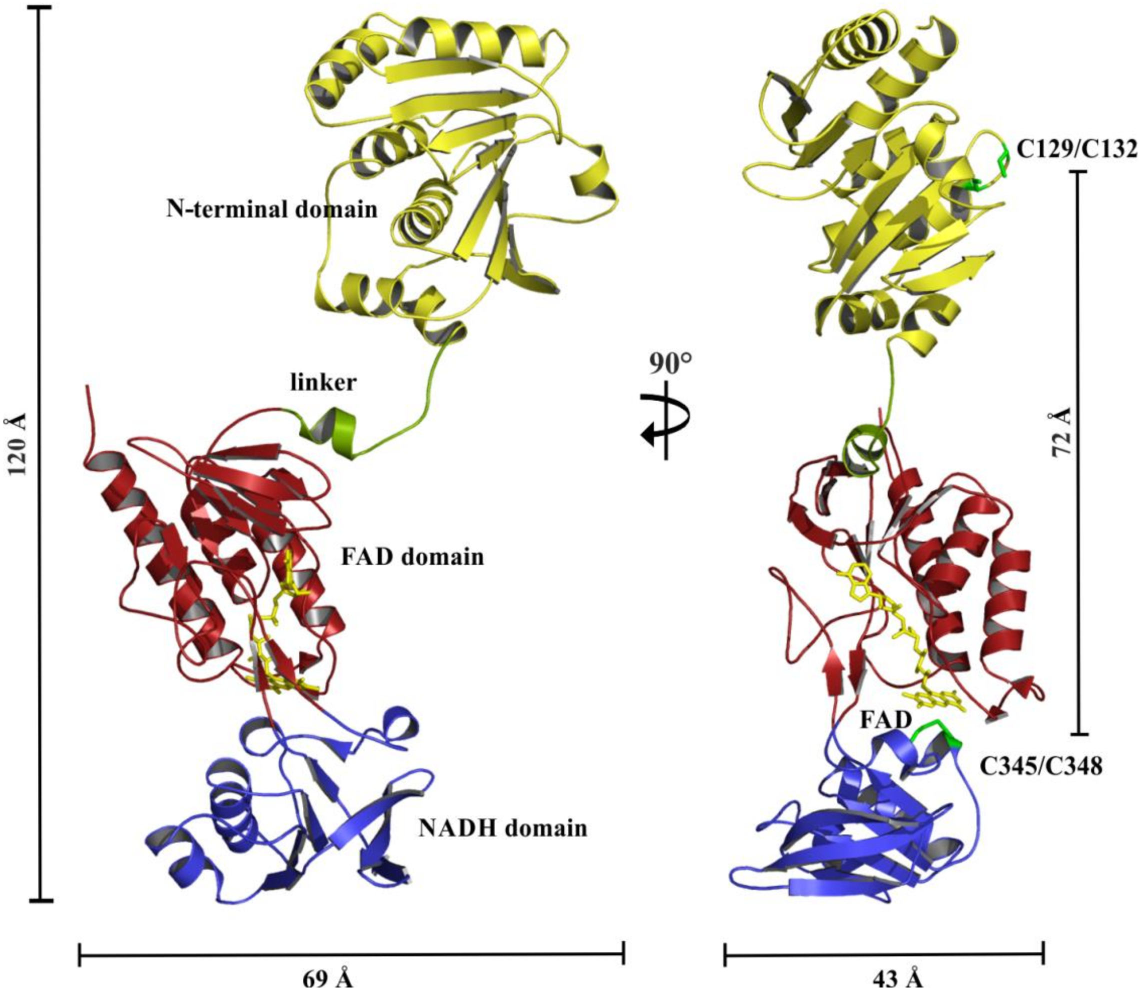

Figure 3.37: Cartoon view of the *E. coli* AhpF crystal structure coloured by domain. The N-terminal domain (yellow) harbours its redox-active dithiol at the residues C129 and C132 (bright green) and is joined via the linker segment (green) to its C-terminal portion, the FAD domain (red) and the NADH/SS domain (blue). The NADH/SS domain comprised of its redox active disulfide at C345/C348 (bright green). In 90° view the flavin cofactor in the FAD domain is depicted clearly in yellow in the centre of the AhpF structure. Both redox active disulfides C129/C132 as well as C345/C348 are highlighted in green colour.

The FAD domain contains a FAD binding site. The cofactor FAD is present in this structure and accommodates well into its binding pocket (Figure 3.37). The NADH/SS domain harbours the NADH binding site as well as the redox-active disulfide (C345/C348) near the flavin (Figure 3.38A). In this crystal structure the redox active NADH (or NAD^+) is not found in its binding pocket in the NADH/SS domain. Cysteinyl residues within CXXC structural motif, which is also common in thioredoxin and TrxR, form the redox-active disulfide C345/C348 in the C-terminal portion as well as C129/C132 in the NTD of *Ec*AhpF. The CXXC motif of the NADH/SS domain (C345/C348) is located closely to the flavin and adapts a short α-helix with a right-handed hooked disulfide conformation (Figure 3.38A). The shortest distance of the CXXC motif to flavin is 3.1 Å, which is the distance between C348 and the isoalloxazine ring of the FAD (Figure 3.38A). The distance between C345 and the C-4-X isoalloxazine is 4.9 Å. The residues C345 and C348 of the NADH/SS domain in this AhpF structure are in an oxidised state (Figure 3.38B). The disulfide bridge between C345 and C348 is clearly formed and its corresponding electron density is visible (Figure 3.38B). The distance between the two sulphur at C345 and C348 is 2.1 Å (Figure 3.38B).

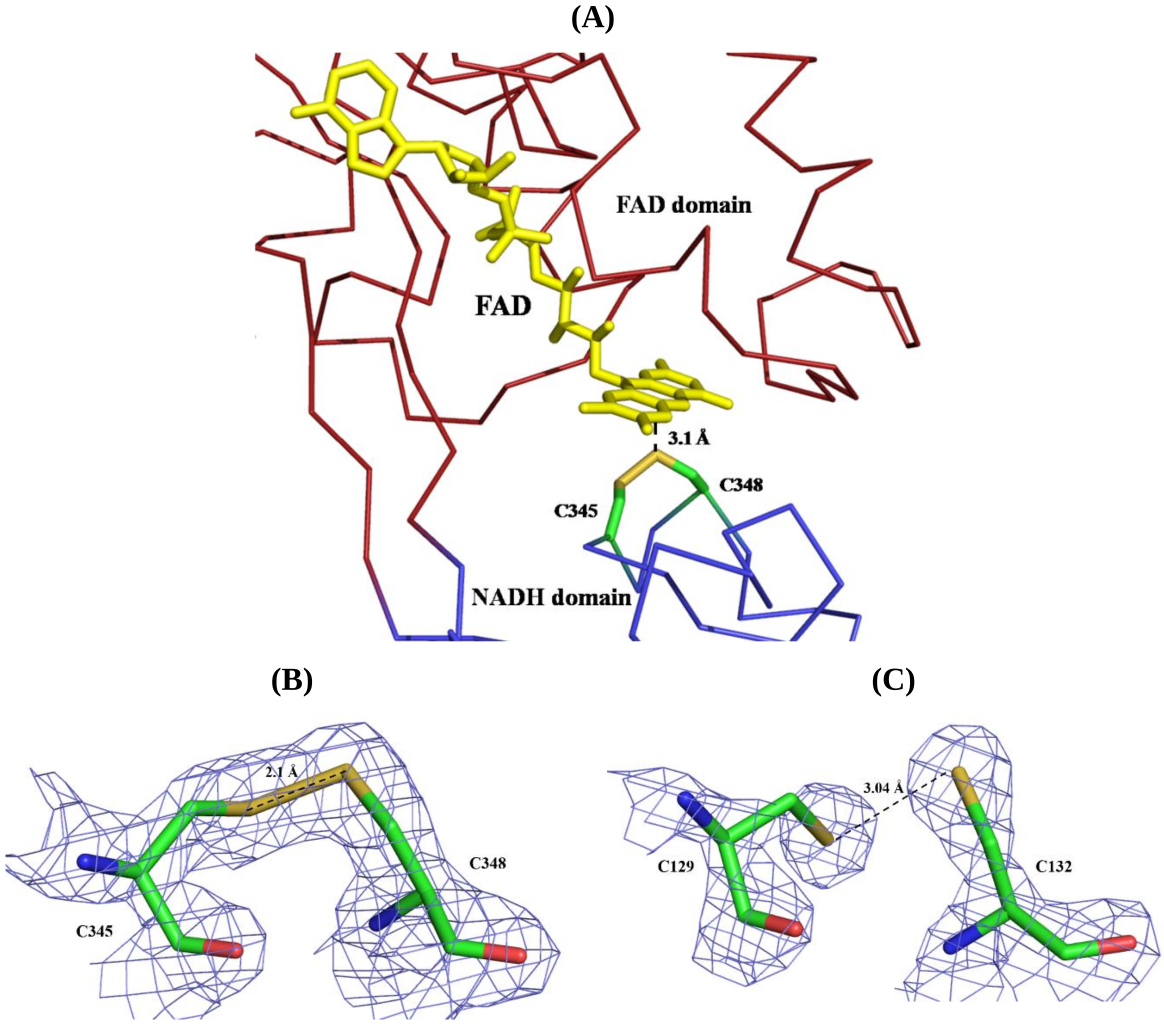

Figure 3.38: Close view to the three redox active centres. *(A)* FADH is in close contact to the Sγ of C348, the most favourable position for reduction by the flavin. *(B)* The redox active centre of the NADH domain, C345 and C348 that is in close contact to the FADH remains oxidised. The *B*-factor for C345 and C348 were refined to 33.5 and 33.2 Å^2, respectively. The 2Fo-Fc electron densities shown are contoured at 1σ (blue lines). *(C)* C129 and C132 in the N-terminal domain are in contrast in reduced state. The sulfur-sulfur distance is highlighted in dashed lines. The *B*-factor for C129 and C132 are 45.3 and 38.8 Å^2, respectively.

The C-terminal FAD- and the NADH/SS domains are joined to the NTD via linker segment (Figure 3.37). The linker segment of AhpF (residue 197-209 aa) adopts a loop-helix conformation. The B-factor of this segment is >70 Å^2 for C$_\alpha$ atoms indicating a disordered and highly flexible region in solution. The residues 197-202 of this linker segment form the flexible loop, whereas the residues 203-209 form the α-helical conformation (Figure 3.37). The residue N208 of the helical conformation forms polar contact to the V312 backbone of the FAD domain, to stabilise the linker segment closely to the FAD domain.

The NTD (1-196) of AhpF not only shows homology to the Thioredoxin, it is also homologous to Glutaredoxin-like (GDX-like) proteins, and it contains a second redox active disulfide (C129/C132) in this AhpF structure (Figure 3.39). Structurally, NTD consists of two “fused” so called N- and C-terminal thioredoxin folds that include two conserved cis proline: *cis*-P62 and *cis*-P172 at the beginning of β-stand 3 and β-stand 7, respectively. The NTD reveals 8-stranded *β*-sheets embraced at one side by six α-helices and on the other side by one α-helix (Figure 3.39). The NTD redox centre (C129/C132) is located at the C-terminal thioredoxin fold and is reduced to its dithiol form (Figure 3.39), although no reducing agent like DTT or TCEP has been used during crystallisation in this depicted structure. The distance between the two sulfurs of C129 and C132 is 3.04 Å (Figure 3.38C). The corresponding electron density is clearly visible between C129 and C132 and reveals the reduced state between the two cysteines (Figure 3.38C). In comparison to C132, C129 is exposed to the surface in the crystal structure, while hydrophobic residues V171 and *cis*-P172 cover C132 and make it therefore solvent inaccessible (Figure 3.39).

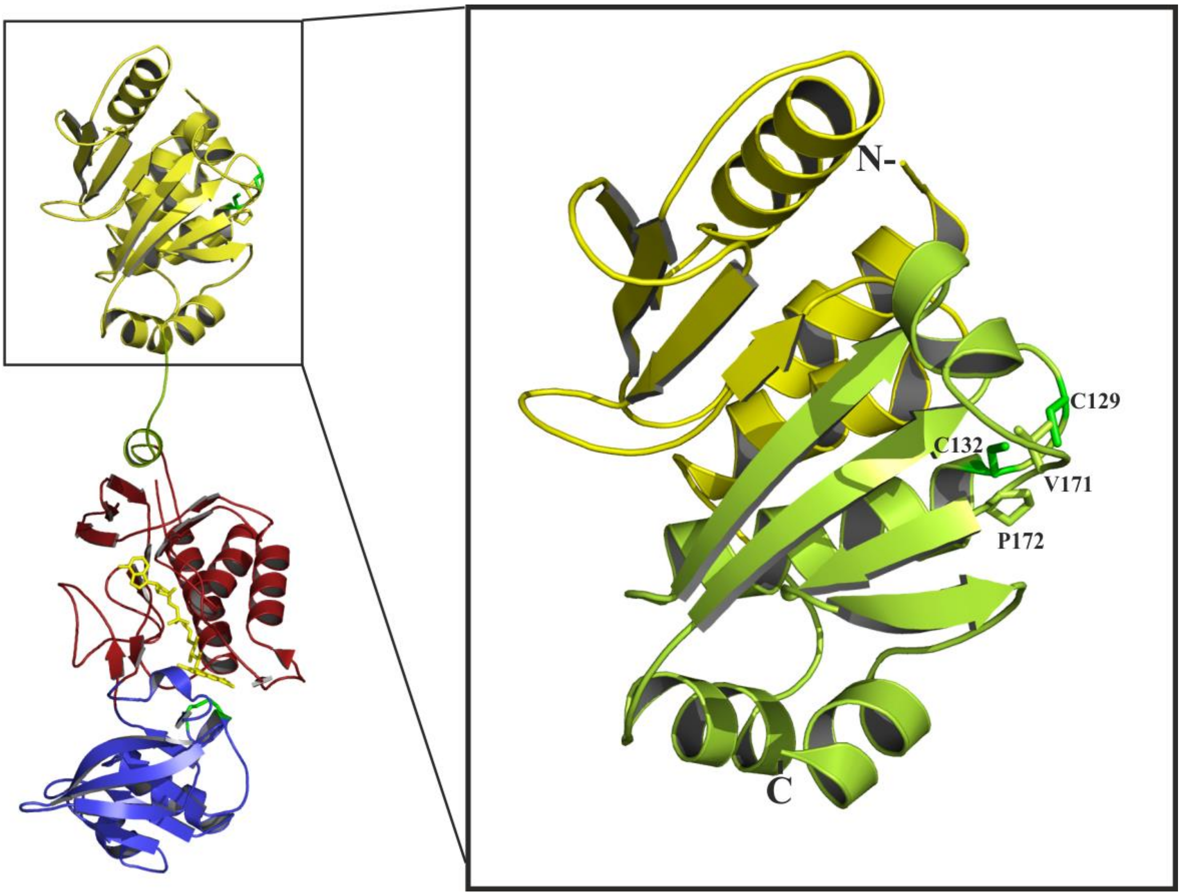

Figure 3.39: Close view to the NTD structure. *E. coli* AhpF structure (left) and a zoomed section of the NTD (1-196). NTD reflects two thioredoxin folds (yellow and green colour for the N-and C-terminal half). The redox active cysteines C129 and C132 are highlighted in green sticks. C129 is in comparison to C132 exposed, while hydrophobic residues V171 and *cis*-P172 shield C132.

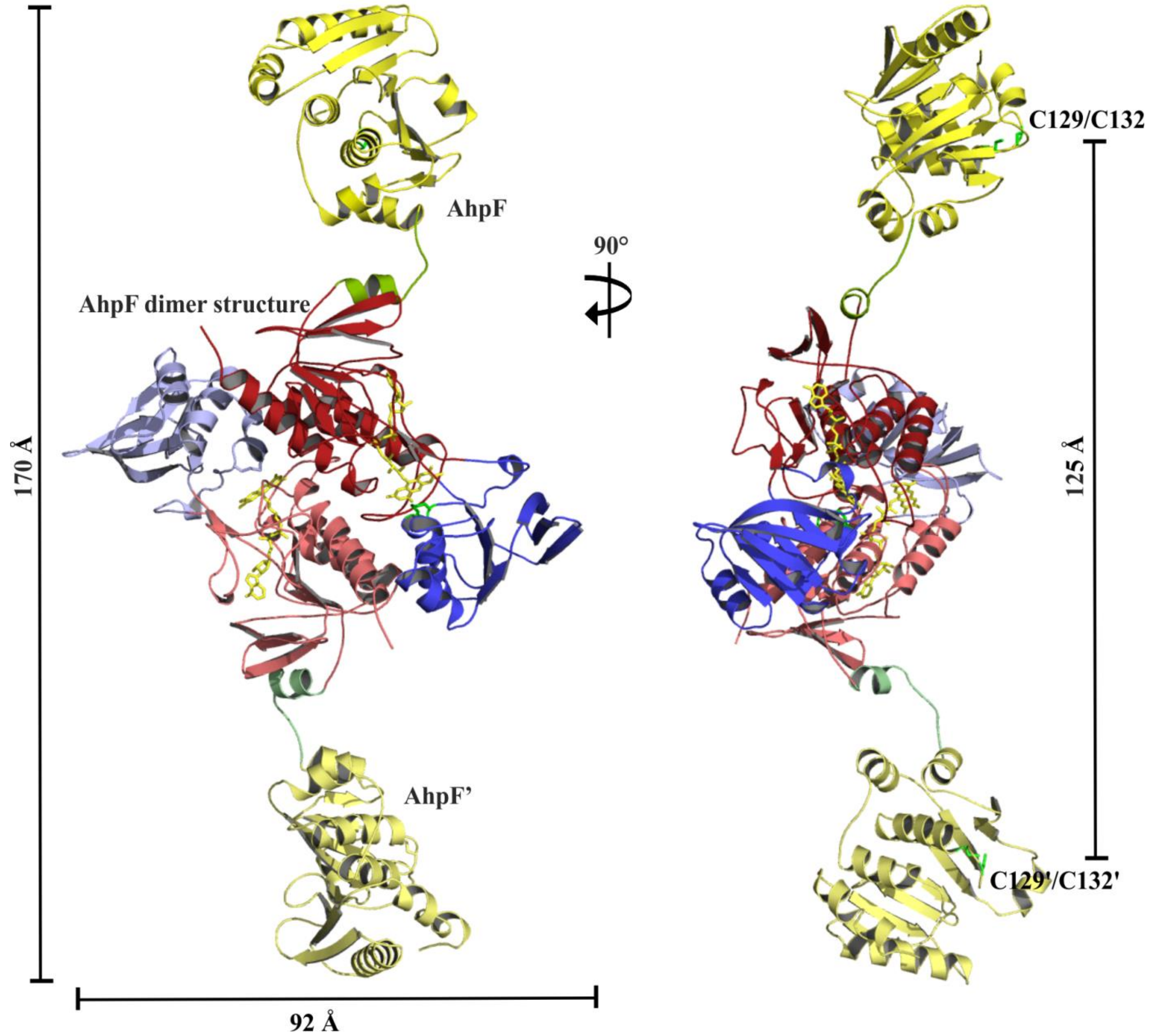

Figure 3.40: *E. coli* AhpF dimer coloured by its four distinct regions, respectively. The second *Ec*AhpF monomer is depicted in lighter shaded colour respectively and generated by its symmetry related molecule. The symbol (') highlights the symmetry related molecule. The two AhpF structures are connected via the FAD domain and the NADH/SS domain.

The dimer conformation of AhpF was generated by its crystallographic 2-fold axis using a symmetry related molecule, revealing a head-to-tail dimerisation. The dimer interface covers mainly the FAD-FAD' domain, which is with 2520 Å^2 around 10 % of the monomeric total solvent accessible area of 25 103 Å^2 [215]. The interface is stabilised by hydrophobic interactions and hydrophilic interactions like hydrogen bonds and salt bridges. The homodimer conformation of *Ec*AhpF reflects a stretched molecule with a maximum length of 170 Å (Figure 3.40), giving the possibility of electron transfer from NTD redox active disulfide bond (C129/C132) to the redox active disulfide bond of AhpC. The distance between the two-homodimeric NTD redox active disulfide bonds C129/C132 is 125 Å (Figure 3.40).

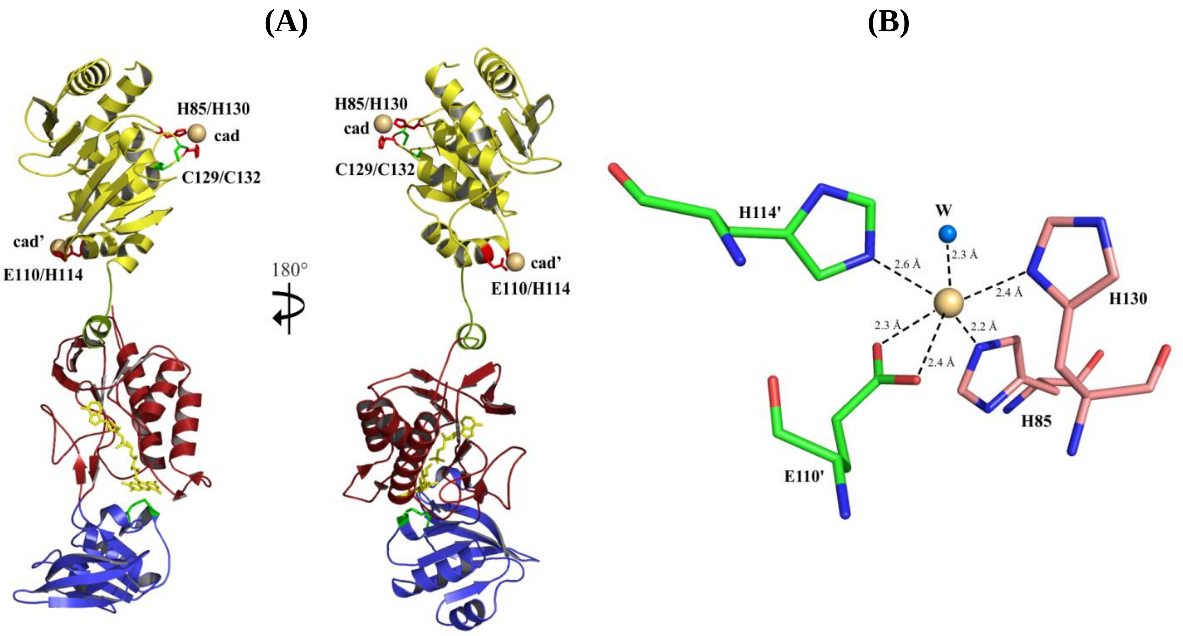

Figure 3.41: Six coordinated bonds of the cadmium ion link AhpF molecules to its symmetry related neighbour. *(A)* Cadmium ion is located in the interface between neighbouring AhpF molecules. Each cadmium ion binds to H85 and H130 of one AhpF molecule and connects another AhpF' molecule via E110 and H114. *(B)* The cadmium ion has in total six coordinated bonds, two to E110' and respectively each to H85, His114', H130 and to one water molecule (W). The symbol (') highlight the symmetry related residue.

Interestingly a cadmium ion with six coordinated bonds was found to be attached to the NTD and it was located adjacent to the redox centre (Figure 3.41A). Two highly conserved and catalytically important histidine side chains (H130 and H85) are protruded on the same side to make a positively charged groove wherein one cadmium ion from the crystallising solution is bound. This heavy metal ion forms additional three coordinated bonds to the symmetry related AhpF molecule residues E100 and H114 and one coordinated bond to a water molecule (Figure 3.41). The occupancy of a cadmium ion is not surprising since the addition of 10 mM cadmium chloride into the crystallisation drop enhances the crystal growth into three dimensions (Figure 3.33). Hence, cadmium chloride stabilises neighbouring symmetry related AhpF molecules. The B factor of the cadmium ion is 45.47 Å^2. Another intriguing perspective of the cadmium ion is the coordinated bond to H130, which is in close distance to the redox active C129 and C132. Therefore, the possibility that a metal ion might be involved in the redox reaction between the NTD of AhpF to the redox active disulfide of AhpC cannot be ruled out.

Refinement statistics

R factor[a] (%)	14.14
R free[b] (%)	18.45
Number of amino acid residues	521
Ramachandran statistics	
Most favored (%)	88.9
Additionally allowed (%)	10.9
Generously (%)	0.2
Disallowed (%)	0.0
R.M.S. deviations	
Bond lengths (Å)	0.020
Bond angles (°)	2.023
Mean atomic B values	
Overall	40.58
Wilson	40.23

Table 3.4: Statistics of crystallographic refinement for *E. coli* AhpF.

[a] R-factor = Σ||FO| - |FC||/Σ|FO|, where FO and FC are measured and calculated structure factors, respectively.

[b] R-free = Σ||FO| - |FC||/Σ|FO|, calculated from 5% of the reflections selected randomly and omitted from the refinement process.

3.5 Alkyl Hydroperoxide Reductase subunit C (AhpC) crystal structure from *E. coli* at 3.3 Å resolution in its oxidised form

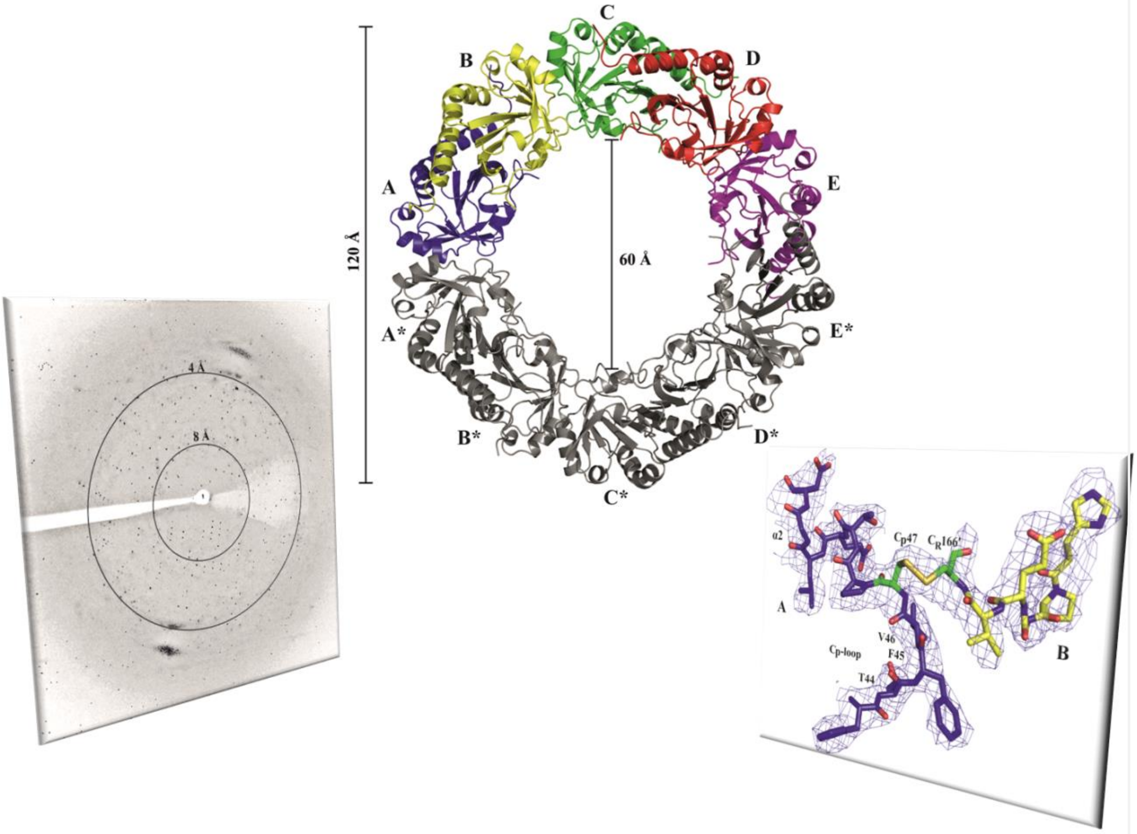
C
B
D
A
E
120 Å
60 Å
A*
E*
B*
D*
C*
4 Å
8 Å
α2
Cp47
C_R166'
A
B
V46
Cp-loop
F45
T44

3.5.1 Production and purification of AhpC from *E. coli* under oxidised condition

In order to investigate the redox reaction between AhpF and AhpC and to get a deeper insight towards the molecular mechanism, AhpC has to be investigated. The cloning of AhpC gene into pET9d-6His plasmid as well as expression and solubility test of AhpC protein were performed by Dr. Neelagandan Kamariah [170]. In order to purify the oxidised form of recombinant proteins AhpC, no DTT was used in all following buffers. To avoid that any DTT remain from the lysis buffer A, the Ni^{2+}-NTA was initially washed with 10 column volumes of respective buffers without DTT and subsequently eluted with an imidazole gradient (0–300 mM) (Figure 3.42A). Buffer A of AhpC purification contain 50 mM Tris/HCl, pH 7.5, 200 mM NaCl, 2 mM PMSF and 2 mM Pefabloc^{SC} (BIOMOL). Afterwards ion-exchange chromatography was carried out using Resource^{TM} Q column (GE Healthcare), to clear impurities that bind to the column, whereas AhpC remains in the flow through. The flow through of AhpC was concentrated and further purified using size exclusion chromatography. Pure AhpC is shown in SDS gel section (Figure 3.42B).

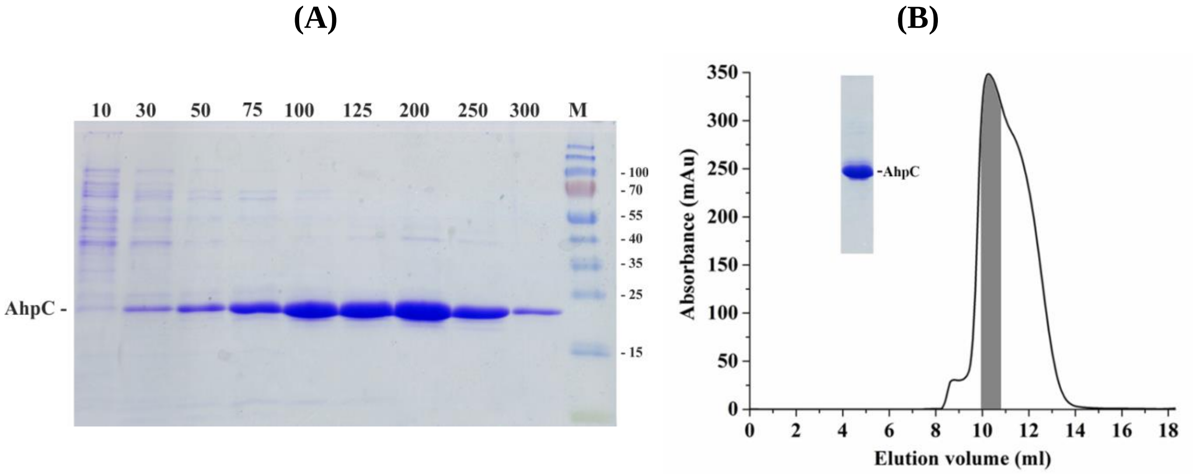

Figure 3.42: AhpC purification in oxidised condition *(A)* The Ni^{2+}-NTA purification was performed in buffer A (50 mM Tris/HCl, 200 mM NaCl, pH 7.5) in absence of DTT using an imidazole gradient (10 – 300 mM) for elution of Ni^{2+}-NTA bound protein. Fractions from 100 – 200 mM imidazole were pooled for further purification. AhpC was injected subsequently into ion-exchange column and remains in the flow through. *(B)* Gel filtration elution diagram of AhpC in S75 column using 50 mM Tris pH 7.5, 200 mM NaCl buffer. The volume of the shaded peak area was pooled and 1 µl of pure eluted protein were applied on a 17% SDS gel.

3.5.2 Crystallisation, data collection and structure determination of AhpC crystals

Crystallisation of AhpC was performed to analyse its three dimensional structure. Pure AhpC of 10 mg/ml concentration was used to set up crystal drops in Hampton Research crystal screen HR-110 and HR-112, and Emerald biosystems Wizard screen 1 and Wizard screen 2, in hanging drop plates with 2 µl droplet size per well at 18 °C. Needle bundles were observed in

Hampton research crystal screen 2 #25 (HR2#25) after two days and in Hampton research crystal screen 2 #23 (HR2#23), small crystal were formed after 14 days. Both conditions have similar composition: HR2#25 contains 1.8 M Ammonium sulfate, 100 mM MES (2- (*N*-morpholino) ethanesulfonic acid), pH 6.5, and 10 mM cobalt chloride, whereas HR2#23 consists of 1.6 M Ammonium sulfate, 100 mM MES, pH 6.5, and 10 % dioxane. Both conditions have been optimised simultaneously. The first larger size crystals that showed reflections in the diffraction image using the in-house machine (Rigaku) were formed under the condition 1.6 M Ammonium sulfate, 100 mM MES, pH 6.5, and 10 % dioxane using 8 mg/ml protein concentration. The best crystals were obtained in 1.8 M ammonium sulfate, 100 mM MES, pH 6.5 and 5 % dioxane, with 8 mg/ml protein concentration (Figure 3.43).

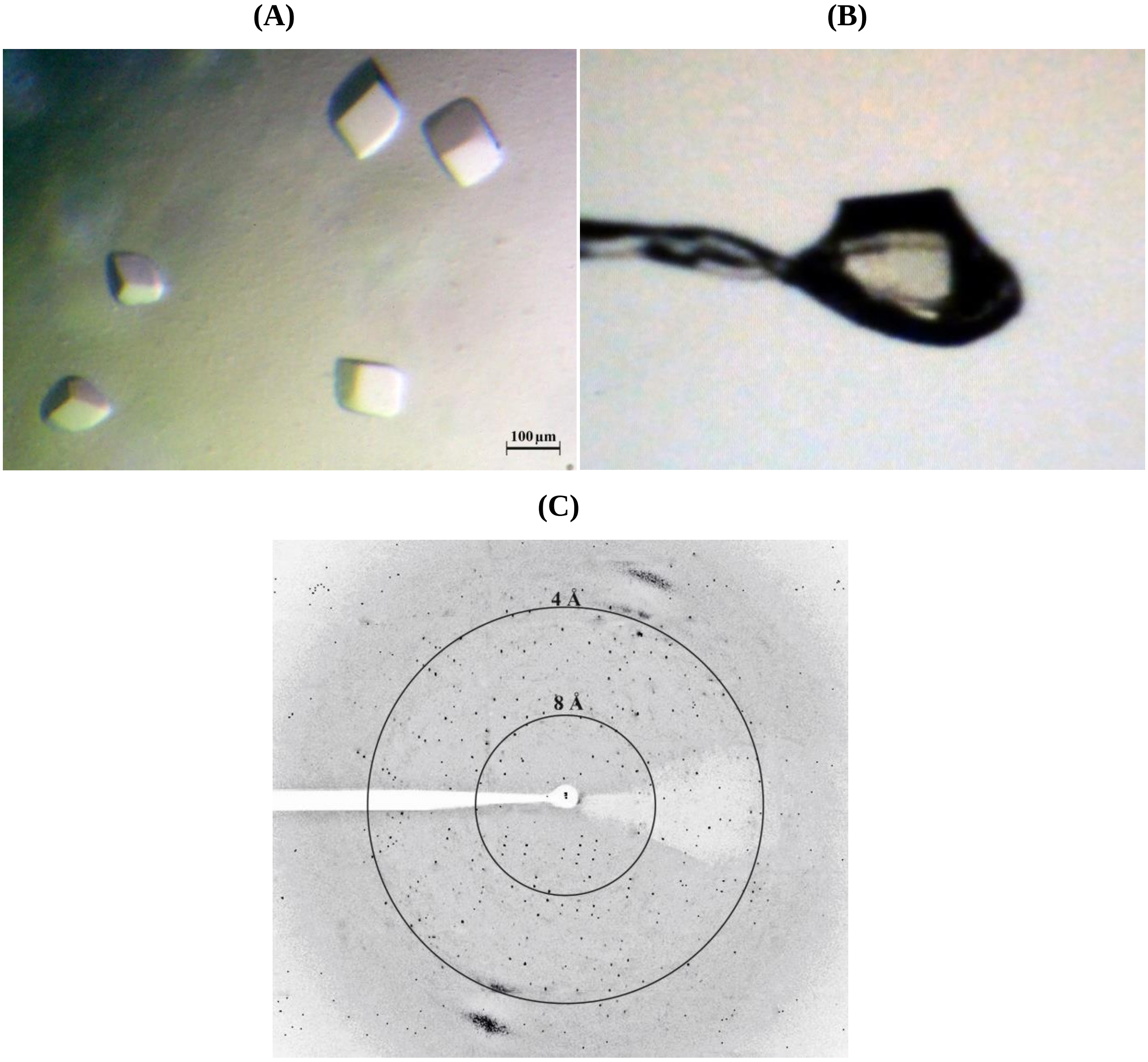

Figure 3.43: Crystal photograph of recombinant *E. coli* AhpC (0.1 mm x 0.1 mm x 0.1 mm) (*A*). *(B)* Single frozen crystal of AhpC mounted in crystal loop for diffraction data collection in NSRRC. *(C)* Representative diffraction image of AhpC from *E. coli* alkyl hydroperoxide reductase.

These crystals were then used for data collection. The crystals were quickly soaked into cryoprotectant solution containing 25% (w/v) glycerol in crystallisation liquid and flash-cooled in liquid nitrogen at 100 K. Together with Dr. Malathy Sony S. Manimekalai, single wavelength datasets for AhpC were collected at 140 K on beamline 13B1 at the National Synchrotron Radiation Research Center (NSRRC, Hsinchu, Taiwan) using a single frozen crystal of AhpC (Figure 3.43B). Using the ADSC Quantum 315 CCD detector, 100° of data were collected with 0.5° oscillation (20 s per 0.5° frame). Single wavelength datasets of AhpC were also collected at the protein crystallography beamline S06 PX at the Swiss Light Source (SLS) with a PILATUS 6M detector by Dr. Neelagandan Kamariah. Data sets were collected as a series of 0.2° oscillation images with 0.2 s exposure time with a detector distance of 500 mm. Representative diffraction pattern of AhpC crystal is presented in Figure 3.43C. All diffraction data reduction, including indexing, integration and scaling were carried out in iMosflm program [207]. The results of data processing and data statistics for AhpC are summarized in Table 3.5.

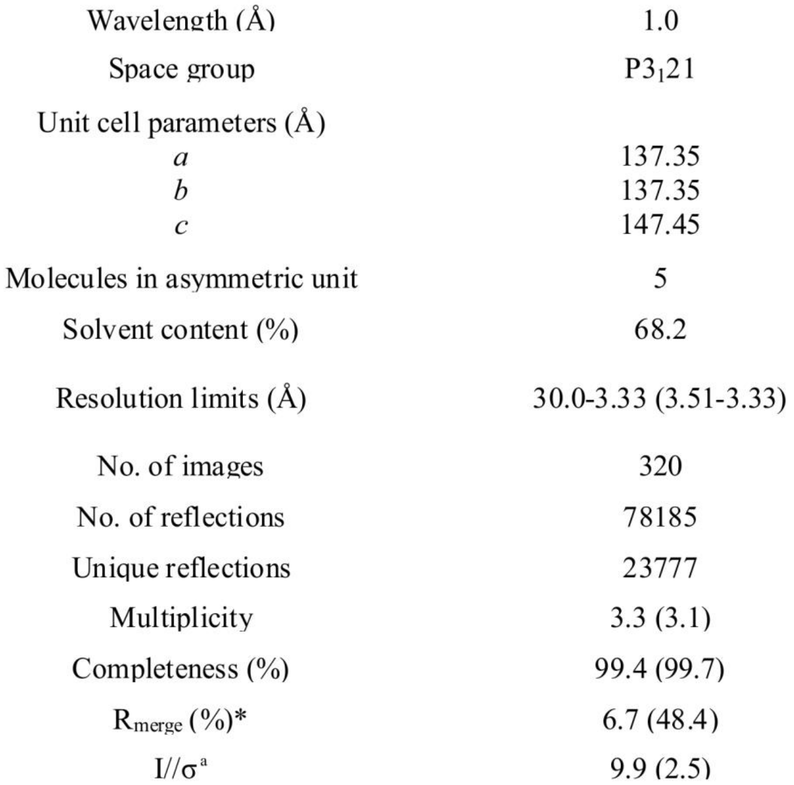

Data collection statistics	**AhpC**
Wavelength (Å)	1.0
Space group	$P3_121$
Unit cell parameters (Å)	
a	137.35
b	137.35
c	147.45
Molecules in asymmetric unit	5
Solvent content (%)	68.2
Resolution limits (Å)	30.0-3.33 (3.51-3.33)
No. of images	320
No. of reflections	78185
Unique reflections	23777
Multiplicity	3.3 (3.1)
Completeness (%)	99.4 (99.7)
R_{merge} (%)*	6.7 (48.4)
$I//\sigma^{a}$	9.9 (2.5)

Table 3.5: Data collection statistics to *E. coli* AhpC.
*Rmerge = ΣΣi|Ih - Ihi|/ΣΣiIh, where Ih is the mean intensity for reflection h. a Values in parentheses refer to the corresponding values of the highest resolution shell (2.07 - 2.00 Å).

AhpC was crystallised in a trigonal system with the space group $P3_121$ and unit cell parameters $a = 137.35$, $b = 137.35$ and $c = 147.45$ Å. The crystals diffracted to 3.33 Å resolution. Assuming five molecules in the asymmetric unit, the solvent content for the AhpC crystal is 68.2 % with a Matthews coefficient (V_m) of 3.87 $Å^3$ per Dalton (Matthews, 1968). Initial phases were obtained by molecular replacement method with the related AhpC structure from *Salmonella typhimurium* (*St*AhpC; PDB 3EMP; [209]) using program PHASER [179]. Chainsaw software was used for model editing [216]. The LLG of 3436 and Z-score for the fast rotational function (RFZ) of 13.8 and for fast translational function (TFZ) of 114.5 in Phaser, highlighting a good solution [179]. To improve the electron density by solvent flattening and to reduce model bias that may occur at crystal structure below 3 Å, the program RESOLVE was used for prime and switch phasing [217]. The preliminary structure was subsequently used for 30 cycles of rigid body refinement using the program Refmac5 [177], obtaining an overall R-factor of 27.28 % and free R-factor of 28.20 %. The initial structure reflects five molecules in one asymmetric unit, where each molecule consisted of 162 amino acids. The overlay of F_O–F_C and $2F_O$–F_C maps of AhpC clearly shows additional green electron density respectively to amino acids at the C-terminus. Iterative cycles of model building and refinement were performed in a combined manner using the programs COOT [181] and REFMAC5 [177] of the CCP4 suite (1994) (Figure 3.34). Each cycle of model building allowed the attachment of additional amino acid to its corresponding green density of the C-terminal region.

3.5.3 Crystal structure of AhpC from *E. coli*

The crystal structure of AhpC from *E. coli* was solved at 3.3 Å resolution and revealed five molecules (A-E) in the asymmetric unit that form a half ring shape conformation. The full ring, decamer structure is generated by its crystallographic two-fold symmetry operation (A'-E') (Figure 3.44). The entire ring complex consists of five homodimers $(\alpha_2)_5$, with an outer diameter of 123.7 Å x 115.4 Å calculated using MOLEMAN2 [218] and an inner diameter of 55 Å and 60 Å measured between opposite molecules A/E' and C/C' using Pymol [175]. The thickness of the ring complex correspond to a monomer molecule and is 50 Å (Figure 3.44). The *E. coli* AhpC structure shows clear electron density for all the main chain atoms except for the C-terminus region, which is highly disordered. The molecules A, C and D showed clear and continuous electron density up to P167, whereas in molecule B it is up to C166 and in molecule E up to V165.

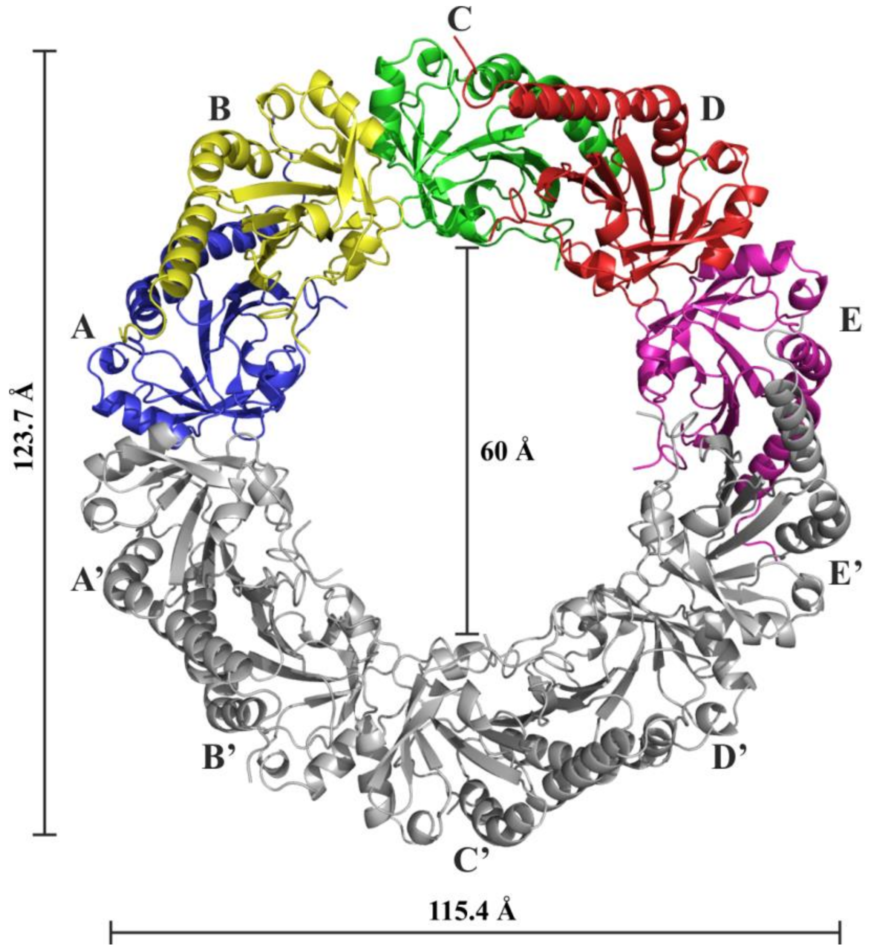

Figure 3.44: Crystal structure of oxidised AhpC from *E. coli*. Decamer $(\alpha_2)_5$ of AhpC. Each asymmetric unit consists of five molecules (A-E), depicted in different colour and its crystallographic symmetry mates, depicted in grey (A'-E'). Dimer formations are between A-B, C-D and E-E'.

Each AhpC monomer consists of seven β-sheets located in the centre of the molecule, flanked at one side by four and the other side by two α-helices. Furthermore, each monomer contains two cysteine residues namely peroxidative cysteine (C_P47) and resolving cysteine (C_R166). In this *E. coli* AhpC structure, electron densities are clearly visible up to C_R166 in A, B, C and D chains. The residues after C_R166 are mostly disordered in all the chains. The monomer molecules in each dimer are related by a two-fold symmetry and no significant structural differences were observed between each monomers in a dimer structure (Figure 3.45A). The dimer structure reflects an oval shape with dimensions of 67.2 Å x 47.9 Å x 36.6 Å, calculated using MOLEMAN2 (Figure 3.45A) [218]. The two molecules of each dimer are related by a two-fold symmetry and are tightly connected to each other (Figure 3.44B). The dimer interface is formed between β7 and β7' of each monomer, which forms when two monomer combined a 14 stranded β-sheet dimer. The β7 and β7' interface is stabilised by salt bridges between the residues K151 and G135 and hydrogen bonds between the residues D119, Q132, I134, E135, V136, A138, R150, and G142 (Figure 3.45A). The active site is composed of the intermolecular disulphide bond between the C_P47 from one monomer with C_R166 from another monomer, interacting in a head to tail manner (Figure 3.45B).

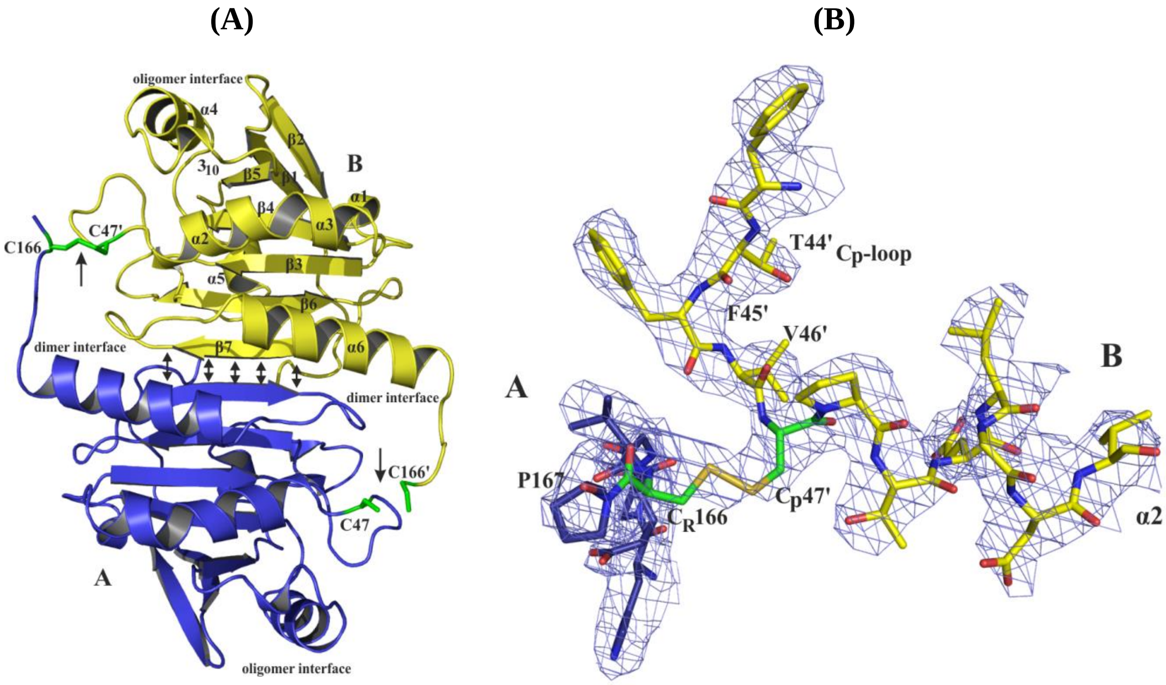

Figure 3.45: Dimer structure of oxidised AhpC from *E. coli*. (A) AhpC dimer between the molecules A (blue) and B (yellow). The redox active cysteines (C47/C166' and C47'/C166) are depicted green, whereof C47'/C166 are forming an intermolecular disulfide bond and C47/C166' are in the dithiol state. The dimer formation between A and B is also stabilised along both β7-sheets with hydrogen bonds and salt bridges, highlighted in arrows. *(B)* Electron density for the redox active C47'/C166 disulfide bond between molecule A (blue) and molecule B (yellow). The 2Fo-Fc density is contoured at 1 σ (blue lines). The symbol (') is used for residues of the partner subunit in the dimer formation.

In *E. coli* AhpC structure, only two disulphide bonds (A166-B47 and C166-D47) were observed among the five AhpC molecules (A-E). This might be due to a highly disordered C-terminus and also possibly due to radiation damage. The two intermolecular redox active disulfide bonds formed by C47 and C166' contribute additional stabilisation to the dimer interface (Figure 3.45A). The 2Fo-Fc electron density map from chain A (residues F43 to V54) and chain B (residues H161 to P167) is shown in Figure 3.45B, reflecting the oxidised state between C47 and C166' (Figure 3.45B). The electron density for the disulfide bridge between the respective C_P47 and C_R166' are clearly visible (Figure 3.45B). C_P47 is located close to the N-terminus of α2-helix and is part of the so-called C_P-loop. In the oxidised form of AhpC, the C_P is unwound to form a flexible loop, which exposed C_P47 to the resolving cysteine C_R166'. C_R166' is located at the very C-terminus of each chain of the crystal structure and is partially exposed (Figure 3.45A).

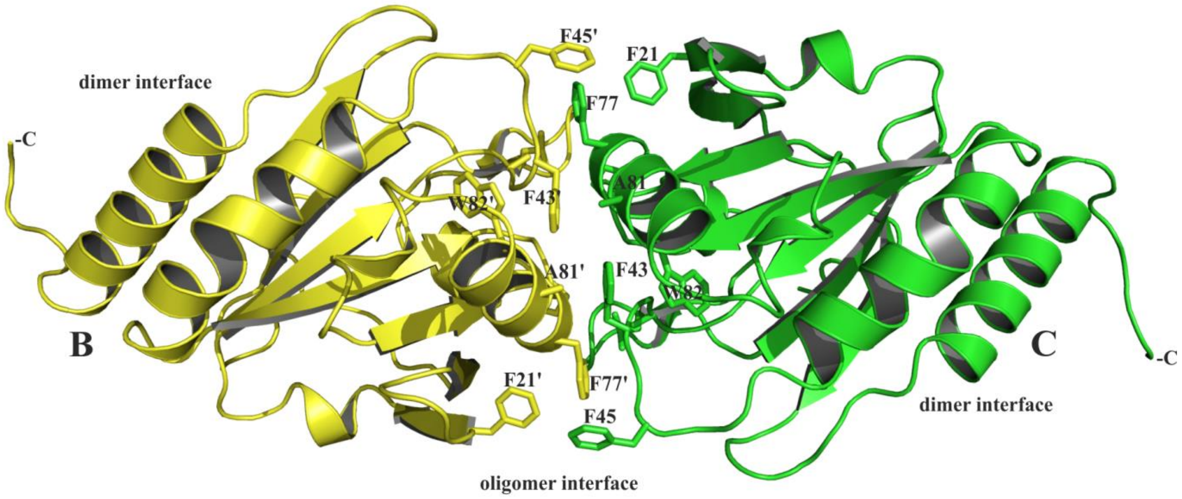

Figure 3.46: Oligomer interface of AhpC. The dimer-dimer interface between chain B (yellow) and chain C (green) reflects no hydrogen bond or salt bridges, rather patches of hydrophobic residues formed by F21, F43, F45, F77, A81 and W82 of each monomer.

The oligomeric assembly at the dimer-dimer interfaces between chain B and chain C are mainly formed by hydrophobic residues F21, A41, F43, F45, F77, A81, W82, P100, G116 and L117. Hydrogen bonds or salt bridges between chain B and C are not found in this interface. This interface consists only of hydrophobic interaction (Figure 3.46).

Refinement statistics

R factor[a] (%)	28.51
R free[b] (%)	29.47
Number of amino acid residues	832
Ramachandran statistics	
Most favored (%)	93.4
Additionally allowed (%)	6.4
Generously (%)	0.3
Disallowed (%)	0.0
R.M.S. deviations	
Bond lengths (Å)	0.004
Bond angles (°)	0.741
Mean atomic B values	
Overall	41.9

Table 3.6: Statistics of crystallographic refinement for *E. coli* AhpC.

[a] R-factor = Σ||FO| - |FC||/Σ|FO|, where FO and FC are measured and calculated structure factors, respectively.

[b] R-free = Σ||FO| - |FC||/Σ|FO|, calculated from 5% of the reflections selected randomly and omitted from the refinement process.

3.6 Single Particle Reconstruction of *E. coli* AhpC in reduced form using Cryo-Electron Microscopy at 12 Å resolution

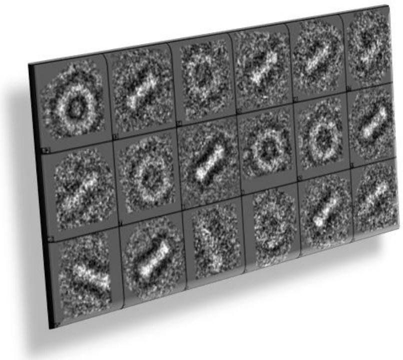

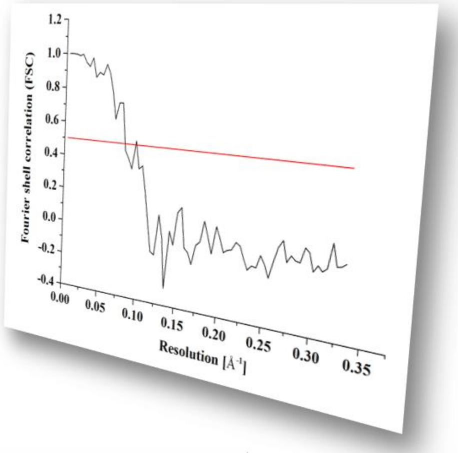

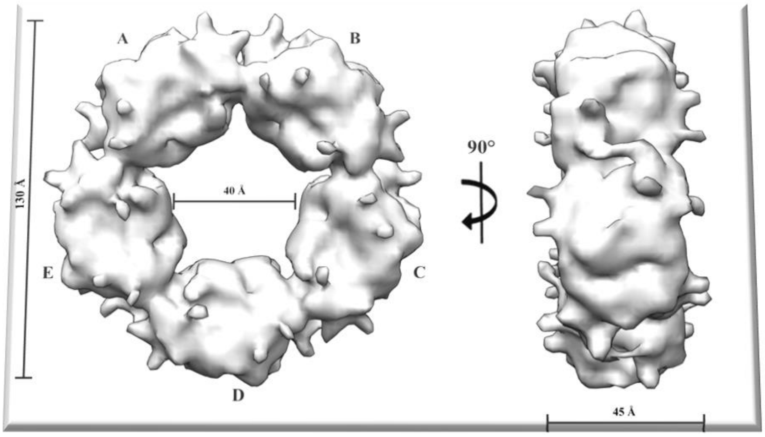

3.6.1 Production and purification of AhpC from *E. coli* under reducing condition

In order to understand the decamer ring formation of AhpC in solution, as shown in the crystal structure (Figure 3.44), dynamic light scattering and cryo Electron Microscopy (cryoEM) of AhpC in oxidised and reduced conditions as well as in different pH have been performed (Figure 3.48). To obtain AhpC in its reduced condition, recombinant protein AhpC was purified in the presence of DTT. Lysis buffer A of AhpC purification contains 50 mM Tris/HCl pH 7.5, 200 mM NaCl, 2 mM PMSF, 2 mM Pefabloc^{SC} (BIOMOL) and 0.8 mM DTT. The 6xHis recombinant AhpC was applied to the Ni^{2+}-NTA column and eluted with an imidazole gradient (0–300mM) (Figure 3.47). Afterwards ion-exchange chromatography was applied using Resource^{TM} Q column (GE Healthcare). AhpC remains in the flow through, whereas impurities bind to the column. The flow through of AhpC was concentrated using Millipore spin concentrator with a molecular-mass cut-off of 10 kDa and then further purified using size exclusion chromatography. Pure AhpC under reducing condition is shown in SDS gel section (Figure 3.47).

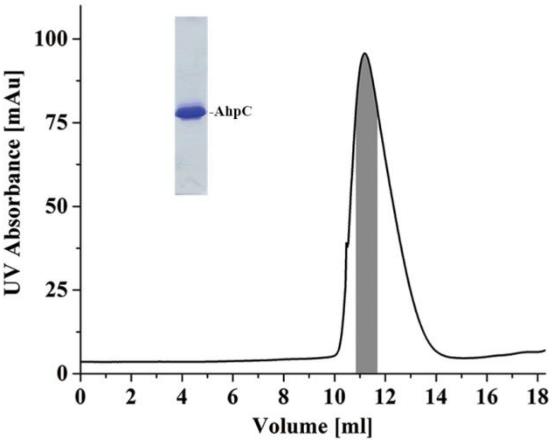

Figure 3.47: *E. coli* AhpC purification under reducing condition. Gel filtration elution diagram of AhpC in S75 column using 50 mM Tris pH 7.5, 200 mM NaCl buffer and 1 mM DTT. The volume of the shaded peak area was pooled and 1 µl of pure eluted protein were applied on a 17% SDS gel (section).

3.6.2 Dynamic Light Scattering (DLS) of reduced and oxidised form of AhpC

Both oxidised and reduced purified AhpC as described in section 2.3.8 were used for dynamic light scattering (DLS). Using Malvern Zetasizer Nano ZS spectrophotometer for DLS, the molecule dimension and molecular weight of AhpC were measured in solution. DLS were collected in low-volume quartz batch cuvette (ZEN2112, Malvern Instruments) using 12 µl of 1 mg/ml protein solution. After 60 s equilibration time, the backscattering at 173° was detected for reduced and oxidised AhpC recombinant protein (Figure 3.48A). The oxidised form of AhpC reveals a hydrodynamic radius of 3.2 nm, dispersity of 21.9 % and a molecular weight of 146.1 kDa ± 32 kDa, whereas the reduced form a hydrodynamic radius of 4 nm, dispersity of 26 % and molecular weight of 184.2 kDa ± 48 kDa. Furthermore, oxidised and reduced form of AhpC in various pH were used for DLS measurement. The oxidised and reduced purified

AhpC were buffer exchanged before DLS. In buffers with pH 5.4, no changes were observed. However, in 100 mM Na-acetate pH 4.4, the reduced form of AhpC, but not the oxidised form reveals an increase of its hydrodynamic radius to 16.2 nm, indicating a higher molecular weight of 4000 kDa.

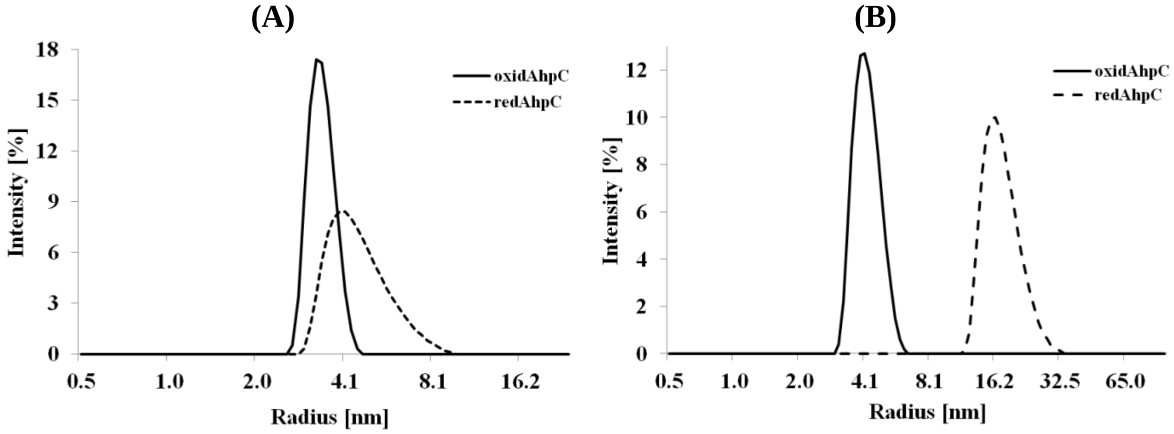

Figure 3.48: Dynamic Lights Scattering experiments of *E. coli* AhpC. *(A)* DLS measurement of AhpC indicates its hydrodynamic radius in oxidised (—) and reduced (---) form in 50 mM Tris/HCl pH 7.5, 200 mM NaCl. The reduced condition contains 1 mM DTT respectively. *(B)* Comparison of oxidised and reduced AhpC in low pH (100 mM Na-acetate pH 4.4).

3.6.3 Single Particle Reconstruction (SPR) of AhpC from *E. coli*

In order to investigate AhpC structure close to physiological condition and to prove that the ring formation is not due to high protein concentration during crystallisation, Single Particle Reconstruction (SPR) using cryo Electron Microscopy was applied.

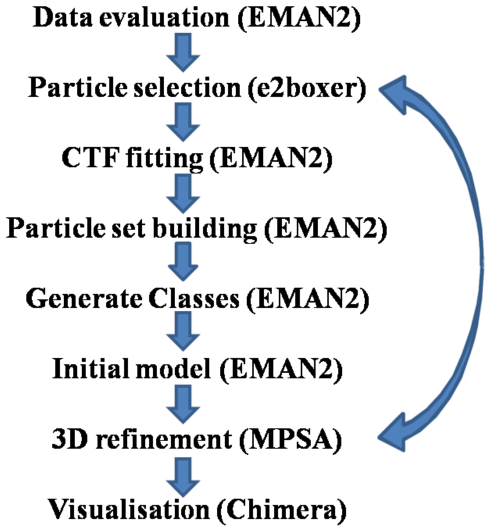
Data evaluation (EMAN2)
Particle selection (e2boxer)
CTF fitting (EMAN2)
Particle set building (EMAN2)
Generate Classes (EMAN2)
Initial model (EMAN2)
3D refinement (MPSA)
Visualisation (Chimera)

Figure 3.49: Cryo EM structure determination strategy. Images were initially imported and evaluated using EMAN2 program [186]. Individual particles were selected semi-automatically, aided by the e2boxer tool, in Swarm mode, from EMAN2 [186] software package. The contrast transfer function (CTF) correction and defocus for each micrograph was estimated with EMAN2 [186]. Initial model was built using EMAN2 software [186] and refinements were performed using multipath simulated annealing (MPSA) software [205]. The final geometry of the AhpC cryo EM structure was checked, compared to the *E. coli* AhpC crystal structure and figures were created using Chimera software [187].

Cryo EM facilities were kindly provided by Prof. Dr. Shee Mei Lok and data sets were kindly imaged by Jonathan Ng Thiam Seng in NUS Centre for BioImaging Sciences at the National University of Singapore (NUS). SPR is a strong tool to investigate large protein molecules under preserved condition in solution within the vitrified buffer. Small amount of purified AhpC with a concentration of 1 mg/ml was applied onto a C-Flat Holey Carbon Grid before quickly vitrified into liquid ethane. After vitrification, samples were kept under liquid nitrogen temperatures. AhpC was applied in reducing condition in buffer A 50 mM Tris/HCl pH 7.5, 200 mM NaCl and 1 mM DTT.

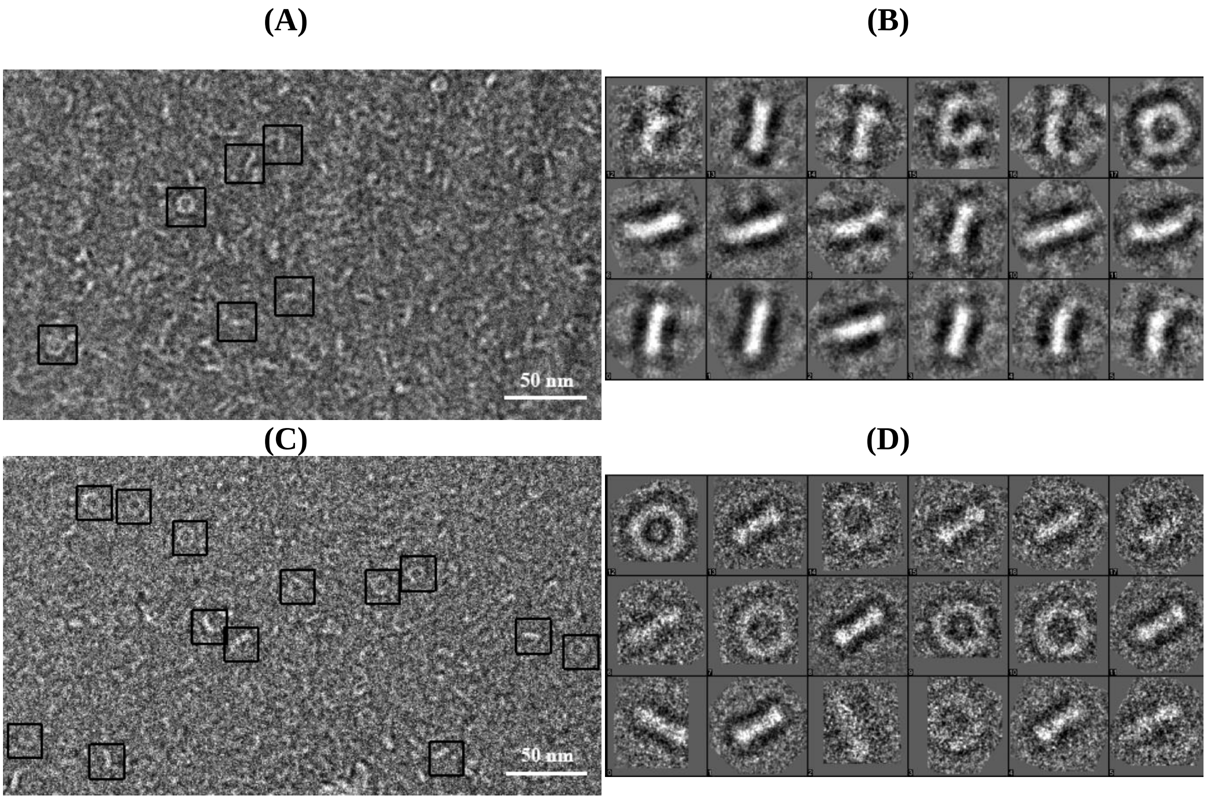

Figure 3.50: Cryo electron microscopy images of *E. coli* AhpC. Micrograph of AhpC in its *(A)* oxidised and (C) reduced form. Selected particles are highlighted in boxes for class averaging. The box size was selected to 192 pixels with a pixel size of 1.14 Å/pixel. Selected class average images of isolated AhpC particles in *(B)* oxidised and *(D)* reduced form.

The electron micrographs reveal ring- and rod shape particles in oxidised and reduced condition of AhpC (Figure 3.50AC). AhpC in oxidised form shows quantity wise more rod shape particles compared to reduced form (Figure 3.50BD). The lengths of the rod shape particle vary in oxidised form, whereas rod shape particle in reduced form remain constant (Figure 3.50BD). The constant length of the rod shape particles in reduced form corresponds well to the diameter of the ring shape particle, indicating that the rod shape particle might be the side view of the ring shape particles. In oxidised form, the classes of rod shape particles have the same length as the reduced form and longer length (Figure 3.50B). However, the images of reduced AhpC reveal larger amount of ring shaped particles than in the oxidised form, allowing the Single Particle Reconstruction (SPR) of reduced AhpC to be performed. A total of 54 images were collected for the 3D reconstruction of reduced AhpC and a set of 1183 isolated molecules were selected for averaging into 40 different classes (Figure 3.49, Figure 3.50BD). The 18 best-generated classes in different perspective were used for initial model building using EMAN2 software (Figure 3.49, Figure 3.50D) [186]. The initial model in reduced form was used as template for refinement by assuming D5 symmetry in the 3D reconstruction using MPSA software [205]. Dr. Victor Kostyuchenko kindly guided me through the EMAN2 software and performed the MPSA refinement.

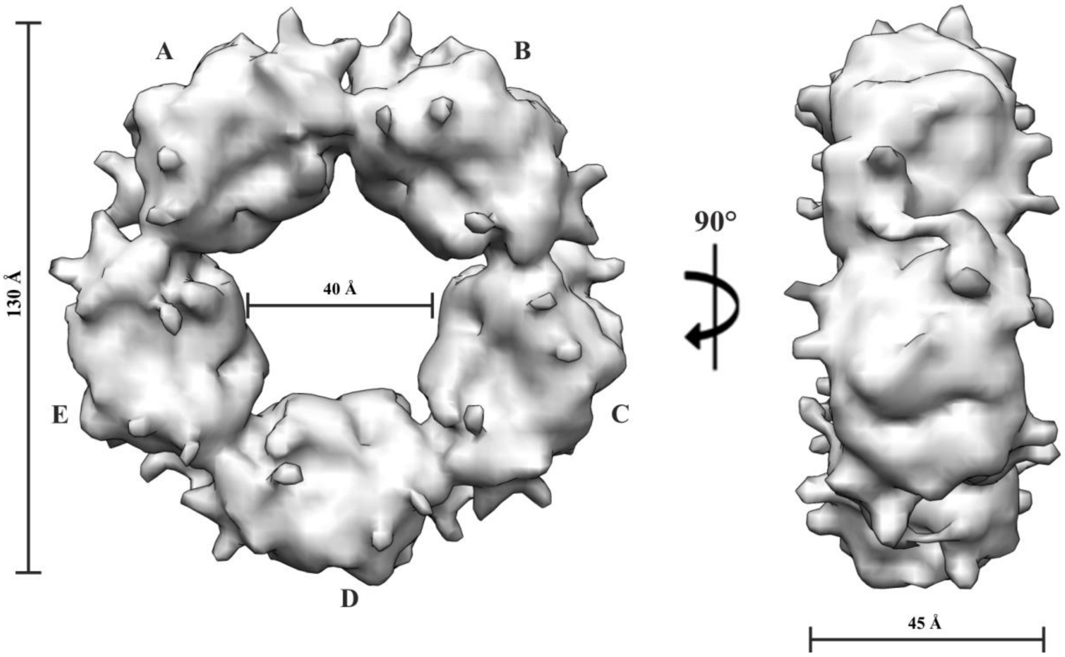

Figure 3.51: 3D reconstruction of AhpC using cryo EM in surface rendered presentation. Overall structure of AhpC on top view reveals a ring shape conformation. The ring structure has a dimension of 130 Å x 130 Å x 45 Å and consists of five well-defined oval shaped bulks labelled as A-E. The 90° view highlights a rod shape conformation.

The 3D reconstructed AhpC structure reflects a ring shape conformation with a dimension of 130 Å x 130 Å x 45 Å (Figure 3.51). The inner and outer diameter of the ring is 40 Å and 130 Å respectively. The ring structure reveals a five-fold symmetry reflected by five oval shaped segments. The segments are separated by narrow gaps. On top view of the ring, at least four small protrudings are projecting out of each segment.

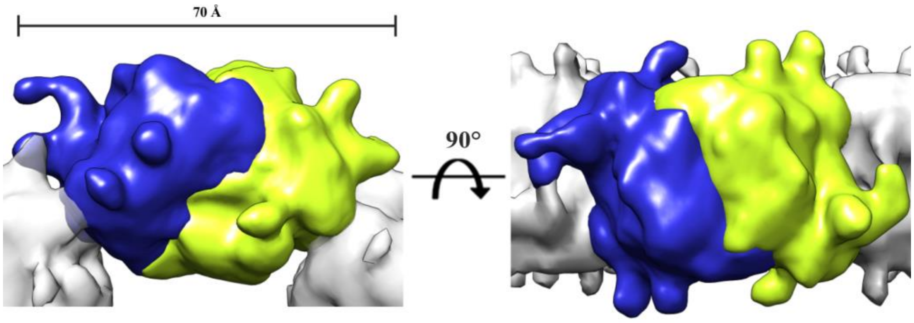

Figure 3.52: Close view of one segment. Each segment has a dimension of 70 Å x 45 Å x 45 Å and reflects an additional two-fold axis, dividing each segment into two symmetrical regions (blue and yellow). On the left, one segment is depicted along its two fold axis. The topview (right) reveals that each region of a segment has three small protruding on both sides. One protruding at one side and two protruding at the other side.

The side view reveals a rod shape conformation, highlighting the presence of small protrudings on both side of the ring formation (Figure 3.51). Each segment has a dimension of 70 Å x 45 Å x 45 Å and reflects an additional two-fold axis, dividing each segment into two regions (Figure 3.52, left). The topview on one segment shows that each region has three small protruding, on one side one protruding and on the other side two protrudings (Figure 3.52, right). The final map resolution is 12.2 Å as measured using Fourier shell correlation of independent half-data sets with a cutoff at 0.5 (Figure 3.53).

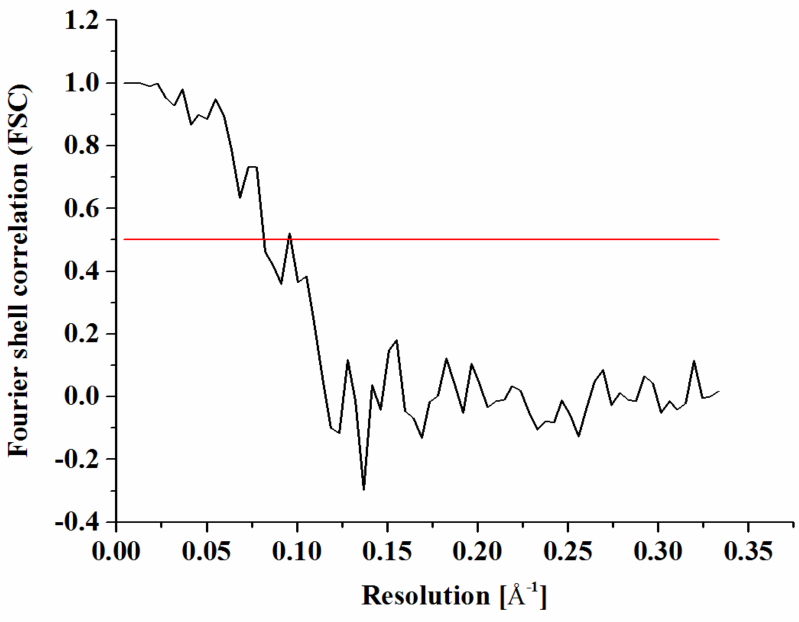

Figure 3.53: Fourier shell correlation (FSC) coefficient function of AhpC cryo EM data set. The FSC function between two halves of the AhpC cryo-EM dataset reveals a resolution of 12.2 Å at FSC=0.5.

Since DLS data of AhpC in pH 4.4 indicates high molecular weight formation, electron micrographs were imaged to visualize the high molecular weight arrangement. For AhpC in pH 4.4, 128 images were kindly collected by Jonathan Ng Thiam Seng in NUS Centre for BioImaging Sciences at the National University of Singapore (NUS) and a set of 2380 isolated molecules were selected for averaging into 40 different classes (Figure 3.54A). The 18 best-generated classes in different perspective, generated using EMAN2 software are depicted in Figure 3.54B [186].

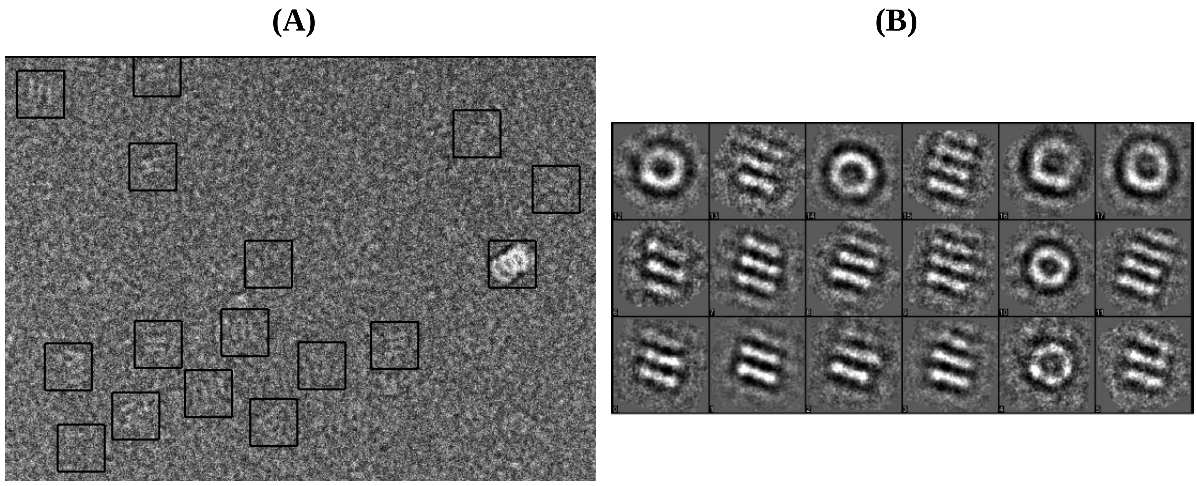

Figure 3.54: Cryo Electron Microscopy images of AhpC in pH 4.4. *(A)* Representative micrograph of AhpC in its reduced form. Selected particles are highlighted in boxes for class averaging. The box size was selected to 128 pixels with a pixel size of 2.28 Å/pixel. *(B)* Selected class average images of isolated AhpC particles in reduced form.

Cryo EM Micrographs depict ring shaped particles and rod shaped particles, whereas rod shaped particles are stacked mainly from two to four (Figure 3.54A). The tilted view indicates that the stacks of rod shape particles are stacks of rings on top of one another (Figure 3.54B).

4. Discussion

4.1 Structural characterisation of subunit *a* binding to ARNO

Since the V-ATPase has been reported to play a crucial role in interaction of signalling proteins such as ARNO (GTP/GDP exchanger, Cytohesin-2) and Arf (small GTPase) via subunit *a* and *c* [1], respectively, high interest arises to obtain more structural information about the regions of ARNO that are involved in its direct association with subunit *a*. The N-terminal part of subunit *a2* protein from mouse that is required for association with ARNO has been mapped in this thesis [96]. Subunit *a2* is one of the four isoforms found in V-ATPase of mouse, which is mainly expressed in Golgi and early endosomes in kidney and liver cells [67] and has been associated with its novel function, acting as pH sensor element in a complex with ARNO and Arf proteins [1, 91] and playing a crucial role in the degradation pathways. In order to identify the binding motif, especially the amino acids involved in subunit *a* to ARNO association, studies were focused with peptides from essential regions of the subunit *a2* of mouse V-ATPase, that showed interaction with ARNO in peptide pull-down experiments [96]. Six peptides of various regions of subunit *a2* ($a2_{1-17}$, $a2_{35-49}$, $a2_{198-214}$, $a2_{215-230}$, $a2_{313-331}$ and $a2_{386-402}$) have been identified to be involved in the association of ARNO, whereof five of these peptides are located within the first 363 amino acids from the N-terminus (Figure 3.14) [10]. NMR structures of two important subunit *a2* peptides $a2_{1-17}$ and $a2_{368-395}$ have been solved in this study (Figure 3.3, Figure 3.9). Both important subunit *a2* peptides $a2_{1-17}$ and $a2_{368-395}$ have been recently shown to interact with ARNO (Arf-GEF) [96]. The peptide $a2_{368-395}$ of subunit *a2* has its binding site with amino acids 396-402 at the end of cytosolic region of the *a2* model, whereas peptide $a2_{1-17}$ of subunit *a2* is at the beginning of the N-terminal region (Figure 4.3) [96].

The NMR structure of $a2_{368-395}$ peptide (Figure 3.9) shows a flexible N- and C-terminal region and an α-helical part, which is in line with its secondary structure prediction using the PSI-PRED program (Figure 3.7B) [210]. The structure of $a2_{368-395}$ contains two helical formations, whereby the helical formation from G378 to Y386 might be essential for the interaction with other proteins such as ARNO as it shows hydrophobic and a negative charged surface potential (Figure 3.9). A flexible loop and a second helix from T372 to K374 can be identified, which might be essential for the interaction or regulation with other domains of ARNO as well. Furthermore, the solution structure of peptide $a2_{1-17}$ (Figure 3.3) indicates an α-helical formation in CD- as well as in NMR spectroscopy experiments. NMR data indicate an α-helical formation at the C-terminus from F5 to L17 and a flexible N-terminal domain from M1 to L4, which is also in line with the predicted structure based on the primary sequence using PSI-PRED program (Figure 3.1B) [210]. To analyse the interaction between $a2_{1\text{-}17}$ peptide and Sec7 domain of ARNO, NMR titration experiments were used as a qualitative peptide binding assay, revealing that the Sec7 domain (R_{61}-D_{252}) of ARNO binds specifically to the $a2_{1\text{-}17}$ peptide. The α-helical degree of $a2_{1\text{-}17}$ peptide (76%), with the amino acid sequence $_{1}$AMGSLFRSESMCLAQLFL$_{17}$ from 5 to 17 is quite high and might be important for the interaction with the Sec7 domain of ARNO. The representative NMR structure of $a2_{1\text{-}17}$ indicates at its α-helical segment one hydrophobic side formed by residues L4, M10, C11, L15, and L_{17} at one side and by L13, A14, F17 and L18 in the opposite side constitutes a promising surface for an hydrophobic and helix-helix interaction between subunit *a* and the Sec7 domain of ARNO. The residues F5, E8, M10 and Q14 indicated by the change of chemical shifts and the loss of intensity (Figure 3.5) are crucial for the association. Further titration studies using NMR confirm the binding between $a2_{1\text{-}17}$ and Sec7 domain of ARNO. ^{1}H-^{15}N HSQC spectra were recorded, when peptide $a2_{1\text{-}17}$ was titrated to the Sec7 domain of ARNO. The spectrum of the Sec7 domain of ARNO shows significant changes in the chemical shift, which come up to 18 peaks. This underlines that $a2_{1\text{-}17}$ probably joins entirely with its α-helical segment to the Sec7 domain. Since the changes in chemical shifts are significant, it can be suggested that the binding between Sec7 and $a2_{1\text{-}17}$ is strong. Furthermore, NMR titration experiments with the N-terminal segment $a_{1\text{-}388}$ from *S. cerevisiae* against Sec7 domain of ARNO show the same chemical shifts as $a2_{1\text{-}17}$ titration (Figure 3.13), which indicate $a_{1\text{-}388}$ interacts in a similar manner to Sec7 proteins like the mammalian $a2_{1\text{-}17}$. Hence the observed $a_{1\text{-}388}$ / Sec7 association supports the importance of subunit *a* and ARNO interaction and to be evolutionary conserved among eukaryotes (Figure 3.13).

The three-dimensional NMR structure of the peptide $a2_{1\text{-}17}$ was used to map and characterise the molecular interface between peptide $a2_{1\text{-}17}$ and the Sec7 domain. Therefore, *in silico* docking experiments were performed between $a2_{1\text{-}17}$ and Sec7 domain, showing that the peptide has its lowest energy in the groove between αG, αH and αJ of the Sec7 domain, that is similar to the Arf 1/6 small GTPases binding site (Figure 4.1) [2]. The peptide $a2_{1\text{-}17}$ forms an interface with its binding amino acids (F5, M10 and Q14) to αG, αH and αI helices of Sec7 domain (Figure 4.1, zoomed section) [2]. The detailed view shows that of $a2_{1\text{-}17}$ binding site on Sec7 domain overlaps with interaction site of the regulatory Switch 2 of Arf1 and Arf6 small GTPases [2]. This might indicate that subunit *a* competes with the Arf protein to the Sec7-ARNO binding site via various interaction sites to the Sec7 domain, to regulate the vesicular trafficking between endocytic receptor-mediated and macropinocytosis pathways [2].

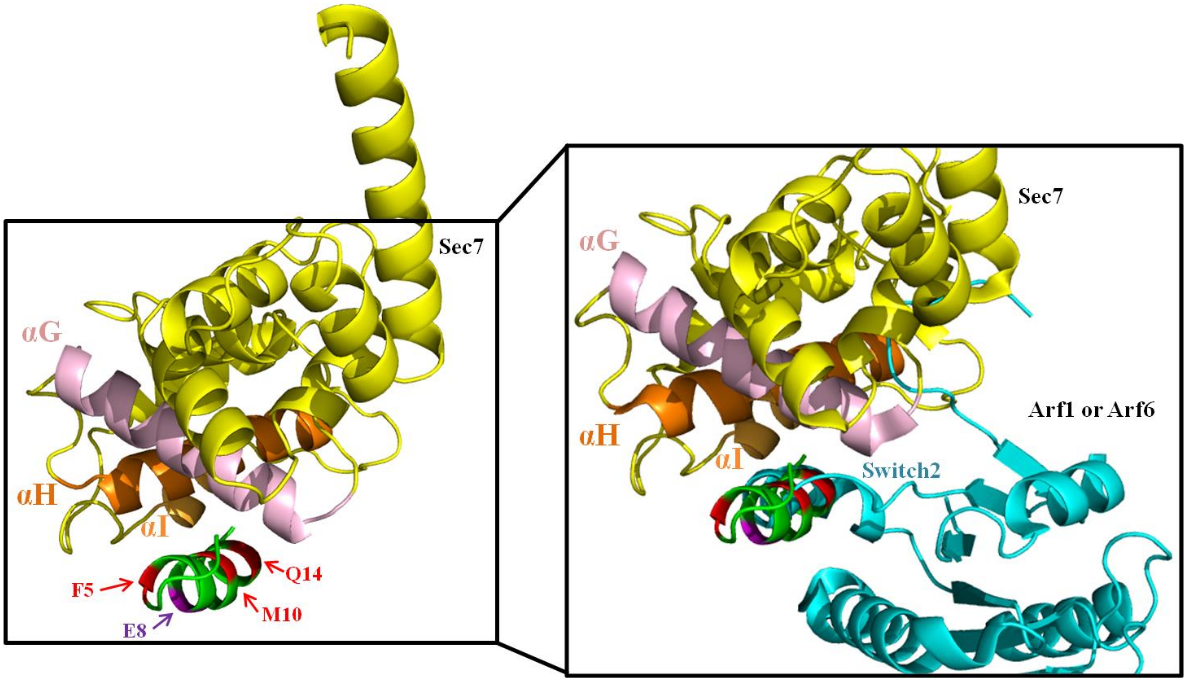

Figure 4.1: Putative binding site of the Sec7 domain to the *a2$_{1-17}$* peptide. Mapping and characterisation of the molecular interface between peptide *a2$_{1-17}$* and Sec7 domain, using *in silico* docking experiments performed with the program AutoDock v.4 [202]. The *in silico* docking experiments reveal the binding site of *a2$_{1-17}$* near the catalytic site of Sec7. The zoomed section includes Arf1 or Arf6 (cyan), whose Switch2 region is sharing competitively the same binding site to Sec7 domain.

Since the interaction of Sec7 domain of ARNO with *a2$_{1-17}$* from *M. musculus* and *a$_{1-388}$* of *S. cerevisiae* has been described earlier in this study, further analysis of different interaction sites of subunit *a* were performed to understand the control and regulation of the vesicular trafficking within the endocytotic and exocytotic pathway. With consideration of the six peptides of the mouse a2 isoform (*a2$_{1-17}$*, *a2$_{35-49}$*, *a2$_{195-214}$*, *a2$_{215-230}$*, *a2$_{313-331}$* and *a2$_{386-402}$*) that showed interaction to ARNO, the N-terminal truncated *a$_{104-363}$* has been constructed to omit the two peptides regions *a2$_{1-17}$* and *a2$_{35-49}$* with the strongest binding to ARNO (Figure 3.14, [96]). Hence, *a$_{104-363}$* has been purified and analysed in ARNO interaction studies. In this Sec7/*a$_{104-363}$* titration experiments, 4 peaks of the Sec7 spectrum showed chemical shifts whereof 1 peak, which is labelled as B occurred in the Sec7/*a$_{1-388}$* titration experiments (Figure 3.13 / Figure 3.16) [2, 3, 67]. In comparison to the NMR titration experiments between Sec7 and *Sca$_{1-388}$* (Figure 3.13), *Sca$_{1-388}$* showed 14 wide chemical shifts, indicating strong association with *a$_{1-388}$* mainly through its very N-terminal segment formed by *a2$_{1-17}$* and *a2$_{35-49}$* [2]. This result indicates that *a$_{104-363}$* is properly folded and still involved in binding to ARNO, which may occur via the homologues segment *a2$_{195-214}$*, *a2$_{215-230}$*, *a2$_{313-331}$* and/or *a2$_{386-402}$*.

In conclusion, in this study the specific and direct association between subunit *a2* formed by the first amino acids (A1- L17) via residues F5, E8 and Q14 and Sec7 of ARNO could be demonstrated. Further studies showed $a2_{1\text{-}17}$ as a significant part for signalling between V-ATPase and ARNO and a potent inhibitor of the enzymatic GDP/GTP-exchange activity of ARNO with both Arf1 and Arf6 as substrate [2]. *In silico* docking experiments revealed, $a2_{1\text{-}17}$ peptide binds to αG, αH and αI helices of Sec7 domain (Figure 4.1), the same binding pocket as Arf1 and Arf6 Switch 2 binding region [203, 219]. This leads to the assumption that $a2_{1\text{-}17}$ peptide competes with Arf1 and Arf6 GTP-binding proteins for the Sec7 binding site. The interacting amino acids F5 and Q14 are conserved in eukaryotic isoforms (Figure 3.6A, Figure 3.14). The data in this study revealed the structural basis and molecular mechanism between V-ATPase and ARNO.

4.2 Solution structure of the N-terminal segment of subunit *a*, $a_{104\text{-}363}$ from *S. cerevisiae* V-ATPase

Besides ARNO interaction studies, small-angle X-ray scattering (SAXS) of $a_{104\text{-}363}$, was carried out. The low resolution structure of $a_{104\text{-}363}$ confirmed its three dimensional folding. The structure reflects an elongated S-shape conformation with the dimension of 114 Å x 42 Å x 39 Å. Sequence alignment using the primary amino acid sequences of subunit *a* from *S. cerevisiae* V-ATPase and of the crystal structure of the cytosolic N-terminal segment of subunit *a*, $a_{1\text{-}301}$ ($Mra_{1\text{-}301}$), from the related archaea type A_1A_O ATP synthase from *Meiothermus ruber* [200] reveals a sequence identity of 12%. However, a structural alignment to the crystal structure of the cytosolic N-terminal segment of subunit *a*, $Mra_{1\text{-}301}$ [200] was performed using the software SUBCOMB [185]. Structural comparison between the homologous region $a_{80\text{-}268}$ ($Mra_{80\text{-}268}$) of the *M. ruber* structure with the low resolution solution structure of $Sca_{104\text{-}363}$ indicates high similarity in their dimension as both structures appear to be elongated. The superpose of the crystal structure of $Mra_{80\text{-}268}$ into the shape of $Sca_{104\text{-}363}$ is well aligned with an r.m.s. deviation of 1.8 Å (Figure 4.2, column 2). Moreover, the superposition of the entire crystal structure of $Mra_{1\text{-}301}$ accommodates also well into the solution structure of $Sca_{104\text{-}363}$ with an r.m.s.d. of 1.66 Å. Since both structures, $Mra_{80\text{-}268}$ and $Mra_{1\text{-}301}$ fit closely to the $Sca_{104\text{-}363}$ shape, it can be suggested that the truncation of 104 amino acids in $Sca_{104\text{-}363}$ does not affect its overall shape nor dimension (Figure 4.2, column 4).

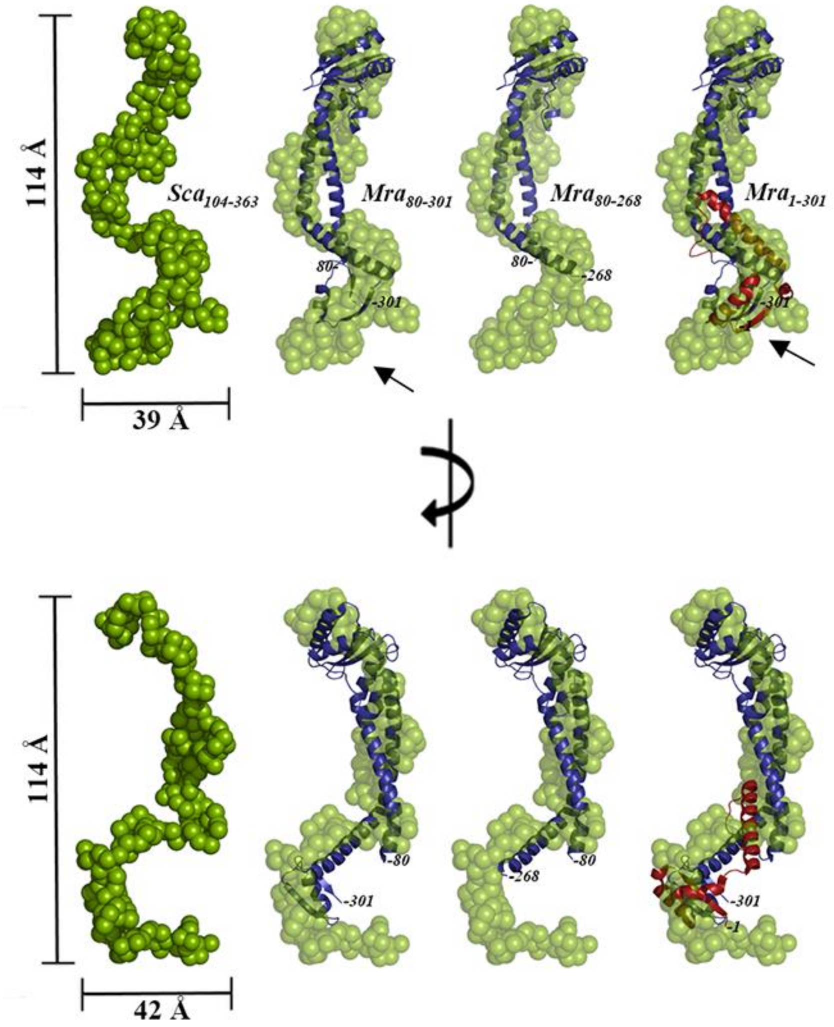

Figure 4.2: Superimposition of *$a_{104\text{-}363}$* with the crystal structure of the homologous subunit *a* (*Mra*). The homologous counterpart $Mra_{1\text{-}302}$, $Mra_{78\text{-}301}$ and $Mra_{80\text{-}268}$ of the A_1A_O ATP synthase from *M. ruber* were used for superimposition depicted in column 2-4, respectively [3, 200]. Column 2 the shape of $Sca_{104\text{-}363}$ is compared to $Mra_{1\text{-}301}$. The arrow in column 2 indicates the C-terminal loops of $Mra_{80\text{-}301}$ and $Sca_{104\text{-}363}$ shape. The protruding segment at the lower segment of $Sca_{104\text{-}363}$ reflects therefore the very C-terminus of $Sca_{104\text{-}363}$. Column 3 demonstrates $Sca_{104\text{-}363}$ superimposed to $Mra_{80\text{-}268}$. Column 4 shows the comparison of $Sca_{104\text{-}363}$ with $Mra_{1\text{-}301}$. The first 78 amino acids of $Mra_{1\text{-}301}$ are excluded in $Sca_{104\text{-}363}$ and highlighted in red. The arrow in column 4 indicates that N- (coloured in red) and C-terminus (blue) are in close contact to each other [3].

Further structural comparison of $Sca_{104\text{-}363}$ and $Mra_{80\text{-}301}$ displays the C-terminal loop of $Mra_{1\text{-}301}$ to the lower segment of the $Sca_{104\text{-}363}$ shape as indicated by an arrow (Figure 4.2, column 2). Therefore, the additional extended segment at the lower region of $Sca_{104\text{-}363}$ may represent the very C-terminus of $Sca_{104\text{-}363}$. Further structural comparisons between $Sca_{104\text{-}363}$ with its homologous segment $Mra_{80\text{-}301}$ as well as with the entire crystal structure $Mra_{1\text{-}301}$ allow to identify the remaining C-terminal 62 amino acids to the lower part of $Sca_{104\text{-}363}$ as highlighted with an arrow (Figure 4.2, column 2/4). Hence, both superpositions indicate that this protruding C-terminal region is located at the bottom loop domain of $Sca_{104\text{-}363}$ (Figure 4.2, column 3). In addition, $Mra_{80\text{-}268}$ can also be superimposed into the shape of $Sca_{104\text{-}363}$ (Figure 4.2, column 3), showing that the lobe of $Mra_{1\text{-}301}$, formed by the residues 268–302, are located at the C-terminal region of $Sca_{104-363}$ shape. The elongated central segment and the two lobes on both ends are still maintained (Figure 4.2A, column 3) [3]. Overall the solution structure highlights the dynamic of a structure with larger dimensions, in comparison to the rigid crystal structure. However, it is surprising that the dimensions and shape of $Sca_{104-363}$ and Mra_{1-301}, are not so different, implying that the first 78 amino acids of the N-terminus (red) are not included in the $Sca_{104-363}$. The comparison of $Sca_{104-363}$ and Mra_{1-301} indicates that N-terminus is located in close contact to the C-terminus (blue), which may highlight an stable and important role of the C-terminus [3].

Furthermore, using the novel solution structure of $Sca_{104-363}$ and its alignment to Mra_{1-301} crystal structure as well as the NMR titration experiments that has been performed earlier in this study with $Sca_{104-363}$ and a_{1-17} to the Sec7 domain of the ARNO, a structural model is proposed as shown in Figure 4.3A. The solution structure of $Sca_{104-363}$ accommodates like a_{1-17} also well into the groove formed by the helices αG, αH and αJ of the Sec7 domain [220], highlighting that the association to Sec7 may occur at the proximal lobe region without steric hindrance and clashes. A close view to the interaction model of the proximal lobe region of $Sca_{104-363}$ and the groove region of the Sec7 domain (Figure 4.3B), indicates that the two helices αH and αJ from the Sec7 domain are in close contact to $Sca_{104-363}$, that explains the chemical shifts in the NMR titration studies (Figure 3.16).

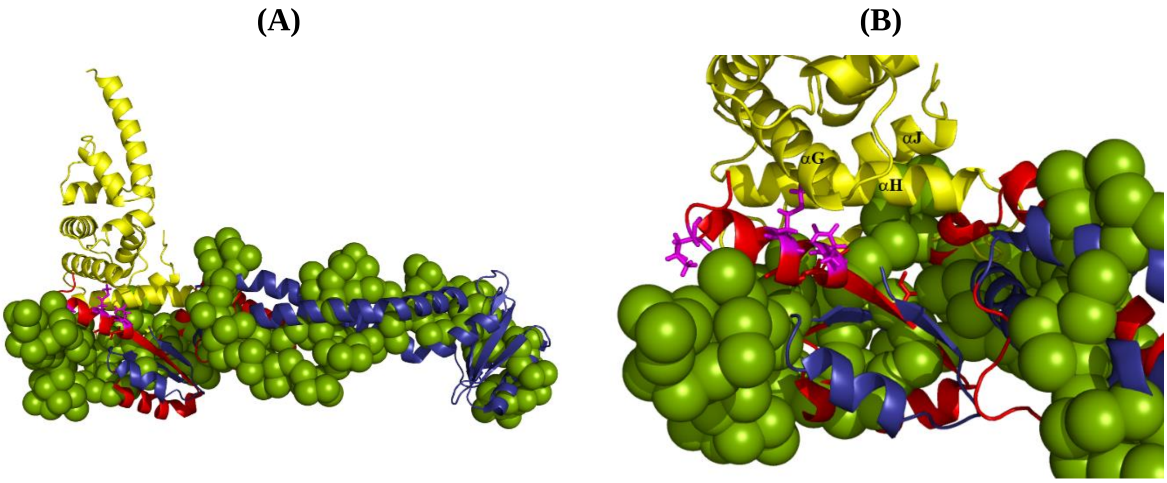

Figure 4.3: Interaction model between $Sca_{104-363}$ (green) and Sec7 domain of ARNO. (*A*) The $Sca_{104-363}$ solution structure and the Mra_{1-301} crystal structure (the N- and C-terminal ends are shown in *red* and *blue*, respectively) [200] were docked according to the $a2_{1-17}$ binding pattern as described earlier in Figure 3.6, whose binding residues are in magenta colour [2]. (*B*) The solution structure of $Sca_{104-363}$ (green) fits well to the groove between αG, αH and αJ of the Sec7 domain (PDB: 1PBV, yellow) [3, 220].

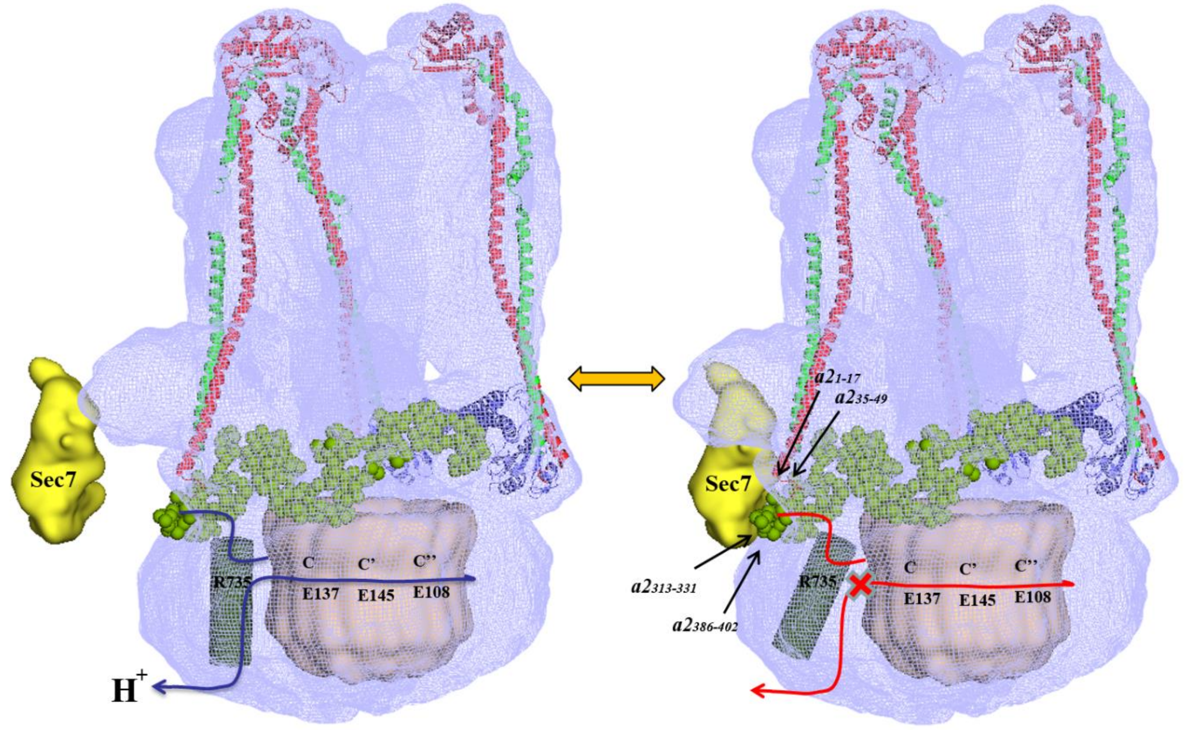

Figure 4.4: Proposed interaction model between V-ATPase and Sec 7 domain of ANRO. The 3D reconstruction of the V-ATPase from *S. cerevisiae* (EM Data Base ID: EMD-5476) [27] was used for the $Sca_{106\text{-}324}$ solution structure (green), subunit C (PDB: 1U7L blue) and the *c*-ring (PDB 2BL2) [221] fitting into their respective position in the EM density. Sec7 (yellow) [220] has been aligned respectively as described in Figure 4.3. The mechanistic model suggests that upon the Sec7 domain binding to the N-terminal $a2_{1\text{-}17}$ or the respective proximal lobe of $Sca_{106\text{-}324}$ will affect the proton translocation at the interface between the *c*-ring and the C-terminal membrane-embedded domain of subunit *a* (green cylinder) [3].

The low resolution structure of $Sca_{104\text{-}363}$ was superimposed into the 3D reconstruction of the *S. cerevisiae* V-ATPase (Figure 4.4) [27] and it fits clearly horizontal, above to the predicted *c*-ring. The $Sca_{104\text{-}363}$ solution structure forms a part of the so-called collar domain. Sec7 binds putatively to both N- and C-terminus at the proximal lobe region of $Sca_{104\text{-}363}$ through its groove located at αG, αH, αI and αJ (Figure 4.4) revealing the binding site of Sec7 and the N-terminal domain of subunit *a* is located near the hinge region, which joins the soluble N-terminal- with the membrane-integrated C-terminal domain involved in proton-translocation. In conclusion, the interaction between Sec7 of ARNO and the N-terminal domain of subunit *a* may cause structural changes at the hinge region of subunit *a*, which might affect the structure of the C-terminal domain (Figure 4.4). These structural alterations may cause also alterations in proton-pumping activity (Figure 4.4) [3].

4.3 Characterisation of the putative C-terminal topology of subunit *a*

Since the recruitment of Arf6 via subunit *c* has been demonstrated [1], it can be suggested that the C-terminal transmembrane part of subunit *a* of the V-ATPase may not be only involved in recruiting and scaffolding of small GTPases to their target membrane but also as a pH-sensor [1]. In several studies, mammalian transmembrane proteins have been identified as having pH sensing capability, whereby histidine residues have been identified in all of these proteins as an important component of the pH sensing mechanism [91]. Regarding the pH sensing of the *a*2 isoform of V-ATPase from mouse, it is suggested that histidine residues in *a*2 are involved in pH sensing. The mouse *a*2 subunit contains 21 histidine residues, of which seven residues (H_{93}, H_{130}, H_{236}, H_{246}, H_{248}, H_{278} and H_{310}) are located in the *a2N* cytosolic tail and are probably not involved in the pH sensing mechanism. The remaining 14 histidine residues are in the hydrophobic C-terminal transmembrane part [91]. The transmembrane part could also have a novel role as a modulator of Arf-GEF activity and ultimately as modulator of activity of Arf-family small GTPases. Furthermore, subunit *a* acts as a proton channel that is physically linked to the catalytic V_1 sector (Figure 4.4). The linkage between the V_1 and V_O part is not known so far. Therefore, the understanding of subunit *a* topology can give insight not only in recruiting and scaffolding of small GTPases like Arf6 and pH sensoring but also in the reversible assembly and disassembly of the V_1 and V_O complex, since subunit *a* is also associated with aldolase [10, 222]. Controversial predictions of six [223, 224], eight [70, 91, 225] or nine [67, 226] transmembrane helices are recently discussed. Because of the problems encountered with the expression and solubility of subunit *a* constructs $a_{468-552}$, $a_{478-537}$, $a_{596-634}$ and $a_{801-840}$ from several sources, further studies were focused with constructs $a_{653-727}$, $a_{673-731}$ and $a_{582-649}$. The proteins $a_{653-727}$, $a_{582-649}$, $a_{673-731}$ and $a_{801-840}$ were expressed and produced in *E. coli*. However, construct $a_{801-840}$ shows a ladder like oligomerisation in SDS-PAGE after purification. The phenomena that constructs close to the membrane embedded or transmembrane region, might not inducible or soluble is not surprising, since they are hydrophobic, which tend to cause the protein to be unfolded, oligomerise or aggregate. In comparison the larger construct $a_{653-727}$ showed a higher expression rate than $a_{673-731}$, therefore $a_{653-727}$ was focused in this study. CD spectrum of purified proteins constructs $a_{653-727}$ and $a_{582-649}$ reflects the consentaneous secondary structure (Figure 3.22). Since the protein constructs $a_{653-727}$, $a_{582-649}$, $a_{673-731}$ and $a_{801-840}$ are soluble, the transmembrane region and their putative soluble region of subunit *a* can be suggested as in Figure 4.5C. The number of transmembrane domain is still unclear, however the expression of the four proteins $a_{653-727}$, $a_{582-649}$, $a_{673-731}$ and $a_{801-840}$ gives new insights to approach the topological conformation of subunit *a*. These proteins are soluble and not membrane embedded. The proteins $a_{582-649}$ and $a_{673-731}$ are in line with *in silico* analysis (Figure 4.5A) [91, 223], whereas the proteins $a_{653-727}$ and $a_{801-840}$ are based on experimental analysis (Figure 4.5B) [38].

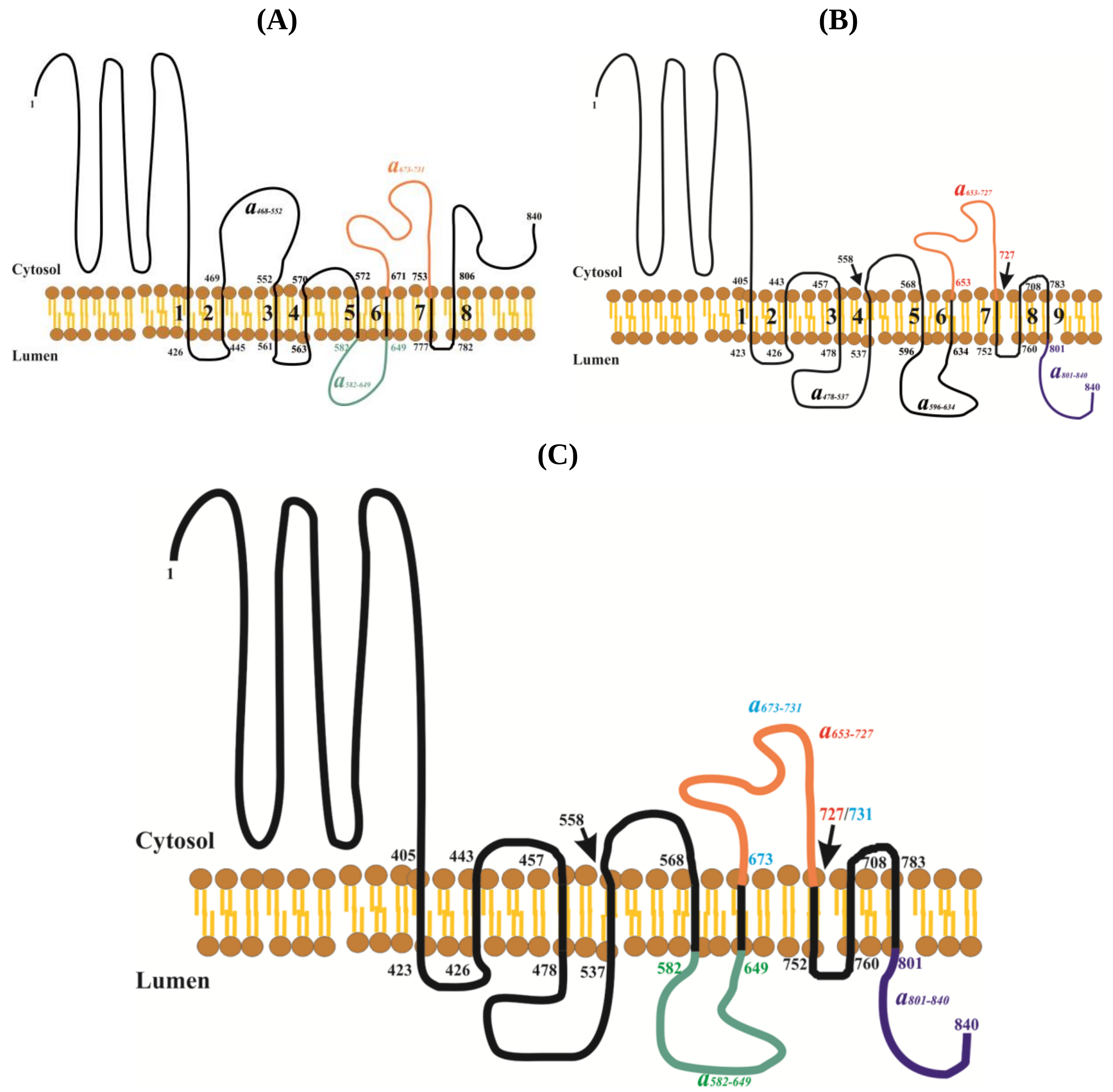
(A)
1
Cytosol
Lumen
a468-552
a673-731
840
469
552
570
572
671
753
806
1
2
3
4
5
6
7
8
426
445
561
563
582
649
777
782
a582-649
(B)
1
Cytosol
Lumen
a653-727
727
558
405
443
457
568
653
708
783
1
2
3
4
5
6
7
8
9
423
426
478
537
596
634
752
760
801
a478-537
a596-634
a801-840
840
(C)
1
Cytosol
Lumen
a673-731
a653-727
727/731
558
405
443
457
568
673
708
783
423
426
478
537
582
649
752
760
801
a801-840
840
a582-649

Figure 4.5: Model of subunit *a* from *S. cerevisiae*. *(A)* Topological model of subunit *a* predicted by *in silico* analysis with eight transmembrane domains [91, 223]. The construct $a_{673-731}$is shown in orange; $a_{582-649}$ in green and $a_{468-552}$ in black colour. *(B)* Topological model of subunit *a* based on cysteine mutagenesis, chemical modification and cloning and expression experiments [38]. The construct $a_{653-727}$ is shown in orange; $a_{801-840}$ is shown in purple and $a_{478-537}$ and $a_{596-634}$ in black colour. *(C)* Suggested topological model of subunit *a*, based on producible protein constructs $a_{653-727}$, $a_{582-649}$, $a_{673-731}$ and $a_{801-840}$, which are not embedded in the membrane.

The two analogue constructs $a_{673-731}$ and $a_{653-727}$, which have overlapping sequences, are predicted to be soluble based on either hydropathy analysis using 'Kyte-Doolittle' algorithm [91, 223] or experimental analysis [38]. Indeed both topological predicted constructs $a_{653-727}$ and $a_{673-731}$ are producible, soluble and can be purified. It can be suggested that the region with the residues 653-731 is not part of the transmembrane domain (Figure 4.5C). Two further analogues constructs $a_{582-649}$ and $a_{596-634}$ from either *in silico* or experimental analysis are having also overlapping amino acid sequences. Interestingly, the shorter construct $a_{596-634}$ [38] is not inducible. The longer constructs $a_{582-649}$ is inducible, soluble and can be purified, and hence more stable. It can be proposed that the region with the residues 596-634 is not part of the transmembrane domain as well. The topology of C-terminal transmembrane part of subunit *a,* which is supposed to be involved in recruiting and scaffolding of small GTPases to their target membrane as well as a pH-sensor, remains unclear and needs further investigation in the future.

4.4 Crystallisation of subunit *a* construct $a_{653\text{-}727}$

To get insights into the 3D structure of subunit *a* (Vph1p), crystallisation trials were done with construct $a_{653\text{-}727}$. Promising results were observed with the formation of needle clusters in an initial stage (Figure 3.23). Several optimisations of these conditions by varying precipitant, salt concentration and changing buffer or pH in grid screens and changing temperatures resulted in the formation of small crystals in a condition containing 0.2 M $MgCl_2$, 0.1 M cacodylate, pH 6.5, 15% PEG3350 (Figure 3.23). However, additional optimisation was performed with varying protein concentration; replacement of salt and adding of paraffin oil, which resulted in little improvements in the size of the crystals by slowing down the equilibration between protein drop and reservoir (Figure 3.24). Additional grid screens and Additive Screen^{TM} were used to reduce the water molecule in the protein structure to promote protein crystallisation. Moreover, micro- and macro-seeding at various steps were carried out (Figure 3.25). First, crystal diffraction could show initial diffraction up to 4-5 Å (Figure 3.26) at the in-house machine at 113 K (Rigaku). The diffraction pattern is not uniform and indicates an anisotropic pattern. Indexing and spot peaking of the diffraction data of ten diffraction images from different angles by HKL2000 suite program [176] showed higher unit cell parameters, indicating that they are twinned and not a single crystal. Diffraction spots are dispersed, but interfering or overlapping with other spots in the same image. Therefore, a series of optimizations were made by varying the different parameters and still under progress. However, additional conditions have to be optimised in future experiments that will result in larger sized and less numbers of crystals that show a diffraction pattern in high resolution.

4.5 Structural and functional characterisation of AhpR from *E. coli*

Besides the pH homeostasis, regulated via V-ATPases, redox homeostasis is highly significant for the survival of the cell. In particular the presence of superoxide and hydroperoxids increases the potential to damage all macromolecules within the cell [4-7]. Especially H_2O_2 (hydrogen peroxide) may inactivate critical enzymes, which contain sulfhydryl residues or iron-sulfur clusters at active-site by oxidizing their reactive thiols or iron (Fenton reaction), respectively [4-7]. The alkyl hydroperoxide reductase (AhpR) is the primary H_2O_2 scavenger and its over-expression reduces the frequency of spontaneous mutants [122, 227]. Since oxidative stress and H_2O_2 are involved in quite a number of diseases, AhpF and AhpC have been characterised to give new insights into oxidative stress [4, 166-169].

4.5.1 The overall structure of AhpF from *E. coli* reveals an elongated conformation

Here in this thesis the full length crystal structure of *E. coli* Alkyl Hydroperoxide Reductase subunit F (*Ec*AhpF) has been solved to 2 Å resolution. The structure revealed for the first time an alternative conformation for the NTD domain which may give new insights into the electron transfer mechanism to its substrate AhpC. The conformation has been further validated by solution structural studies using small angle X-ray scattering (SAXS).

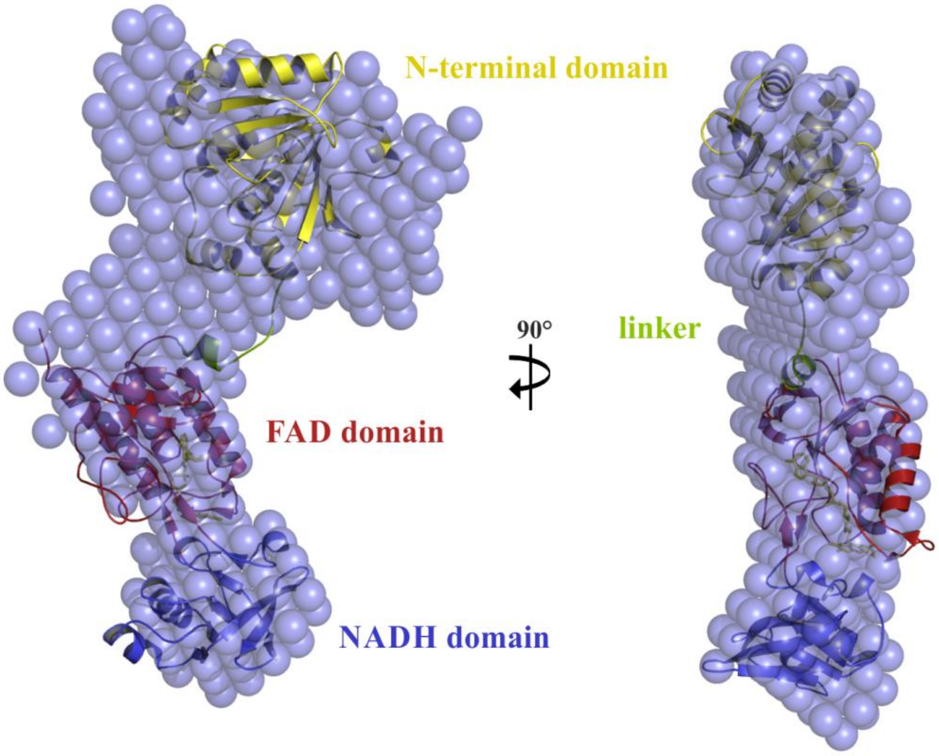

Figure 4.6: Superimpose of the *E. coli* AhpF solution structure and its crystal structure. The superimposition of the AhpF solution structure and the crystal structure were performed using SUBCOMB and reveals a high overall similarity in their dimension as well as in domain formation [185, 228].

Structural comparison of the overall AhpF crystal structure (Figure 3.37) and the low-resolution structure in solution (Figure 3.31), reveal a similar conformation of both, the AhpF crystal and solution structure (Figure 4.6). The low-resolution structure of AhpF, shown in blue spheres, as well as its crystal structure reflects an elongated and stretched conformation (Figure 4.6). The crystal structure of *Ec*AhpF compares well with the solution shape with an r. m. s. deviation of 1.19 Å. The NTD, FAD and NADH domains were fitted to the upper, middle and lower domains of the shape, respectively (Figure 4.6). In both structures all four regions, NTD, linker segment, FAD as well as the NADH domain are distinguishable and in line to each other (Figure 4.6). The dimensions of the solution structure are quite similar to the monomeric crystal structure. Only the upper domain is wider when compared to the crystal structure that may indicate a dynamic NTD in solution. The proposed dimer configuration of AhpF, as proposed in line with Thioredoxin Reductase (TrxR) is not visible in this solution structure, assuming AhpF to be in an catalytic inactive state, since neither NAD(P)H nor AhpC is present in solution.

4.5.2 The elongated conformation of AhpF gives new insights into its catalytic cycle

Structural comparison of the AhpF crystal structure from *E. coli* (*Ec*AhpF) to the homologous AhpF structure from *Salmonella typhimurium* (*St*AhpF) indicates that the folding of all four segments remains similar in both structures, when all domains have been compared separately (NTD domain: r.m.s.d of 0.54 Å for 192 Cα; FAD domain: r.m.s.d. of 0.64 Å for 184 Cα; NADH/SS domain: r.m.s.d of 0.72 Å for 119 Cα) (Figure 4.7) [135]. The *Ec*AhpF and *St*AhpF share high protein sequence identity of 95.4% and do not have any significant mutations that alter the structure and function. Furthermore, superimposition between the full-length *Ec*AhpF crystal structure solved in this thesis and the crystal structure of the C-terminal portion of the *E. coli* AhpF (A212-A521; *Ec*AhpF$_{212\text{-}521}$) reveals an r.m.s.d. value of 0.77 Å [137]. Major structural deviations are not found between both C-terminal portions. However, new in this full-length AhpF crystal structure from *E. coli* is the appearance of the 212 N-terminal amino acids, corresponding to the NTD (1-195) and linker region (196-209). Furthermore, the overall *Ec*AhpF conformation is different to *St*AhpF (Figure 4.7) [135]. *Ec*AhpF is stretched to an elongated conformation, so that NTD and the C-terminal segment, including the FAD and NADH/SS domain are apart to each other. *Ec*AhpF appears to be in an open conformation with the dimension of 120.5 x 58.9 x 44.2 Å, whereas *St*AhpF is in a compact and closed conformation [135] (Figure 4.7). In *Ec*AhpF, the two-redox centres C345/C348 in the NADH/SS domain as well as C129/C132 in the NTD reveal a distance of 72 Å, whereas the distance of the two redox centres in *St*AhpF is 35 Å (Figure 4.7). The NTD domain of *Ec*AhpF is rotated and translated by about 178º and 1.25 Å, respectively, when compared with *St*AhpF and the screw axis is almost perpendicular to the molecule and passes through the linker region that is connecting the NTD domain to the FAD domain (Figure 4.7). The residues near the screw axis can be considered as a hinge region for this motion. The linker region residues K201 to E205 are involved in the hinge motion for the NTD domain rotation. K201 and A202, is likely to be important as a hinge region residues as they are highly disordered in the *Ec*AhpF structure. Because of the possible hinge motion in the linker region, significant structural differences are observed (Figure 4.7). In the open conformation of *Ec*AhpF, the helix is locally unfolded (LU, A203-N208), while in *St*AhpF the helical region is fully folded (FF, K201-K209), in order to accommodate the large movement of the NTD domain (Figure 4.7). Although the residues 197-202 of this linker segment are fully folded, structural superimposition of the α-helix in the linker region of *Ec*AhpF reveals similar positioning as in *St*AhpF (Figure 4.7). In both structures, the α-helix is stabilised by residue N208 that forms polar contact to the V312 backbone of the FAD domain, keeping the α-helix of the linker segment close to the FAD domain.

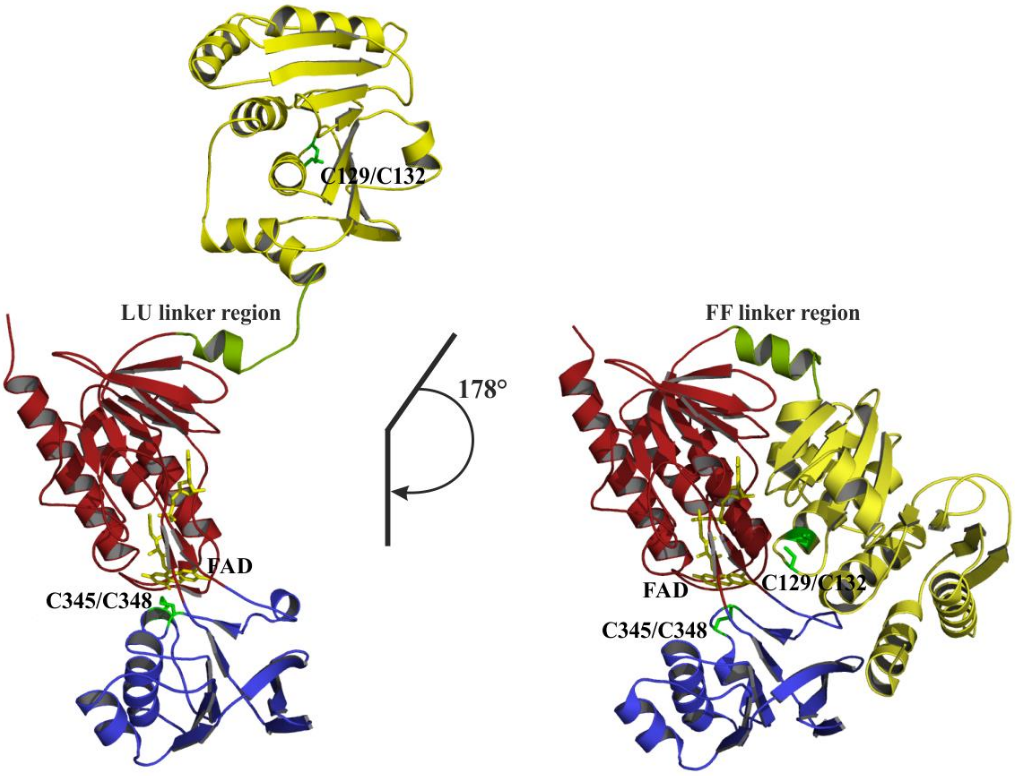

Figure 4.7: Structural comparison between *Ec*AhpF and *St*AhpF. The most significant structural difference observed is the positioning of the NTD domain. NTD domain of *Ec*AhpF is rotated and translated by about 178º and 1.25 Å compared to *St*AhpF. The helix in the linker region is in *Ec*AhpF locally unfolded (LU) (A203-N208) and in *St*AhpF is the helix fully folded (FF) (K201-K209), suggesting a large movement of the NTD domain along the α-helix in the linker region [135, 228].

Furthermore, the *St*AhpF linker has hydrogen bonding interactions (T197 to A193 and K201 to D114) with the NTD domain while the *Ec*AhpF linker region does not form any such interactions. The comparison also revealed a significant conformation difference in the NADH domain between the *Ec*AhpF and *St*AhpF structures. The *St*AhpF NADH domain is compared to the *Ec*AhpF NADH domain rotated about 9° and shifted about 0.79 Å about the screw axis running parallel through the centre of the molecule. The twisting region are formed by the residues K325-R327 and Q448-L451 in both structures. The residues K325, W326 and Q448 act as a mechanical hinge. Besides these structural similarities, the redox centre at the NADH domain shows significant structural difference observed between the *Ec*AhpF and *St*AhpF structures. In *Ec*AhpF, the C345-XX-C348 motif sits above the flavin moiety of the FAD molecule, forming a short helix with a right handed hook conformation, while in *St*AhpF, the C345-XX-C348 motif adopts a non-helical conformation and shifted away from the flavin moiety because of the bound chloride.

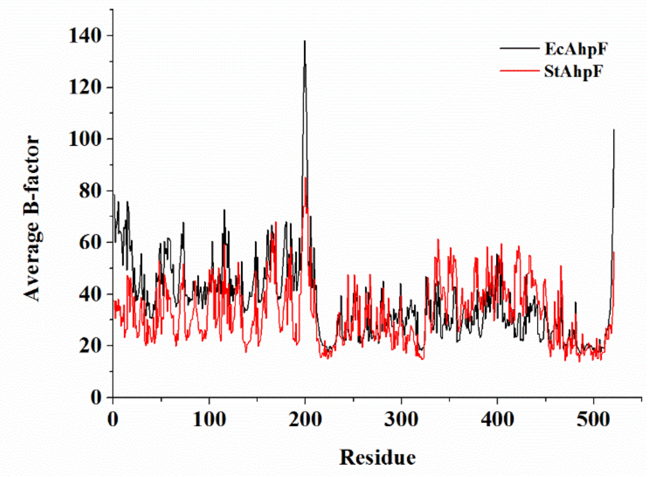

Figure 4.8: Overlay of *Ec*AhpF and *St*AhpF B-factors. The elongated NTD domain of *Ec*AhpF have high B-factor (63.1 Å^2) for main chain atom than the bent conformation (33.6 Å^2) of *St*AhpF. The B-factors from both FAD domains are similar, while the NADH domain from *St*AhpF reveals a slight higher B-factor than the NADH domain from *Ec*AhpF.

The B-factor comparison between *Ec*AhpF and *St*AhpF reveals that the elongated NTD domain has a high B-factor (63.1 Å^2) for main chain atom than the bent conformation (33.6 Å^2), indicating a local motion at this region (Figure 4.8). The α-helix formation (203-209) of *Ec*AhpF reveals a B-factor ~50 Å^2 for C_α atoms and the loop formation (197-202) > 70 Å^2 for C_α atoms, indicating a disordered and highly flexible loop formation in solution. Particularly G198, A199, E200 and K201 are revealing a B-factor > 110 for C_α atoms and may undergo the largest conformational change (Figure 4.8). The average B-factor of the main chain Cα atom for FAD domain is 24.11 and 24.92 Å^2 for *St*AhpF and *Ec*AhpF, respectively. The NADH domain of both structures reveals a difference in their average B-factor. The slight NADH domain rotation might be responsible for the higher B-factor in the *St*AhpF (41.57 Å^2) when compared to the *Ec*AhpF (31.18 Å^2). Overall it can be suggested that AhpF alternates between a close and open conformation, while

C345/C348 reduces C129/C132 in the close conformation and C129/C132 reduces the redox active disulfide C47/C166 of AhpC in the open conformation (Figure 4.7).

Moreover, because of the high structural and sequence similarity of *Ec*AhpF to TrxR [138, 142, 146], the mechanism for TrxR can be deduced analogously for *Ec*AhpF as shown in Figure 4.9. TrxR corresponds to the C-terminal portion and Thioredoxin (Trx) to the NTD of AhpF. Sequence alignment between the C-terminal portion alone and TrxR from *E. coli* reveals a sequence identity of 32 %, whereas NTD alone and Trx1 or Trx-2 reveal an identity of 13.8 % and 10.8 %, respectively. So far two structural states of TrxR are known, the flavin reducing state (FR) and the flavin-oxidised state (FO) (Figure 1.15) [138, 142, 146]. Structural comparison of the *Ec*AhpF C-terminal portion with TrxR from *E. coli* with flavin in the oxidised state (PDB: 1TRB) reveals an r.m.s.d. value of 1.35 Å for 292 Cα positions, reflecting a high similarity [138, 146].

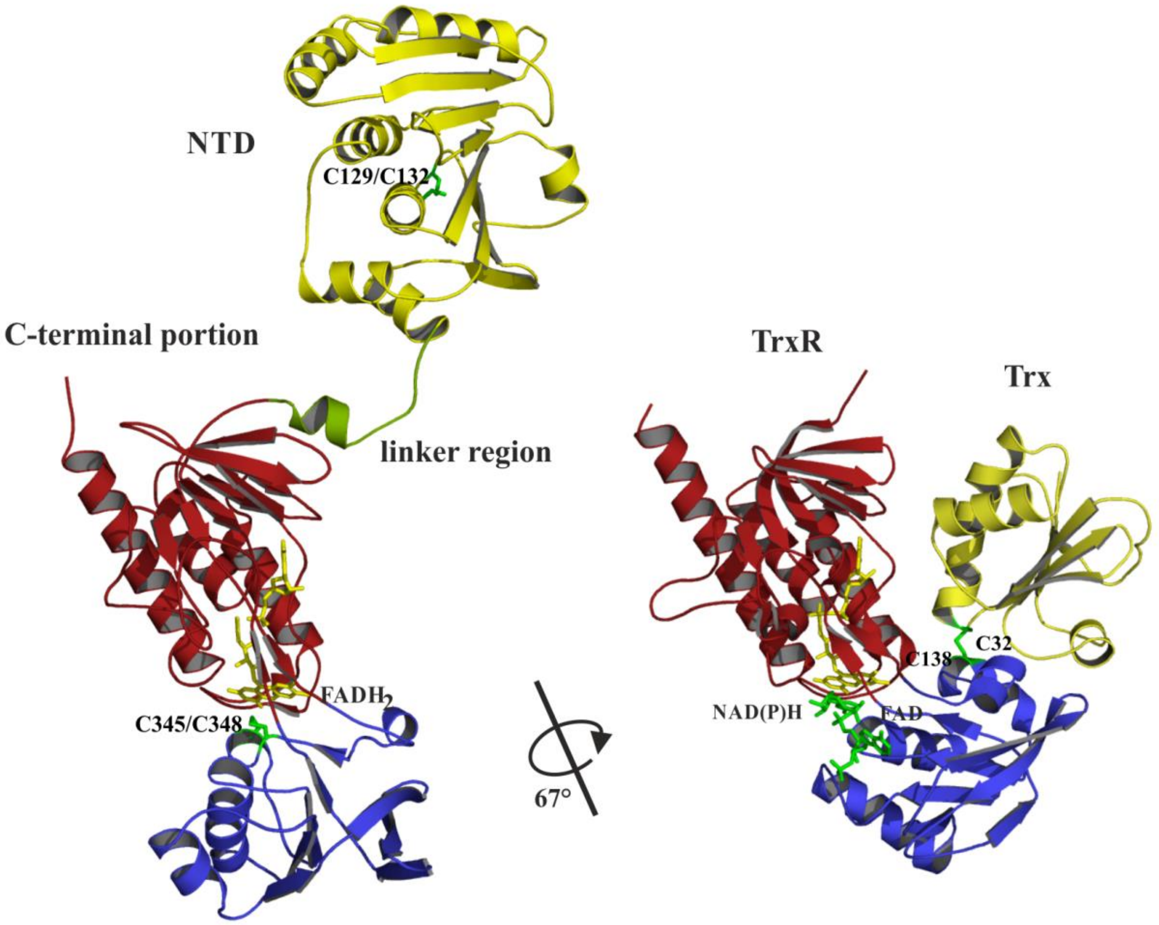

Figure 4.9: Structural comparison between *Ec*AhpF and TrxR-Trx complex from *E. coli*. The TrxR corresponds to the C-terminal portion and the Trx to the NTD of *Ec*AhpF [142]. The position of Trx is close to NADH domain while the NTD domain of *Ec*AhpF is apart from the C-terminal portion. The *Ec*AhpF structure has an additional linker region, which is absent in the TrxR-Trx complex. In both structures, the FAD- and NADH domain are very similar. If the FAD domain aligned separately, the NAD(P)H domain of TrxR is rotated by 67° [142, 228]

The flavin reducing conformation of *Ec*AhpF can be deduced by structural comparison to the reduced TrxR in its so called “twisted conformation” co-crystallised with Trx (PDB: 1F6M) (Figure 4.9) [142]. Both structures, in particular NADH- as well as the FAD domain of the C-terminal portion are very similar when the domains are aligned separately (FAD domain: r.m.s.d. of 0.64 Å for 119 Cα; NADH/SS domain: r.m.s.d of 0.72 Å for 89 Cα). If the FAD domain aligned separately, the NAD(P)H domain of TrxR is rotated by 67° (Figure 4.9). Similar to TrxR, the NADH domain of AhpF is assumed to adopt such a rotation. When such a rotation is also applied to AhpF, the entire NADH/SS domain comes closely to FAD, bringing a bound NAD(P)H to the *re*-face of the isoalloxazine ring of flavin [135, 137, 142] (Figure 4.9). The nicotinamide ring of NAD(P)H and the isoalloxazine ring system with its C-4-X above the isoalloxazine N-5 are brought to close contact for electron transfer [138, 142]. The rotation brings also the reduced dithiol (C345/C348) to the surface [142] (Figure 4.9). In this exposed position, reduced dithiol (C345/C348) can be easily oxidised via the redox active centre C129/C132 of NTD. When the NADH/SS domain turns 67° back, C345/C348 comes back to the *re*-face of the isoalloxazine ring, and the $NAD(P)^+$ to the surface for exchange with new NAD(P)H [142]. During the rotation of the NADH domain, the NTD might not be in its close conformation as shown in *St*AhpF (PDB: 1HYU) [135], otherwise severe clashes may occur between NTD and the NADH domain (Figure 4.7). It can be proposed that NTD remains as in the *Ec*AhpF crystal structure in an open and elongated conformation or in another so far unknown conformation, where no steric hindrance prevents this rotation. Such a NADH domain rotation similar to TrxR, can be indeed proposed for AhpF, since both proteins have beside high structural similarities also redundant function [136, 140]. The C-terminal portion of *Ec*AhpF reduces the NTD specifically, even when the C-terminal portion and NTD are expressed separately, but not the related Trx [136, 140]. Moreover, the C-terminal portion like TrxR reduces both Trx and NTD, when both expressed separately [136, 140]. Considering that the C-terminal portion of *Ec*AhpF prefers NADH and TrxR uses preferably NADPH for the reduction process (more details in section 4.5.4), the maintainance of reduced NTD relies on the cost of both NADH and NADPH, while reduced Trx only on the pool of NADPH. The reason for the specificity of the C-terminal portion of *Ec*AhpF to NTD and that in turn also to the *Ec*AhpC, but not Trx might be due to regulatory control or/and to save valuable NADH within the cell especially during an oxidative attack [140]. NTD, but not Trx recognises *Ec*AhpC specifically, this ensures that the majority of NADH in a cell is utilised into *Ec*AhpC, the first line of defense during oxidative stress.

4.5.3 The putative catalytic cycle of *Ec*AhpF

Due to the high structural similarity of *Ec*AhpF to TrxR and the close conformation of *St*AhpF [135], the entire mechanism of the AhpF catalytic cycle can be deduced analogously as shown in Figure 4.11. Overall it can be suggested that AhpF has two alternate movements, one at the NADH domain and another one at the NTD. In *Ec*AhpF, the NTD domain is in an open conformation to reduce the AhpC and the NADH domain adopts the stable FO conformation, where disulphide centre C345/C348 of the NADH domain are in face with flavin (Figure 4.11 conformation a). The NADH domain of *Ec*AhpF may also adopt two distinct conformational changes namely flavin oxidised (FO) and flavin reduced (FR) states similar to the TrxR-Trx complex from *E. coli* [142]. While changing to the FR state, the NADH domain twists about 67° and would permit reduction of FAD by NADH and dithiol-disulfide interchange with NTD (Figure 4.11 conformation b). The second movement alternates between the close and open conformation, while C345/C348 reduces C129/C132 in the close conformation and C129/C132 reduces the redox active disulfide (C47/C166) of AhpC in the open conformation (Figure 4.11).

The redox active centre C129/C132 of NTD is only brought close to C345/C348 disulfide centre of the C-terminal region, when C345/C348 is exposed to the surface and the linker region turns 178° downwards (Figure 4.11 conformation b-c). While turning, the locally unfolded residues 196-202 of the open conformation are bending downwards, following the helical turn. The residues 196-200 of this linker segment remain disordered in the fully folded *St*AhpF structure, whereas the residues 201-203 are forming the additional α-helical turn that brings NTD downwards. It is noteworthy that the details of the AhpF transition state during the hydride transfer from C345/C348 to C129/C132 are not clearly understood. The crystal structure of *St*AhpF (Figure 4.11, conformation c) may represent a possible position of NTD in which electrons maybe transferred from the NADH/SS domain (C345/C348) to the NTD redox active disulfide bond (C129/C132) [135]. However, while C345/C348 reduces C129/C132, the NADH domain or the NTD as shown in the reduced TrxR structure and *St*AhpF respectively, may have to go an additional conformational alteration, to bring C345/C348 and C129/C132 in closer contact (Figure 4.11 conformation d). After reducing the disulfide C129/C132 via C345/C348 of the NADH/SS domain, the NTD undergoes the conformational change, back to its elongated open conformation, giving the possibility of hydride transfer from the NTD redox active disulfide bond (C129/C132) to the redox active disulfide bond (C47/C166) of AhpC (Figure 4.11, conformation d). In this conformational change, the linker region that connects NTD to the C-terminal portion of *Ec*AhpF must undergo a 178° turn back to its elongated conformation, while the α-helix (203-208) unfolds to its LU state, containing only one helical turn (Figure 4.11 conformation d). The catalytic cycle of AhpF is completed after the transfer of electrons from NAD(P)H to the redox active disulfides C47/C166 of AhpC via its three integrated redox centres of *Ec*AhpF. Both conformational changes, the bending of NTD and twisting of the NADH domain, may occur in a well co-ordinated manner, in order to trap the NTD by the NADH domain to reduce the C129/C132 disulphide.

While the motion of TrxR is solely a twisting of the ball within the socket [142], the homologues AhpF has an additional hinge down movement of the NTD (Figure 4.11). The newly proposed alternate hinge movement of the NTD reveals also large conformational changes, which are plausible, since no steric hindrance or clashes with other domains may occur. Furthermore, the NTD is neither involved in the dimer-dimer interface between two AhpF molecules nor involved in any domain interaction within an AhpF molecule. NTD is therefore not locked in its position. Such large conformational movements of domains have been observed in a number of enzymes. Similar large hinge up and down movement has been observed in calmodulin and in GroEL [229, 230]. For integrin a so called ‘bent and upright’ conformation has been proposed [231]. Large rotation that involves breaking and remaking of interface contacts were described for iron binding to lactoferrin [232].

This thesis revealed a new AhpF conformation in that NTD is playing a crucial part in acting as a substrate for the C-terminal portion, and reduced NTD acts as a major catalytic component in protein disulfide reductase activity for AhpC reduction [132, 135, 140, 142].

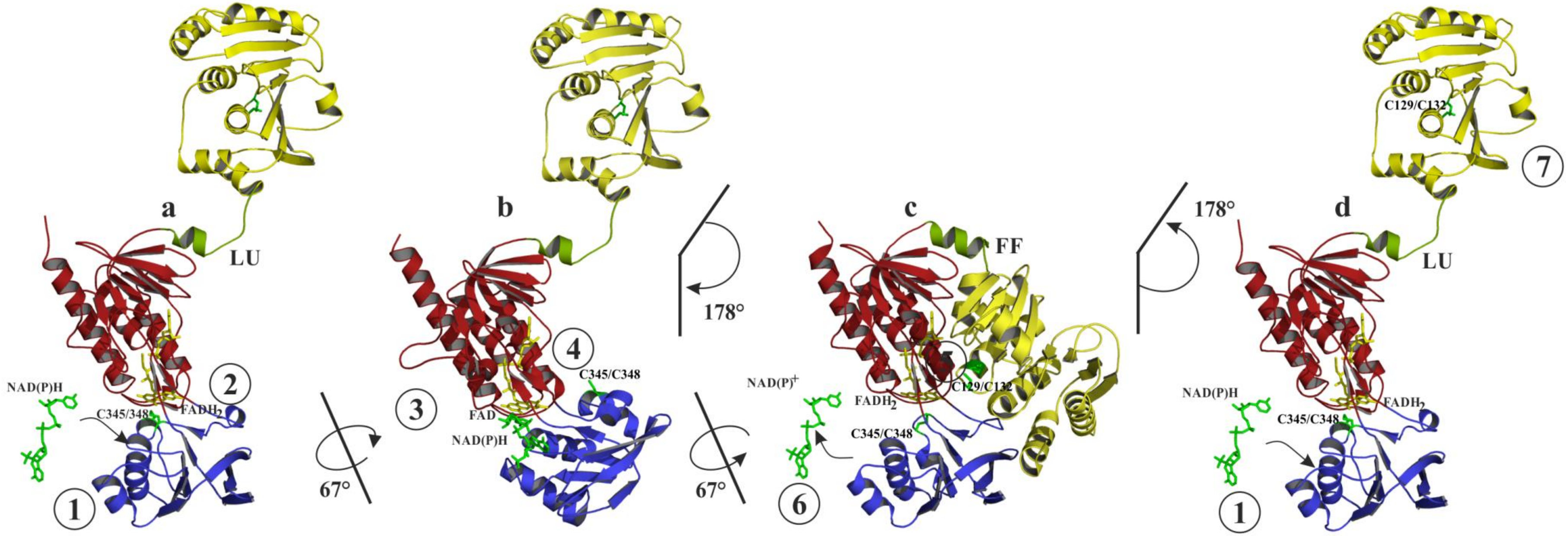

Figure 4.10: The putative catalytic cycle of AhpF from *E. coli* shown in a monomeric conformation. AhpF molecules are coloured according to their domains. The second monomer of the AhpF dimer is not depicted in this figure for easier visualisation. The catalytic cycle of AhpF involves in total three conformations, including two alternate movements of the NADH/SS domain and NTD. Different conformational states are depicted and labelled a-d. In each conformation two simultaneous steps occur (a) *Ec*AhpF in its open conformation, NAD(P)H binds to NADH/SS domain and $FADH_2$ reduces C345/C348. (b) Proposed *Ec*AhpF structure modelled based to the reduced TrxR structure (PDB: 1F6M), that involves 67° rotation of the NADH domain, bringing a bound NADH close to flavin and C345/C348 exposed at the surface of the structure [142]. In this conformation NAD(P)H reduces FAD to $FADH_2$ and C345/C348 is in its position to reduce C129/C132 of the NTD. (c) NTD undergoes large conformational changes, bringing C129/C132 closer to C345/C348 for hydride transfer as shown in the homologous AhpF structure from *S. typhimurium* [135]. The redox active centre C345/C348 of the NADH/SS domain or NTD in the *St*AhpF crystal structure may have to go in this step an additional conformational change, to bring C345/C348 and C129/C132 in closer contact. Subsequently, the NADH domain rotates back and releases $NAD(P)^+$. Disulfide bond C345/C348 turns also back into close distance to $FADH_2$, where it will be reduced. (d) *Ec*AhpC turns back into its elongated open conformation to reduce the redox active disulfide bond (C47/C166) of AhpC. The catalytic cycle of AhpF restarts with the binding of NAD(P)H to NADH/SS domain [228].

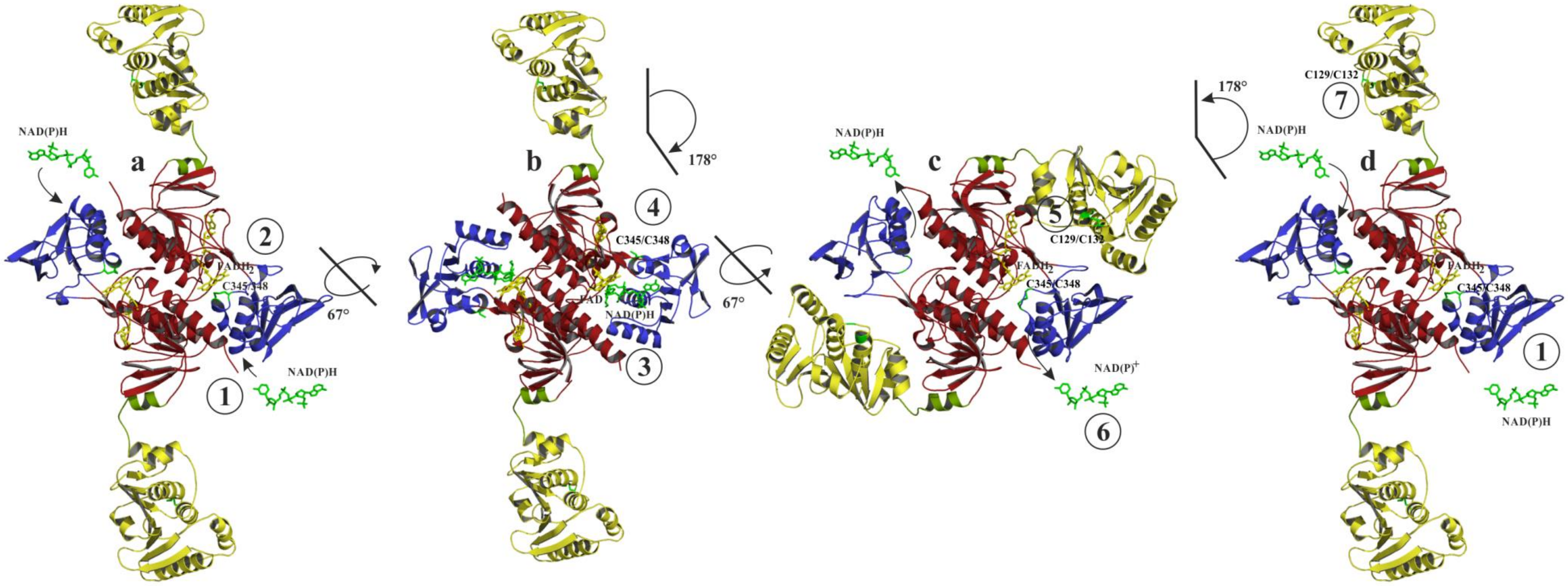
NAD(P)H
a
②
FADH2
C345/C348
67°
①
NAD(P)H
b
178°
④
C345/C348
FAD
NAD(P)H
③
67°
NAD(P)H
c
⑤
C129/C132
FADH2
C345/C348
NAD(P)+
⑥
178°
C129/C132
⑦
NAD(P)H
d
FADH2
C345/C348
①
NAD(P)H

Figure 4.11: The putative catalytic cycle of AhpF from *E. coli* in dimer formation. AhpF molecules are coloured according to their domains. The catalytic cycle of AhpF in dimer conformation may occur as described in Figure 4.10 and involves three conformation including two alternate movements of NADH/SS domain and NTD. Different conformational states are depicted and labelled a-d [135, 142, 228].

4.5.4 The redox active sites of AhpF from *E. coli*

The detailed comparison of the redox active centres of *Ec*AhpF structure with *St*AhpC as well as with TrxR reveals similarities as well as deviations (Figure 4.12). Like the *St*AhpF crystal structure, *Ec*AhpF lacks the NADH cofactor in its NADH binding pocket, since no NADH was added during crystallisation [135]. Instead, sulfate, glycerol and PEG molecule from the crystallisation solution occupies the NADH binding channel (Figure 4.12). In comparison, the TrxR structure with $NADP^+$ bound (PDB 1TDF, [138]) contains a conserved G-X-G-X-X-A motif common for $NADP^+$ binding proteins as well as positive charged and conserved H175 and R176, favouring the contact of 2'phosphate of adenine into its binding pocket (Figure 4.12) [233]. *Ec*AhpF has similar to *St*AhpF, instead of A a conserved G, common for NADH binding enzymes with the motif G-X-G-X-X-G (Figure 4.12) [234]. Furthermore, *Ec*AhpF has instead of the positive charged H175 and R176 the negative charged E385 and the bulky F386 in the binding pocket, creating an unfavourable condition for the negatively charged phosphate (Figure 4.12). This suggests a preference of NADH to NADPH in *Ec*AhpF.

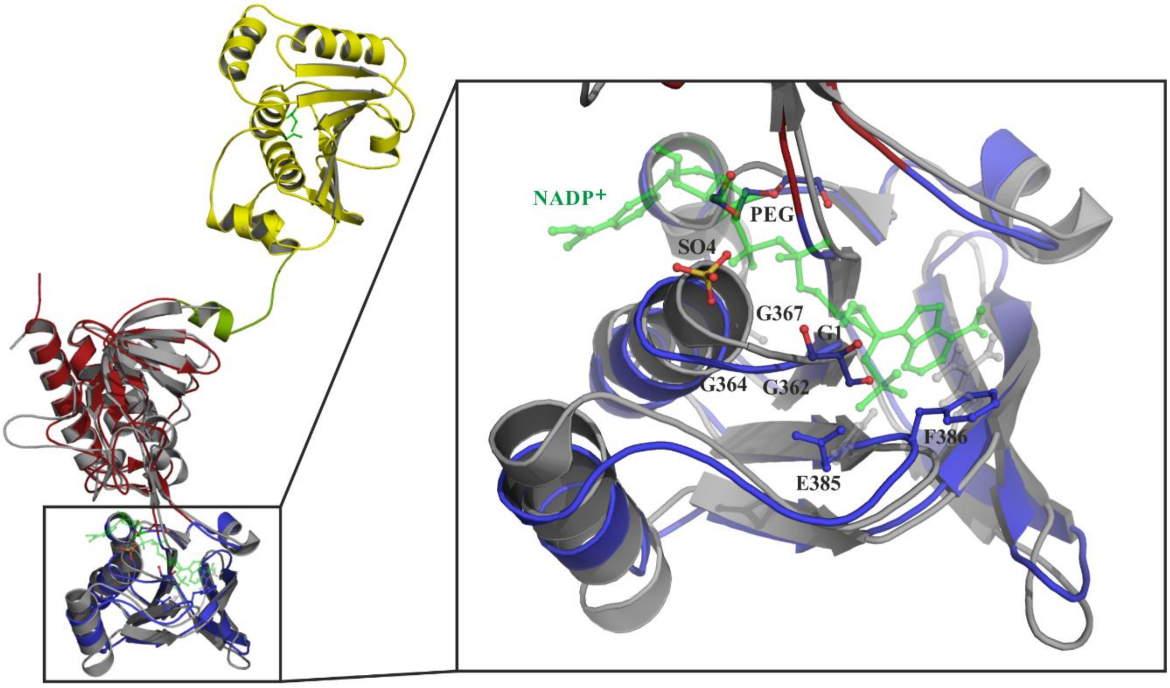

Figure 4.12: NADH binding pocket of *Ec*AhpF and TrxR from *E. coli*. TrxR structure (grey) contains a bound $NADP^+$ (green) (PDB 1TDF, [138]), a conserved motif G-X-G-X-X-A common for $NADP^+$ binding proteins and the positive charged H175 and R176 (transparent). *Ec*AhpF has a NADH binding pocket with the G-X-G-X-X-G motif [234], that contains a sulphate, a glycerol and a PEG molecule. Instead of the positive charged H175 and R176, *Ec*AhpF has the negative charged E385 and the bulky F386 in the binding pocket, creating an unfavourable condition for the negatively charged phosphate.

The cofactor FAD is present in this structure and accommodates well into its binding pocket (Figure 3.37) similar to the crystal structure of *Ec*AhpF$_{212\text{-}521}$ [137]. The NADH/SS domain harbours the NADH binding site as well as the redox active disulfide (C345/C348) located near flavin (Figure 3.38B). Cysteinyl residues C345/C348 with CXXC structural motif, also common in thioredoxin and TrxR, form the redox-active disulfide in the NADH/SS domain of the C-terminal portion. This CXXC motif of the NADH/SS domain is located closely to the flavin and adapts a short α-helix with a right handed hooked disulfide conformation (Figure 3.38A). The residues C345 and C348 of the NADH/SS domain are in this AhpF structure in an oxidised state and forming a well-defined disulfide bridge (Figure 3.38C). The disulfide bond C345/C348 remains stable and not reducible, even the usage of 20 mM DTT and 1 mM TCEP (tris (2-carboxyethyl) phosphine) while crystallisation could not open this disulfide bond. Probably the close distance to FAD stabilised its configuration. The closest distance between FAD and the redox active disulfide C345/C348 is from the C-4-X of the isoalloxazine ring system to the sulphur of C348 residue with a distance of 3.1 Å (Figure 3.38), which is similar to the crystal structure of *Ec*AhpF$_{212\text{-}521}$, that reveals a distance of 3.0 Å [137].

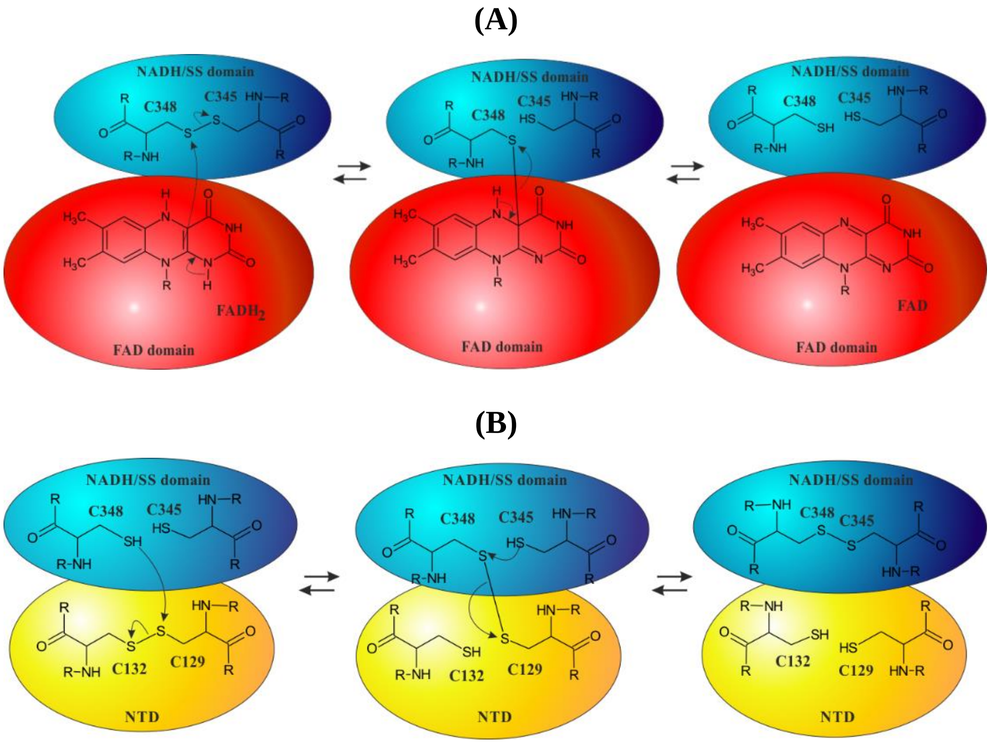

Figure 4.13: The proposed electron transfer among the redox active centres in *Ec*AhpF. (*A*) The C345/C348 disulfide bridge of the NADH/SS domain (blue) is in close proximity to FAD in FAD domain (red) for electron transfer. C348 is the proposed direct electron acceptor. (*B*) The redox active C129/C132 in the NTD (yellow) is subsequently in close contact to C345/C348 for hydride transfer. C129 is playing a crucial role during the electron transfer.

The close distance of the homologous C349 to flavin in *S. typhimurium* has been proposed earlier in spectral analysis using circular dichroism in visible spectrum of single and double *St*AhpF cysteine/serine mutants [139], which is in line with the *Ec*AhpF crystal structure. It can be therefore proposed that C348 is the hydride acceptor in this redox reaction as shown in Figure 4.13A. The NTD redox centre (C129/C132), which is located in the C-terminal thioredoxin fold is in its reduced (dithiol) form of this *Ec*AhpF structure (Figure 3.38D), although no reducing agent like DTT or TCEP has been used in this depicted structure. The sulfur-sulfur distance between the cysteines is 3.04 Å (Figure 3.38D). C129 is in comparison to C132 exposed, while hydrophobic residues V171 and *cis*-P172 shield C132. Since C129 is more accessible than C132, it can be suggested that it may play two crucial roles during the *Ec*AhpF catalytic cycle as shown in Figure 4.13AB. C129 might be the point of attack in its disulfide form during hydride transfer from C345/C348 redox centre as well as the attacking nucleophile during electron transfer from AhpF to AhpC. In this *Ec*AhpF crystal structure, C129/C132 is fully reduced even no reducing agent has been used during crystallisation. It can be assumed that C129/C132 disulfide bridges were reduced by the C345/C348 redox centre to its dithiol form (Figure 4.13B). Furthermore, since AhpC was not present in crystallisation solution nor other electron acceptor, C129/C132 remain trapped in its reduced state in this crystal structure (Figure 3.38C, Figure 4.13B). From this 2 Å AhpF crystal structure can be concluded that two cysteines C348 and C129 of the two redox active disulfide bonds are important for the electron transfer from FADH to AhpC.

4.6 Structural characterisation of AhpC from *E. coli*

Besides AhpF, the Alkyl Hydroperoxide Reductase (AhpR) consists of a second protein, namely AhpC. The crystal structure of AhpC has been solved in this thesis to 3.3 Å resolution in its oxidised form. Overall the crystal structure of AhpC from *E. coli* reveals five molecules (A-E) in an asymmetric unit, that forms a decamer structure, generated by its crystallographic two-fold symmetry operation (A'-E') (Figure 3.44). Comparison of structural features of the AhpC structure from *E. coli* with other currently available AhpC models highlights special features of the oxidised state of this structure. Besides the clearly visible disulfide bridge between C_P47 and C_R166' (Figure 3.45B), is the unwound C_P-loop, another feature which is formed due to the local unfolding of α2-helix, that exposes C_P47 with its sulfenic acid (C_P-SOH) and allows therefore C_R166' to condensate with the release of water to an intermolecular disulfide bond (C_PS-SC_R). The overall topology of AhpC from *E. coli* (*Ec*AhpC) is similar to AhpC from *S. typhimurium* (*St*AhpC). Superposition using secondary structure matching of

*Ec*AhpC and *St*AhpC (PDB: 1YEP) gives r.m.s. deviation of 0.82 Å for common 796 Cα residues [134]. Likewise to *St*AhpC, the two cysteines, C47 of one *Ec*AhpC molecule and C166' of another *Ec*AhpC' form a disulfide bond to stabilise its dimer formation in the crystal structure (Figure 3.45). The dimeric interface of *Ec*AhpC covers 1258.2 $Å^2$ at each monomer, which is 14.3 % of the solvent accessible surface area of a monomer [215]. This dimer interface is stabilised besides the two disulfide bridges, mainly by hydrogen bonds and salt bridges at its β7 interface (Figure 3.45A). The distance between the two redox active disulfide within one dimer is 40 Å and therefore likely to be functionally independent. The sulphur atom of C166 is partially exposed to the surface, whereas that of C47 is completely buried (Figure 3.45). C166 is therefore likely to be the point of attack for the hydride transfer from C129 of *Ec*AhpF and C47 the active centre for the peroxidation of H_2O_2 (Figure 3.45A) [153]. The C166 reduction via C129 of AhpF is likely a two-step reaction, in which the first reaction takes place between C166 of *Ec*AhpC and C129 of *Ec*AhpF to form a mixed disulfide bond between the two molecules, whereas the second reaction breaks the disulfide bond through an attack on C129 by C132 of *Ec*AhpF (Figure 4.14).

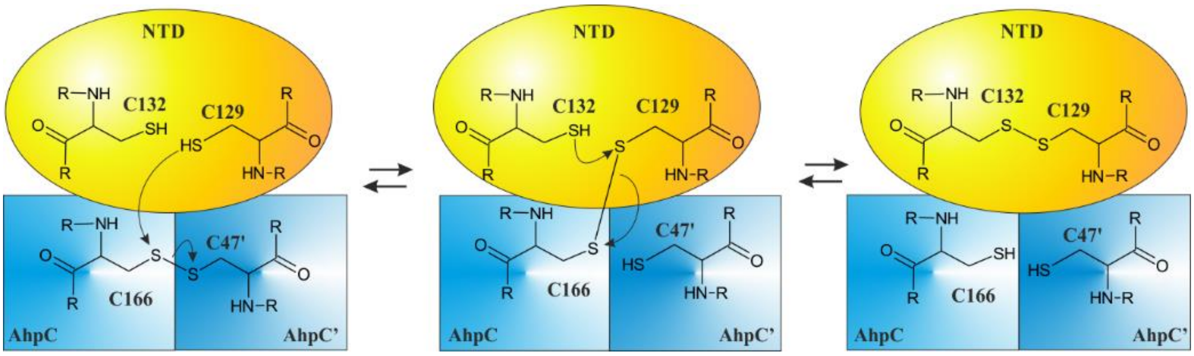

Figure 4.14: The proposed electron transfer between the redox active centre of *Ec*AhpF and *Ec*AhpC. The final of electron transfer of *Ec*AhpF is completed after hydride transfer from the crucial C129 to the partially exposed C166 of AhpC.

The suggestion that C166 of *Ec*AhpC is the point of attack of C129 of AhpF is in-line with earlier studies shown that only C132S AhpF incubated with TNB-linked C46S AhpC generated a significant amount of higher molecular weight complex [235].

4.6.1 The catalytic cycle of AhpC from *E. coli*

Oxidised AhpC is only functional active for its peroxidative activity after reduction of its cysteines to their thiol form via AhpF. In this reduced state, when all cysteines are in thiol form, the dimer as well as the decamer formation remains stable, even no disulfide bond stabilises the dimer interface. It can be suggested that the redox active disulfides between the corresponding AhpC dimer undergo conformational changes between the oxidised and reduced state to stabilise the dimer as well as oligomer interfaces. Structural comparison with the crystal structure of the *St*AhpC(C47S) mutant in its so called reduced state (PDB: 1N8J) may help to understand the catalytic cycle of the redox active disulfide bond, which is located near to the dimer interface (Figure 3.45A, Figure 4.15) [153]. The structural comparison reveals that the dimer interface of *St*AhpC(C47S) is formed between β7 and β7' of each monomer, which is similar to the oxidised structure of *Ec*AhpC (Figure 4.15). The β7 and β7' interface is as shown in the oxidised AhpC structure (Figure 3.45A) stabilised by hydrogen bonds and salt bridges (Figure 4.15). However, there are two major differences at the dimer interface between the oxidised and reduced AhpC structure.

The first difference involves the redox active cysteines C47/C166 and the α2-helix, in which C47 is located. In the oxidised form of AhpC, the dimer interface is stabilised by the two disulfide bonds, while the C_P-loop at C47 is unwound. Due to the local unfolding of α2-helix, C_P47 is exposed to form an intermolecular disulfide bond with C166 the resolving cysteine (C_PS-SC_R) (Figure 3.45B, Figure 4.16A). The remaining C-terminal residues after C166 are highly flexible and not visible in this crystal structure and may have no function in the oxidised state (Figure 4.16A). In the reduced state, α2-helix winds to its fully folded (FF) conformation, bringing C47 and C166' more than 10 Å apart and the sulphurs to opposite directions (Figure 4.16B) [147]. This conformational change brings peroxidatic cysteine C_P47 to its active site. During hydroperoxide decomposition, C_P47 is oxidised to cysteine sulfenic acid, which leads to local unfolding (LU) of the active site at C47 and converts the C_P loop into a solvent accessible area and bringing C47 back to its position in oxidised state. In this oxidised state position, C47 is

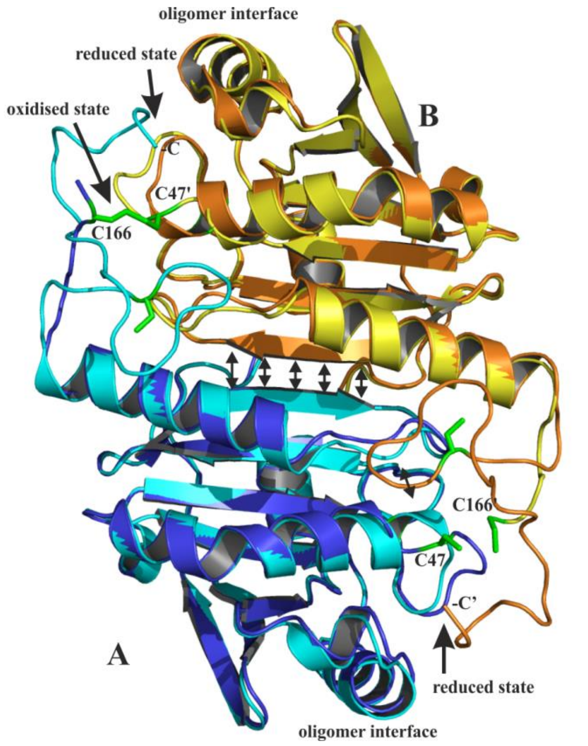

Figure 4.15: Superposition of AhpC dimer crystal structures. The *Ec*AhpC crystal structure in oxidised form is depicted in yellow and blue colour, whereas the reduced *St*AhpC crystal structure (PDB: 1N8J) in orange and cyan colour. The dimer interface at β7 and β7' is similar between the *Ec*AhpC oxidised and *St*AhpC reduced form [153, 228].

exposed to form a disulfide bond with the resolving cysteine C_R166 (Figure 3.45B). The disulfide bond is holding the two partner monomers together in oxidised state (Figure 4.16A).

The other major difference is the C-terminal amino acids after C166, which are not flexible in the reduced *St*AhpC(C47S) structure and hence visible in the crystal structure (Figure 4.16) [147]. The C-terminal end of one monomer reaches across the dimer interface to the other monomer in the reduced state, to hold both monomer together at the dimer interface (Figure 4.15**,** Figure 4.16B) [147]. It can be observed that in the reduced *St*AhpC, the residues from C166 onwards are forming defined hydrogen bonds at two regions to their partner molecule. The first region includes the residues C166, K169 and A168, forming four hydrogen bonds to G139', G142', R143' and T49', respectively, highlighted by arrows (Figure 4.16B). Interestingly, T49 is located at α2-helix. The winding to the fully folded α2-helix forms an additional interface for hydrogen bond to A168 (Figure 4.16B).

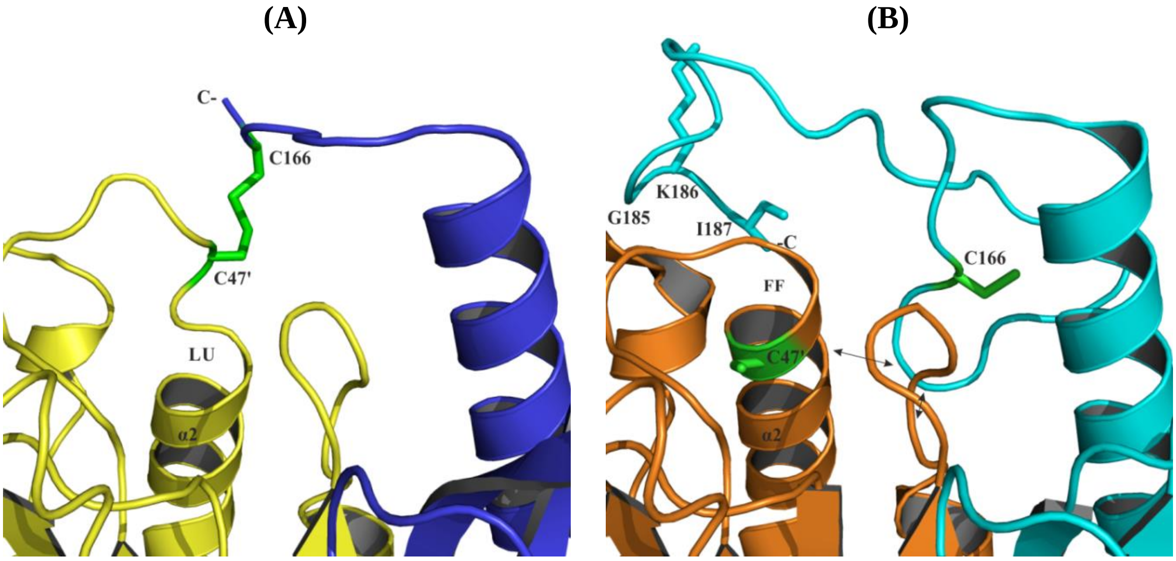

Figure 4.16: Structural comparison between AhpC oxidised and reduced dimer crystal structures. The oxidised *Ec*AhpC crystal structure is depicted in yellow and blue, whereas the reduced *St*AhpC crystal structure (PDB: 1N8J) in orange and cyan colour. *(A)* In the oxidised state the α2-helix at C47' is locally unfolded (LU), that brings C47' exposed to form disulfide bond with the resolving cysteine C_R166 (green stick). *(B)* In the reduced state α2-helix at C47 is locally fully folded (FF). The winding of α2-helix to its fully folded conformation brings C47 and C166' more than 10 Å apart and facing to opposite directions. Furthermore, the C-terminal amino acids after C166' are visible and forming two patches of defined hydrogen bonds to its neighbouring monomer. The fully folded α2-helix forms an additional hydrogen bond to A168, whereas the very C-terminal end, G185 and I187 form three hydrogen bonds to F43, S86 and T88, respectively [153, 228].

The second region includes the residues at the very C-terminus, G185 and I187, which form three hydrogen bonds to F43, S86 and T88, respectively (Figure 4.16B). In the oxidised state, as indicated in the *Ec*AhpC crystal structure, the C-terminus releases the other monomer in the dimer interface and becomes flexible again, to give space for the disulfide bond formation and probably recognising *Ec*AhpF (Figure 4.16A). The catalytic cycle can be summarised in two simultaneous movements between oxidised and reduced AhpC. The first movement is the alternate local folding and unfolding of α2-helix, bringing C47 in its active site in fully folded α2-helix or exposed for disulfide formation with C166. The second movement occurs at the C-terminal residues after C166. These residues alternate between flexible in oxidised state and rigid in reduced state. In other words, in the oxidised state the disulfide bond stabilises and in reduced state the C-terminus stabilises the dimer formation (Figure 4.16).

4.6.2 The decameric ring formation of AhpC from *E. coli*

Several studies reported that the dimer form of peroxiredoxin exhibits less activity than the decamer form [236-238]. This observation is supported with the crystal structure in oxidised state (Figure 3.44), which shows that the redox active disulfide bond is in proximity to the oligomeric interface (Figure 3.44, Figure 3.45A). Hence oxidised or reduced state may have an influence to favour the dimer or decamer state.

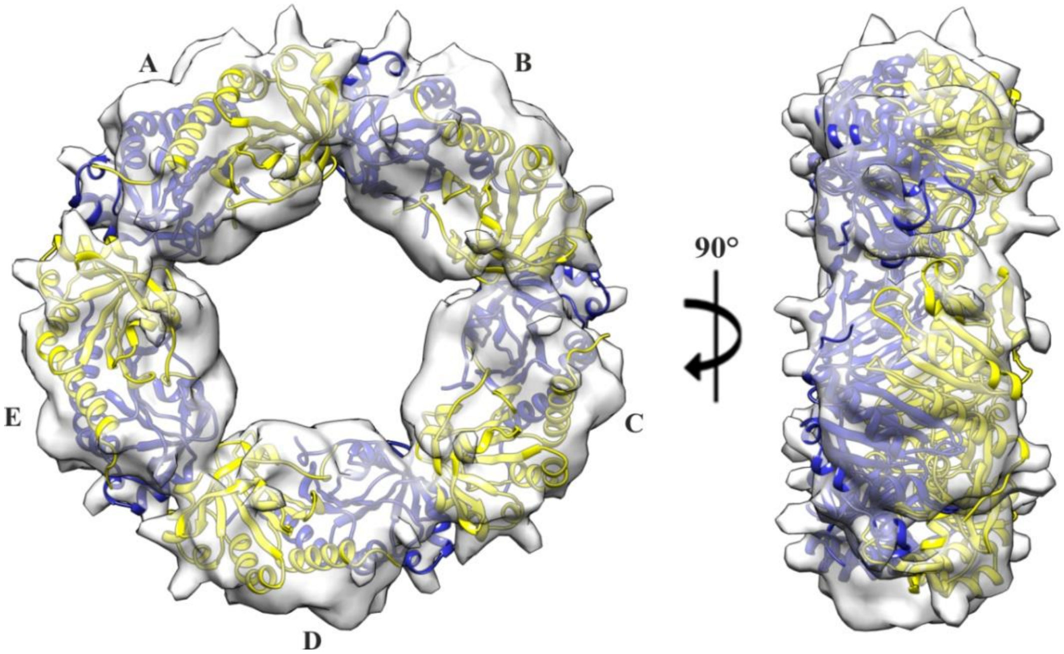

Figure 4.17: Structural comparison between the crystal structure and 3D reconstruction of *Ec*AhpC. The superposition of the *Ec*AhpC crystal structure in oxidised form and the 3D reconstruction in reduced form reveal similar dimension and a correlation coefficient of 0.91 [187, 228].

To understand the relationship between the oxidised and reduced state to dimer and oligomer state of AhpC, DLS and cryoEM studies have been performed in this thesis, to give a clear insight, close to physiological conditions. DLS measurements of oxidised and reduced AhpC reveal the presence of oligomers in solution (Figure 3.48). The electron micrographs reveal that AhpC forms ring- and rod-shape like formation under oxidising and reducing conditions, which correspond to top- and sideview of the 3D reconstruction of AhpC (Figure

3.50). The lengths of the rod shape particle vary in the oxidised form, while it has constant length in reduced form (Figure 3.50), corresponding well to the diameter of the ring shape particle and indicating that the rod shape particle might be the side view of the ring shape particles. In the oxidised form rod shape particles have both similar length like the reduced form and a longer shape (Figure 3.50BD). The images of reduced AhpC reveal larger amount of ring shaped particles than in the oxidised form, allowing the performance of Single Particle Reconstruction (SPR) of reduced AhpC (Figure 3.51).

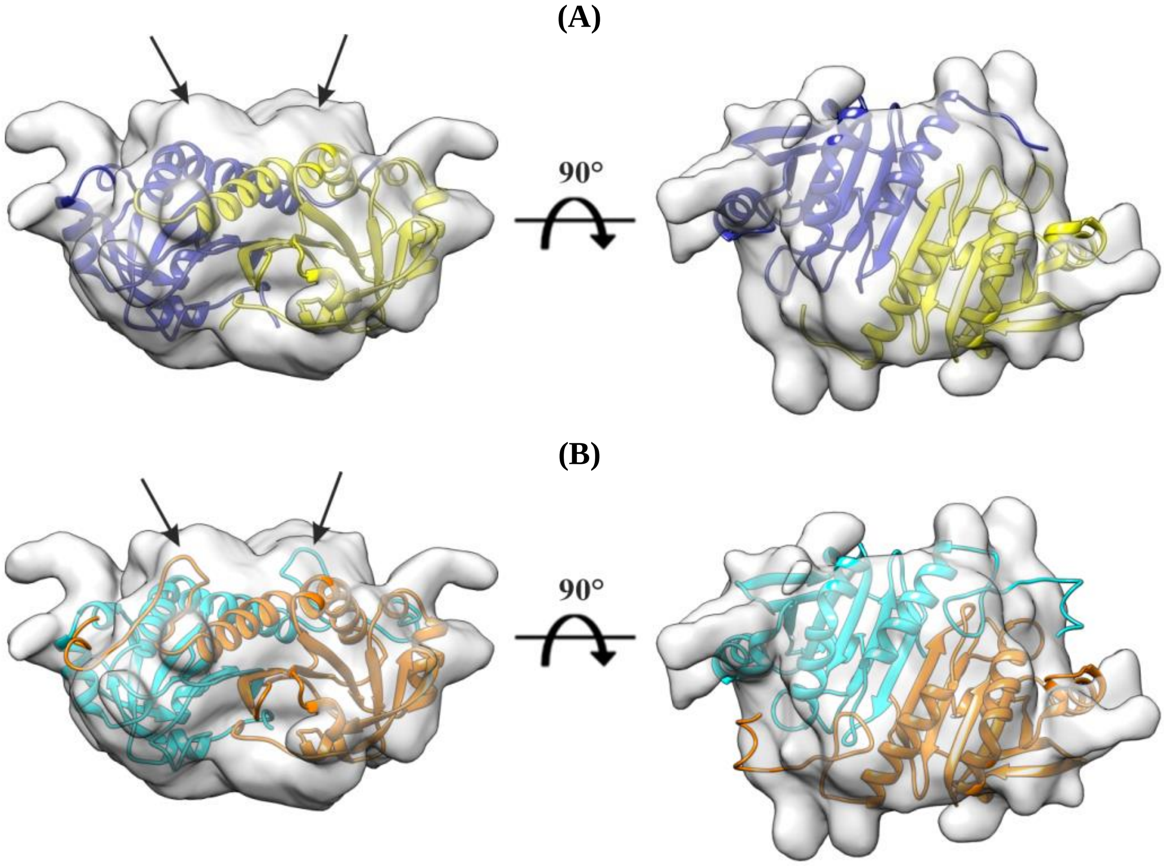

Figure 4.18: Superposition of AhpC crystal dimer structures and its corresponding 3D reconstruction. *(A)* Close view of the superposition to one oval shaped segment and two AhpC monomers (blue and yellow) in oxidised form and *(B)* in reduced form (cyan and orange). The dimension of the 3D reconstruction of AhpC is larger than the crystal structure in oxidised form, highlighted with an arrow. The superposition of the 3D reconstruction and the crystal structure of AhpC in reduced form indicate that the additional volume represents the rigid C-terminal region of the reduced structure [153, 228].

The 3D reconstruction indicates similar shape and dimension to the AhpC crystal structure in oxidised state (Figure 4.17). Structural comparison highlights that the oxidised AhpC crystal structure accommodates well into the density of the 12 Å resolution 3D-reconstruction of reduced AhpC, with a correlation coefficient of 0.91 as calculated using Chimera program (Figure 4.17) [187]. Each of the five oval shape segments of the reduced 3D reconstruction corresponds to two AhpC monomers (Figure 4.17). The close view to the superposition of one oval shape segment and the crystal structure of AhpC in the oxidised form reveal that an oval shape segment has larger dimension than the corresponding oxidised crystal structure, which is highlighted with an arrow (Figure 4.18A). The superposition of the 3D reconstruction and the AhpC crystal structure in reduced form indicates that the additional volume might represent the C-terminal region responsible for the dimerisation in reduced form (Figure 4.18B). Since under oxidised condition the C-terminal region is flexible and hence not visible in the crystal structure, the additional volume in the 3D reconstruction under reducing conditions might represent the C-terminal region (Figure 4.18AB).

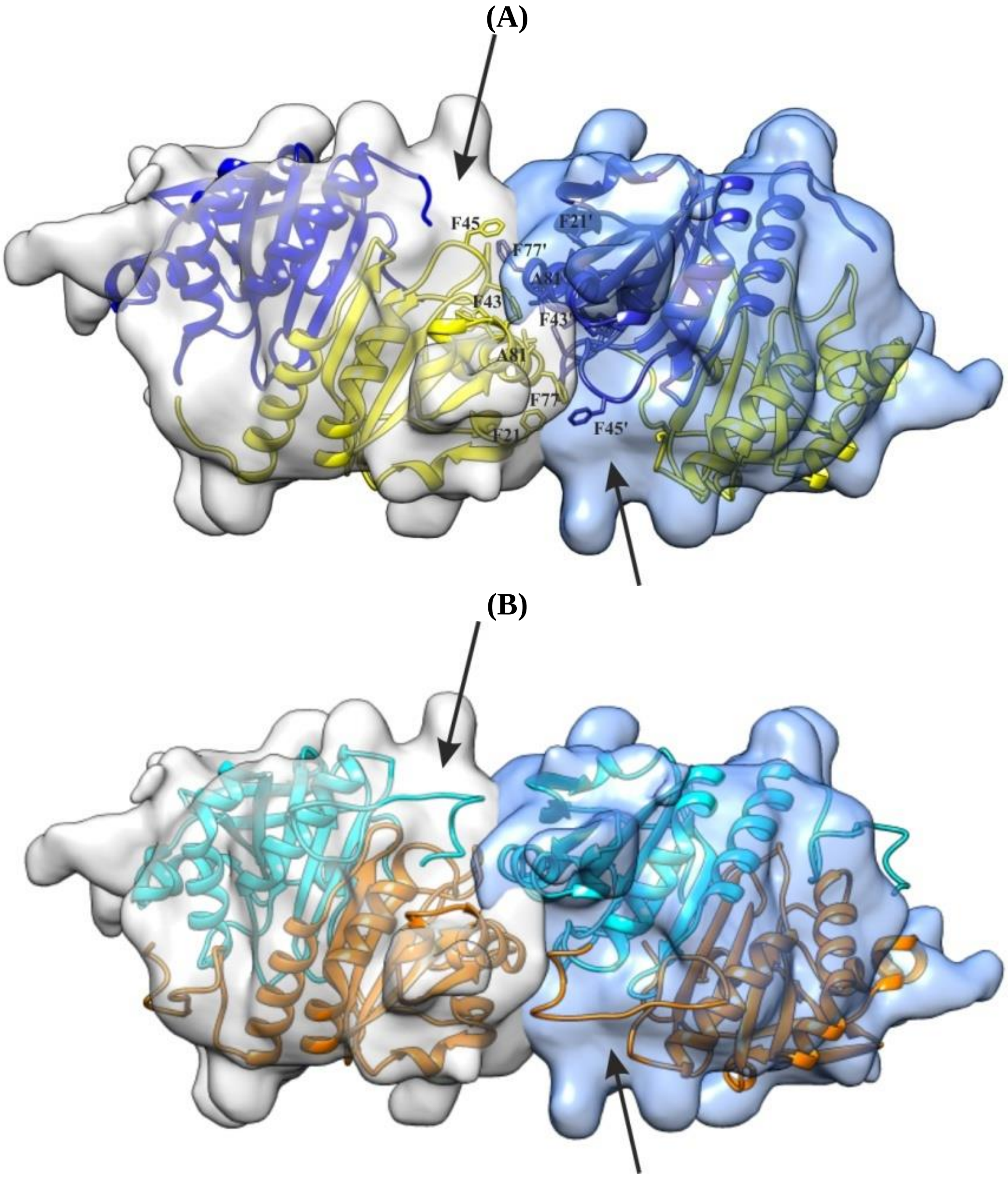

Figure 4.19: The close view to the hydrophobic oligomer interface between two dimer structures. *(A)* Superposition of AhpC crystal structure in oxidised form (*Ec*AhpC) and *(B)* in reduced form (*St*AhpC) in its corresponding 3D reconstruction. Oxidised and reduced dimer structure are coloured in their colour respectively [153, 228].

Overall, the surface-rendered EM reconstruction correlates well with the solvent-accessible surface revealed by the X-ray crystal structure of AhpC. The close view to the hydrophobic oligomer interface between chain B and chain C of the *Ec*AhpC structure (Figure 3.46) and its overlay to the surface rendered 3D reconstruction reveal that the hydrophobic residues, formed by F21, F43, F45, F77, A81 and W82 are well accommodated into the 3D reconstruction (Figure 4.19A). The additional surfaces are highlighted with arrow assuming the location of the C-terminal end of AhpC in reduced state (Figure 4.19B). Indeed, close view to the hydrophobic oligomer interface of the *St*AhpC crystal structure in reduced form and the superposition to the 3D reconstruction, respectively confirm the presence of the C-terminus at this region (Figure 4.19B). However, the C-terminus of the AhpC crystal structure cannot cover the entire space, which leads to the possibility that the C-terminal end might have different arrangement in the 3D reconstruction (Figure 4.19B).

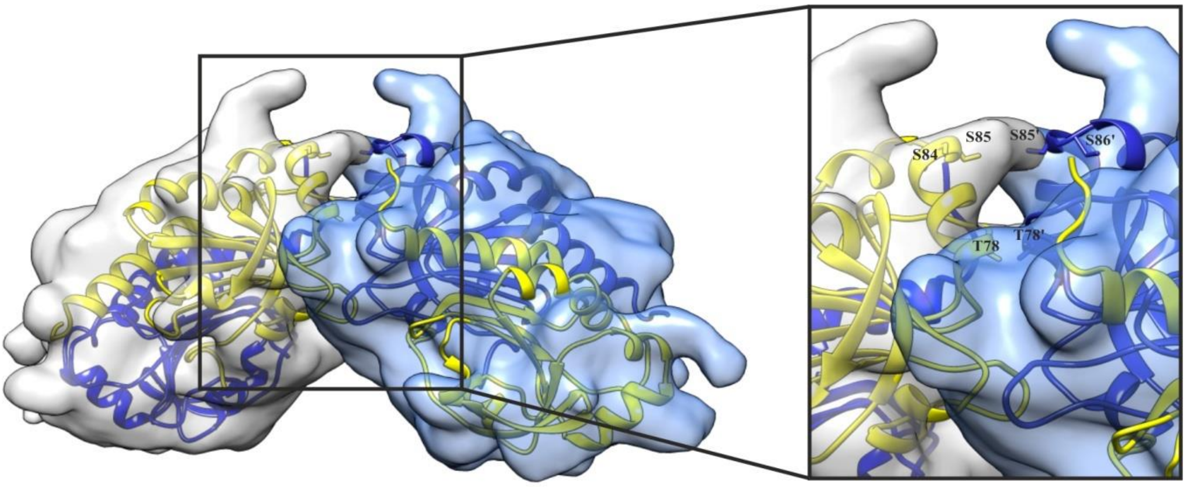

Figure 4.20: The side view to the hydrophobic oligomer interface between two dimer structures. The 3D reconstruction reveals a connection between two monomer subunits. The close view is highlighted in the section on the right side. The superposed AhpC crystal structure indicates the presence of three serines (S84, S85 and S86) and one threonine (T78). There might be a chance that under physiological condition hydrophilic hydrogen bonds may help to stabilise the so far known hydrophobic oligomeric interface of AhpC crystal structures [228].

The side view of the hydrophobic oligomer interface reveals connection between the monomeric AhpC molecules (Figure 4.20). The superimposed *E. coli* AhpC crystal structure indicates the presence of three serines (S84, S85 and S86) and one threonine (T78) in the respective AhpC monomer. In the crystal structure no hydrogen bonds occur in this interface. There might be a chance that under physiological condition hydrophilic hydrogen bonds may help to stabilise the so far known hydrophobic oligomeric interface of AhpC crystal structures (Figure 4.20). Threonine T78 has been shown to be crucial for the decamerisation [239]. Mutations T78I or T78D disrupt the decamer formation and revealed a 100-fold lower catalytic efficiency, indicating that the oligomeric interface and the decameric structure are very important for the activity [239]. The importance to form a ring structure for its catalytic activity has been observed in recent studies in our lab, performed by Dr. Neelagandan Kamariah. C-terminal truncation of *Ec*AhpC containing the residues 1-172 (*Ec*AhpCΔ172) reveals mainly a dimer formation in reduced state, shown in size exclusion chromatography, dynamic light scattering (DLS), and SDS-PAGE (data not shown), indicating the importance of the C-terminus in AhpC ring formation. A strict dimer formation was not observed in the *Ec*AhpCΔ172 oxidised form. Interestingly electron micrographs of the reduced *Ec*AhpCΔ172 construct, produced by Dr. Neelagandan Kamariah and Jonathan Ng Thiam Seng do not show ring like- or rod shape particles (data not shown), which lead to assume that the flexible C-terminal residues are important for decameric ring formation in reduced state.

In order to get an insight, whether *Ec*AhpC has an additional molecular chaperon activity as proposed so far for eukaryotic cells [100, 163-165], DLS and cryo EM were performed in this thesis. It has been proposed that peroxidase function predominates in the lower MW forms, whereas the chaperone function predominates in the higher MW complexes. DLS of oxidised and reduced *Ec*AhpC reveal the formation of low molecular weight complexes (LMW) close to physiological pH (Figure 3.48A). Since *E. coli* cells are not only exposed to hydroperoxides but also exposed to low pH in phagosomes of macrophages or in the lower intestine of their host, the formation of high molecular weight (HMW) complexes was investigated at different pH. Oxidised and reduced purified *Ec*AhpC were therefore buffer exchanged for DLS measurements. In buffers until pH 5.4 no changes in complex formation were observed. However, in 100 mM Na-acetate pH 4.4 only the reduced form of *Ec*AhpC reveals an increase of its hydrodynamic radius to 16.2 nm indicating a higher molecular weight of 4000 kDa, while the oxidised form remains in LMW complexes (Figure 3.48B). To confirm such a high molecular weight formation of *Ec*AhpC, electron micrographs were imaged to visualize the HMW arrangement. Selected micrographs and 18 best-generated classes reveal the presence of ring shaped particles and rod shaped particles, whereas rod shaped particles are stacked mainly from two to four to each other (Figure 3.54). The tilted views in selected micrographs indicate that the stacks of rod shape particles are stacks of rings on top of one another (Figure 3.54). It can be proposed that besides the peroxidative reductase activity of *Ec*AhpC against hydroperoxide, bacterial AhpC may has an additional redox-regulated chaperon activity. In this study, DLS data and EM micrographs reveal that *Ec*AhpC forms high molecular weight complexes in low pH revealing the second function of AhpC as molecular chaperon in bacterial cells. The ring structures are stacked from 2 to 7 rings on top of another giving the possibility to prevent aggregation of proteins in low pH within its tube shape conformation (Figure 3.54).

4.6.3 The importance of the open conformation of AhpF and decameric ring formation of AhpC for the catalytic activity of AhpR from *E. coli*

Analytical ultracentrifugation [134, 151] as well as size exclusion chromatography of AhpC in this thesis (Figure 3.42), leads to the assumption that AhpC is in an obligate dimer conformation and the dimer interface is stronger than the hydrophobic oligomer interface. The peroxidase assay performed in this thesis revealed that *Ec*AhpF-*Ec*AhpC is catalytic active and *Ec*AhpF catalyses NADH independently of AhpC (Figure 3.29). However since activity studies have been shown that decameric AhpC is much more catalytic active than the dimer AhpC, it can be suggested that AhpC is preferred in decamer formation during catalysis [236-238]. Also the peroxidase assay with *Ec*AhpF-*Ec*AhpCΔ172, performed by Dr. Neelagandan Kamariah, revealed lesser NADH oxidation, indicating an importance of the C-terminal region for the catalytic activity (data not shown). Since electron micrographs of reduced *Ec*AhpCΔ172 construct, do not show ring like- or rod shape particles (data not shown), the assumption can be made that the decameric ring formation has a positive influence to the catalytic activity. Also *St*AhpC mutations T78I and T78D disrupt the decamer formation and revealed a 100-fold lower catalytic efficiency [239]. Since decamer formation is important but not essential for activity it can be assumed that the recovery of AhpC via AhpF for its catalytic activity may occur in dimer as well as in decamer state. To observe the presence of AhpC decameric ring formation in solution, cryoEM micrographs of AhpC in oxidised and reduced form were imaged, reflecting despite the slight dispersed protein behaviour a number of ring and rod shaped particles (Figure 3.50AC).

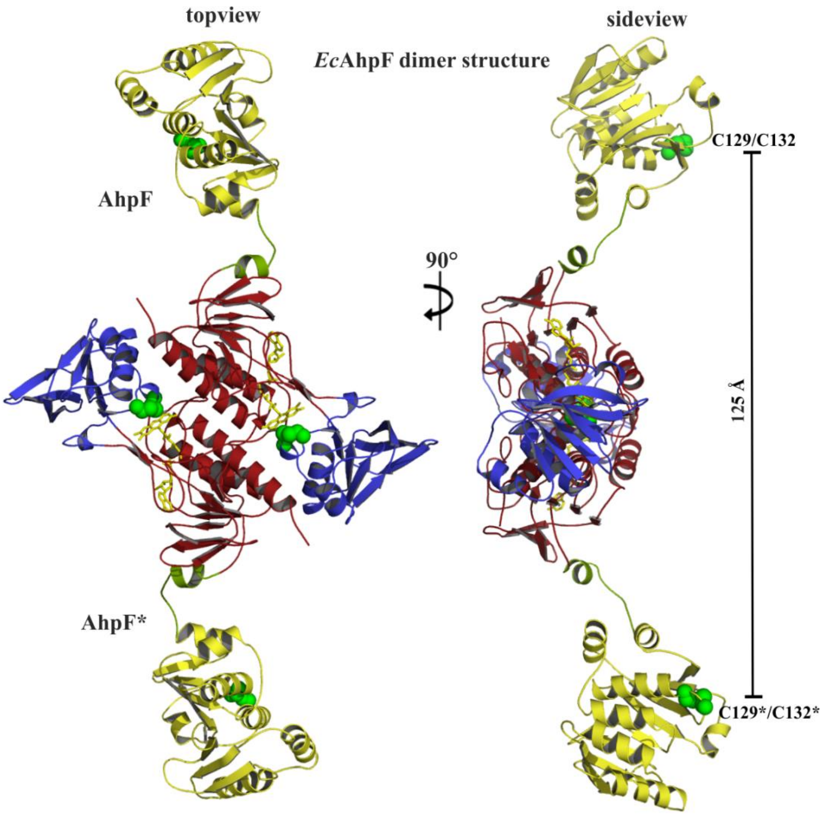
topview
*Ec*AhpF dimer structure
sideview
AhpF
AhpF*
90°
C129/C132
125 Å
C129*/C132*

Figure 4.21: *Ec*AhpF crystal structure in dimer conformation. Disulfide bond are shown in green spheres and *Ec*AhpF is depicted in its corresponding domain colours. The open conformation of *Ec*AhpF crystal structure in dimer conformation was generated using its symmetry related molecule and reveal a distance of 125 Å between both redox active disulfide bond at the NTD, in topview (left) and side view (right).

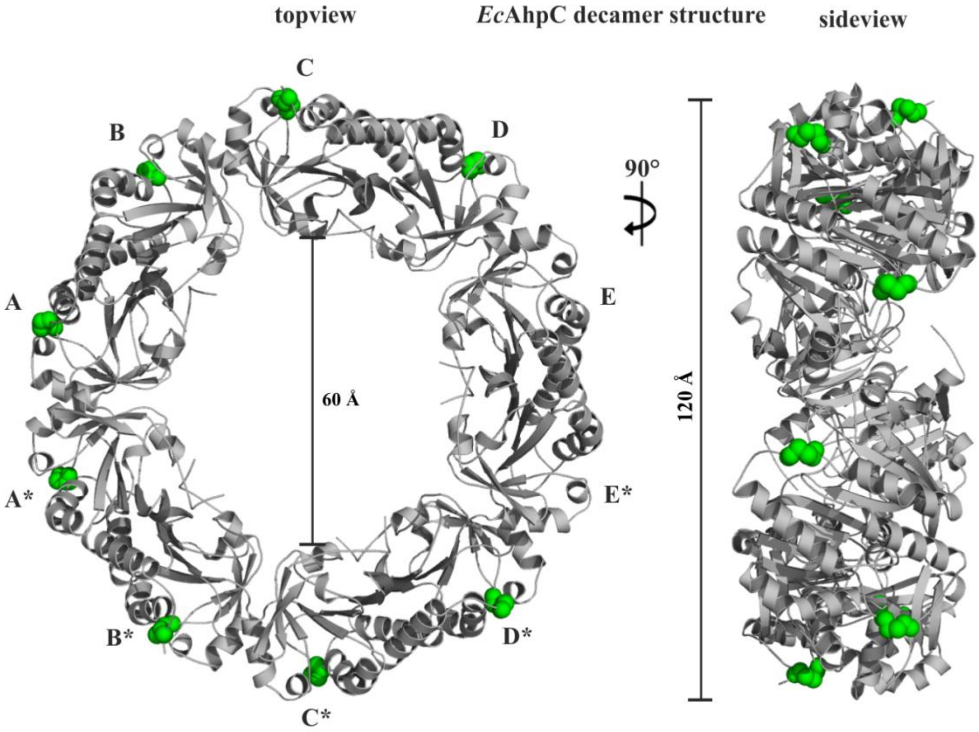
topview
*Ec*AhpC decamer structure
sideview
C
B
D
A
E
60 Å
A*
E*
B*
D*
C*
90°
120 Å

Figure 4.22: Crystal structure of AhpC from *E. coli*. The decameric ring structure of EcAhpC is depicted in grey colour and cysteins are shown in green spheres, topview (left) and side view (right).

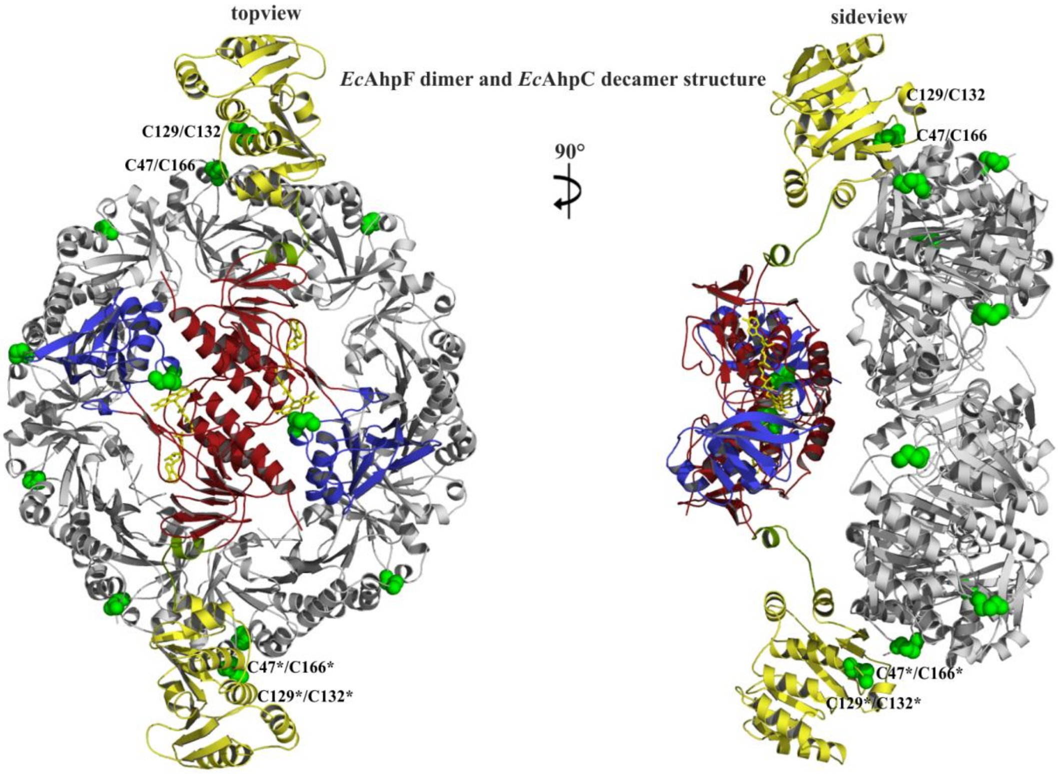

Figure 4.23: Putative orientation of the catalytic active state of AhpR from *E. coli*. *Ec*AhpF dimer coloured in its domain, respectively. Redox active cysteins are shown in green spheres and *Ec*AhpC is depicted in grey colour. AhpF dimer structure was docked to the AhpC decamer structure. The distance between the two homo-dimeric redox active disulfide bonds C129/C132 of *Ec*AhpF is long enough to bridge the longest distance of 120 Å between two opposing redox active disulfide bonds in AhpC structure. AhpF accommodates well on top of the AhpC ring. The side view of this docking reveals that redox active disulfides (C129/C132) in the NTD of AhpF, which are responsible for hydride transfer to (C47/C166) of AhpC are located closely to C47/C166 [228].

It can be suggested that AhpC remains in a steady state between different oligomeric states while being catalytic inactive. It can be furthermore assumed that AhpF reduces AhpC preferable in its decamer state. Purification studies of the related Peroxiredoxin and NADH Peroxiredoxin Reductase from *Thermus aquaticus* reveal that both proteins once contaminated with each other are not possible to be separated using Superdex 200 [240]. Peroxiredoxin and NADH Peroxiredoxin Reductase elute together as complex with molecular mass of 400 kDa, which may indicate a possible complex formation between AhpC in the decamer state and AhpF in dimer state, as highlighted in Figure 4.23B [240]. In this thesis, size exclusion chromatography and DLS data of *Ec*AhpF reveal a molecular size of ~120 kDa that reflects a dimer formation of this protein in solution (Figure 3.28). Taken both crystal structures, AhpF and AhpC presented in this thesis a hypothetical mechanistic model of AhpR can be proposed. The open conformation of the homo-dimer *Ec*AhpF reflects to be stretched to a maximum length of 170 Å (Figure 3.40), giving the possibility of electron transfer from NTD redox active disulfide bond (C129/C132) to the redox active disulfide bond of AhpC (C47/C166). The distance between the two homo-dimeric redox active disulfide bonds C129/C132 of *Ec*AhpF is 125 Å, which is indeed long enough to cover the decameric structure of *Ec*AhpC (Figure 3.40, Figure 4.23A) and the longest distance of 120 Å between two opposing redox active disulfide bonds. Manual docking of *Ec*AhpF homo-dimer to *Ec*AhpC homo-decamer reveals that AhpF accommodates well on top of the AhpC ring (Figure 4.23B). The molecular surface around *Ec*AhpF C129 and *Ec*AhpC C166 show a general shape match. The side view of this docking reveals that both redox active disulfides (C129/C132) in the NTD of AhpF, which are responsible for hydride transfer to (C47/C166) of AhpC are located closely to C47/C166 (Figure 4.23B). Furthermore the solution structure of *Ec*AhpF derived by SAXS (Figure 4.6) reflects an open and stretch conformation similar to the AhpF crystal structure, so that the possibility of maximum length of 125 Å as a dimer conformation in the presence of AhpC is still given in solution (Figure 4.6A). Indeed, current ITC (isothermal titration calorimetry) experiments with various *Ec*AhpF domains to *Ec*AhpC were performed by Wilson Nartey in Prof. Grüber's lab that reveal *Ec*AhpF interacts only via its NTD, while the C-terminal portion show no interaction (data not shown). However, cryoEM studies of *Ec*AhpF and *Ec*AhpC could not show complex formation, suspecting a transient interaction between AhpF and AhpC in *E. coli* (data not shown). Only a transient interaction may explain the high catalytic activity rather than a rigid *Ec*AhpF-*Ec*AhpC complex. The Micrographs and DLS data from AhpC in oxidised and reduced form indicate the possibility of decamer formation in solution (Figure 3.48, Figure 3.50). It is shown that AhpC in reduced form has the tendency to form more ring shape conformation. This seems plausible since once AhpF reduce an oxidised AhpC dimer, reduced AhpC dimers tend to form decamer formation. Once a decameric ring is formed, the catalytic activity is higher, since AhpF adapts well on top of the ring (Figure 4.23). The proposed catalytic cycle of AhpF as described in paragraph 4.5.2 (Figure 4.11) occurs without steric hindrance to AhpC (Figure 4.24). This suggested catalytic model of *Ec*AhpF involves, in total, three conformations including two alternate movements of NADH/SS domain and NTD. The two large movements alternate between the stretch and twisted conformation at the NADH domain and the close and open conformation at the NTD (Figure 4.11). The 67° rotation of the NADH domain brings the bound NADH close to flavin and C345/C348 exposed at the surface of the structure (Figure 4.11b) [129]. This movement can occur without any clashes to the AhpC decameric structure, when AhpF remains on the ring structure (Figure 4.24b).

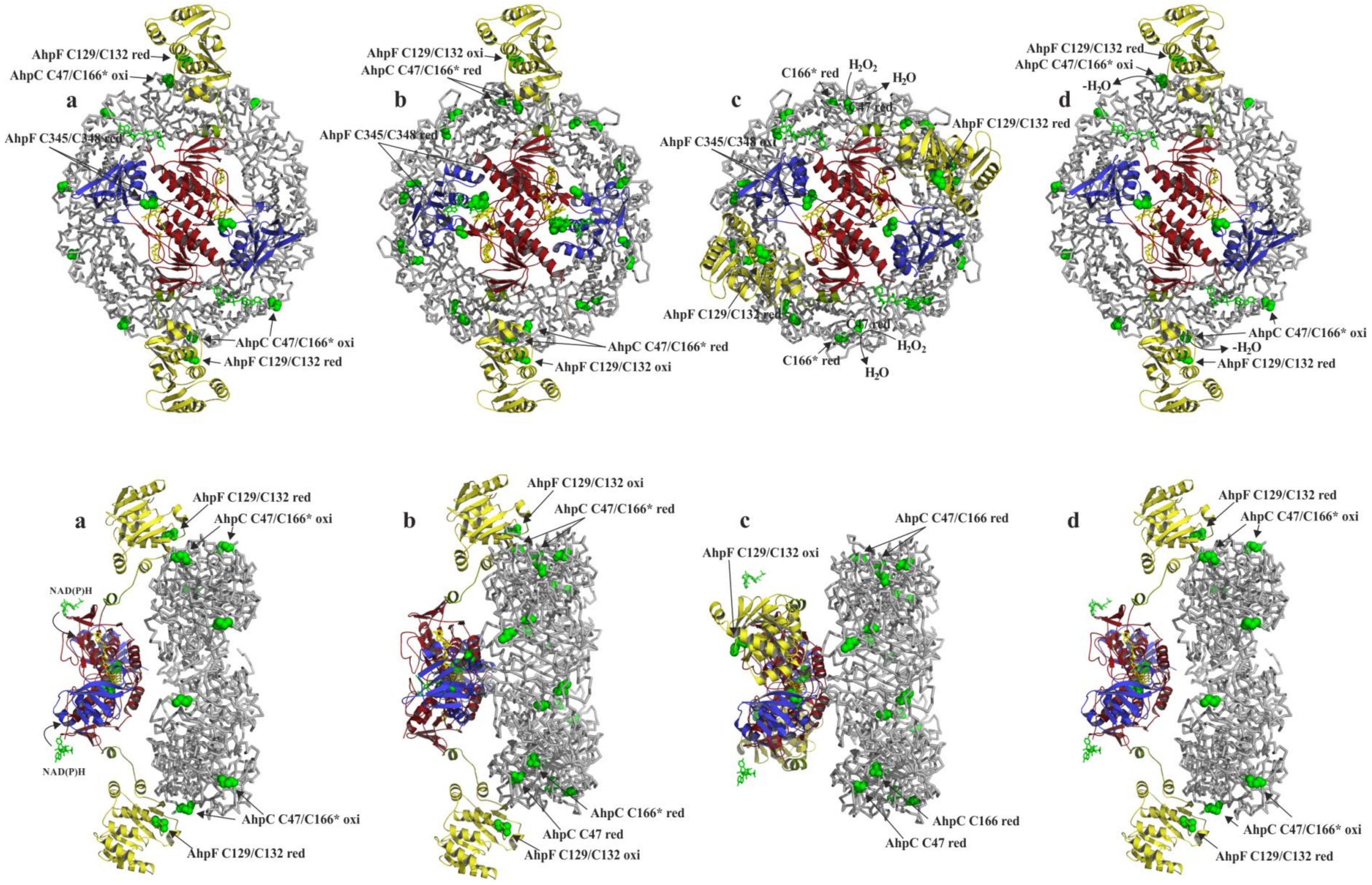
AhpF C129/C132 red
AhpC C47/C166* oxi
a
AhpF C345/C348 red
AhpC C47/C166* oxi
AhpF C129/C132 red
AhpF C129/C132 oxi
AhpC C47/C166* red
b
AhpF C345/C348 red
AhpC C47/C166* red
AhpF C129/C132 oxi
C166* red
H_2O_2
H_2O
c
C47 red
AhpF C129/C132 red
AhpF C345/C348 oxi
AhpF C129/C132 red
C47 red
H_2O_2
C166* red
H_2O
AhpF C129/C132 red
AhpC C47/C166* oxi
$-H_2O$
d
AhpC C47/C166* oxi
$-H_2O$
AhpF C129/C132 red
a
AhpF C129/C132 red
AhpC C47/C166* oxi
NAD(P)H
NAD(P)H
AhpC C47/C166* oxi
AhpF C129/C132 red
b
AhpF C129/C132 oxi
AhpC C47/C166* red
AhpC C166* red
AhpC C47 red
AhpF C129/C132 oxi
c
AhpC C47/C166 red
AhpF C129/C132 oxi
AhpC C166 red
AhpC C47 red
d
AhpF C129/C132 red
AhpC C47/C166* oxi
AhpC C47/C166* oxi
AhpF C129/C132 red

Figure 4.24: Putative catalytical model of *Ec*AhpR. AhpF accommodates well on top of the AhpC ring. The in paragraph 4.6.1 and Figure 4.11 described mechanistic model of *Ec*AhpF may occur in close contact to AhpC decamer structure to accelerate the catalytic activity of AhpR. All three conformations of AhpF including the two large movements at the NADH domain and NTD occur without clashes and steric hindrances to AhpC. For the reduced AhpC conformation in (b) and (c), the reduced AhpC structure from *S. typhimurium* was applied (PDB: 1N8J) [153, 228].

Furthermore, the second movement involves the 178° turn of the NTD towards the twisted NADH domain that brings C345/C348 and C129/C132 to close distance. After C345/C348 reduce C129/C132 in the close conformation, the NTD moves 178° back towards AhpC ring, where C129/C132 of AhpF reduce the redox active disulfide (C47/C166) of AhpC in the open conformation (Figure 4.11c-d, Figure 4.24c-d). Also the second large movement of the NTD occurs without any steric hindrance and clashes with *Ec*AhpC. After C129/C132 of *Ec*AhpF reduce the redox active disulfide (C47/C166) of AhpC, AhpC winds from LU to its FF conformation at its α2 helix (Figure 4.16A, Figure 4.24b). At the FF conformation the thiol of the peroxidatic cysteine C47 is prone to be attacked by hydroperoxide. Hydroperoxide oxidises C47 to cysteine sulfenic acid (RSOH). The oxidation of C47 leads to unwind α2 helix to a local unfolded (LU) state that brings C47 back to its position in the oxidised form [153]. In this oxidised state position, C47 is exposed to form a disulfide bond with the resolving cysteine C_R166 (Figure 3.45, Figure 4.24d). The disulfide bond is holding the two oxidised AhpC partner monomers together, while the C-terminal amino acids after C166 becomes flexible so that the redox active C129/C132 of NTD of the AhpF structure can reduce redox active disulfide (C47/C166) without any clashes or steric hindrance (Figure 4.10, Figure 4.24d) [147].

This thesis showed that under oxidative stress and low pH for example in phagosomes, *E. coli* cells have evolved intriguing strategies to survive. Here the dual function for AhpC as peroxidative reductase and molecular chaperone has been presented. The peroxidative mechanisms for the dithiol-disulfide exchange from AhpF to AhpC were poorly understood, because the conformation of AhpF and its catalytic relevant intermediate while reducing AhpC was not known so far. Furthermore, the physiological relevance for decameric ring formation of AhpC has not been clear. Here, the molecular mechanism between *Ec*AhpF and *Ec*AhpC was described for the first time. The new AhpF open conformation has been solved, in that NTD is playing a crucial part in acting as a substrate for the C-terminal portion of AhpF, and reduced NTD acts as a major catalytic component in protein disulfide reductase activity for AhpC reduction [132, 135, 140, 142]. CryoEM and DLS data reveal the decamer ring formation of AhpC in solution (Figure 3.48**,** Figure 3.50). The open conformation of AhpF and proposed mechanistic model explain the preference of AhpF to reduce AhpC in decamer ring formation then AhpC dimer form in its peroxidative activity (Figure 4.24). The function as molecular chaperone has been observed using cryoEM, showing two to seven AhpC rings stacked on top of each other, therefore forming a tube shape conformation and protecting proteins for denaturation.

5. Conclusions

Conclusions

Subunit *a* has been described as pH sensor element of V_1V_O ATPase, where it was found to interact with ARNO (ADP-ribosylation factor Nucleotide site Opener) [1], an activator of small GTPase, Arf6 (ADP-ribosylation factor 6) in a pH dependent manner. Here, two important peptides $a2_{1-17}$ and $a2_{368-395}$ of subunit *a2* (mouse V-ATPase), involved in ARNO binding, have been structurally characterised by using NMR spectroscopy. The structures of both peptides show proper folding of α-helical formation. Moreover, the amino acids inside the N-terminal part ($a2_{1-17}$) of subunit *a*, responsible for subunit *a*-ARNO association, have been identified. The interaction site of $a2_{1-17}$ with the Sec7 domain of ARNO reveals a defined binding of residues F6, E8 and Q14 [2]. Further cloning, expression and NMR titration studies of subunit *a* construct $a_{104-363}$ that lacks the two ARNO binding sites reveal weak interaction to ARNO. Small Angle X-ray Scattering (SAXS) of $a_{104-363}$, reveals an elongated S-shaped conformation, which highlights the importance of its C-terminus in proton pumping and vesicle formation [3].

Alkyl Hydroperoxide Reductase (AhpR) is the primary hydroperoxide scavenger. In this thesis the two subunits of *Escherichia coli* AhpR, the 56 kDa alkyl hydroperoxide reductase subunit F (AhpF) and 210 kDa homodecamer subunit C (AhpC) have been solved in 2 Å and 3.3 Å resolution, respectively. The AhpC crystal structure has been solved in its oxidised state revealing a ring shape conformation, whereas AhpC structure in its reduced state has been reconstructed to 12 Å resolution, using single particle cryo electron microscopy (cryoEM). DLS data and the elution diagram of gel filtration reveal AhpF as dimer whereas DLS data and EM micrographs indicate AhpC as decamer in solution. Taken the elongated open conformation of AhpF and the ring shape AhpC crystal structures, the so far known crystal structure of AhpF and AhpC from *Salmonella typhimurium* and the mechanism from the homologous Thioredoxin Reductase (TrxR) and Thioredoxin, the first overall mechanism of AhpR was described and giving new insights into the molecular mechanism of AhpR in rescuing the cell from reactive oxygen species (ROS), like hydroperoxides.

Besides hydroperoxide, bacterial cells are exposed to low pH in phagosomes of macrophages. In this thesis, DLS data and EM micrographs reveal that AhpC forms high molecular weight complexes revealing the second function of AhpC as a molecular chaperon. The ring structures are stacked from 2 to 7 rings on top of another giving the possibility to prevent aggregation of proteins in low pH within its tube shape conformation.

6. References

1. Hurtado-Lorenzo, A., Skinner, M., Annan, J.E., Futai, M., Sun-Wada, G.-H., Bourgoin, S., Casanova, J., Wildeman, A., Bechoua, S., Ausiello, D.A., Brown, D., and Marshansky, V. (2006). *V-ATPase interacts with ARNO and Arf6 in early endosomes and regulates the protein degradative pathway.* Nat. Cell Biol. **8**: 124-136.

2. Hosokawa, H., Dip, P.V., Merkulova, M., Bakulina, A., Zhuang, Z., Khatri, A., Jian, X., Keating, S.M., Bueler, S.A., Rubinstein, J.L., Randazzo, P.A., Ausiello, D.A., Grüber, G., and Marshansky, V. (2013). *The N termini of a-subunit isoforms are involved in signaling between vacuolar* H^+*-ATPase (V-ATPase) and cytohesin-2.* J. Biol. Chem. **288**: 5896-5913.

3. Dip, P.V., Saw, W.G., Roessle, M., Marshansky, V., and Grüber, G. (2012). *Solution structure of subunit a,* $a_{104\text{-}363}$*, of the Saccharomyces cerevisiae V-ATPase and the importance of its C-terminus in structure formation.* J. Bioenerg. Biomembr. **44**: 341-350.

4. Ames, B.N. (1983). *Dietary carcinogens and anticarcinogens. Oxygen radicals and degenerative diseases.* Science **221**: 1256-1264.

5. Fridovich, I. (1978). *The biology of oxygen radicals.* Science **201**: 875-880.

6. Gutteridge, J.M. and Halliwell, B. (1989). *Iron toxicity and oxygen radicals.* Baillieres Clin. Haematol. **2**: 195-256.

7. Sies, H. (1993). *Strategies of antioxidant defense.* Eur. J. Biochem. **215**: 213-219.

8. Casey, J.R., Grinstein, S., and Orlowski, J. (2010). *Sensors and regulators of intracellular pH.* Nat. Rev. Mol. Cell Biol. **11**: 50-61.

9. Whitten, S.T., Garcia-Moreno, E.B., and Hilser, V.J. (2005). *Local conformational fluctuations can modulate the coupling between proton binding and global structural transitions in proteins.* Proc. Natl. Acad. Sci. **102**: 4282-4287.

10. Grüber, G. and Marshansky, V. (2008). *New insights into structure-function relationships between archeal ATP synthase* (A_1A_0) *and vacuolar type ATPase* (V_1V_0)*.* Bioessays **30**: 1096-1109.

11. Forgac, M. (2007). *Vacuolar ATPases: Rotary proton pumps in physiology and pathophysiology.* Nat. Rev. Mol. Cell Biol. **8**: 917-929.

12. Beyenbach, K.W. and Wieczorek, H. (2006). *The V-type* H^+ *ATPase: Molecular structure and function, physiological roles and regulation.* J. Exp. Biol. **209**: 577-589.

13. Breton, S. and Brown, D. (2007). *New insights into the regulation of V-ATPase-dependent proton secretion.* Am. J. Physiol. Renal Physiol. **292**: F1-F10.

14. Brown, D. and Breton, S. (2000). H^+*V-ATPase-dependent luminal acidification in the kidney collecting duct and the epididymis/vas deferens: vesicle recycling and transcytotic pathways.* J. Exp. Biol. **203**: 137-145.

15. Nishi, T. and Forgac, M. (2002). *The vacuolar (H^+)-ATPases - Nature's most versatile proton pumps.* Nat. Rev. Mol. Cell Biol. **3**: 94-103.

16. Yao, G., Feng, H., Cai, Y., Qi, W., and Kong, K. (2007). *Characterization of vacuolar-ATPase and selective inhibition of vacuolar-H^+-ATPase in osteoclasts.* Biochem. Biophys. Res. Commun. **357**: 821-827.

17. Nelson, N. and Harvey, W.R. (1999). *Vacuolar and Plasma Membrane Proton-Adenosinetriphosphatases.* Physiol. Rev. **79**: 361-385.

18. Lepier, A., Azuma, M., Harvey, W.R., and Wieczorek, H. (1994). *K^+/H^+ antiport in the tobacco hornworm midgut: the K^+-transporting component of the K^+ pump.* J. Exp. Biol. **196**: 361-373.

19. Wieczorek, H., Grüber, G., Harvey, W.R., Huss, M., and Merzendorfer, H. (1999). *The plasma membrane H^+-V-ATPase from tobacco hornworm midgut.* J. Bioenerg. Biomembr. **31**: 67-74.

20. Zhuang, Z., Linser, P.J., and Harvey, W.R. (1999). *Antibody to H^+ V-ATPase subunit E colocalizes with portasomes in alkaline larval midgut of a freshwater mosquito (Aedes aegypti).* J. Exp. Biol. **202**: 2449-2460.

21. Morel, N. (2003). *Neurotransmitter disease: The dark side of the vacuolar-H^+ATPase.* Biol. Cell **95**: 453-457.

22. Maranda, B., Brown, D., Bourgoin, S., Casanova, J.E., Vinay, P., Ausiello, D.A., and Marshansky, V. (2001). *Intra-endosomal pH-sensitive recruitment of the Arf-nucleotide exchange factor ARNO and Arf6 from cytoplasm to proximal tubule endosomes.* J. Biol. Chem. **276**: 18540-18550.

23. Ashery, U., Koch, H., Scheuss, V., Brose, N., and Rettig, J. (1999). *A presynaptic role for the ADP ribosylation factor (ARF)-specific GDP/GTP exchange factor msec7-1.* Proc. Natl. Acad. Sci. **96**: 1094-1099.

24. Franco, M., Boretto, J., Robineau, S., Monier, S., Goud, B., Chardin, P., and Chavrier, P. (1998). *ARNO3, a Sec7-domain guanine nucleotide exchange factor for ADP ribosylation factor 1, is involved in the control of Golgi structure and function.* Proc. Natl. Acad. Sci. **95**: 9926-9931.

25. Santy, L.C. and Casanova, J.E. (2001). *Activation of ARF6 by ARNO stimulates epithelial cell migration through downstream activation of both Rac1 and phospholipase D.* J. Cell Biol. **154**: 599-610.

26. Smith, A.N., Lovering, R.C., Futai, M., Takeda, J., Brown, D., and Karet, F.E. (2003). *Revised nomenclature for mammalian vacuolar-Type H^+-ATPase subunit genes.* Mol. Cell **12**: 801-803.

27. Benlekbir, S., Bueler, S.A., and Rubinstein, J.L. (2012). *Structure of the vacuolar-type ATPase from Saccharomyces cerevisiae at 11-Å resolution.* Nat. Struct. Mol. Biol. **19**: 1356-1362.

28. Kitagawa, N., Mazon, H., Heck, A.J.R., and Wilkens, S. (2008). *Stoichiometry of the peripheral stalk subunits E and G of yeast V_1-ATPase determined by mass spectrometry.* J. Biol. Chem. **283**: 3329-3337.

29. Ohira, M., Smardon, A.M., Charsky, C.M.H., Liu, J., Tarsio, M., and Kane, P.M. (2006). *The E and G subunits of the yeast V-ATPase interact tightly and are both present at more than one copy per V_1 complex.* J. Biol. Chem. **281**: 22752-22760.

30. Rishikesan, S., Gayen, S., Thaker, Y.R., Vivekanandan, S., Manimekalai, M.S.S., Yau, Y.H., Shochat, S.G., and Grüber, G. (2009). *Assembly of subunit d (Vma6p) and G (Vma10p) and the NMR solution structure of subunit G (G1-59) of the Saccharomyces cerevisiae V_1V_O ATPase.* Biochim. Biophys. Acta **1787**: 242-251.

31. Supek, F., Supekova, L., Mandiyan, S., Pan, Y.C.E., Nelson, H., and Nelson, N. (1994). *A novel accessory subunit for vacuolar H^+-ATPase from chromaffin granules.* J. Biol. Chem. **269**: 24102-24106.

32. Jansen, E.J.R., Holthuis, J.C.M., McGrouther, C., Burbach, J.P.H., and Martens, G.J.M. (1998). *Intracellular trafficking of the vacuolar H^+-ATPase accessory subunit Ac45.* J. Cell Sci. **111**: 2999-3006.

33. Ludwig, J., Kerscher, S., Brandt, U., Pfeiffer, K., Getlawi, F., Apps, D.K., and Schagger, H. (1998). *Identification and characterization of a novel 9.2-kDa membrane sector-associated protein of vacuolar proton-ATPase from chromaffin granules.* J. Biol. Chem. **273**: 10939-10947.

34. Demirci, F.Y.K., White, N.J., Rigatti, B.W., Lewis, K.F., and Gorin, M.B. (2001). *Identification, genomic structure, and screening of the vacuolar proton-ATPase membrane sector-associated protein M8-9 gene within the COD1 critical region (Xp11.4).* Mol. Vis. **7**: 234-239.

35. Merzendorfer, H., Huss, M., Schmid, R., Harvey, W.R., and Wieczorek, H. (1999). *A Novel Insect V-ATPase Subunit M9.7 Is Glycosylated Extensively.* J. Biol. Chem. **274**: 17372-17378.

36. Gogarten, J.P., Starke, T., Kibak, H., Fishman, J., and Taiz, L. (1992). *Evolution and isoforms of V-ATPase subunits.* J. Exp. Biol. **172**: 137-147.

37. Karet, F. (2005). *Physiological and Metabolic Implications of V-ATPase Isoforms in the Kidney.* J. Bioenerg. Biomembr. **37**: 425-429-429.

38. Nishi, T., Kawasaki-Nishi, S., and Forgac, M. (2003). *Expression and Function of the Mouse V-ATPase d Subunit Isoforms.* J. Biol. Chem. **278**: 46396-46402.

39. Sun-Wada, G.-H., Murata, Y., Namba, M., Yamamoto, A., Wada, Y., and Futai, M. (2003). *Mouse Proton Pump ATPase C Subunit Isoforms (C2-a and C2-b) Specifically Expressed in Kidney and Lung.* J. Biol. Chem. **278**: 44843-44851.

40. Sun-Wada, G.-H., Yoshimizu, T., Imai-Senga, Y., Wada, Y., and Futai, M. (2003). *Diversity of mouse proton-translocating ATPase: presence of multiple isoforms of the C, d and G subunits.* Gene **302**: 147-153.

41. Murata, Y., Sun-Wada, G.-H., Yoshimizu, T., Yamamoto, A., Wada, Y., and Futai, M. (2002). *Differential Localization of the Vacuolar H^+ Pump with G Subunit Isoforms (G1 and G2) in Mouse Neurons.* J. Biol. Chem. **277**: 36296-36303.

42. Strompen, G., Dettmer, J., Stierhof, Y.D., Schumacher, K., Jürgens, G., and Mayer, U. (2005). *Arabidopsis vacuolar H^+-ATPase subunit E isoform 1 is required for Golgi organization and vacuole function in embryogenesis.* Plant J. **41**: 125-132.

43. Nishi, T. (2005). *Subunit isoforms controlling the functions of the V-ATPase.* Seikagaku. J. Jap. Biochem. Soc. **77**: 354-358.

44. Wassmer, T., Kissmehl, R., Cohen, J., and Plattner, H. (2006). *Seventeen a-subunit isoforms of Paramecium V-ATPase provide high specialization in localization and function.* Mol. Biol. Cell **17**: 917-930.

45. Manolson, M.F., Proteau, D., Preston, R.A., Stenbit, A., Roberts, B.T., Hoyt, M.A., Preuss, D., Mulholland, J., Botstein, D., and Jones, E.W. (1992). *The VPH1 gene encodes a 95-kDa integral membrane polypeptide required for in vivo assembly and activity of the yeast vacuolar $H(^+)$-ATPase.* J. Biol. Chem. **267**: 14294-14303.

46. Manolson, M.F., Wu, B., Proteau, D., Taillon, B.E., Roberts, B.T., Hoyt, M.A., and Jones, E.W. (1994). *STV1 gene encodes functional homologue of 95-kDa yeast vacuolar $H(^+)$- ATPase subunit Vph1p.* J. Biol. Chem. **269**: 14064-14074.

47. Kane, P.M. (1995). *Disassembly and reassembly of the yeast vacuolar H^+-ATPase in vivo.* J. Biol. Chem. **270**: 17025-17032.

48. Armbrüster, A., Christina, H., Anne, H., Karin, S., Börsch, M., and Grüber, G. (2005). *Evidence for major structural changes in subunit C of the vacuolar ATPase due to nucleotide binding.* FEBS Lett. **579**: 1961-1967.

49. Armbrüster, A., Svergun, D.I., Coskun, Ü., Juliano, S., Bailer, S.M., and Grüber, G. (2004). *Structural analysis of the stalk subunit Vma5p of the yeast V-ATPase in solution.* FEBS Lett. **570**: 119-125.

50. Hong-Hermesdorf, A., Brux, A., Grüber, A., Grüber, G., and Schumacher, K. (2006). *A WNK kinase binds and phosphorylates V-ATPase subunit C.* FEBS Lett. **580**: 932-939.

51. Vitavska, O., Merzendorfer, H., and Wieczorek, H. (2005). *The V-ATPase subunit C binds to polymeric F-actin as well as to monomeric G-actin and induces cross-linking of actin filaments.* J. Biol. Chem. **280**: 1070-1076.

52. Curtis, K.K., Francis, S.A., Oluwatosin, Y., and Kane, P.M. (2002). *Mutational Analysis of the Subunit C (Vma5p) of the Yeast Vacuolar H^+-ATPase.* J. Biol. Chem. **277**: 8979-8988.

53. Drory, O., Frolow, F., and Nelson, N. (2004). *Crystal structure of yeast V-ATPase subunit C reveals its stator function.* EMBO Rep **5**: 1148-1152.

54. Rishikesan, S., Thaker, Y.R., and Grüber, G. (2011). *NMR solution structure of subunit E (fragment E_{1-69}) of the Saccharomyces cerevisiae V_1V_O ATPase.* J. Bioenerg. Biomembr. **43**: 187-193.

55. Rishikesan, S. and Grüber, G. (2011). *Structural elements of the C-terminal domain of subunit E ($E_{133-222}$) from the Saccharomyces cerevisiae V_1V_0 ATPase determined by solution NMR spectroscopy.* J. Bioenerg. Biomembr. **43**: 447-455.

56. Rishikesan, S., Manimekalai, M.S.S., and Grüber, G. (2010). *The NMR solution structure of subunit G (G_{61-101}) of the eukaryotic V_1V_O ATPase from Saccharomyces cerevisiae.* Biochim. Biophys. Acta Biomembr. **1798**: 1961-1968.

57. Rishikesan, S., Thaker, Y.R., Priya, R., Gayen, S., Manimekalai, M.S.S., Hunke, C., and Grüber, G. (2008). *Spectroscopical identification of residues of subunit G of the yeast V-ATPase in its connection with subunit E.* Mol. Membr. Biol. **25**: 400 - 410.

58. Oot, R.A. and Wilkens, S. (2012). *Subunit interactions at the V_1-Vo interface in yeast vacuolar ATPase.* J. Biol. Chem. **287**: 13396-13406.

59. Sagermann, M., Stevens, T.H., and Matthews, B.W. (2001). *Crystal structure of the regulatory subunit H of the V-type ATPase of Saccharomyces cerevisiae.* Proc. Natl. Acad. Sci. **98**: 7134-7139.

60. Basak, S., Lim, J., Manimekalai, M.S., Balakrishna, A.M., and Grüber, G. (2013). *Crystal and NMR structures give insights into the role and dynamics of subunit F of the eukaryotic V-ATPase from Saccharomyces cerevisiae.* J. Biol. Chem. **288**: 11930-11939.

61. Thaker, Y.R., Roessle, M., and Grüber, G. (2007). *The boxing glove shape of subunit d of the yeast V-ATPase in solution and the importance of disulfide formation for folding of this protein.* J. Bioenerg. Biomembr. **39**: 275-289.

62. Basak, S., Gayen, S., Thaker, Y.R., Manimekalai, M.S., Roessle, M., Hunke, C., and Grüber, G. (2011). *Solution structure of subunit F (Vma7p) of the eukaryotic V_1V_O ATPase from Saccharomyces cerevisiae derived from SAXS and NMR spectroscopy.* Biochim. Biophys. Acta **1808**: 360-368.

63. Findlay, J.B. and Harrison, M.A. (2002). *A protein chemical approach to channel structure and function: the proton channel of the vacuolar H^+-ATPase.* Novartis Found. Symp. **245**: 207-218, 218-222, 261-264.

64. Harrison, M., Durose, L., Song, C.F., Barratt, E., Trinick, J., Jones, R., and Findlay, J.B. (2003). *Structure and function of the vacuolar H^+-ATPase: moving from low-resolution models to high-resolution structures.* J. Bioenerg. Biomembr. **35**: 337-345.

65. Kawasaki-Nishi, S., Nishi, T., and Forgac, M. (2001). *Arg-735 of the 100-kDa subunit a of the yeast V-ATPase is essential for proton translocation.* Proc. Natl. Acad. Sci. **98**: 12397-12402.

66. Kawasaki-Nishi, S., Nishi, T., and Forgac, M. (2001). *Yeast V-ATPase complexes containing different isoforms of the 100-kDa a-subunit differ in coupling efficiency and in vivo dissociation.* J. Biol. Chem. **276**: 17941-17948.

67. Nishi, T. and Forgac, M. (2000). *Molecular cloning and expression of three isoforms of the 100-kDa a subunit of the mouse vacuolar proton-translocating ATPase.* J. Biol. Chem. **275**: 6824-6830.

68. Oka, T., Murata, Y., Namba, M., Yoshimizu, T., Toyomura, T., Yamamoto, A., Sun-Wada, G.H., Hamasaki, N., Wada, Y., and Futai, M. (2001). *a4, a unique kidney-specific isoform of mouse vacuolar* H^+*-ATPase subunit a.* J. Biol. Chem. **276**: 40050-40054.

69. Sun-Wada, G.-H., Toyomura, T., Murata, Y., Yamamoto, A., Futai, M., and Wada, Y. (2006). *The a3 isoform of V-ATPase regulates insulin secretion from pancreatic beta-cells.* J. Cell Sci. **119**: 4531-4540.

70. Toyomura, T., Oka, T., Yamaguchi, C., Wada, Y., and Futai, M. (2000). *Three subunit a isoforms of mouse vacuolar* H^+*-ATPase. Preferential expression of the a3 isoform during osteoclast differentiation.* J. Biol. Chem. **275**: 8760-8765.

71. Toyomura, T., Murata, Y., Yamamoto, A., Oka, T., Sun-Wada, G.H., Wada, Y., and Futai, M. (2003). *From lysosomes to the plasma membrane: localization of vacuolar-type* H^+*-ATPase with the a3 isoform during osteoclast differentiation.* J. Biol. Chem. **278**: 22023-22030.

72. Kawasaki-Nishi, S., Bowers, K., Nishi, T., Forgac, M., and Stevens, T.H. (2001). *The Amino-terminal Domain of the Vacuolar Proton-translocating ATPase a Subunit Controls Targeting and in Vivo Dissociation, and the Carboxyl-terminal Domain Affects Coupling of Proton Transport and ATP Hydrolysis.* J. Biol. Chem. **276**: 47411-47420.

73. Leng, X.H., Manolson, M.F., and Forgac, M. (1998). *Function of the COOH-terminal domain of Vph1p in activity and assembly of the yeast V-ATPase.* J. Biol. Chem. **273**: 6717-6723.

74. Thaker, Y.R., Hunke, C., Yau, Y.H., Shochat, S.G., Li, Y., and Grüber, G. (2009). *Association of the eukaryotic* V_1V_O *ATPase subunits a with d and d with A.* FEBS Lett. **583**: 1090-1095.

75. Landolt-Marticorena, C., Williams, K.M., Correa, J., Chen, W., and Manolson, M.F. (2000). *Evidence That the NH2 Terminus of Vph1p, an Integral Subunit of the* V_O *Sector of the Yeast V-ATPase, Interacts Directly with the Vma1p and Vma13p Subunits of the* V_1 *Sector.* J. Biol. Chem. **275**: 15449-15457.

76. Wilkens, S. and Forgac, M. (2001). *Three-dimensional structure of the vacuolar ATPase proton channel by electron microscopy.* J. Biol. Chem. **276**: 44064-44068.

77. Shao, E. and Forgac, M. (2004). *Involvement of the nonhomologous region of subunit A of the yeast V-ATPase in coupling and in vivo dissociation.* J. Biol. Chem. **279**: 48663-48670.

78. Apps, D.K., Percy, J.M., and Perez-Castineira, J.R. (1989). *Topography of a vacuolar-type* H^+*-translocating ATPase: chromaffin-granule membrane ATPase I.* Biochem J. **263**: 81-88.

79. Perin, M.S., Fried, V.A., Stone, D.K., Xie, X.S., and Sudhof, T.C. (1991). *Structure of the 116-kDa polypeptide of the clathrin-coated vesicle/synaptic vesicle proton pump.* J. Biol. Chem. **266**: 3877-3881.

80. Landolt-Marticorena, C., Kahr, W.H., Zawarinski, P., Correa, J., and Manolson, M.F. (1999). *Substrate- and inhibitor-induced conformational changes in the yeast V-ATPase provide evidence for communication between the catalytic and proton-translocating sectors.* J Biol. Chem. **274**: 26057-26064.

81. Leng, X.-H., Nishi, T., and Forgac, M. (1999). *Transmembrane topography of the 100-kDa a subunit (Vph1p) of the yeast vacuolar proton-translocating ATPase.* J. Biol. Chem. **274**: 14655-14661.

82. Leng, X.H., Manolson, M.F., Liu, Q., and Forgac, M. (1996). *Site-directed mutagenesis of the 100-kDA subunit (Vph1p) of the yeast vacuolar* (H^+)*-ATPase.* J. Biol. Chem. **271**: 22487-22493.

83. Wang, Y., Inoue, T., and Forgac, M. (2004). *TM2 but not TM4 of subunit c'' interacts with TM7 of subunit a of the yeast V-ATPase as defined by disulfide-mediated cross-linking.* J. Biol. Chem. **279**: 44628-44638.

84. Duarte, A.M., Wolfs, C.J., van Nuland, N.A., Harrison, M.A., Findlay, J.B., van Mierlo, C.P., and Hemminga, M.A. (2007). *Structure and localization of an essential transmembrane segment of the proton translocation channel of yeast* H^+*-V-ATPase.* Biochim. Biophys. Acta Biomembr. **1768**: 218-227.

85. Stehberger, P.A., Schulz, N., Finberg, K.E., Karet, F.E., Giebisch, G., Lifton, R.P., Geibel, J.P., and Wagner, C.A. (2003). *Localization and regulation of the ATP6V0A4 (a4) vacuolar* H^+*-ATPase subunit defective in an inherited form of distal renal tubular acidosis.* J. Am. Soc. Nephrol. **14**: 3027-3038.

86. Kornak, U., Schulz, A., Friedrich, W., Uhlhaas, S., Kremens, B., Voit, T., Hasan, C., Bode, U., Jentsch, T.J., and Kubisch, C. (2000). *Mutations in the a3 subunit of the vacuolar* H^+*-ATPase cause infantile malignant osteopetrosis.* Hum. Mol. Gen. **9**: 2059-2063.

87. Frattini, A., Orchard, P.J., Sobacchi, C., Giliani, S., Abinun, M., Mattsson, J.P., Keeling, D.J., Andersson, A.-K., Wallbrandt, P., Zecca, L., Notarangelo, L.D., Vezzoni, P., and Villa, A. (2000). *Defects in TCIRG1 subunit of the vacuolar proton pump are responsible for a subset of human autosomal recessive osteopetrosis.* Nat. Genet. **25**: 343-346.

88. Kornak, U., Reynders, E., Dimopoulou, A., van Reeuwijk, J., Fischer, B., Rajab, A., Budde, B., Nurnberg, P., Foulquier, F., Lefeber, D., Urban, Z., Gruenewald, S., Annaert, W., Brunner, H.G., van Bokhoven, H., Wevers, R., Morava, E., Matthijs, G., Van Maldergem, L., and Mundlos, S. (2008). *Impaired glycosylation and cutis laxa caused by mutations in the vesicular* H^+*-ATPase subunit ATP6V0A2.* Nat. Genet. **40**: 32-34.

89. Williamson, W.R., Wang, D., Haberman, A.S., and Hiesinger, P.R. (2010). *A dual function of V_O-ATPase a1 provides an endolysosomal degradation mechanism in Drosophila melanogaster photoreceptors.* J. Cell Biol. **189**: 885-899.

90. Peri, F. and Nüsslein-Volhard, C. (2008). *Live imaging of neuronal degradation by microglia reveals a role for V_O-ATPase a1 in phagosomal fusion in vivo.* Cell **133**: 916-927.

91. Marshansky, V. (2007). *The V-ATPase a2-subunit as a putative endosomal pH-sensor.* Biochem. Soc. Trans. **35**: 1092-1099.

92. Moss, J. and Vaughan, M. (1998). *Molecules in the ARF Orbit.* J. Biol. Chem. **273**: 21431-21434.

93. Massenburg, D., Han, J.S., Liyanage, M., Patton, W.A., Rhee, S.G., Moss, J., and Vaughan, M. (1994). *Activation of rat brain phospholipase D by ADP-ribosylation factors 1,5, and 6: separation of ADP-ribosylation factor-dependent and oleate-dependent enzymes.* Proc. Natl. Acad. Sci. **91**: 11718-11722.

94. Franco, M., Peters, P.J., Boretto, J., Van Donselaar, E., Neri, A., D'Souza-Schorey, C., and Chavrier, P. (1999). *EFA6, a sec7 domain-containing exchange factor for ARF6, coordinates membrane recycling and actin cytoskeleton organization.* EMBO J. **18**: 1480-1491.

95. Turner, C.E. and Brown, M.C. (2001). *Cell motility: ARNO and ARF6 at the cutting edge.* Curr. Biol. **11**: R875-R877.

96. Merkulova, M., Bakulina, A., Thaker, Y.R., Grüber, G., and Marshansky, V. (2010). *Specific motifs of the V-ATPase a2-subunit isoform interact with catalytic and regulatory domains of ARNO.* Biochim. Biophys. Acta **1797**: 1398-1409.

97. Santy, L.C., Frank, S.R., Hatfield, J.C., and Casanova, J.E. (1999). *Regulation of ARNO nucleotide exchange by a PH domain electrostatic switch.* Curr. Biol. **9**: 1173-1176.

98. Diab, H.I. and Kane, P.M. (2013). *Loss of vacuolar H^+-ATPase (V-ATPase) activity in yeast generates an iron deprivation signal that is moderated by induction of the peroxiredoxin TSA2.* J. Biol. Chem. **288**: 11366-11377.

99. Milgrom, E., Diab, H., Middleton, F., and Kane, P.M. (2007). *Loss of vacuolar proton-translocating ATPase activity in yeast results in chronic oxidative stress.* J. Biol. Chem. **282**: 7125-7136.

100. Jang, H.H., Lee, K.O., Chi, Y.H., Jung, B.G., Park, S.K., Park, J.H., Lee, J.R., Lee, S.S., Moon, J.C., Yun, J.W., Choi, Y.O., Kim, W.Y., Kang, J.S., Cheong, G.W., Yun, D.J., Rhee, S.G., Cho, M.J., and Lee, S.Y. (2004). *Two enzymes in one; two yeast peroxiredoxins display oxidative stress-dependent switching from a peroxidase to a molecular chaperone function.* Cell **117**: 625-635.

101. Saccoccia, F., Di Micco, P., Boumis, G., Brunori, M., Koutris, I., Miele, A.E., Morea, V., Sriratana, P., Williams, D.L., Bellelli, A., and Angelucci, F. (2012). *Moonlighting*

by different stressors: crystal structure of the chaperone species of a 2-Cys peroxiredoxin. Structure **20**: 429-439.

102. Davis-Kaplan, S.R., Ward, D.M., Shiflett, S.L., and Kaplan, J. (2004). *Genome-wide analysis of iron-dependent growth reveals a novel yeast gene required for vacuolar acidification.* J. Biol. Chem. **279**: 4322-4329.

103. Yamaguchi-Iwai, Y., Ueta, R., Fukunaka, A., and Sasaki, R. (2002). *Subcellular localization of Aft1 transcription factor responds to iron status in Saccharomyces cerevisiae.* J. Biol. Chem. **277**: 18914-18918.

104. Outten, C.E., Falk, R.L., and Culotta, V.C. (2005). *Cellular factors required for protection from hyperoxia toxicity in Saccharomyces cerevisiae.* Biochem. J. **388**: 93-101.

105. Thorpe, G.W., Fong, C.S., Alic, N., Higgins, V.J., and Dawes, I.W. (2004). *Cells have distinct mechanisms to maintain protection against different reactive oxygen species: oxidative-stress-response genes.* Proc Natl Acad Sci U S A **101**: 6564-6569.

106. Lechardeur, D., Fernandez, A., Robert, B., Gaudu, P., Trieu-Cuot, P., Lamberet, G., and Gruss, A. (2010). *The 2-Cys peroxiredoxin alkyl hydroperoxide reductase c binds heme and participates in its intracellular availability in Streptococcus agalactiae.* J. Biol. Chem. **285**: 16032-16041.

107. Merzendorfer, H., Huss, M., Schmid, R., Harvey, W.R., and Wieczorek, H. (1999). *A novel insect V-ATPase subunit M9.7 is glycosylated extensively.* J. Biol. Chem. **274**: 17372-17378.

108. Glass, G.A., DeLisle, D.M., DeTogni, P., Gabig, T.G., Magee, B.H., Markert, M., and Babior, B.M. (1986). *The respiratory burst oxidase of human neutrophils. Further studies of the purified enzyme.* J. Biol. Chem. **261**: 13247-13251.

109. Mehdy, M.C. (1994). *Active Oxygen Species in Plant Defense against Pathogens.* Plant Physiol. **105**: 467-472.

110. Pericone, C.D., Overweg, K., Hermans, P.W., and Weiser, J.N. (2000). *Inhibitory and bactericidal effects of hydrogen peroxide production by Streptococcus pneumoniae on other inhabitants of the upper respiratory tract.* Infect. Immun. **68**: 3990-3997.

111. Seaver, L.C. and Imlay, J.A. (2001). *Hydrogen peroxide fluxes and compartmentalization inside growing Escherichia coli.* J. Bacteriol. **183**: 7182-7189.

112. Storz, G., Tartaglia, L.A., and Ames, B.N. (1990). *The OxyR regulon.* Antonie Van Leeuwenhoek **58**: 157-161.

113. Gaudu, P., Touati, D., Niviere, V., and Fontecave, M. (1994). *The NAD(P)H:flavin oxidoreductase from Escherichia coli as a source of superoxide radicals.* J. Biol. Chem. **269**: 8182-8188.

114. Messner, K.R. and Imlay, J.A. (1999). *The identification of primary sites of superoxide and hydrogen peroxide formation in the aerobic respiratory chain and sulfite reductase complex of Escherichia coli.* J. Biol. Chem. **274**: 10119-10128.

115. Seaver, L.C. and Imlay, J.A. (2004). *Are respiratory enzymes the primary sources of intracellular hydrogen peroxide?* J. Biol. Chem. **279**: 48742-48750.

116. Winterbourn, C.C., Hampton, M.B., Livesey, J.H., and Kettle, A.J. (2006). *Modeling the reactions of superoxide and myeloperoxidase in the neutrophil phagosome: implications for microbial killing.* J. Biol. Chem. **281**: 39860-39869.

117. Mishra, S. and Imlay, J. (2012). *Why do bacteria use so many enzymes to scavenge hydrogen peroxide?* Arch. Biochem. Biophys. **525**: 145-160.

118. Paul, B. and Sbarra, A.J. (1968). *The role of the phagocyte in host-parasite interactions: XIII. The direct quantitative estimation of* H_2O_2 *in phagocytizing cells.* Biochim. Biophys. Acta **156**: 168-178.

119. Lee, C., Lee, S.M., Mukhopadhyay, P., Kim, S.J., Lee, S.C., Ahn, W.S., Yu, M.H., Storz, G., and Ryu, S.E. (2004). *Redox regulation of OxyR requires specific disulfide bond formation involving a rapid kinetic reaction path.* Nat. Struct. Mol. Biol. **11**: 1179-1185.

120. Zheng, L., Cash, V.L., Flint, D.H., and Dean, D.R. (1998). *Assembly of iron-sulfur clusters. Identification of an iscSUA-hscBA-fdx gene cluster from Azotobacter vinelandii.* J. Biol. Chem. **273**: 13264-13272.

121. Aslund, F., Zheng, M., Beckwith, J., and Storz, G. (1999). *Regulation of the OxyR transcription factor by hydrogen peroxide and the cellular thiol-disulfide status.* Proc. Natl. Acad. Sci. **96**: 6161-6165.

122. Storz, G., Christman, M.F., Sies, H., and Ames, B.N. (1987). *Spontaneous mutagenesis and oxidative damage to DNA in Salmonella typhimurium.* Proc. Natl. Acad. Sci. **84**: 8917-8921.

123. Storz, G., Jacobson, F.S., Tartaglia, L.A., Morgan, R.W., Silveira, L.A., and Ames, B.N. (1989). *An alkyl hydroperoxide reductase induced by oxidative stress in Salmonella typhimurium and Escherichia coli: genetic characterization and cloning of ahp.* J. Bacteriol. **171**: 2049-2055.

124. Storz, G., Tartaglia, L.A., Farr, S.B., and Ames, B.N. (1990). *Bacterial defenses against oxidative stress.* Trends Genet. **6**: 363-368.

125. Zheng, M., Wang, X., Templeton, L.J., Smulski, D.R., LaRossa, R.A., and Storz, G. (2001). *DNA microarray-mediated transcriptional profiling of the Escherichia coli response to hydrogen peroxide.* J. Bacteriol. **183**: 4562-4570.

126. Tartaglia, L.A., Storz, G., and Ames, B.N. (1989). *Identification and molecular analysis of oxyR-regulated promoters important for the bacterial adaptation to oxidative stress.* J. Mol. Biol. **210**: 709-719.

127. Chae, H.Z., Robison, K., Poole, L.B., Church, G., Storz, G., and Rhee, S.G. (1994). *Cloning and sequencing of thiol-specific antioxidant from mammalian brain: alkyl hydroperoxide reductase and thiol-specific antioxidant define a large family of antioxidant enzymes.* Proc. Natl. Acad. Sci. **91**: 7017-7021.

128. Tartaglia, L.A., Storz, G., Brodsky, M.H., Lai, A., and Ames, B.N. (1990). *Alkyl hydroperoxide reductase from Salmonella typhimurium. Sequence and homology to thioredoxin reductase and other flavoprotein disulfide oxidoreductases.* J. Biol. Chem. **265**: 10535-10540.

129. Hofmann, B., Hecht, H.J., and Flohe, L. (2002). *Peroxiredoxins.* Biol. Chem. **383**: 347-364.

130. Link, A.J., Robison, K., and Church, G.M. (1997). *Comparing the predicted and observed properties of proteins encoded in the genome of Escherichia coli K-12.* Electrophoresis **18**: 1259-1313.

131. Jacobson, F.S., Morgan, R.W., Christman, M.F., and Ames, B.N. (1989). *An alkyl hydroperoxide reductase from Salmonella typhimurium involved in the defense of DNA against oxidative damage. Purification and properties.* J. Biol. Chem. **264**: 1488-1496.

132. Poole, L.B. (1996). *Flavin-dependent alkyl hydroperoxide reductase from Salmonella typhimurium. 2. Cystine disulfides involved in catalysis of peroxide reduction.* Biochemistry **35**: 65-75.

133. Rhee, S.G., Kang, S.W., Netto, L.E., Seo, M.S., and Stadtman, E.R. (1999). *A family of novel peroxidases, peroxiredoxins.* Biofactors **10**: 207-209.

134. Wood, Z.A., Poole, L.B., Hantgan, R.R., and Karplus, P.A. (2002). *Dimers to doughnuts: redox-sensitive oligomerization of 2-cysteine peroxiredoxins.* Biochemistry **41**: 5493-5504.

135. Wood, Z.A., Poole, L.B., and Karplus, P.A. (2001). *Structure of intact AhpF reveals a mirrored thioredoxin-like active site and implies large domain rotations during catalysis.* Biochemistry **40**: 3900-3911.

136. Poole, L.B., Godzik, A., Nayeem, A., and Schmitt, J.D. (2000). *AhpF can be dissected into two functional units: tandem repeats of two thioredoxin-like folds in the N-terminus mediate electron transfer from the thioredoxin reductase-like C-terminus to AhpC.* Biochemistry **39**: 6602-6615.

137. Bieger, B. and Essen, L.O. (2001). *Crystal structure of the catalytic core component of the alkylhydroperoxide reductase AhpF from Escherichia coli.* J. Mol. Biol. **307**: 1-8.

138. Waksman, G., Krishna, T.S., Williams, C.H., Jr., and Kuriyan, J. (1994). *Crystal structure of Escherichia coli thioredoxin reductase refined at 2 Å resolution. Implications for a large conformational change during catalysis.* J. Mol. Biol. **236**: 800-816.

139. Li Calzi, M. and Poole, L.B. (1997). *Requirement for the two AhpF cystine disulfide centers in catalysis of peroxide reduction by alkyl hydroperoxide reductase.* Biochemistry **36**: 13357-13364.

140. Reynolds, C.M. and Poole, L.B. (2000). *Attachment of the N-terminal domain of Salmonella typhimurium AhpF to Escherichia coli thioredoxin reductase confers AhpC reductase activity but does not affect thioredoxin reductase activity.* Biochemistry **39**: 8859-8869.

141. Ren, B., Tibbelin, G., de Pascale, D., Rossi, M., Bartolucci, S., and Ladenstein, R. (1998). *A protein disulfide oxidoreductase from the archaeon Pyrococcus furiosus contains two thioredoxin fold units.* Nat. Struct. Biol. **5**: 602-611.

142. Lennon, B.W., Williams, C.H., Jr., and Ludwig, M.L. (2000). *Twists in catalysis: alternating conformations of Escherichia coli thioredoxin reductase.* Science **289**: 1190-1194.

143. Reynolds, C.M. and Poole, L.B. (2001). *Activity of one of two engineered heterodimers of AhpF, the NADH:peroxiredoxin oxidoreductase from Salmonella typhimurium, reveals intrasubunit electron transfer between domains.* Biochemistry **40**: 3912-3919.

144. Poole, L.B. and Ellis, H.R. (1996). *Flavin-dependent alkyl hydroperoxide reductase from Salmonella typhimurium. 1. Purification and enzymatic activities of overexpressed AhpF and AhpC proteins.* Biochemistry **35**: 56-64.

145. Ellis, H.R. and Poole, L.B. (1997). *Roles for the two cysteine residues of AhpC in catalysis of peroxide reduction by alkyl hydroperoxide reductase from Salmonella typhimurium.* Biochemistry **36**: 13349-13356.

146. Kuriyan, J., Krishna, T.S., Wong, L., Guenther, B., Pahler, A., Williams, C.H., and Model, P. (1991). *Convergent evolution of similar function in two structurally divergent enzymes.* Nature **352**: 172-174.

147. Wood, Z.A., Schröder, E., Robin Harris, J., and Poole, L.B. (2003). *Structure, mechanism and regulation of peroxiredoxins.* Trends Biochem. Sci. **28**: 32-40.

148. Guimaraes, B.G., Souchon, H., Honore, N., Saint-Joanis, B., Brosch, R., Shepard, W., Cole, S.T., and Alzari, P.M. (2005). *Structure and mechanism of the alkyl hydroperoxidase AhpC, a key element of the Mycobacterium tuberculosis defense system against oxidative stress.* J. Biol. Chem. **280**: 25735-25742.

149. Kitano, K., Kita, A., Hakoshima, T., Niimura, Y., and Miki, K. (2005). *Crystal structure of decameric peroxiredoxin (AhpC) from Amphibacillus xylanus.* Proteins **59**: 644-647.

150. Papinutto, E., Windle, H.J., Cendron, L., Battistutta, R., Kelleher, D., and Zanotti, G. (2005). *Crystal structure of alkyl hydroperoxide-reductase (AhpC) from Helicobacter pylori.* Biochim. Biophys. Acta **1753**: 240-246.

151. Schröder, E., Littlechild, J.A., Lebedev, A.A., Errington, N., Vagin, A.A., and Isupov, M.N. (2000). *Crystal structure of decameric 2-Cys peroxiredoxin from human erythrocytes at 1.7 Å resolution.* Structure **8**: 605-615.

152. Tairum, C.A., Jr., de Oliveira, M.A., Horta, B.B., Zara, F.J., and Netto, L.E. (2012). *Disulfide biochemistry in 2-cys peroxiredoxin: requirement of Glu50 and Arg146 for the reduction of yeast Tsa1 by thioredoxin.* J. Mol. Biol. **424**: 28-41.

153. Wood, Z.A., Poole, L.B., and Karplus, P.A. (2003). *Peroxiredoxin evolution and the regulation of hydrogen peroxide signaling.* Science **300**: 650-653.

154. Flohe, L., Toppo, S., Cozza, G., and Ursini, F. (2011). *A comparison of thiol peroxidase mechanisms.* Antioxid. Redox Signal. **15**: 763-780.

155. Fourquet, S., Huang, M.E., D'Autreaux, B., and Toledano, M.B. (2008). *The dual functions of thiol-based peroxidases in* H_2O_2 *scavenging and signaling.* Antioxid. Redox Signal. **10**: 1565-1576.

156. Rhee, S.G., Chae, H.Z., and Kim, K. (2005). *Peroxiredoxins: a historical overview and speculative preview of novel mechanisms and emerging concepts in cell signaling.* Free Radic. Biol. Med. **38**: 1543-1552.

157. Ferrer-Sueta, G., Manta, B., Botti, H., Radi, R., Trujillo, M., and Denicola, A. (2011). *Factors affecting protein thiol reactivity and specificity in peroxide reduction.* Chem. Res. Toxicol. **24**: 434-450.

158. Hall, A., Parsonage, D., Poole, L.B., and Karplus, P.A. (2010). *Structural evidence that peroxiredoxin catalytic power is based on transition-state stabilization.* J. Mol. Biol. **402**: 194-209.

159. Nagy, P., Karton, A., Betz, A., Peskin, A.V., Pace, P., O'Reilly, R.J., Hampton, M.B., Radom, L., and Winterbourn, C.C. (2011). *Model for the exceptional reactivity of peroxiredoxins 2 and 3 with hydrogen peroxide: a kinetic and computational study.* J. Biol. Chem. **286**: 18048-18055.

160. Cha, M.K., Yun, C.H., and Kim, I.H. (2000). *Interaction of human thiol-specific antioxidant protein 1 with erythrocyte plasma membrane.* Biochemistry **39**: 6944-6950.

161. Rabilloud, T., Heller, M., Rigobello, M.P., Bindoli, A., Aebersold, R., and Lunardi, J. (2001). *The mitochondrial antioxidant defence system and its response to oxidative stress.* Proteomics **1**: 1105-1110.

162. Wagner, E., Luche, S., Penna, L., Chevallet, M., Van Dorsselaer, A., Leize-Wagner, E., and Rabilloud, T. (2002). *A method for detection of overoxidation of cysteines: peroxiredoxins are oxidized in vivo at the active-site cysteine during oxidative stress.* Biochem. J. **366**: 777-785.

163. Barranco-Medina, S., Lazaro, J.J., and Dietz, K.J. (2009). *The oligomeric conformation of peroxiredoxins links redox state to function.* FEBS Lett. **583**: 1809-1816.

164. Kumsta, C. and Jakob, U. (2009). *Redox-regulated chaperones.* Biochemistry **48**: 4666-4676.

165. Moon, J.C., Hah, Y.S., Kim, W.Y., Jung, B.G., Jang, H.H., Lee, J.R., Kim, S.Y., Lee, Y.M., Jeon, M.G., Kim, C.W., Cho, M.J., and Lee, S.Y. (2005). *Oxidative stress-dependent structural and functional switching of a human 2-Cys peroxiredoxin isotype II that enhances HeLa cell resistance to H_2O_2-induced cell death.* J. Biol. Chem. **280**: 28775-28784.

166. Amstad, P., Crawford, D., Muehlematter, D., Zbinden, I., Larsson, R., and Cerutti, P. (1990). *Oxidants stress induces the proto-oncogenes, C-fos and C-myc in mouse epidermal cells.* Bull. Cancer **77**: 501-502.

167. Cerutti, P.A. (1985). *Prooxidant states and tumor promotion.* Science **227**: 375-381.

168. Farr, S.B. and Kogoma, T. (1991). *Oxidative stress responses in Escherichia coli and Salmonella typhimurium.* Microbiol. Rev. **55**: 561-585.

169. Floyd, R.A. (1990). *Role of oxygen free radicals in carcinogenesis and brain ischemia.* FASEB J. **4**: 2587-2597.

170. Grüber, G., Godovac-Zimmermann, J., Link, T.A., Coskun, U., Rizzo, V.F., Betz, C., and Bailer, S.M. (2002). *Expression, purification, and characterization of subunit E, an essential subunit of the vacuolar ATPase.* Biochem. Biophys. Res. Commun. **298**: 383-391.

171. Goddard, T. and Kneller, D. (1997). *SPARKY 3, University of California, San Francisco, CA.*

172. Güntert, P., Mumenthaler, C., and Wüthrich, K. (1997). *Torsion angle dynamics for NMR structure calculation with the new program D.* J. Mol. Biol. **273**: 283-298.

173. Cornilescu, G., Delaglio, F., and Bax, A. (1999). *Protein backbone angle restraints from searching a database for chemical shift and sequence homology.* J. Biomol. NMR **13**: 289-302.

174. Koradi, R., Billeter, M., and Wüthrich, K. (1996). *MOLMOL: a program for display and analysis of macromolecular structures.* J. Mol. Graph. **14**: 51-55, 29-32.

175. DeLano, W. (2002). *The PyMOL Molecular Graphics System.* DeLano Scientific.

176. Zbyszek, O. and Wladek, M. (1997). *Processing of X-ray diffraction data collected in oscillation mode.* Meth. Enzymol. **276**: 307-326.

177. Murshudov, G.N., Vagin, A.A., and Dodson, E.J. (1997). *Refinement of macromolecular structures by the maximum-likelihood method.* Acta Crystallogr. D Biol. Crystallogr. **53**: 240-255.

178. Vagin, A. and Teplyakov, A. (2010). *Molecular replacement with MOLREP.* Acta Crystallogr. D Biol. Crystallogr. **66**: 22-25.

179. McCoy, A.J., Grosse-Kunstleve, R.W., Adams, P.D., Winn, M.D., Storoni, L.C., and Read, R.J. (2007). *Phaser crystallographic software.* J. Appl. Crystallogr. **40**: 658-674.

180. Brunger, A.T., Adams, P.D., Clore, G.M., DeLano, W.L., Gros, P., Grosse-Kunstleve, R.W., Jiang, J.S., Kuszewski, J., Nilges, M., Pannu, N.S., Read, R.J., Rice, L.M., Simonson, T., and Warren, G.L. (1998). *Crystallography & NMR system: A new software suite for macromolecular structure determination.* Acta Crystallogr. D Biol. Crystallogr. **54**: 905-921.

181. Emsley, P. and Cowtan, K. (2004). *Coot: model-building tools for molecular graphics.* Acta Crystallogr. D Biol. Crystallogr. **60**: 2126-2132.

182. Ramachandran, G.N., Ramakrishnan, C., and Sasisekharan, V. (1963). *Stereochemistry of polypeptide chain configurations.* J. Mol. Biol. **7**: 95-99.

183. Laskowski, R.A., MacArthur, M.W., Moss, D.S., and Thornton, J.M. (1993). *PROCHECK: a program to check the stereochemical quality of protein structures.* J. Appl. Crystallogr. **26**: 283-291.

184. Svergun, D. (1993). *A direct indirect method of small-angle scattering data treatment.* J. Appl. Crystallogr. **26**: 258-267.

185. Svergun, D.I., Petoukhov, M.V., and Koch, M.H. (2001). *Determination of domain structure of proteins from X-ray solution scattering.* Biophys. J. **80**: 2946-2953.

186. Tang, G., Peng, L., Baldwin, P.R., Mann, D.S., Jiang, W., Rees, I., and Ludtke, S.J. (2007). *EMAN2: an extensible image processing suite for electron microscopy.* J. Struct. Biol. **157**: 38-46.

187. Pettersen, E.F., Goddard, T.D., Huang, C.C., Couch, G.S., Greenblatt, D.M., Meng, E.C., and Ferrin, T.E. (2004). *UCSF Chimera--a visualization system for exploratory research and analysis.* J. Comput. Chem. **25**: 1605-1612.

188. Laemmli, U.K. (1970). *Cleavage of Structural Proteins during the Assembly of the Head of Bacteriophage T4.* Nature **227**: 680-685.

189. Thaker, Y.R., Hunke, C., Yau, Y.H., Shochat, S.G., Li, Y., and Grüber, G. (2009). *Association of the eukaryotic V1VO ATPase subunits a with d and d with A.* FEBS Lett. **583**: 1090-1095.

190. Manavalan, P. and Johnson, W.C. (1987). *Variable selection method improves the prediction of protein secondary structure from circular dichroism spectra.* Anal. Biochem. **167**: 76-85.

191. Sreerama, N. and Woody, R.W. (1993). *A Self-Consistent Method for the Analysis of Protein Secondary Structure from Circular Dichroism.* Anal. Biochem. **209**: 32-44.

192. Provencher, S.W. (1982). *A constrained regularization method for inverting data represented by linear algebraic or integral equations.* Comput. Phys. Commun. **27**: 213-227.

193. Andrade, M.A., Chacon, P., Merelo, J.J., and Moran, F. (1993). *Evaluation of secondary structure of proteins from UV circular dichroism spectra using an unsupervised learning neural network.* Protein Eng. Des. Sel. **6**: 383-390.

194. Deléage, G. and Geourjon, C. (1993). *An interactive graphic program for calculating the secondary structure content of proteins from circular dichroism spectrum.* Comput. Appl. Biosci. **9**: 197-199.

195. Bohm, G., Muhr, R., and Jaenicke, R. (1992). *Quantitative analysis of protein far UV circular dichroism spectra by neural networks.* Protein Eng. **5**: 191-195.

196. Boulin, C., Kempf, R., Koch, M.H.J., and McLaughlin, S.M. (1986). *Data appraisal, evaluation and display for synchrotron radiation experiments: Hardware and software.* Nucl. Instrum. Methods Phys. Res. A **249**: 399-407.

197. Roessle, M.W., Klaering, R., Ristau, U., Robrahn, B., Jahn, D., Gehrmann, T., Konarev, P., Round, A., Fiedler, S., Hermes, C., and Svergun, D. (2007). *Upgrade of the small-angle X-ray scattering beamline X33 at the European Molecular Biology Laboratory, Hamburg.* J. Appl. Crystallogr. **40**: s190-s194.

198. Round, A.R., Franke, D., Moritz, S., Huchler, R., Fritsche, M., Malthan, D., Klaering, R., Svergun, D.I., and Roessle, M. (2008). *Automated sample-changing robot for solution scattering experiments at the EMBL Hamburg SAXS station X33.* J. Appl. Crystallogr. **41**: 913-917.

199. Guinier, A. and Fournet, G. (1955). *Small-angle Scattering of X-rays.* Wiley, New York.

200. Srinivasan, S., Vyas, N.K., Baker, M.L., and Quiocho, F.A. (2011). *Crystal structure of the cytoplasmic N-terminal domain of subunit I, a homolog of subunit a, of V-ATPase.* J. Mol. Biol. **412**: 14-21.

201. Huey, R., Morris, G.M., Olson, A.J., and Goodsell, D.S. (2007). *A semiempirical free energy force field with charge-based desolvation.* J. Comput. Chem. **28**: 1145-1152.

202. Seeliger, D. and de Groot, B.L. (2010). *Ligand docking and binding site analysis with PyMOL and Autodock/Vina.* J. Comput. Aided Mol. Des. **24**: 417-422.

203. Renault, L., Guibert, B., and Cherfils, J. (2003). *Structural snapshots of the mechanism and inhibition of a guanine nucleotide exchange factor.* Nature **426**: 525-530.

204. Wüthrich, K. (1986). *NMR of Proteins and Nuclei acids.* Wiley, Interscience.

205. Liu, X., Jiang, W., Jakana, J., and Chiu, W. (2007). *Averaging tens to hundreds of icosahedral particle images to resolve protein secondary structure elements using a Multi-Path Simulated Annealing optimization algorithm.* J. Struct. Biol. **160**: 11-27.

206. Schäfer, I.B., Bailer, S.M., Düser, M.G., Börsch, M., Bernal, R.A., Stock, D., and Grüber, G. (2006). *Crystal Structure of the Archaeal* A_1A_O *ATP Synthase Subunit B from Methanosarcina mazei Gö1: Implications of Nucleotide-binding Differences in the Major* A_1A_O *Subunits A and B.* J. Mol. Biol. **358**: 725-740.

207. Battye, T.G., Kontogiannis, L., Johnson, O., Powell, H.R., and Leslie, A.G. (2011). *iMOSFLM: a new graphical interface for diffraction-image processing with MOSFLM.* Acta Crystallogr. D Biol. Crystallogr. **67**: 271-281.

208. Krissinel, E. and Henrick, K. (2004). *Secondary-structure matching (SSM), a new tool for fast protein structure alignment in three dimensions.* Acta Crystallogr. D Biol. Crystallogr. **60**: 2256-2268.

209. Nelson, K.J., Parsonage, D., Hall, A., Karplus, P.A., and Poole, L.B. (2008). *Cysteine pK(a) values for the bacterial peroxiredoxin AhpC.* Biochemistry **47**: 12860-12868.

210. McGuffin, L., Bryson, K., and Jones, D. (2000). *The PSIPRED protein structure prediction server.* Bioinformatics **16**: 404-405.

211. Page, R., Peti, W., Wilson, I.A., Stevens, R.C., and Wüthrich, K. (2005). *NMR screening and crystal quality of bacterially expressed prokaryotic and eukaryotic proteins in a structural genomics pipeline.* Proc. Natl. Acad. Sci. **102**: 1901-1905.

212. Waterhouse, A.M., Procter, J.B., Martin, D.M., Clamp, M., and Barton, G.J. (2009). *Jalview Version 2--a multiple sequence alignment editor and analysis workbench.* Bioinformatics **25**: 1189-1191.

213. Svergun, D.I. (1999). *Restoring Low Resolution Structure of Biological Macromolecules from Solution Scattering Using Simulated Annealing.* Biophys. J. **76**: 2879-2886.

214. Matthews, B.W. (1968). *Solvent content of protein crystals.* J. Mol. Biol. **33**: 491-497.

215. Krissinel, E. and Henrick, K. (2007). *Inference of macromolecular assemblies from crystalline state.* J. Mol. Biol. **372**: 774-797.

216. Stein, N. (2008). *CHAINSAW: a program for mutating pdb files used as templates in molecular replacement.* J. Appl. Crystallogr. **41**: 641-643.

217. Terwilliger, T. (2004). *Using prime-and-switch phasing to reduce model bias in molecular replacement.* Acta Crystallogr. D Biol. Crystallogr. **60**: 2144-2149.

218. Kleywegt, G.J. (2007). *Quality control and validation.* Methods Mol. Biol. **364**: 255-272.

219. Mossessova, E., Gulbis, J.M., and Goldberg, J. (1998). *Structure of the guanine nucleotide exchange factor Sec7 domain of human arno and analysis of the interaction with ARF GTPase.* Cell **92**: 415-423.

220. Cherfils, J., Menetrey, J., Mathieu, M., Le Bras, G., Robineau, S., Beraud-Dufour, S., Antonny, B., and Chardin, P. (1998). *Structure of the Sec7 domain of the Arf exchange factor ARNO.* Nature **392**: 101-105.

221. Murata, T., Yamato, I., Kakinuma, Y., Leslie, A.G., and Walker, J.E. (2005). *Structure of the rotor of the V-Type Na^+-ATPase from Enterococcus hirae.* Science **308**: 654-659.

222. Clague, M.J., Urbe, S., Aniento, F., and Gruenberg, J. (1994). *Vacuolar ATPase activity is required for endosomal carrier vesicle formation.* J Biol. Chem. **269**: 21-24.

223. Ochotny, N., Van Vliet, A., Chan, N., Yao, Y., Morel, M., Kartner, N., von Schroeder, H.P., Heersche, J.N., and Manolson, M.F. (2006). *Effects of human a3 and a4 mutations that result in osteopetrosis and distal renal tubular acidosis on yeast V-ATPase expression and activity.* J. Biol. Chem. **281**: 26102-26111.

224. Smith, A.N., Finberg, K.E., Wagner, C.A., Lifton, R.P., Devonald, M.A., Su, Y., and Karet, F.E. (2001). *Molecular cloning and characterization of Atp6n1b: a novel fourth murine vacuolar* H^+*-ATPase a-subunit gene.* J. Biol. Chem. **276**: 42382-42388.

225. Kota, Z., Pali, T., Dixon, N., Kee, T.P., Harrison, M.A., Findlay, J.B., Finbow, M.E., and Marsh, D. (2008). *Incorporation of transmembrane peptides from the vacuolar* $H(^+)$*-ATPase in phospholipid membranes: spin-label electron paramagnetic resonance and polarized infrared spectroscopy.* Biochemistry **47**: 3937-3949.

226. Leng, X.H., Nishi, T., and Forgac, M. (1999). *Transmembrane topography of the 100-kDa a subunit (Vph1p) of the yeast vacuolar proton-translocating ATPase.* J. Biol. Chem. **274**: 14655-14661.

227. Seaver, L.C. and Imlay, J.A. (2001). *Alkyl hydroperoxide reductase is the primary scavenger of endogenous hydrogen peroxide in Escherichia coli.* J. Bacteriol. **183**: 7173-7181.

228. Dip, P.V., Kamariah, N., Balakrishna, A.M., Manimekalai, M.S.S., Kostyuchenko, V.A., Ng, J.T.S., Lok, S.M., Roessle, M., Eisenhaber, B., Eisenhaber, F., and Grüber, G. (2013). *The structural plasticity of AhpR during the catalysis mechanism enables the E. coli cell survival under oxidative and acidic stressors.* in preparation.

229. Gerstein, M. and Krebs, W. (1998). *A database of macromolecular motions.* Nucleic Acids Res. **26**: 4280-4290.

230. Ma, J., Sigler, P.B., Xu, Z., and Karplus, M. (2000). *A dynamic model for the allosteric mechanism of GroEL.* J. Mol. Biol. **302**: 303-313.

231. Campbell, I.D. and Humphries, M.J. (2011). *Integrin structure, activation, and interactions.* Cold Spring Harb. Perspect. Biol. **3**.

232. Gerstein, M., Anderson, B.F., Norris, G.E., Baker, E.N., Lesk, A.M., and Chothia, C. (1993). *Domain closure in lactoferrin. Two hinges produce a see-saw motion between alternative close-packed interfaces.* J. Mol. Biol. **234**: 357-372.

233. Hanukoglu, I. and Gutfinger, T. (1989). *cDNA sequence of adrenodoxin reductase. Identification of NADP-binding sites in oxidoreductases.* Eur. J. Biochem. **180**: 479-484.

234. Wierenga, R.K., Terpstra, P., and Hol, W.G. (1986). *Prediction of the occurrence of the ADP-binding beta alpha beta-fold in proteins, using an amino acid sequence fingerprint.* J. Mol. Biol. **187**: 101-107.

235. Jonsson, T.J., Ellis, H.R., and Poole, L.B. (2007). *Cysteine reactivity and thiol-disulfide interchange pathways in AhpF and AhpC of the bacterial alkyl hydroperoxide reductase system.* Biochemistry **46**: 5709-5721.

236. Chauhan, R. and Mande, S.C. (2001). *Characterization of the Mycobacterium tuberculosis H37Rv alkyl hydroperoxidase AhpC points to the importance of ionic interactions in oligomerization and activity.* Biochem. J. **354**: 209-215.

237. Kitano, K., Niimura, Y., Nishiyama, Y., and Miki, K. (1999). *Stimulation of peroxidase activity by decamerization related to ionic strength: AhpC protein from Amphibacillus xylanus.* J. Biochem. **126**: 313-319.

238. Nogoceke, E., Gommel, D.U., Kiess, M., Kalisz, H.M., and Flohe, L. (1997). *A unique cascade of oxidoreductases catalyses trypanothione-mediated peroxide metabolism in Crithidia fasciculata.* Biol. Chem. **378**: 827-836.

239. Parsonage, D., Youngblood, D.S., Sarma, G.N., Wood, Z.A., Karplus, P.A., and Poole, L.B. (2005). *Analysis of the link between enzymatic activity and oligomeric state in AhpC, a bacterial peroxiredoxin.* Biochemistry **44**: 10583-10592.

240. Logan, C. and Mayhew, S.G. (2000). *Cloning, overexpression, and characterization of peroxiredoxin and NADH peroxiredoxin reductase from Thermus aquaticus.* J. Biol. Chem. **275**: 30019-30028.

7. Author's publication related to the projects

Merkulova, M., McKee, M., **Dip, P.V.**, Grüber, G., and Marshansky, V. (2010). *N-terminal domain of the V-ATPase a2-subunit displays integral membrane protein properties.* Protein Sci. **19**: 1850-1862.

Dip, P.V., Saw, W.G., Roessle, M., Marshansky, V., and Grüber, G. (2012). *Solution structure of subunit a, $a_{104-363}$, of the Saccharomyces cerevisiae V-ATPase and the importance of its C-terminus in structure formation.* J. Bioenerg. Biomembr. **44**: 341-350.

Hosokawa, H., **Dip, P.V.**, Merkulova, M., Bakulina, A., Zhuang, Z., Khatri, A., Jian, X., Keating, S.M., Bueler, S.A., Rubinstein, J.L., Randazzo, P.A., Ausiello, D.A., Grüber, G., and Marshansky, V. (2013). *The N termini of a-subunit isoforms are involved in signaling between vacuolar H^+-ATPase (V-ATPase) and cytohesin-2.* J. Biol. Chem. **288**: 5896-5913.

Merkulova, M., Bakulina, A., **Dip, P.V.**, Thaker, Y.R., Hosokawa, H., Grüber, G., and Marshansky, V. (2013). *Structural model of a2-subunit N-terminus and its binding interface for cytohesin-2: Implication for regulation of V-ATPase function.* in preparation.

Dip, P.V., Kamariah, N., Balakrishna, A.M., Manimekalai, M. S. S., Kostyuchenko, V.A., Ng, J.T.S., Lok, S.M., Roessle, M., Eisenhaber, B., Eisenhaber, F., and Grüber, G. (2013). *The structural plasticity of AhpR during the catalytic mechanism enables the E. coli cell survival under oxidative and acidic stressors.* in preparation.

8. Conference attendance

"Satellite meeting of the 15th International photosynthesis congress", Singapore (18th to 20th August 2010).

9. Posters and Abstracts

Joint 6th International Conference on Structural Biology and Functional Genomics, National University of Singapore (NUS), Singapore from 6th-8thDec. 2010
Title: "*Structural and functional insights of subunit a of V-ATPase*".

50th Annual Meeting of the American Society for Cell Biology (ASCB), Philadelphia, Pennsylvania, USA from 11th-15th Dec. 2010
Title: "*V-ATPase modulates enzymatic activity of Arf-GEF ARNO and controls protein degradative* pathway".

17th European Bioenergetics Conference (EBEC), Albert-Ludwigs University of Freiburg, Germany from 15th – 20th Sep. 2012
Title: "*Structural insights into subunit a, $a_{104-363}$, of the Saccharomyces cerevisiae V-ATPase*". Biochim. Biophys. Acta **1817**: S144–S153

125th Anniversary - Annual Meeting at Experimental Biology (EB), Boston, Massachusetts, USA from 20th – 24th Apr. 2013
Poster A - Title: "*V-ATPase is a novel evolutionarily conserved cytohesin-signaling receptor*."
Poster B - Title:" *Structural model of a2-subunit N-terminus and its binding interface for cytohesin-2: Implication for regulation of V-ATPase function*."

10. Awards

Singapore International Graduate Award (SINGA) 2009-2013
(Scholar Ref. Number: 20092010S10303)